ATTACHMENT III – FIGURES

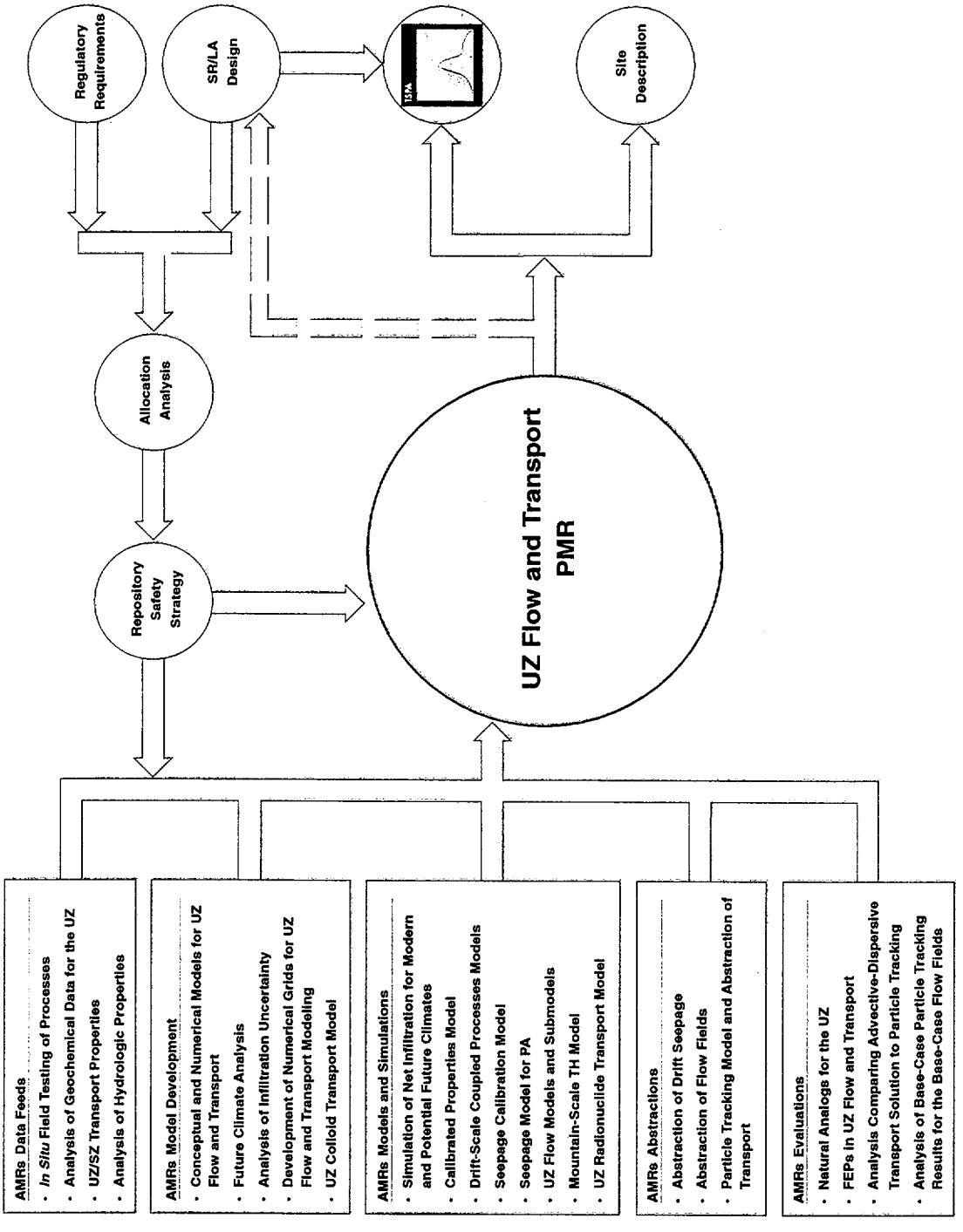

Figure 1-1. Schematic Diagram Showing the Relationships among Major YMP Documents, Including Analysis/Model Reports (AMRs), PMRs, SDs, SRR, and TSPA Documents

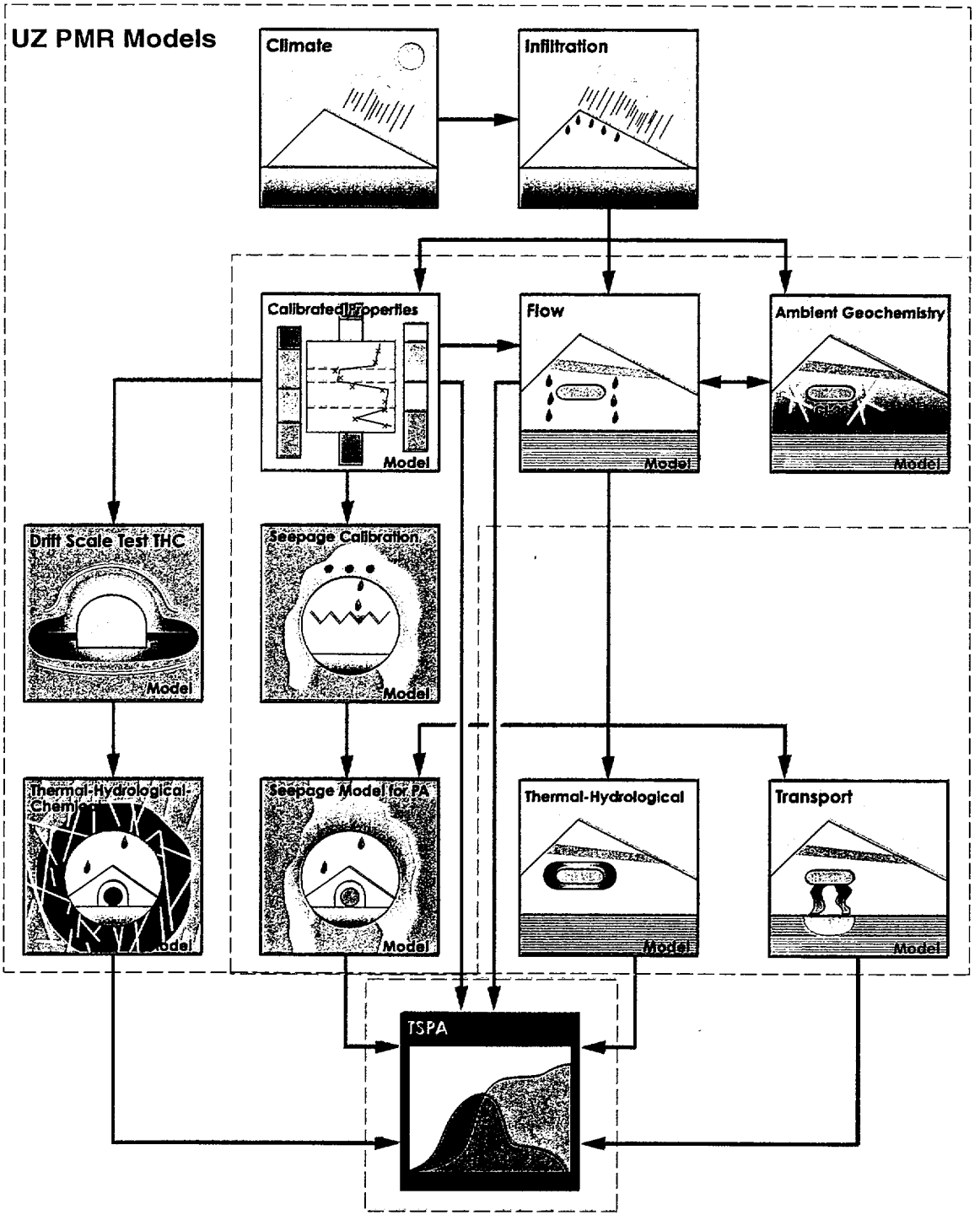

Figure 1-2. Main Models Included in the UZ PMR, Their Interrelations, and Their Connections to TSPA

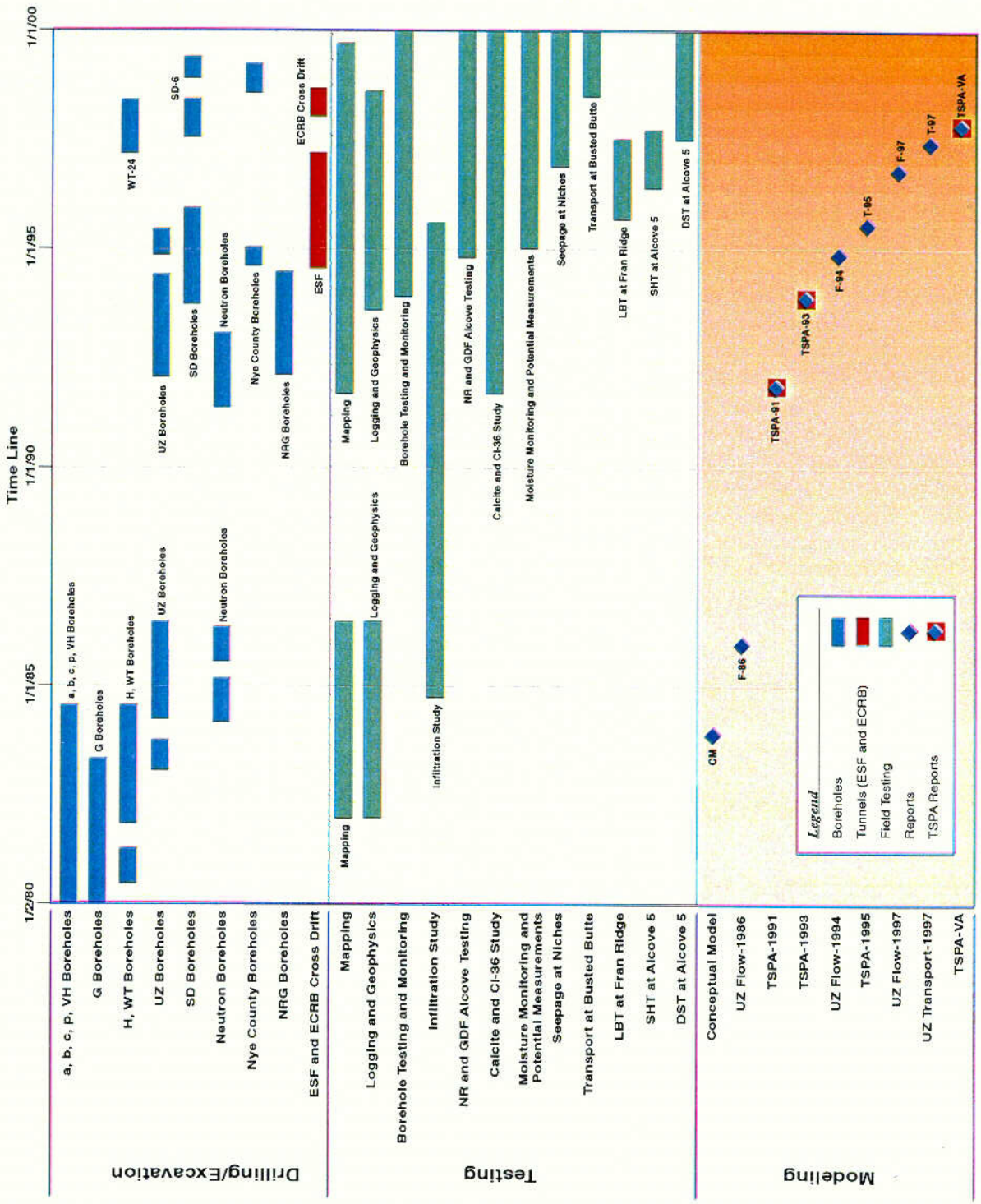

Figure 2.1-1. Chronology of Drilling/Excavation, Testing, and Modeling Activities of the UZ Site Characterization Program at Yucca Mountain

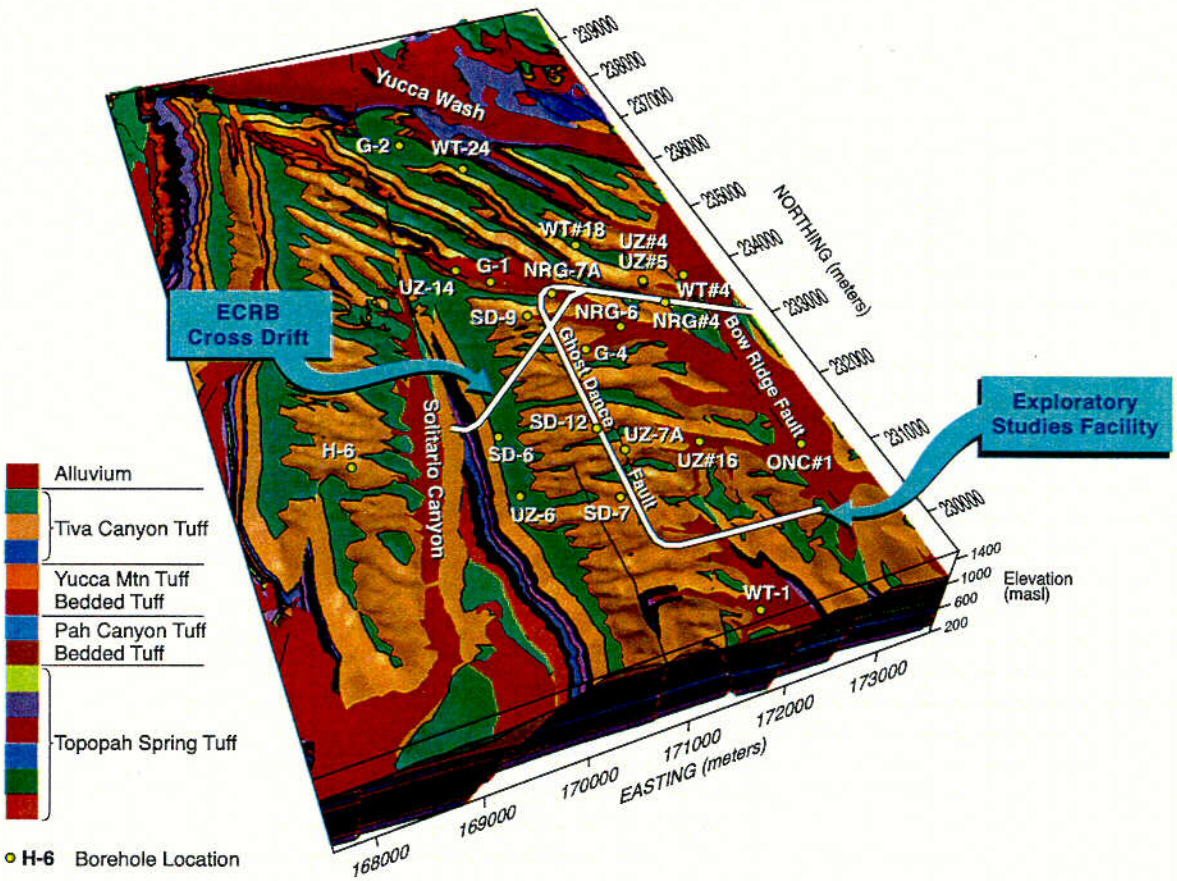

Figure 2.1-2. Schematic Illustration of the Main Surface-Based Deep Boreholes and Underground Drifts of the ESF, and the Major Faults in the Vicinity of Yucca Mountain

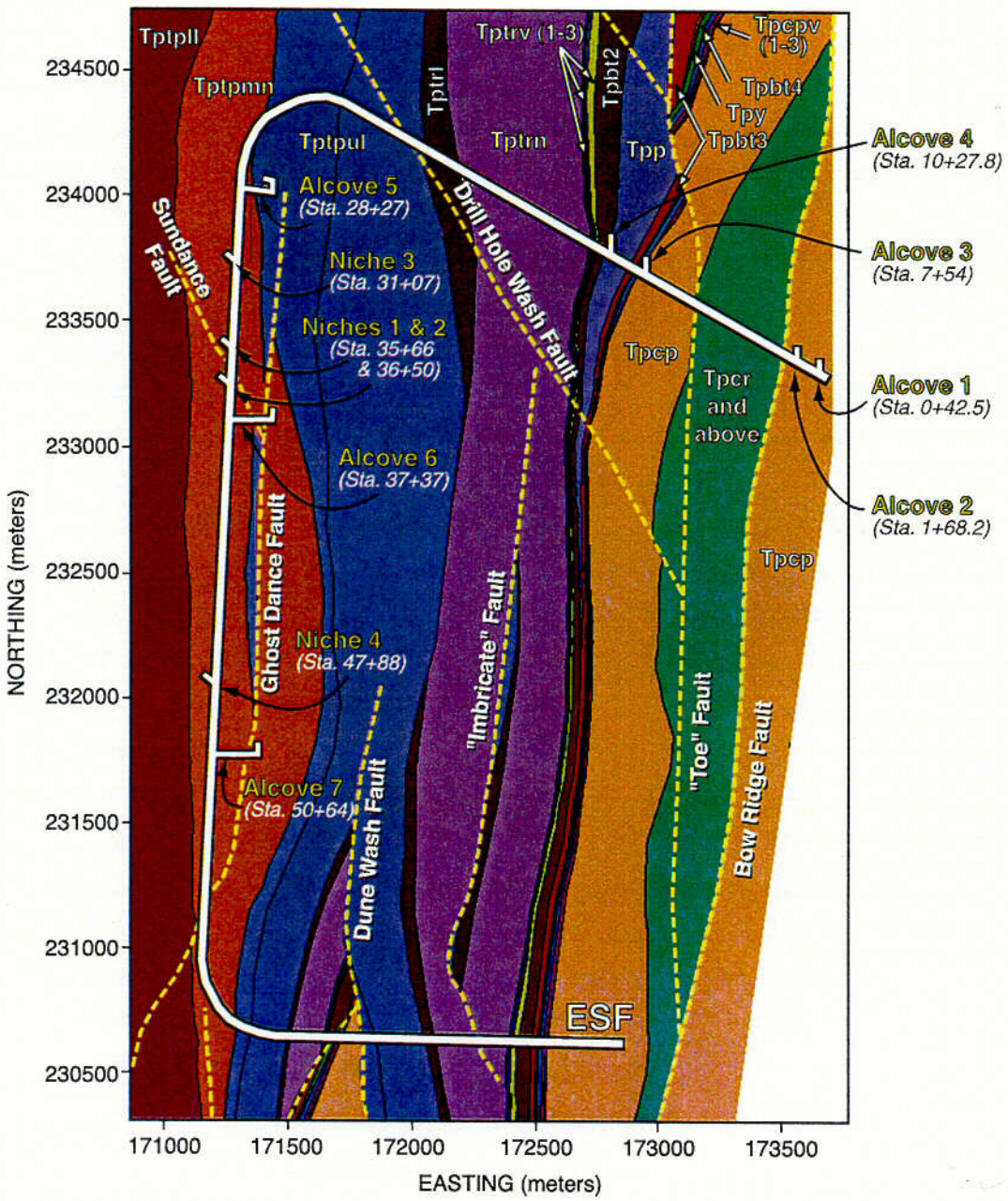

Figure 2.1-3. Schematic Illustration of Alcove and Niche Locations in the Exploratory Studies Facility at Yucca Mountain

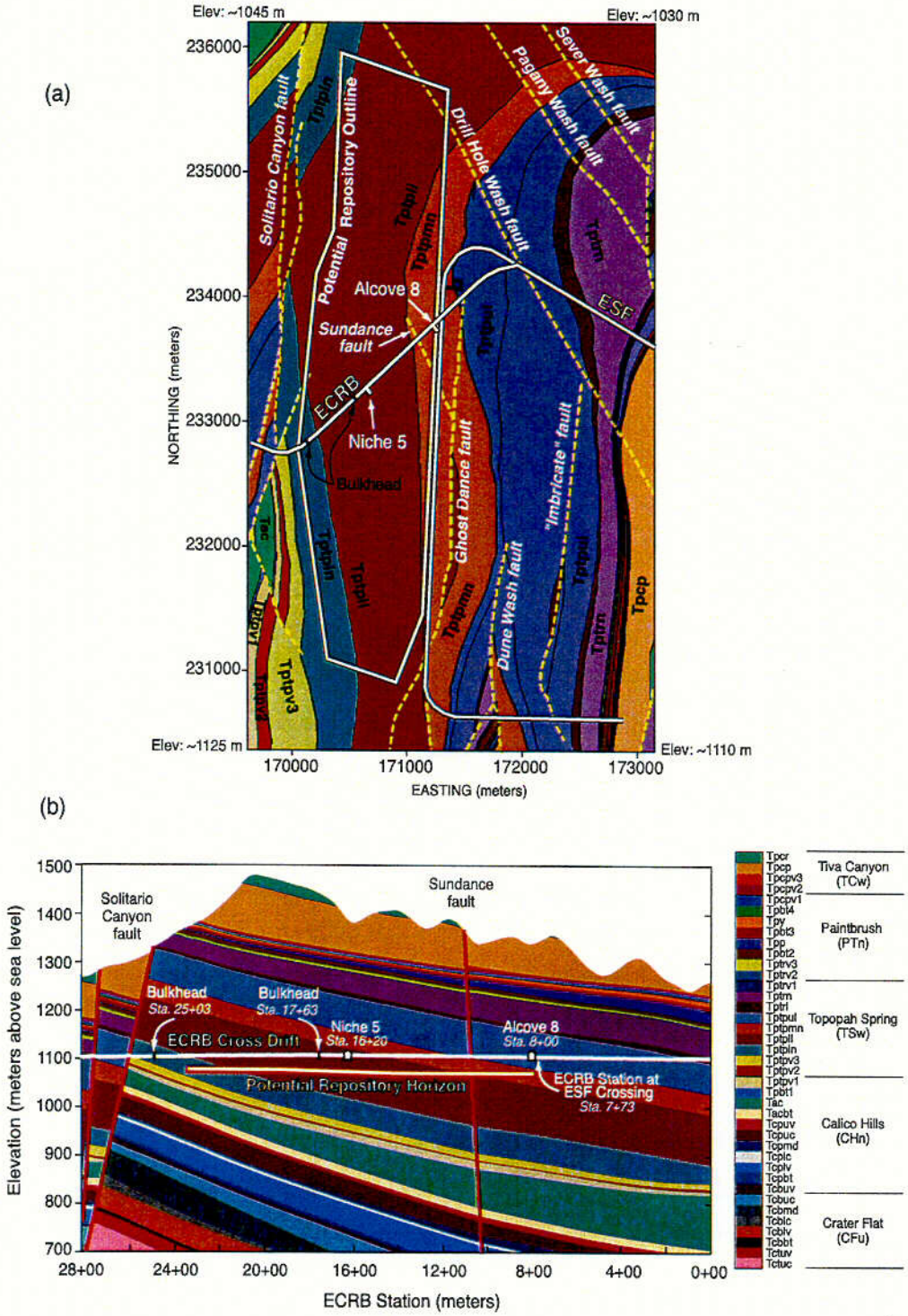

Figure 2.1-4. Schematic Illustration of the ECRB Cross Drift, Geological Units and Test Sites. (a) Generalized geological map at the Cross Drift level. (b) Generalized geological cross-section along the ECRB Cross Drift, showing the potential repository horizon.

Geologic Mapping and Geophysical Studies on Surface and in ESF

(a) Drilling of Borehole SD-6 on the Crest of Yucca Mountain

(b) Pavement Cleared for Ghost Dance Fault Mapping

Objectives:
- Determine lithology and structural features of tuff units.
- Evaluate distribution of fractures and faults.

Approaches:
- Map features on bedrock, in trenches, and along ESF drifts.
- Conduct geophysical logging along boreholes.
- Deploy geophysical tomographic imaging techniques on the surface and in underground drifts.

Results:
- Refined geological maps of bedrock, washes and faults.
- Improved geological framework of tuff layers and fault offsets.
- Detailed line surveys and full peripheral maps along drifts.
- Interpreted fracture density distributions between surface and underground drifts.

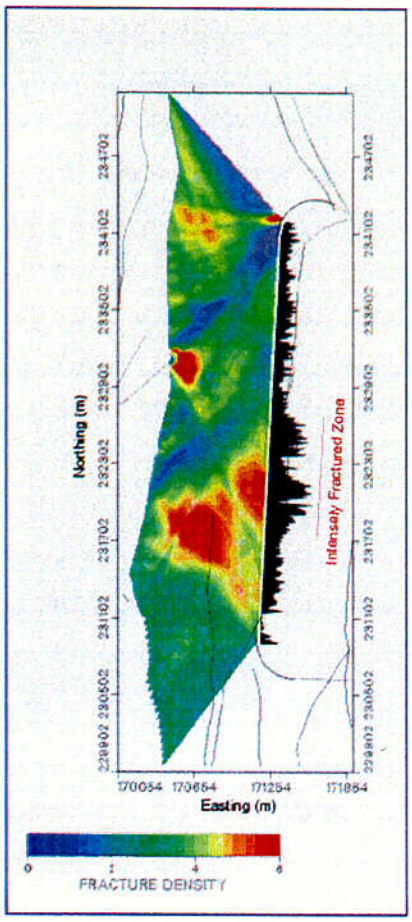

(c) Fracture Density Distributions by Detailed Line Survey and Seismic Tomograph

Figure 2.2-1. Geological and Geophysical Studies on the Surface and along the ESF

Infiltration Study on the Bedrock and in Washes

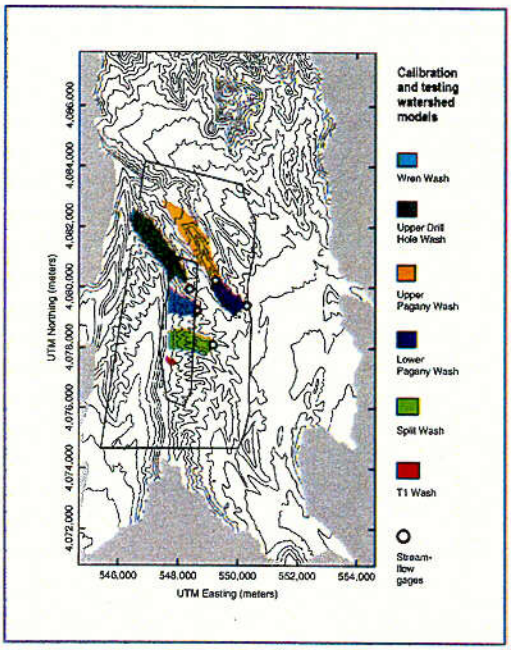

(a) Location of Washes Instrumented for Watershed Study

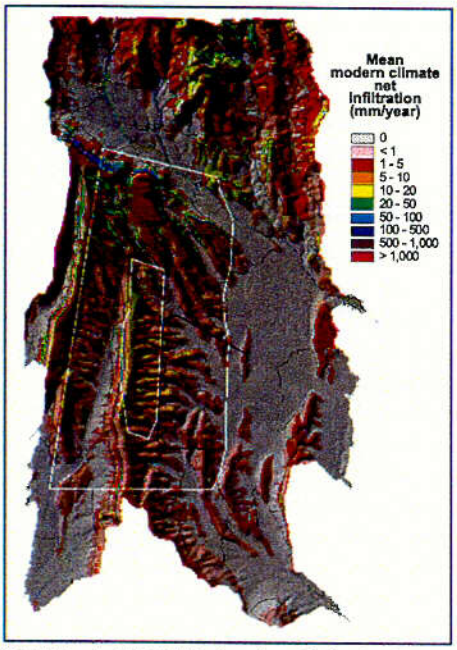

(b) Estimated Net Infiltration (mm/yr) for the Mean Modern Climate Scenario

Objectives:
- Provide upper boundary conditions for UZ Flow and Transport Model.
- Evaluate infiltration processes and mechanisms for determining net infiltration under current dry and future wet conditions.

Approaches:
- Conduct periodic neutron logging in network of shallow boreholes.
- Record climate changes and evaluate evapotranspiration potentials.
- Instrument washes to evaluate run-on and run-off processes.

(c) Neutron Logging at Pagany Wash

Results:
- Improved infiltration maps for current, monsoon, and glacial-transition climates.
- Quantification of relationships between precipitation and net infiltration.
- Quantification of downward flux and lateral run-on and run-off processes.

Figure 2.2-2. Infiltration Study on the Bedrock and in Washes (USGS 2000, U0010, Sections 6.3 and 7.1)

Drift Seepage Test at Niche 3650

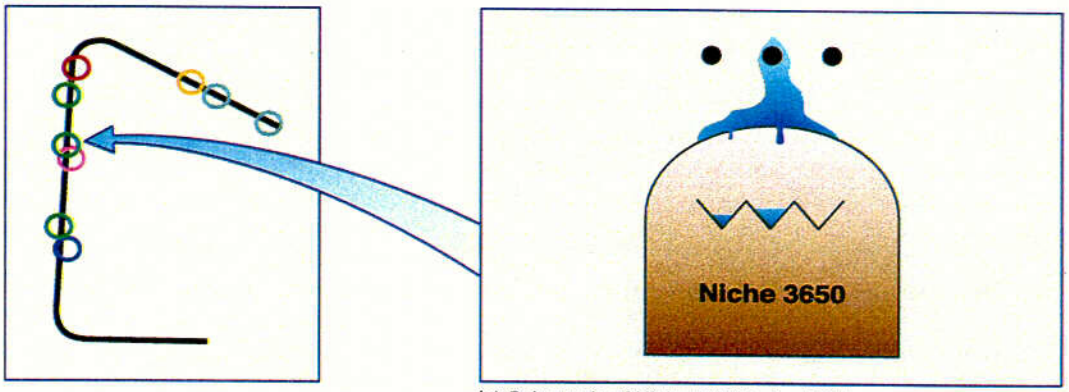

(a) Schematic of Niche 3650 in the ESF

Objectives:
- Quantify seepage threshold below which no seepage occurs.
- Evaluate capillary barrier mechanism and measure drift-scale parameters.

Approaches:
- Use air injection tests to characterize the niche site with resolution of 0.3-m scale (one tenth of drift dimensions).
- Use pulse releases to represent episodic percolation events.
- Determine seepage thresholds by sequences of liquid releases with reducing rates.
- Derive in situ fracture characteristic curves with wetting front arrival analyses.

Results:
- Measured seepage threshold ranges from 200 mm/yr to 136,000 mm/yr at localized release intervals.
- Six out of sixteen tested intervals did not seep.
- Observed both flow along high-angle fractures and flow through fracture network.
- Derived fracture capillary parameters and characteristic curves, with equivalent fracture porosity as high as 2.4%.

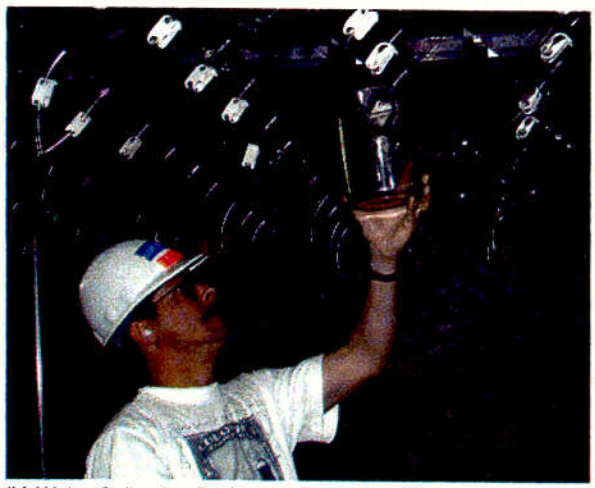

(b) Water Collection During a Drift Seepage Test

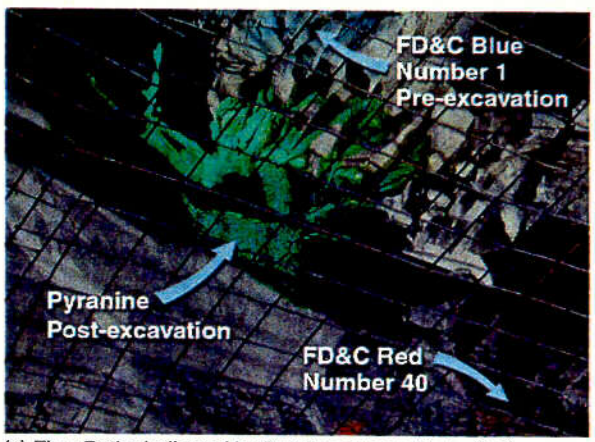

(c) Flow Paths Indicated by Dye Tracers on Niche Ceiling

Figure 2.2-3. Drift Seepage Test at Niche 3650 (CRWMS M&O 2000, U0015, Section 6.2.)

In Situ Wet Feature Observed at Niche 3566

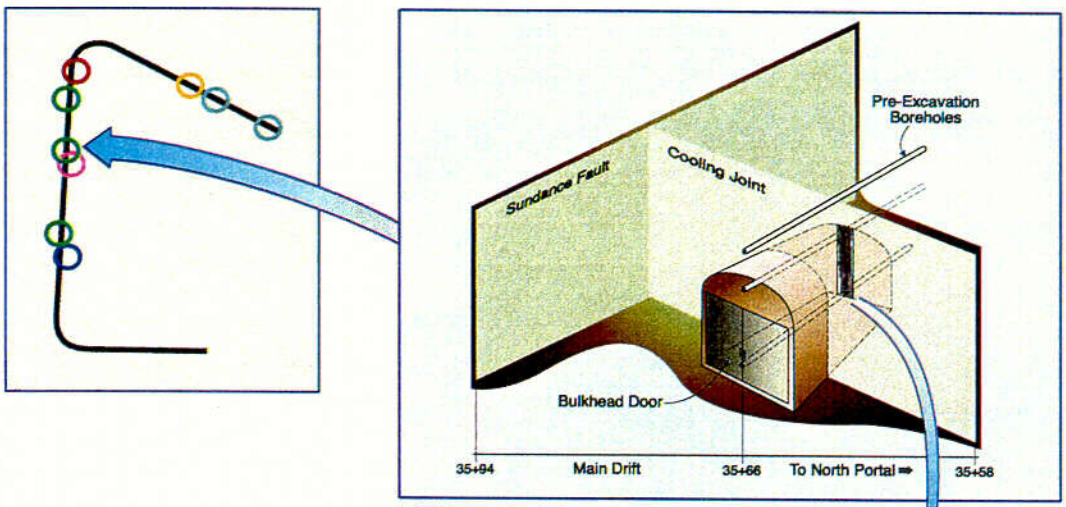

(a) Schematic of Sealed Niche 3566 in the ESF

Objectives:

- Characterize the hydrologic setting of a site with bomb-pulse ^{36}Cl signals, the Sundance fault and its first cooling joint.
- Quantify seepage processes.

Approaches:

- Mine the niche without spreading water to the ceiling during excavation.
- Close the bulkhead to prevent moisture removal by ventilation.
- Monitor the rock and drift over long time periods.

Results:

- One damp feature observed after dry excavation at end of the niche. It dried up before bulkhead installation and did not rewet after long-term monitoring over two years.

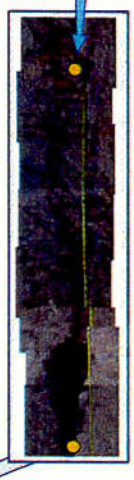

(b) Photograph of a Damp Feature in the Brecciated Zone at the Back of Niche 3566

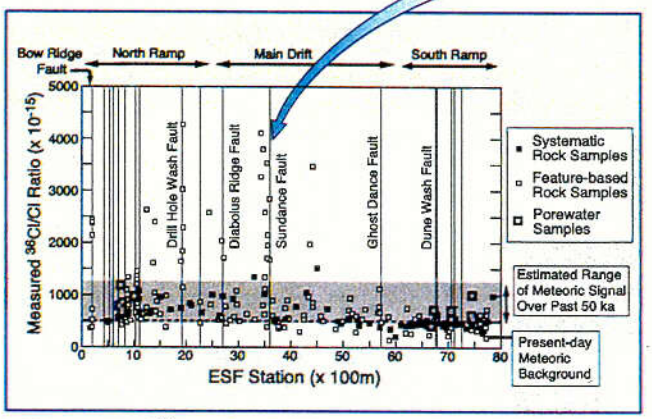

(c) Distribution of $^{36}Cl/Cl$ in the ESF

Figure 2.2-4. Damp Feature Observed during Dry Excavation of Niche 3566 and Bomb-Pulse $^{36}Cl/Cl$ Signals along the ESF (Wang et al. 1999, pp. 331–332; CRWMS M&O 2000, U0085, Section 6.6)

Drift Seepage Test at ECRB Cross Drift Niche 1620

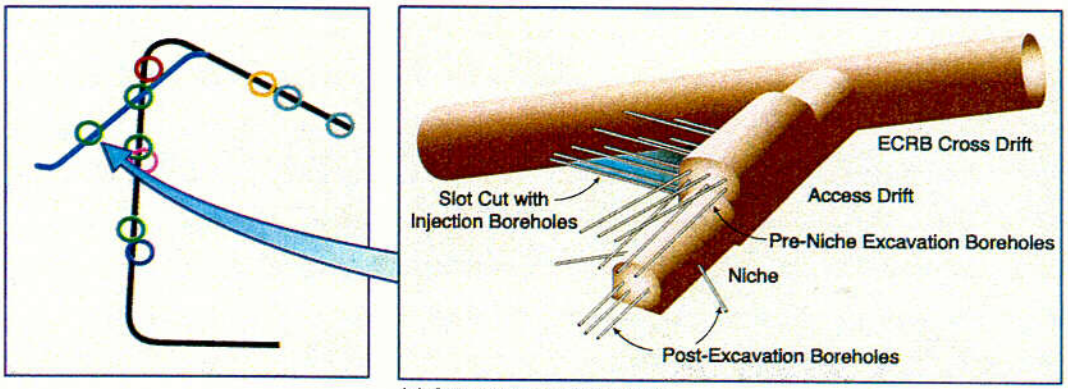

(a) Schematic of Niche 3107

Objectives:

- Quantify seepage into drift in the lower lithophysal unit at a cavity-rich zone.
- Characterize the pneumatic and liquid flows in the presence of lithophysal cavities and porous tuff.
- Determine the differences between lower lithophysal unit and middle non-lithophysal unit of the potential repository rock.
- Quantify fracture-matrix interaction at lower lithophysal unit.

Approaches:

- Observe flow paths during dry excavation, use air-injection tests to characterize liquid release intervals, and conduct drift seepage tests with liquid releases at different rates.
- Adopt, improve, and extend the methodologies used in tests conducted in the middle non-lithophysal niches and test beds.

Results:

- Pre-excavation air-injection test results suggest that lower lithophysal unit has higher permeability than middle non-lithophysal unit.
- Access drift has been excavated with an Alpine Miner.
- Seepage tests are prepared to be conducted after niche excavations.

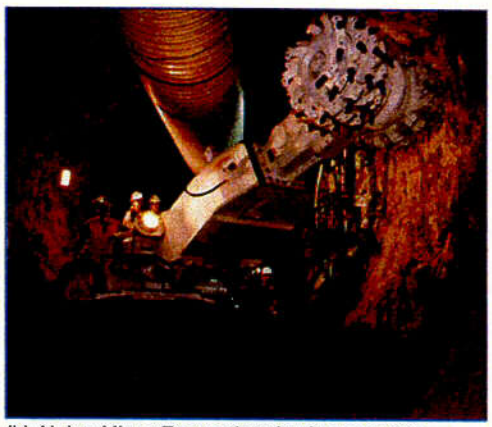

(b) Alpine Miner Excavating the Access Drift

(c) Example of a Cavity in the Lower Lithophysal Tuff Unit

(d) Scanner Image along Borehole AK-1 at Niche1620

Figure 2.2-5. Lower Lithophysal Seepage Test at ECRB Cross Drift Niche 1620

Fracture-Matrix Interaction Test at Alcove 6

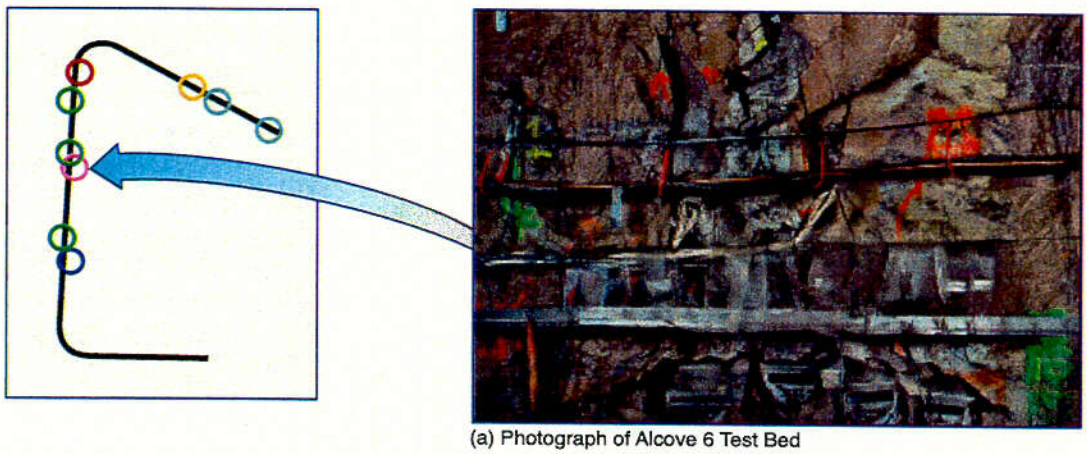

(a) Photograph of Alcove 6 Test Bed

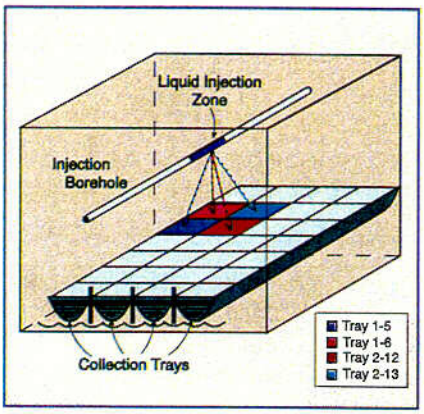

(c) Schematic of Liquid Release Test

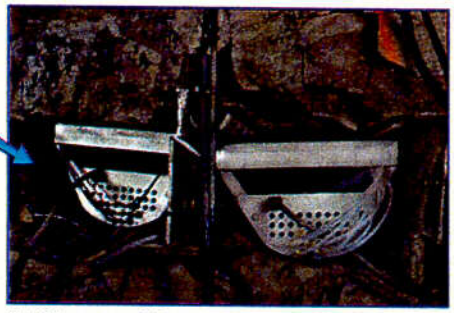

(b) Close-up of Trays on the Slot

Objectives:

- Quantify fracture-matrix interaction and the fraction of fracture flow.

Approaches:

- Use a slot below boreholes to capture fracture flows.
- Estimate the fracture/matrix flow partitioning by mass balance.
- Use borehole sensors to detect wetting front arrivals.

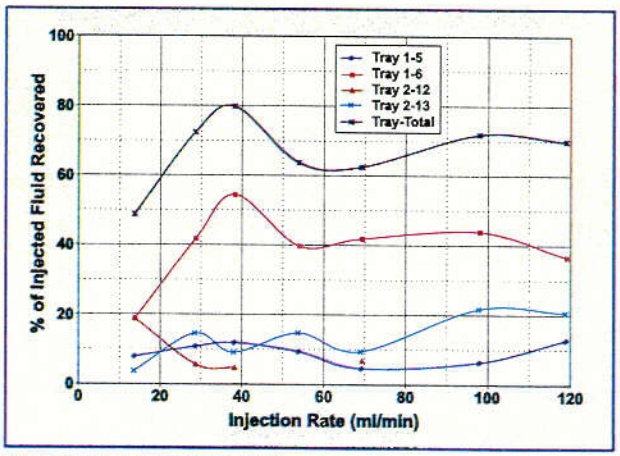

(d) Water Collected in the Slot

Results:

- A maximum of 80% of injected water was recovered for high-rate injection tests (i.e. 80% fracture flow).
- Out flows occurred in step increments which could be related to water stored in fracture flow paths.

Figure 2.2-6. Fracture-Matrix Interaction Test at Alcove 6 (CRWMS M&O 2000, U0015, Section 6.6)

Fault Flow Damping Test at Alcove 4

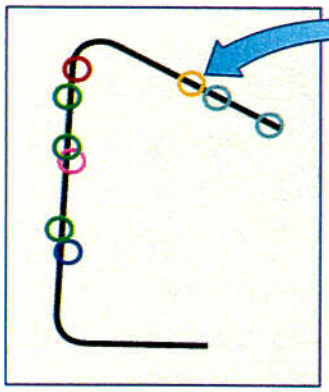

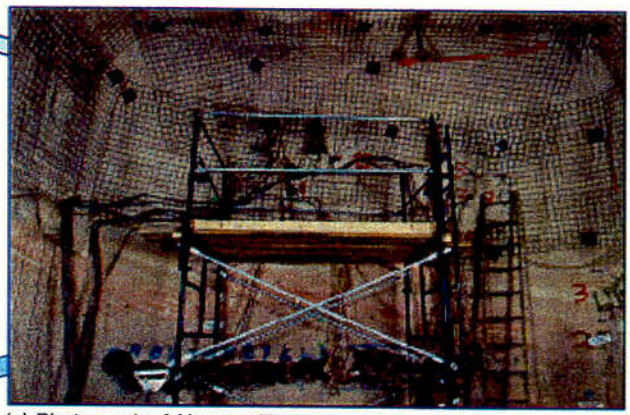

(a) Photograph of Alcove 4 Test Bed

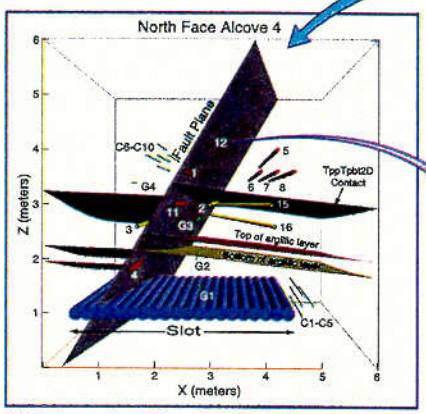

(c) Schematic of Boreholes at Alcove 4

(b) Close-up of Tray on the Left-Hand Side of the Slot

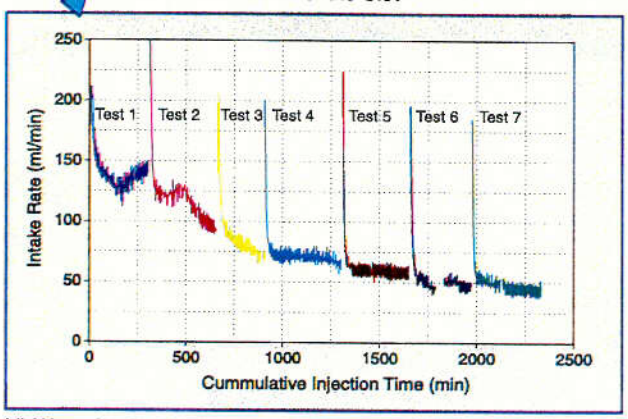

(d) Water Intake Rate at a PTn Fault

Objectives:

- Evaluate flow mechanism in the Paintbrush nonwelded tuff unit.
- Quantify the damping and lateral diversion processes along a fault and along bedded tuff interfaces.

Approaches:

- Select a test bed containing bedded tuff layers (including an argillic layer), a fault, and a fracture.
- Release water under constant-head conditions to determine the intake rates.
- Monitor wetting front arrivals and measure potential changes in boreholes.

Results:

- Water intake rate in the fault decreased as more water was introduced into the release zone.
- Clay swelling is one mechanism proposed to interpret the field data.
- Detection of down-gradient increases in saturation occurred over shorter time intervals with each liquid release test.

Figure 2.2-7. Paintbrush Fault and Porous Matrix Test at Alcove 4 (CRWMS M&O 2000, U0015, Section 6.7)

El Niño Infiltration Test at Alcove 1

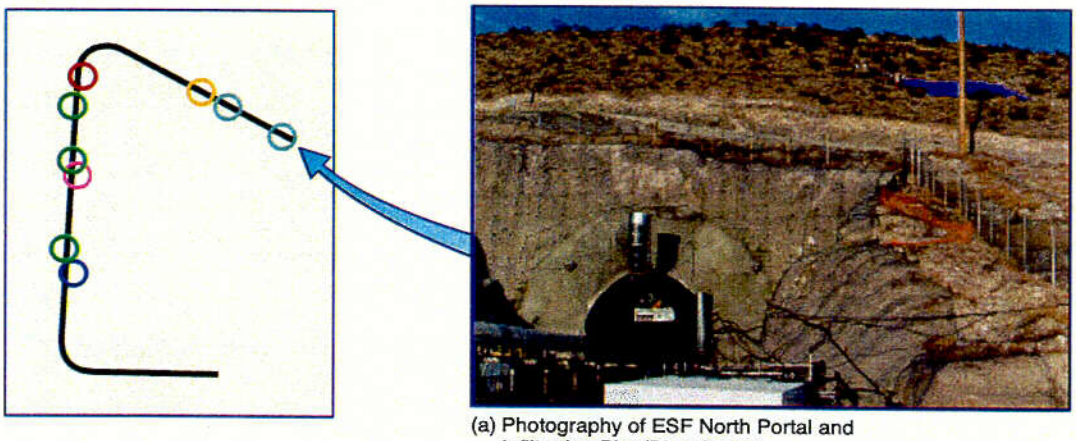

(a) Photography of ESF North Portal and Infiltration Plot (Blue Cover)

Objectives:

- Quantify large-scale infiltration and seepage processes in the bedrock.
- Evaluate matrix diffusion mechanism in long-term flow and transport tests.

Approaches:

- Water applied on the surface 30 m directly above the alcove.
- Tests conducted in two phases: March - August 1998 and May 1999 - present, with Phase 1 focusing on flow and Phase 2 focusing on tracer transport.

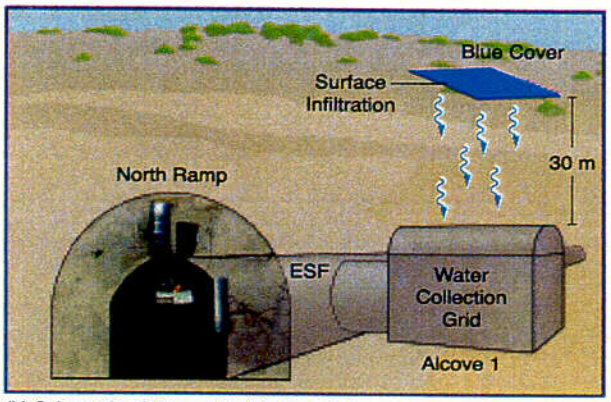

(b) Schematic of Alcove 1 Infiltration Test

Results:

- Over 100,000 liters infiltrated in Phase 1, with observed seepage rates of up to 300 liter/day.
- First seepage was observed 58 days after Phase 1 test initiation. Pressure/flow response of the system was observed to be ~2 days once a nearly steady-state system had developed.
- High concentrations of LiBr were used in Phase 2 tracer test.
- First tracer breakthrough in Phase 2 observed in 28 days with a nearly steady-state flow system using a conservative tracer.
- Tracer recovery data were used to compare with model predictions and to evaluate the importance of matrix diffusion.

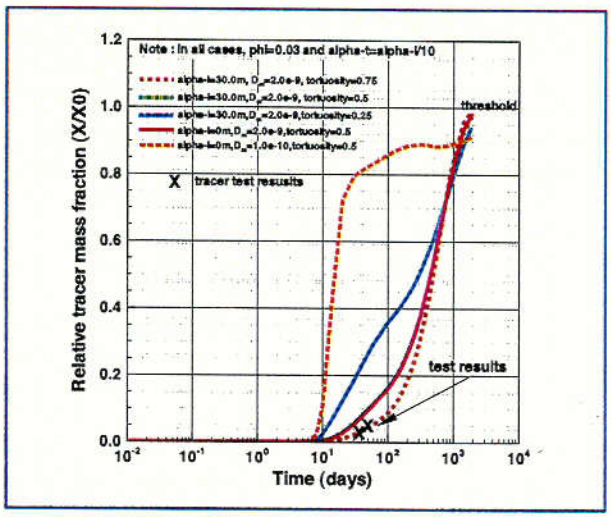

(c) Tracer Breakthoughs Test Results and Model Predictions with Matrix Diffusion

Figure 2.2-8. El Niño Infiltration and Seepage Test at Alcove 1

C12

Alcove 8-Niche 3107 Cross-Drift Test

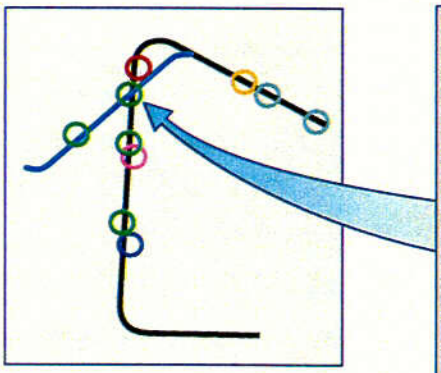

Objectives:
- Quantify large-scale infiltration and seepage processes in the potential repository horizon.
- Evaluate matrix diffusion mechanism in long-term flow and transport tests across an lithophysal-nonlithophysal interface.

Approaches:
- Water releases are in Alcove 8 and seepage collections are in Niche 3107.
- Niche 3107 is instrumented with seepage collectors and wetting front sensors.
- Geophysical tomographs are conducted in vertically slanted boreholes.

Status:
- Drill-and-blast phase of Alcove 8 excavation was completed in 1999.
- Tests are prepared to be conducted after alcove excavation.

Supporting Results:
- Seepage tests at Niche 3107 behind bulkhead demonstrate the existence of seepage threshold under high humidity conditions.
- During ECRB Cross Drift construction, no water was observed to seep into the ESF Main Drift 20 m below.

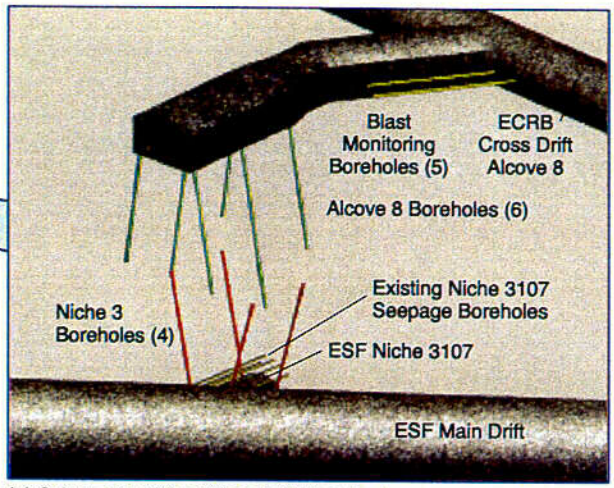

(a) Schematic of the Cross Drift Test Bed

(b) Photograph of Partial Excavated Alcove 8 in ECRB Cross Drift

(c) Photograph of Water Collection Trays on the Ceiling of the ESF Main Drift

Figure 2.2-9. Cross-Drift Test between ECRB Cross Drift Alcove 8 and ESF Main Drift Niche 3107 (CRWMS M&O 2000, U0015, Section 6.9)

Geochemical Measurements on Borehole and ESF Samples

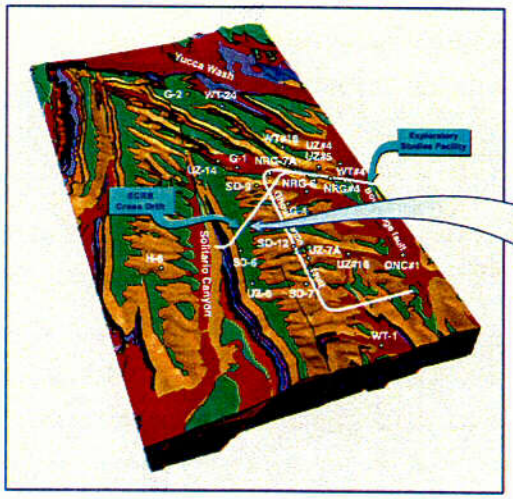

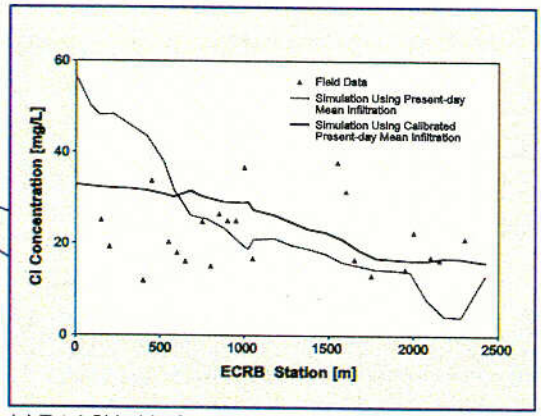

(a) Total Chloride Contents Along the ECRB Cross Drift

Objectives:

- Provide data to define geochemical evolution of water in the UZ.
- Provide data to estimate percolation flux at depth.

Approaches:

- Collect gas and perched water samples by pumping.
- Extract pore water by compression, ultracentrifuge, or vacuum distillation.
- Determine major ion concentrations by chemical analyses.

Results:

- Total dissolved solid and chloride are used to estimate infiltration rates and percolation fluxes.
- Pore waters are related to soil-zone processes: evapotranspiration, dissolution and precipation of pedogenic calcite and amorphous silica.
- Deep pore waters are used to evaluate restricted water-rock interactions and significant lateral movement within Calico Hills unit.

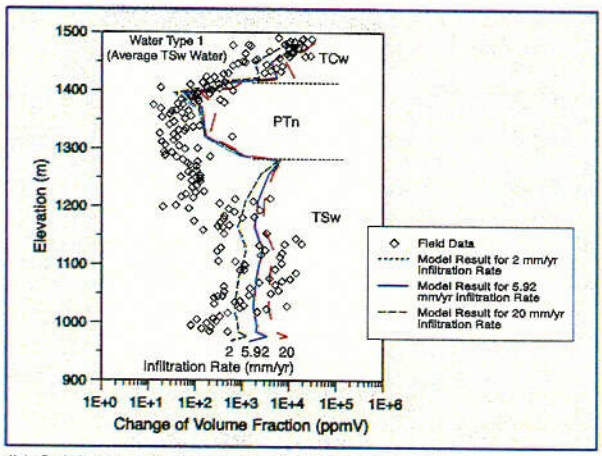

(b) Calcite Distributions Used for Infiltration and Percolation Evaluations

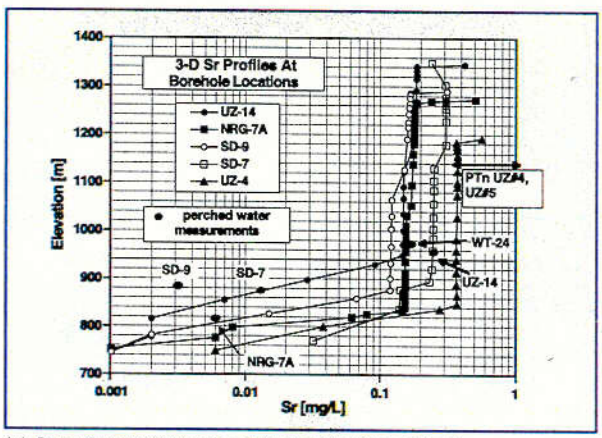

(c) Strontium Profiles Used for Zeolite Quantification

Figure 2.2-10. Geochemical Studies of Tuff Samples (CRWMS M&O 2000, U0050, Section 6.5; Sonnenthal and Bodvarsson 1999, p. 146)

Isotopic Measurements on Fracture Minerals and Perched Waters

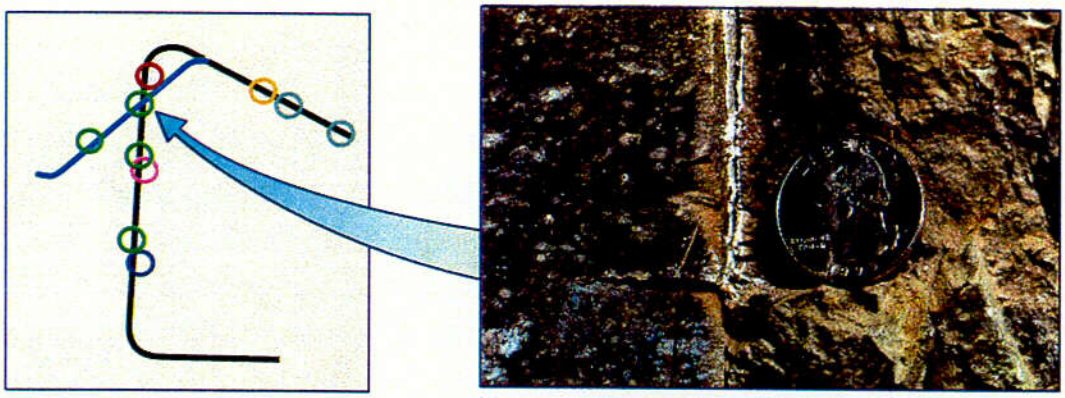

(a) Photograph of a Fracture with Calcite Infill

Objectives:
- Provide isotopic data to define age evolution of water in the UZ.
- Provide data to delineate flow paths over geological time scales.

Approaches:
- Leach salts from UZ cores or cutting for ^{36}Cl and Sr isotopic analyses.
- Extract water for tritium, hydrogen and oxygen stable isotopes, and carbon isotopic analyses.
- Digest mineral samples for analyses of Sr isotope ratios and of U series nuclides.

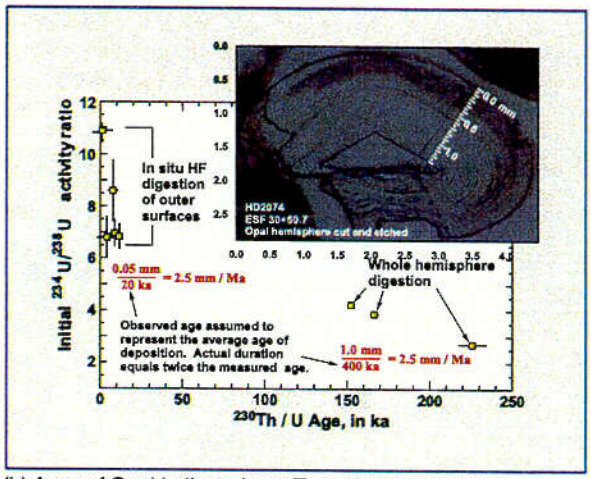

(b) Ages of Opal Indicate Long Term Flow in Fractures

Results:
- Bomb-pulse $^{36}Cl/Cl$ signals are present in the vicinity of some fault zones in the ESF.
- Detectable levels of tritium are present in ~6% of pore waters sampled.
- Bomb-pulse $^{36}Cl/Cl$ and tritium signals are not present in perched waters.
- Age of perched waters, mixing between fast and slow flows, climate of recharge are estimated by carbon and stable isotope analyses.
- $^{234}U/^{238}U$ activity ratios indicate recharge through fractures and minimal exchange between pore water and fracture water.

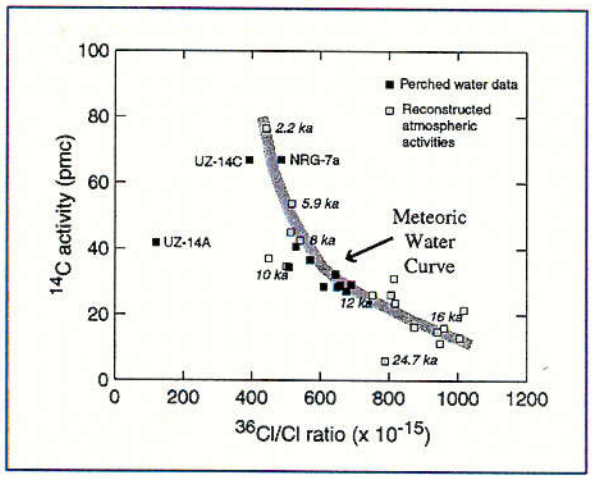

(c) Perched Water Ages Determined by ^{14}C and $^{36}Cl/Cl$ Data

Figure 2.2-11. Isotopic Studies of Tuff Samples (CRWMS M&O 2000, U0085, Section 6.6)

UZ Transport Test at Busted Butte

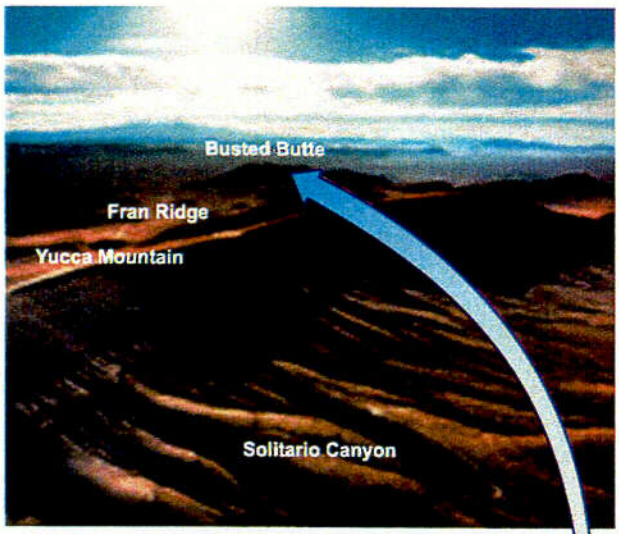

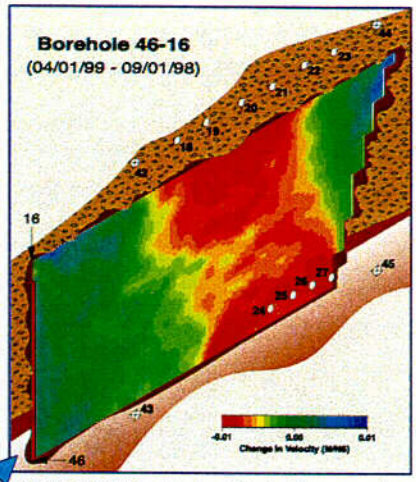

(a) Ground Penetrating Radar Tomograph of Injected Plume (Phase 2)

Objectives:

- Quantify UZ transport processes in Calico Hills nonwelded unit.
- Measure retardation coefficients in the field to compare with laboratory measured values.

Approaches:

- A test bed was excavated 70 m below the surface in mainly vitric CHn underlying the vitrophyre.
- A mixture of conservative and sorbing tracers is used in tracer injection tests.
- Absorbent pads are used to sample periodically the tracer distributions below injections.
- Ground-penetrating radar tomography, together with electrical resistivity tomography and neutron logging, are used to track plume migrations.

Results:

- Phase 1A was conducted with single point injections from April 1998 to mineback in 1999. Capillary driven flow mechanism is confirmed.
- Phase 2 tests with areal injections are on-going with breakthroughs and plume migrations monitored.

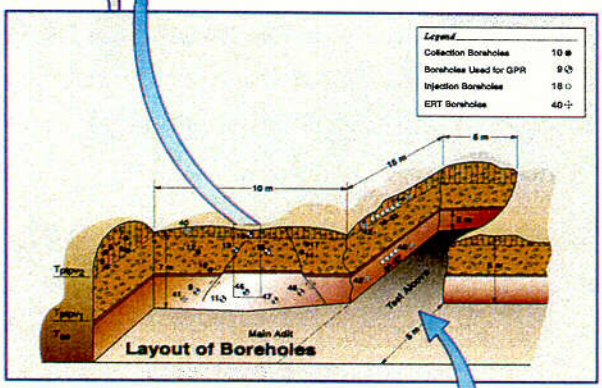

(b) Schematic of Busted Butte Test Area

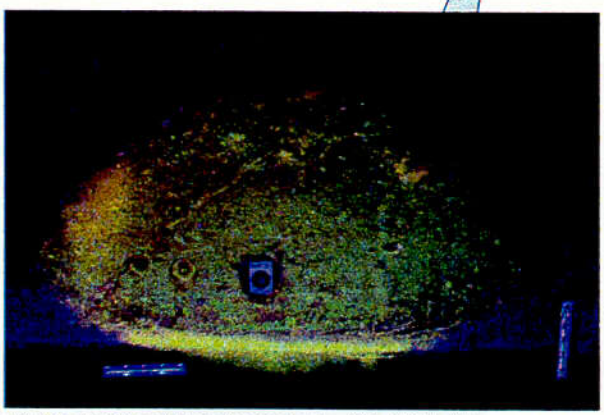

(c) Tracer Plume from Injection in the Side Wall of the Main Adit, Opposite to the Test Alcove (Phase 1A)

Figure 2.2-12. UZ Transport Test at Busted Butte (CRWMS M&O 2000, U0100, Section 6.8)

C16

Single Heater Test at Alcove 5

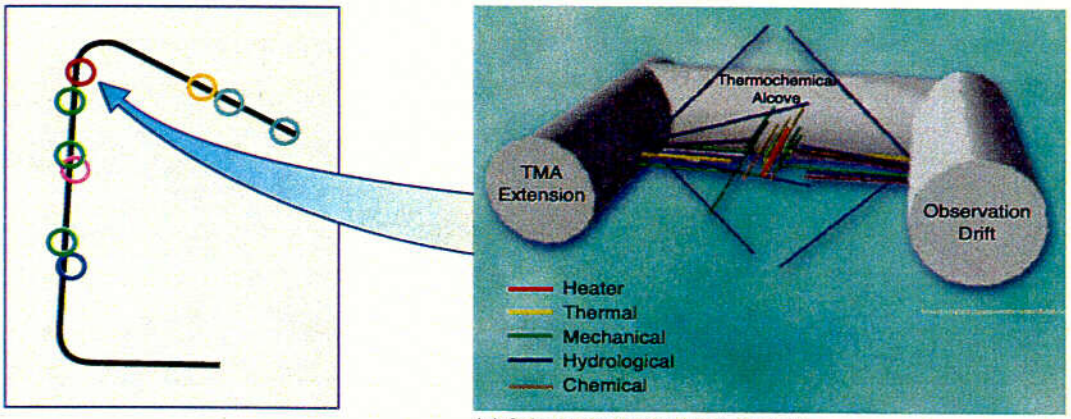

(a) Schematic of Single Heater Test

Objectives:

- Evaluate THMC coupled processes around a line heater source in fractured tuff.
- Develop testing methodologies and modeling approaches for high temperature conditions.

Approaches:

- Heating with a 5-m long 4-kW heater lasted 9 months in 1996 and 1997.
- Borehole sensing and cross-hole testing were used before, during, and after heating period.

Results:

- Extent of dry-out of about 1 m around the heater hole was measured with geophysical techniques (ERT, GRP and neutron).
- Condensate zone below the heater was measured to be larger than above the heater horizon.
- Chemical composition of water collected during heating in packed borehole intervals was analyzed.
- Characterization data by air-injection tests and mechanical displacement measurements located high-k flow paths.

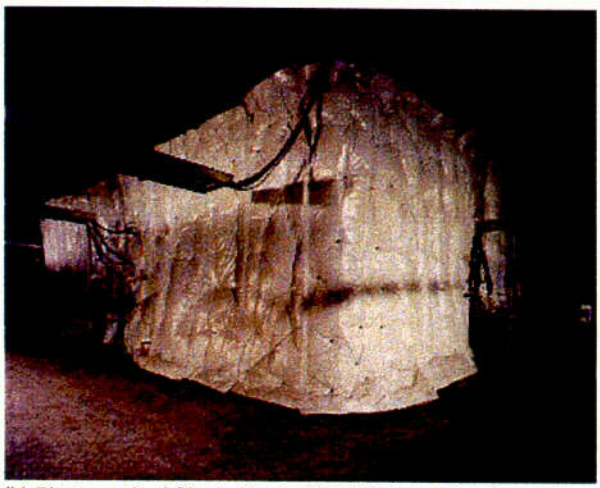

(b) Photograph of Single Heater Test Block Insulated

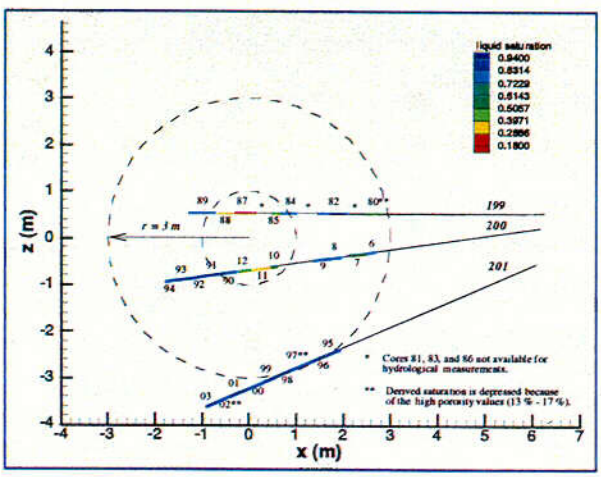

(c) Distributed Liquid Saturation in Cores After Cooling Phase

Figure 2.2-13. Single Heater Test at Alcove 5 (Tsang and Birkholzer 1999, pp. 411-415)

Drift Scale Test at Alcove 5

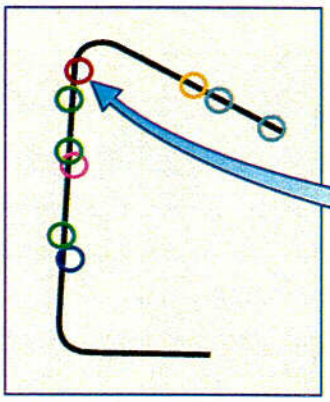

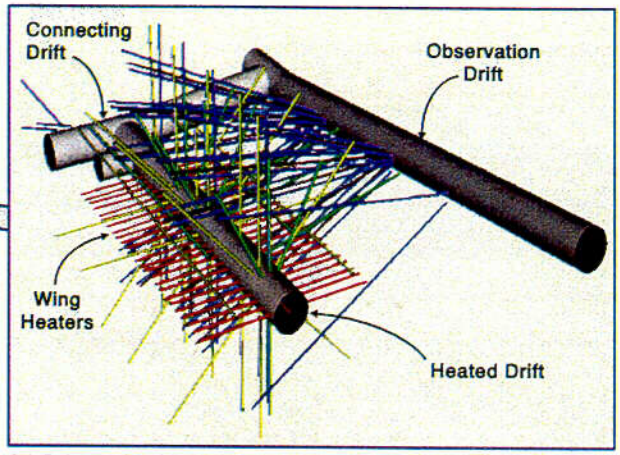

(a) Schematic of Drift Scale Test

Objectives:

- Evaluate THCM coupled processes in emplacement drift scale with full-scale heaters.
- Evaluate multi-drift heating effects with wing heaters to simulate multi-drift test conditions in fractured tuff.

Approaches:

- Install extensive borehole sensor arrays for monitoring of heating responses.
- Perform periodic geophysical imaging, pneumatic testing, and fluid sampling to measure the thermally induced coupled effects.

Results:

- Drift wall temperature reached ~190°C after 2 years of heating (since December 1997 at 187 kW).
- Condensate accumulated mainly below the wing heaters at early times.
- Wetting and drying zones were identified by periodic air-injection tests and geophysical methods.
- Gas phase CO_2 concentration increased strongly in large region around the heaters.
- Interactions of calcite and silicate minerals were indicated by chemical analyses of water collected.

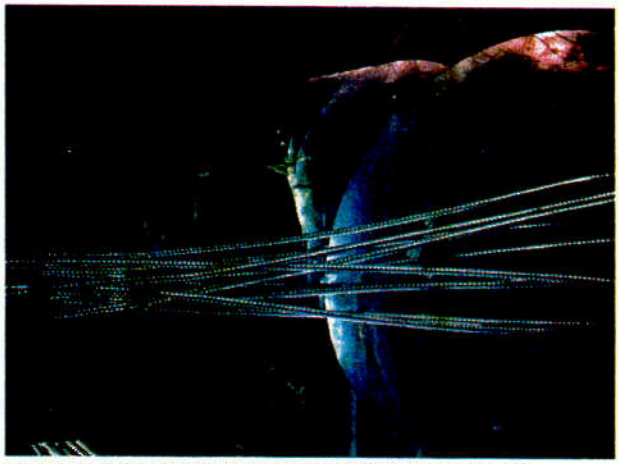

(b) Photograph of Full Scale Heaters within Heated Drift

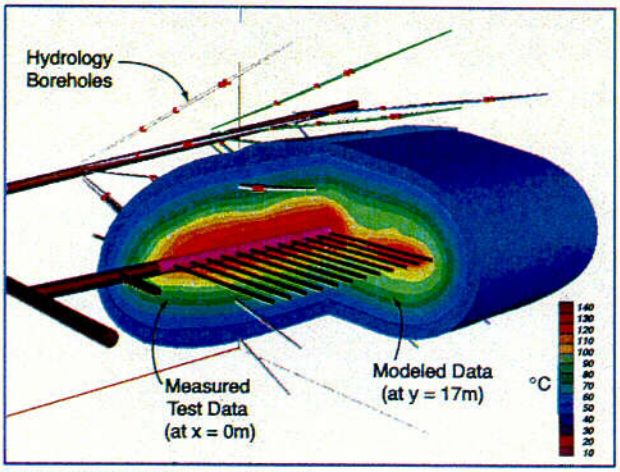

(c) Comparison of Measured and Modeled Temperature Distributions

Figure 2.2-14. Drift Scale Test at Alcove 5 (CWRMS M&O 2000, U0110/N0120, Section 6.2)

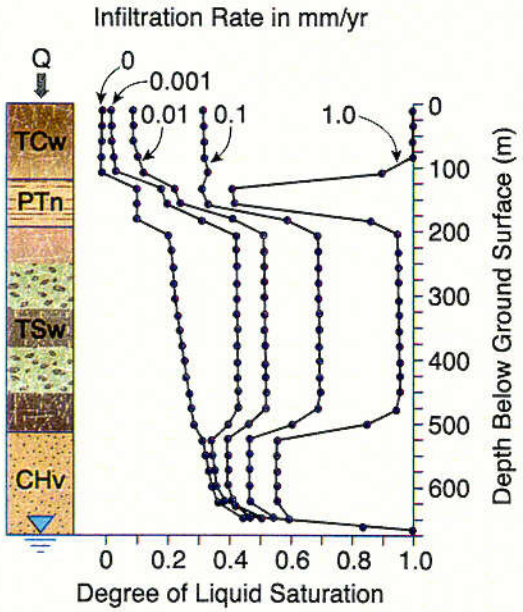

(a) 1-D Model of ambient saturation conditions for different percolation flux values UZ Flow – 1986

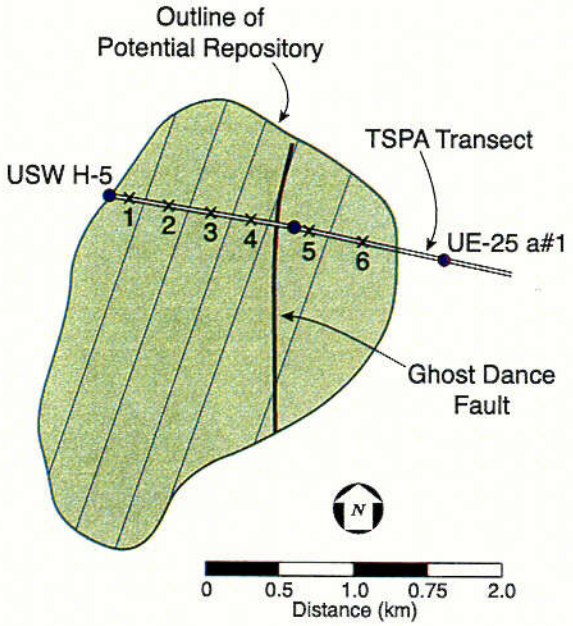

(b) 6 1-D Columns in 1 transect with 1mm/yr infiltration, composite-porosity and weep models TSPA – 1991

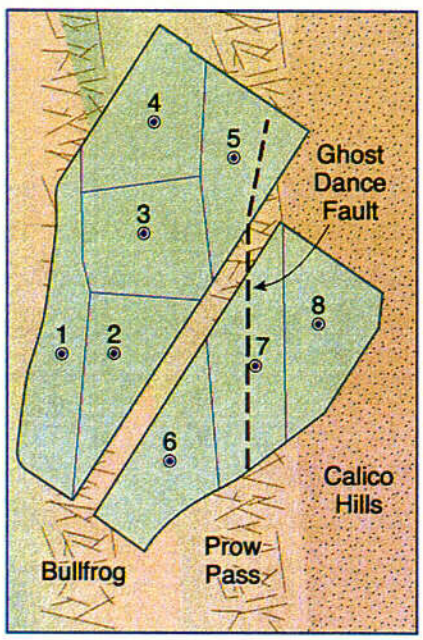

(c) 8 1-D Columns from different areas, 0-5 mm/yr infiltration during dry periods and 10 mm/yr during wet periods TSPA – 1993

Figure 2.4-1. One-Dimensional Column Simulations with the UZ-1986, the TSPA-1991, and the TSPA-1993 Models (Rulon et al. 1986, Barnard et al. 1992, and Wilson et al. 1994)

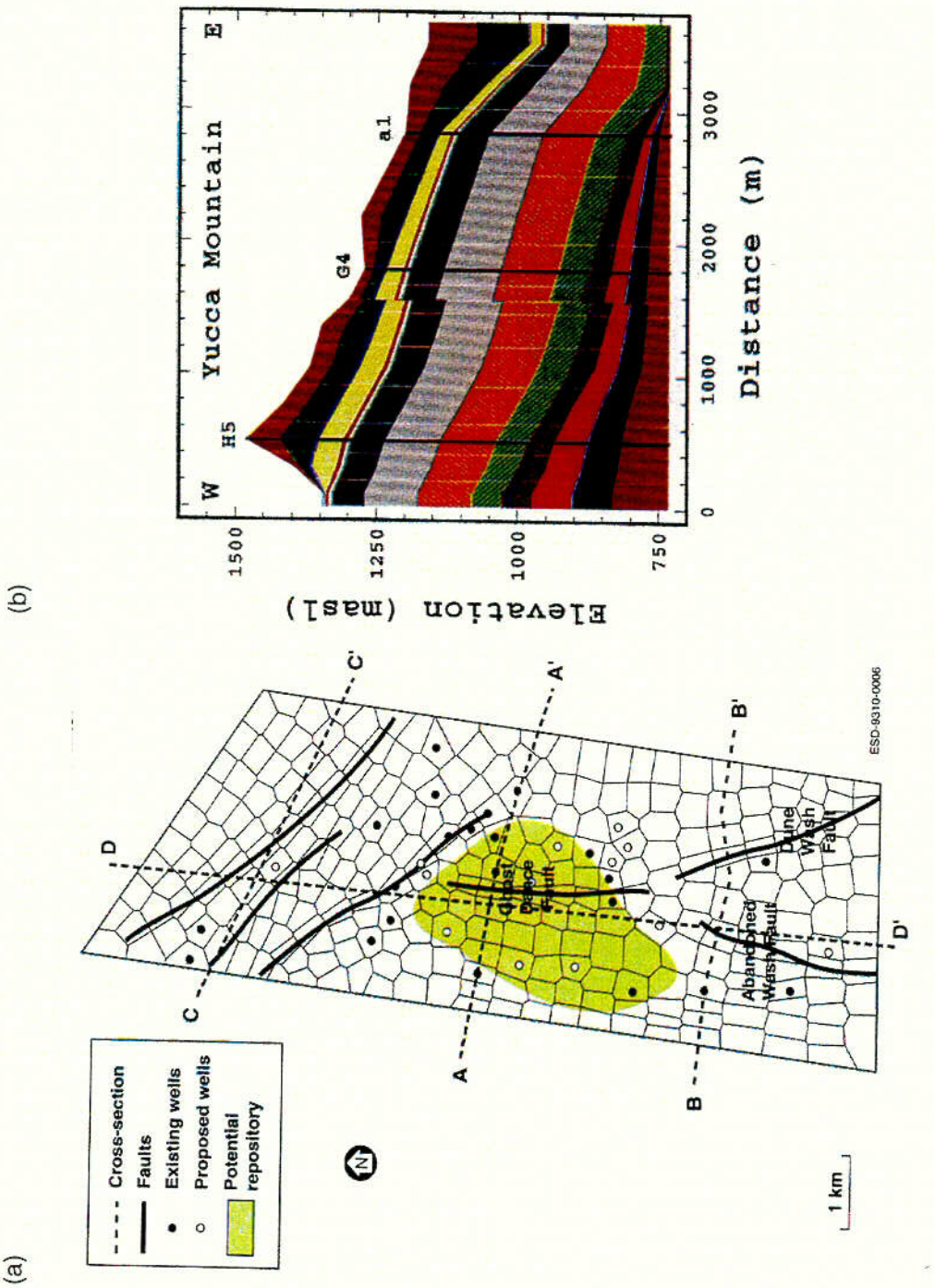

Figure 2.4-2. The Mesh and Approximations Used in the UZ-1995 Model (Wittwer et al. 1995, pp. 46-47)

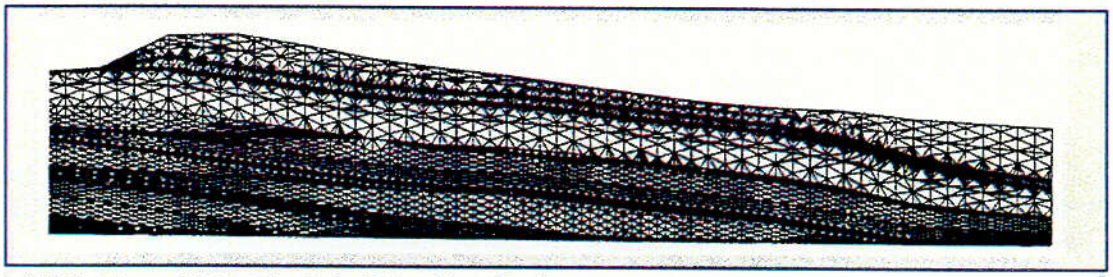

(a) Finite Element Grid of the Antler Ridge Cross Section

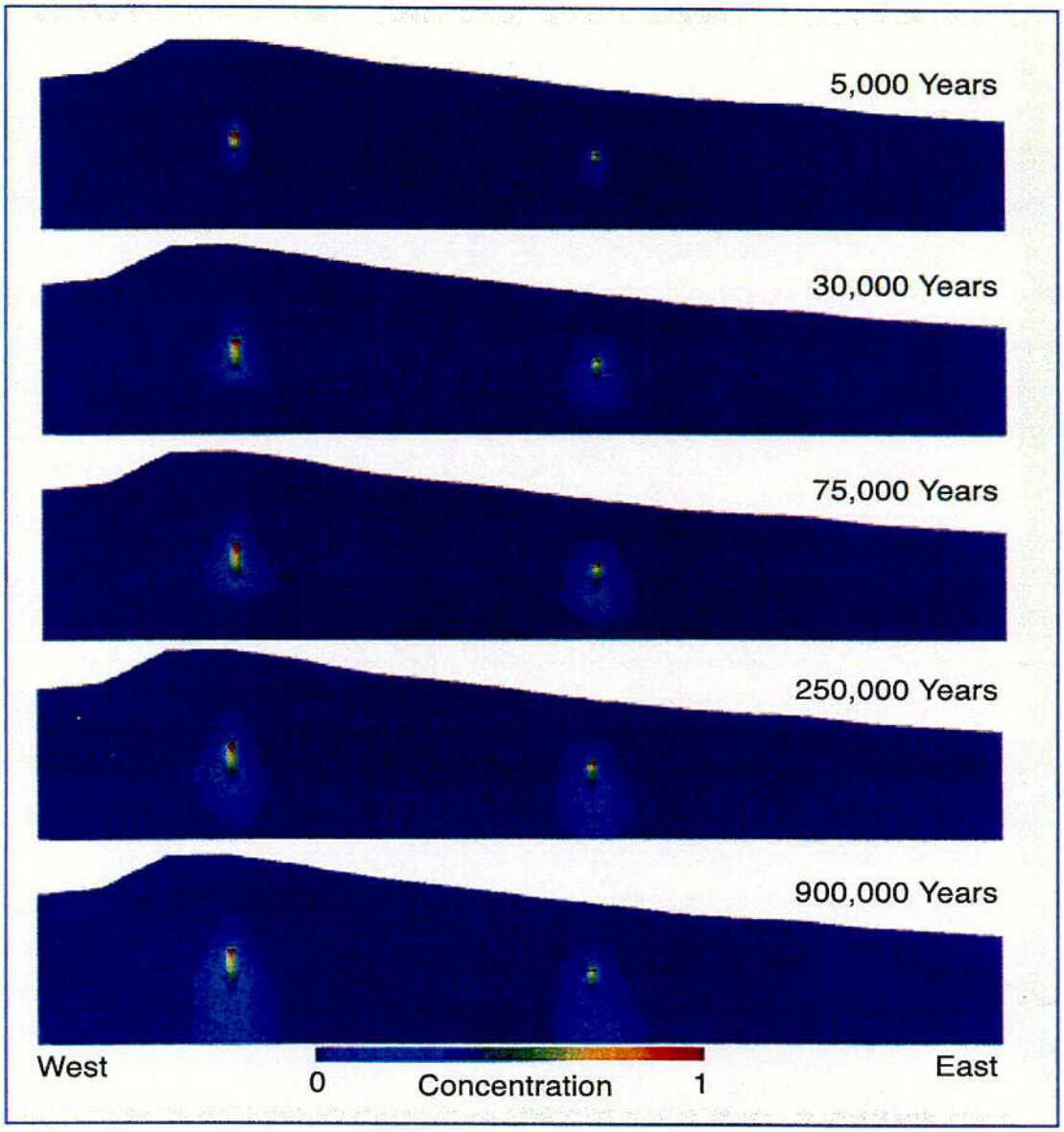

(b) Simulations of Transport of ^{237}Np from the Potential Repository

Figure 2.4-3. Simulations of ^{237}Np Transport by the UZ Transport-1995 Model (Robinson et al. 1995, p. 61, p. 125)

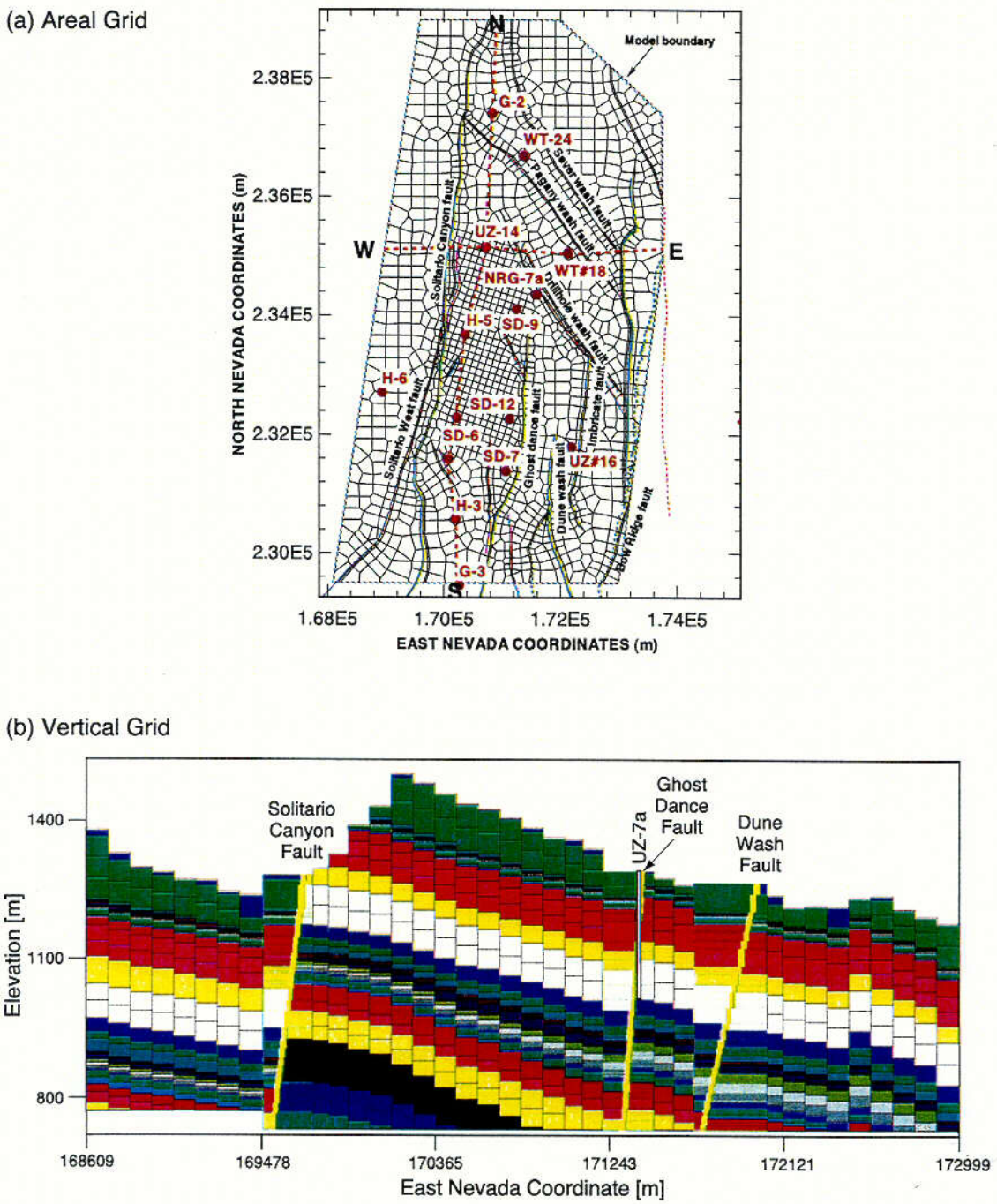

Figure 2.4-4. The Mesh and the Approximations Used in the UZ-1997 Model for TSPA-VA (adapted from Wu et al. 1999b, pp. 190-193)

c22

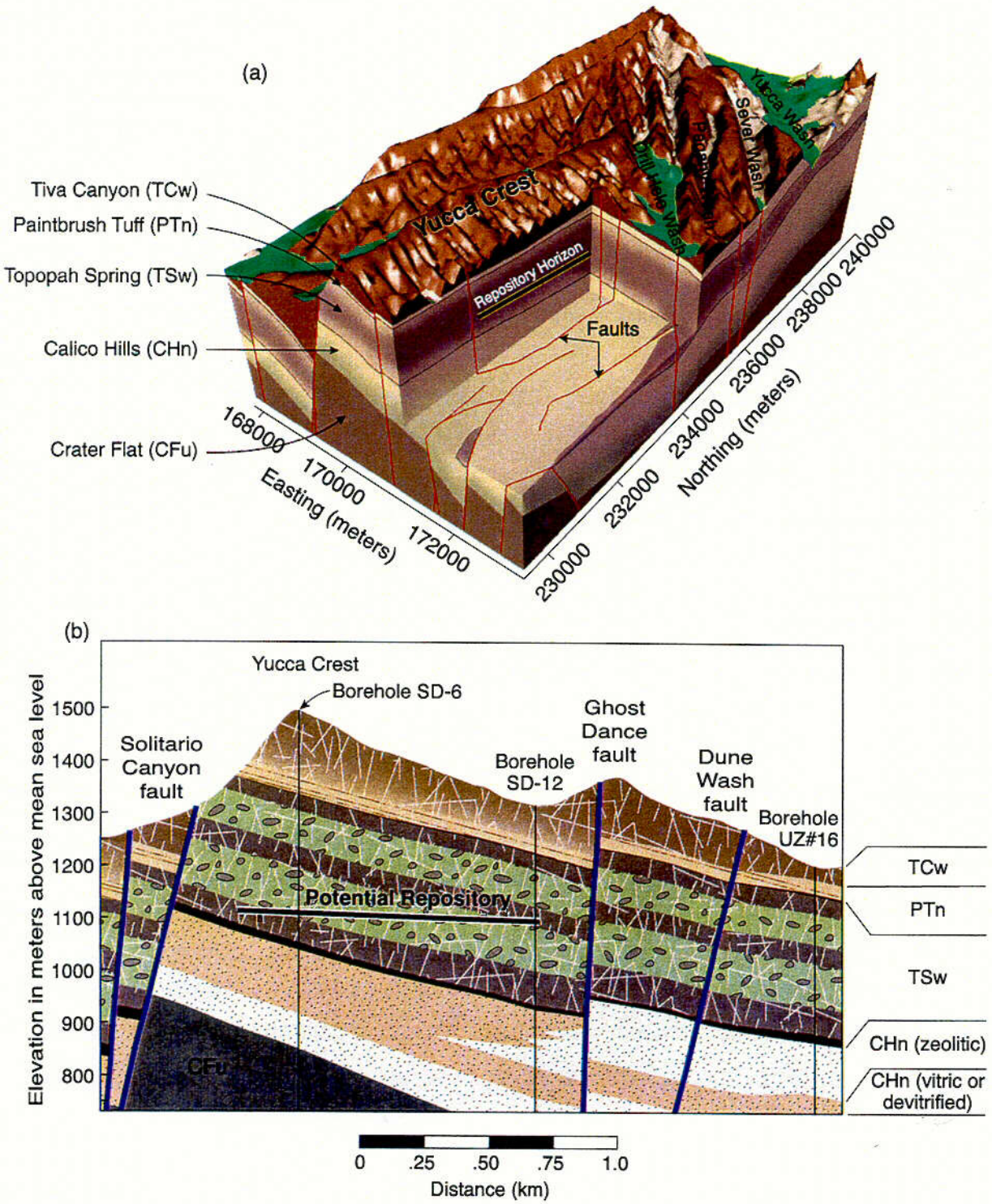

Figure 3.2-1. Yucca Mountain Site-Scale Geology: (a) in 3-D Perspective and (b) along an East-West Cross Section (adapted from GFM3.1 data, CRWMS M&O 2000, I0035)

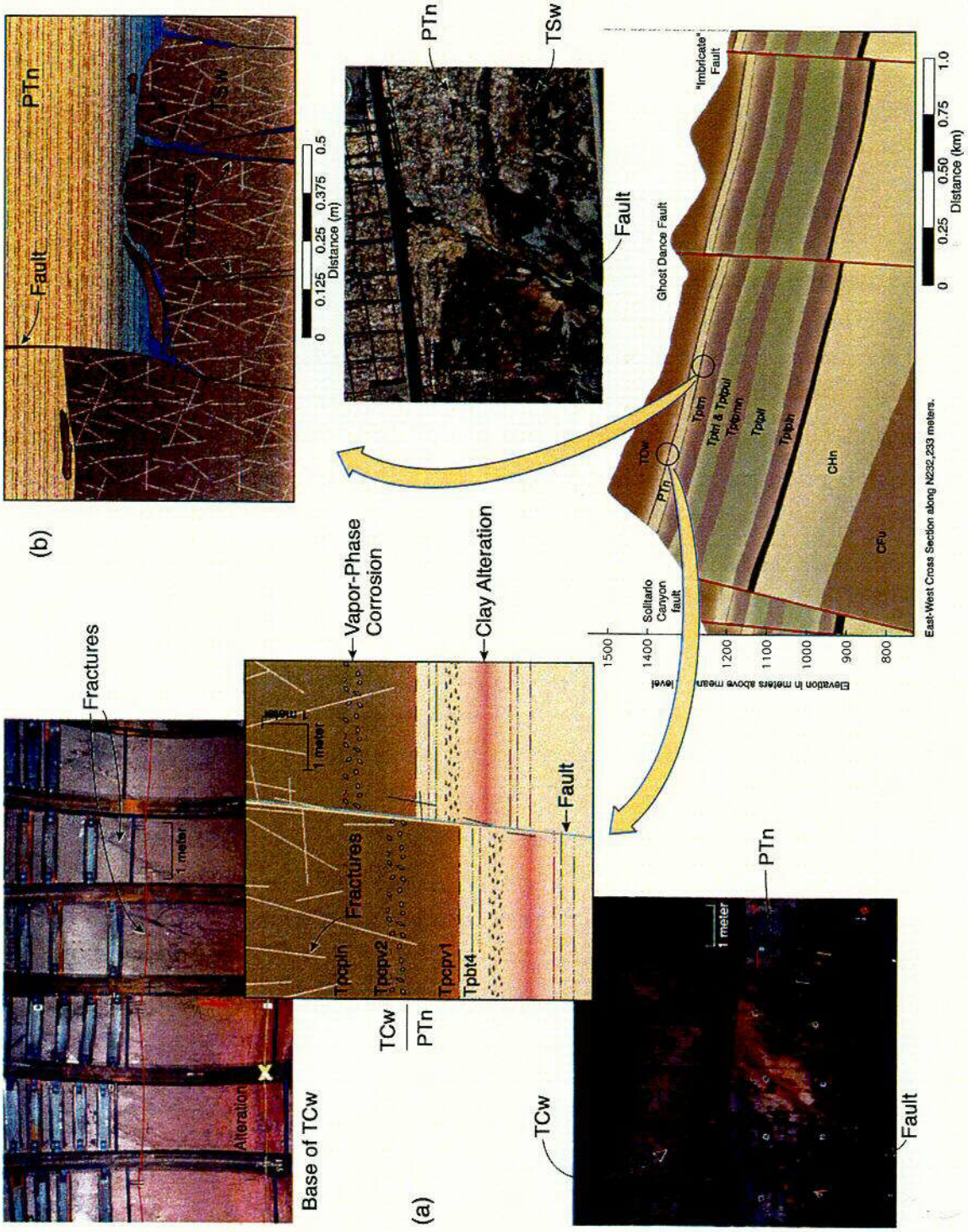

Figure 3.2-2. Lithostratigraphic Transitions at the Upper and Lower Margins of the PTn Hydrogeological Unit. (a) Photos and schematic at the TCw-PTn interface, where tuffs grade downward from densely welded to nonwelded, accompanied by an increase in matrix porosity and a decrease in fracture frequency. (b) Photo and schematic at the PTn-TSw interface, where tuffs grade downward from nonwelded to densely welded, accompanied by a decrease in matrix porosity and an increase in fracture frequency.

C24

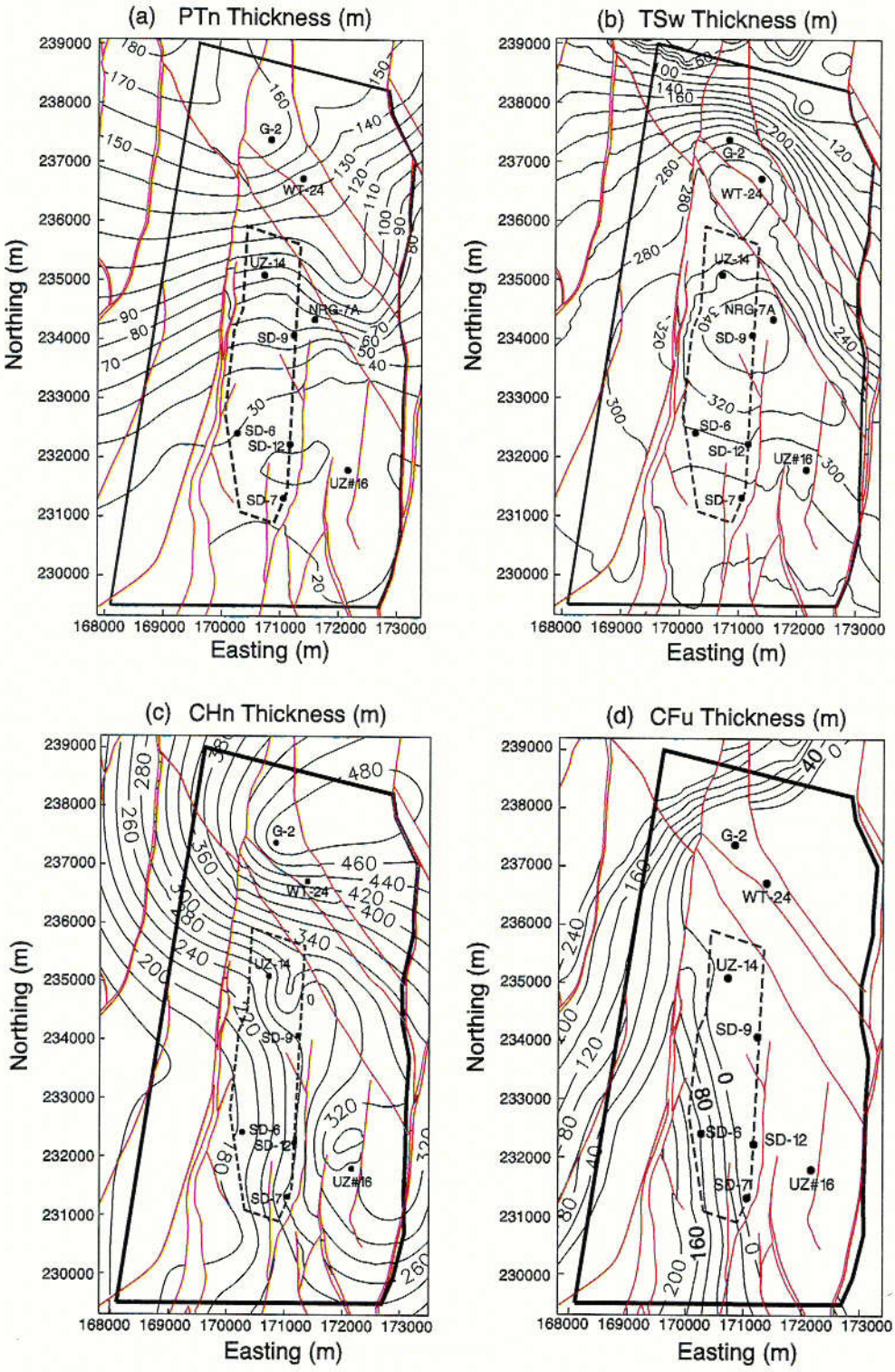

Figure 3.2-3. Thickness Contour Plots of the (a) PTn, (b) TSw, (c) CHn, and (d) CFu Hydrogeological Units (Adapted from DTN: MO9901MWDGFM31.000). Contours are in meters.

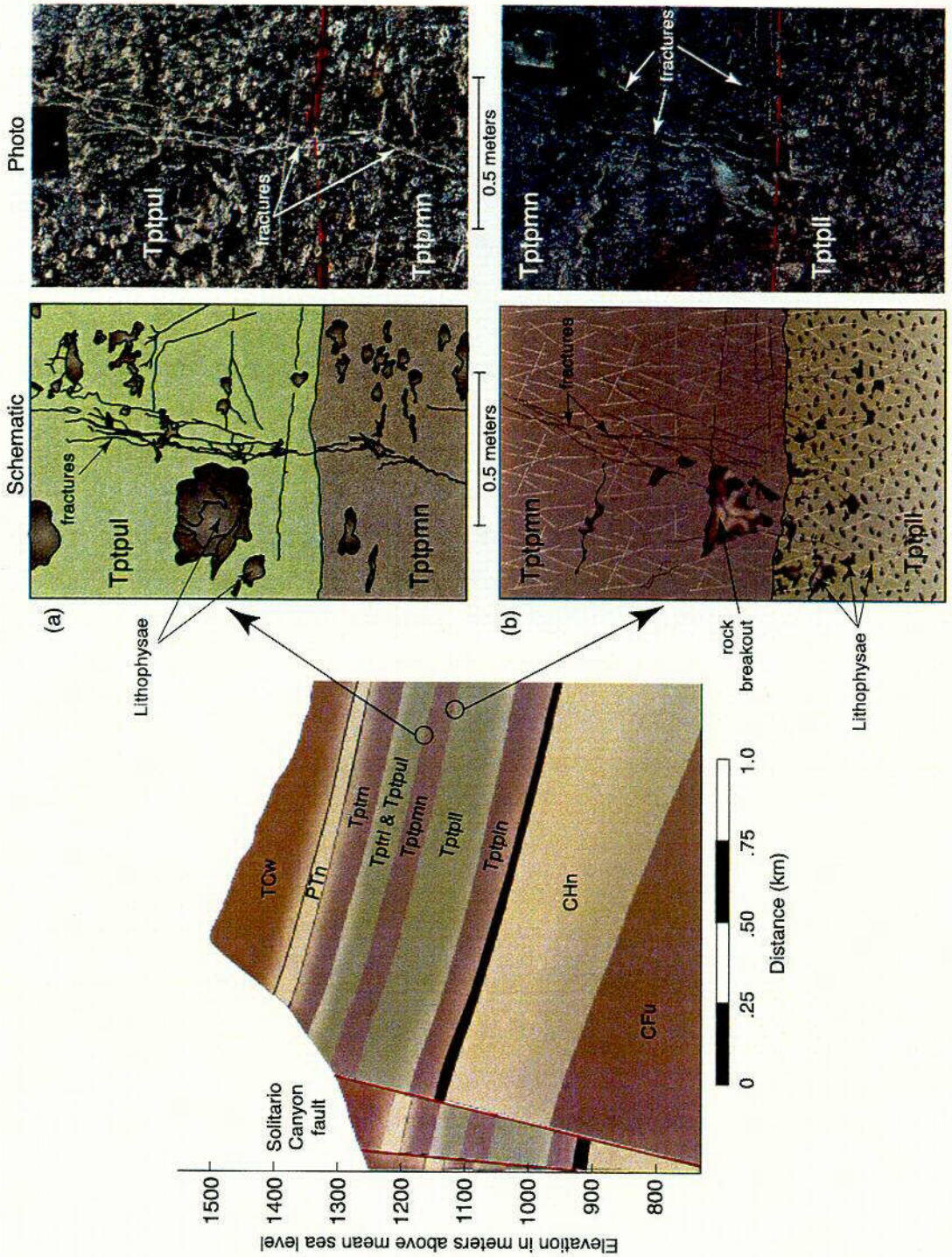

Figure 3.2-4. Lithophysal Transitions within the TSw Unit. (a) Photo and schematic of the contact between the upper nonlithophysal (Tptpul) and the middle nonlithophysal (Tptpmn) zones showing a downward decrease in lithophysal volume. (b) Photo and schematic of the contact between the middle nonlithophysal (Tptpmn) and lower lithophysal (Tptpll) zones showing a downward increase in lithophysal volume. Fractures in the nonlithophysal unit are generally smoother, more planar, and more continuous than fractures in the lithophysal units.

C26

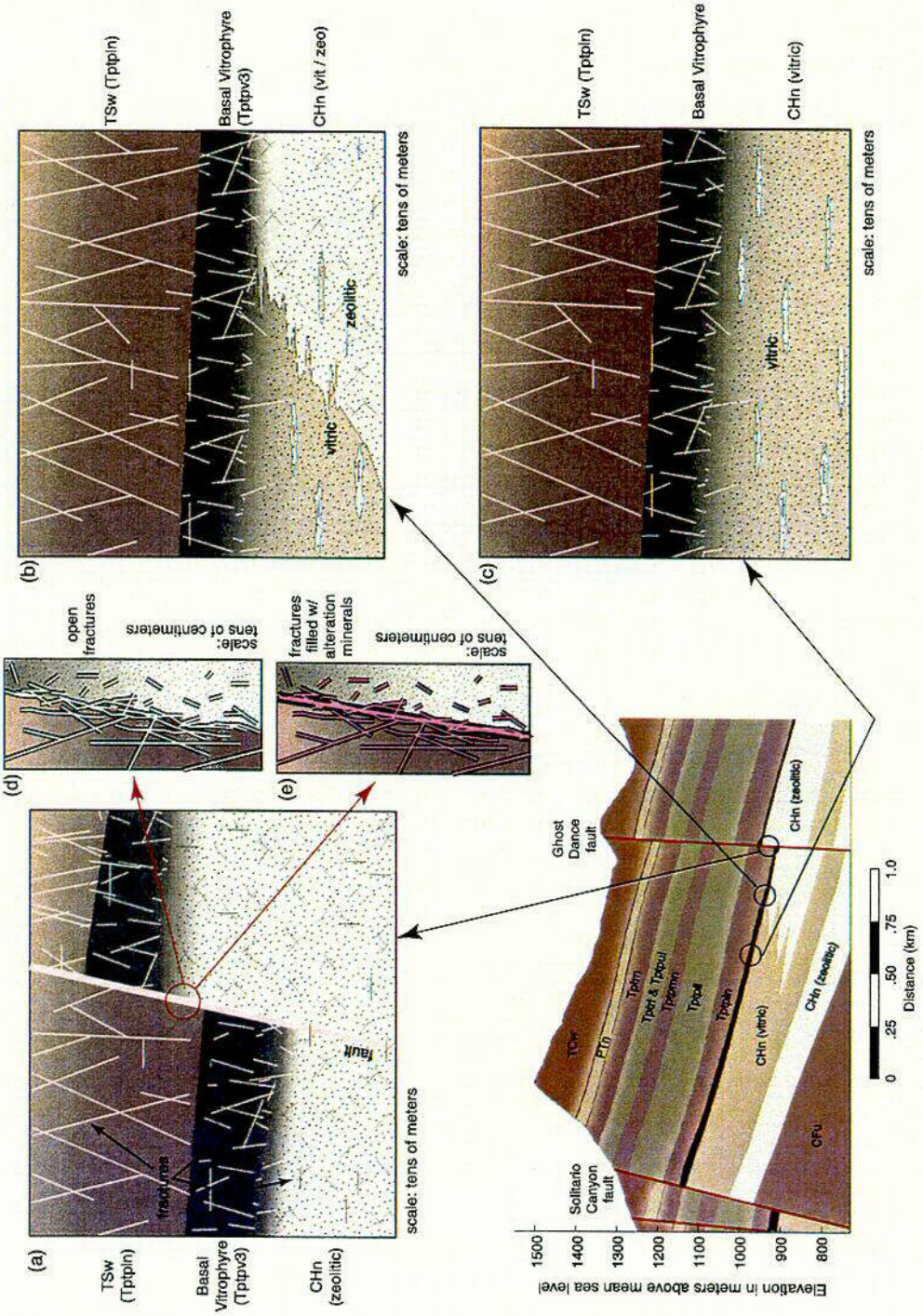

Figure 3.2-5. Lithostratigraphic Transitions at the TSw-CHn Interface. (a) Schematic with prevalent alteration at the TSw-CHn contact. (b) Schematic with variable alteration at the TSw-CHn contact. (c) Schematic with minimal alteration at the TSw-CHn contact. (d) Schematic representation of a fault zone as a well-connected fracture network that may represent a fast flow pathway. (e) Schematic representation of a fault zone showing alteration within the fracture network that creates a flow barrier.

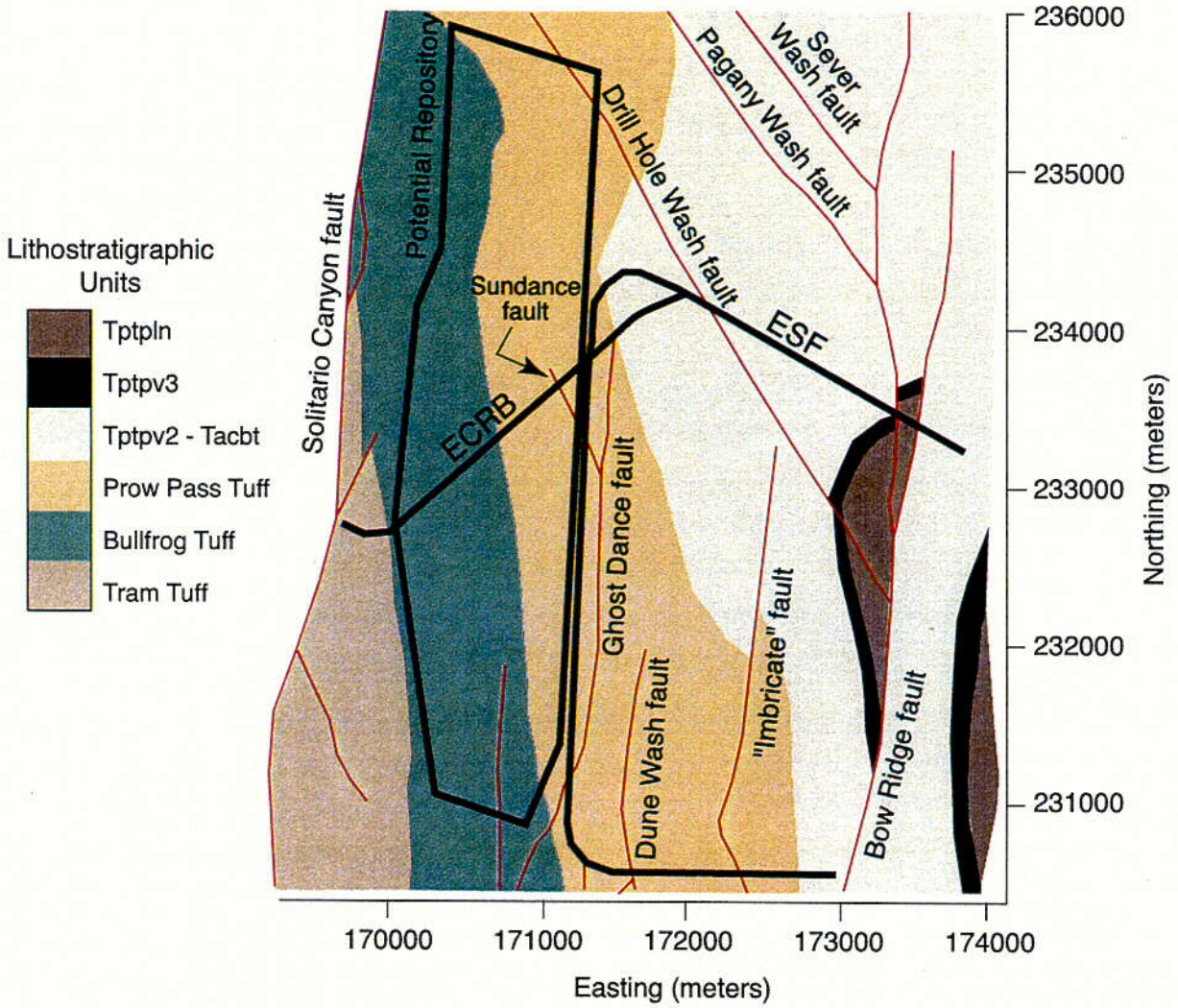

Figure 3.2-6. Occurrence of Lithostratigraphic Units at the Water Table (730 meters above sea level) (Adapted from DTN: MO9901MWDGFM31.000)

C28

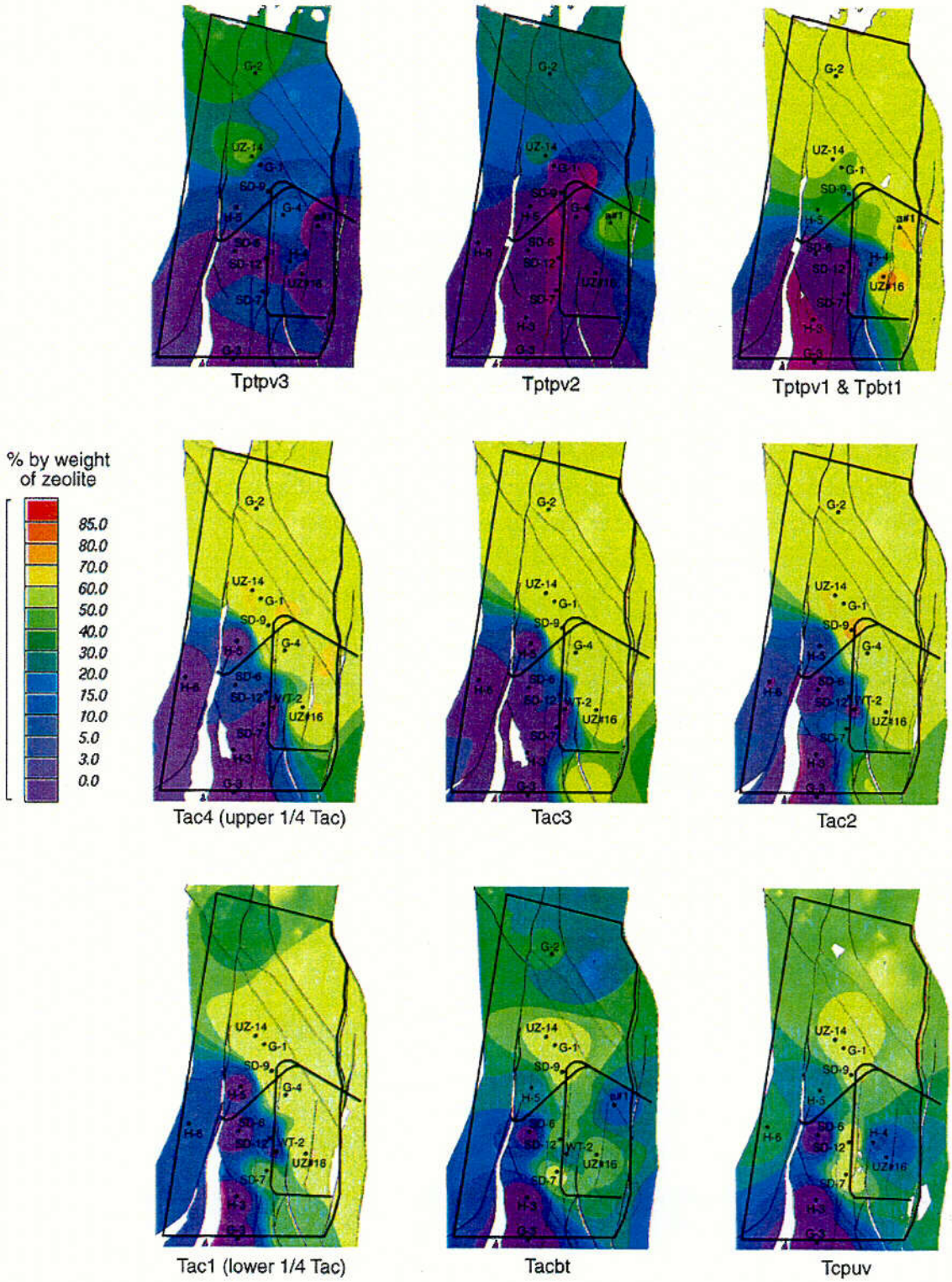

Figure 3.2-7. Distribution of Zeolites in Certain Layers below the Potential Repository Horizon. (CRWMS M&O 2000, I0045, Section 6.3.2; DTN: MO9910MWDISMMM.003). Areas with less than or equal to 3% zeolite are considered vitric, or unaltered.

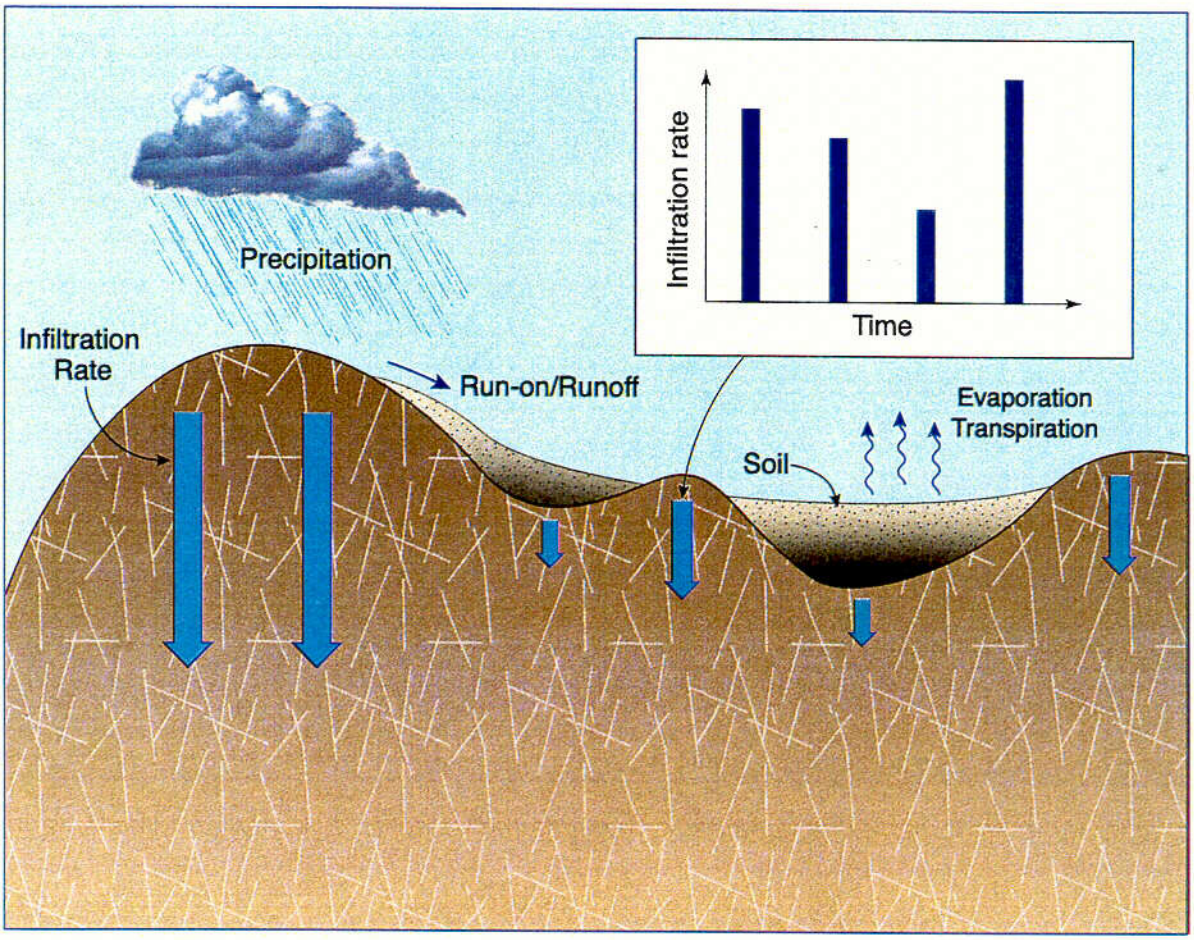

Figure 3.3-1. Schematic Showing Temporal and Spatial Variabilities of Net Infiltration Rates Resulting From the Nature of the Storm Events and Variation in Soil Cover and Topography. The size of the arrow indicates the relative magnitude of infiltration rates.

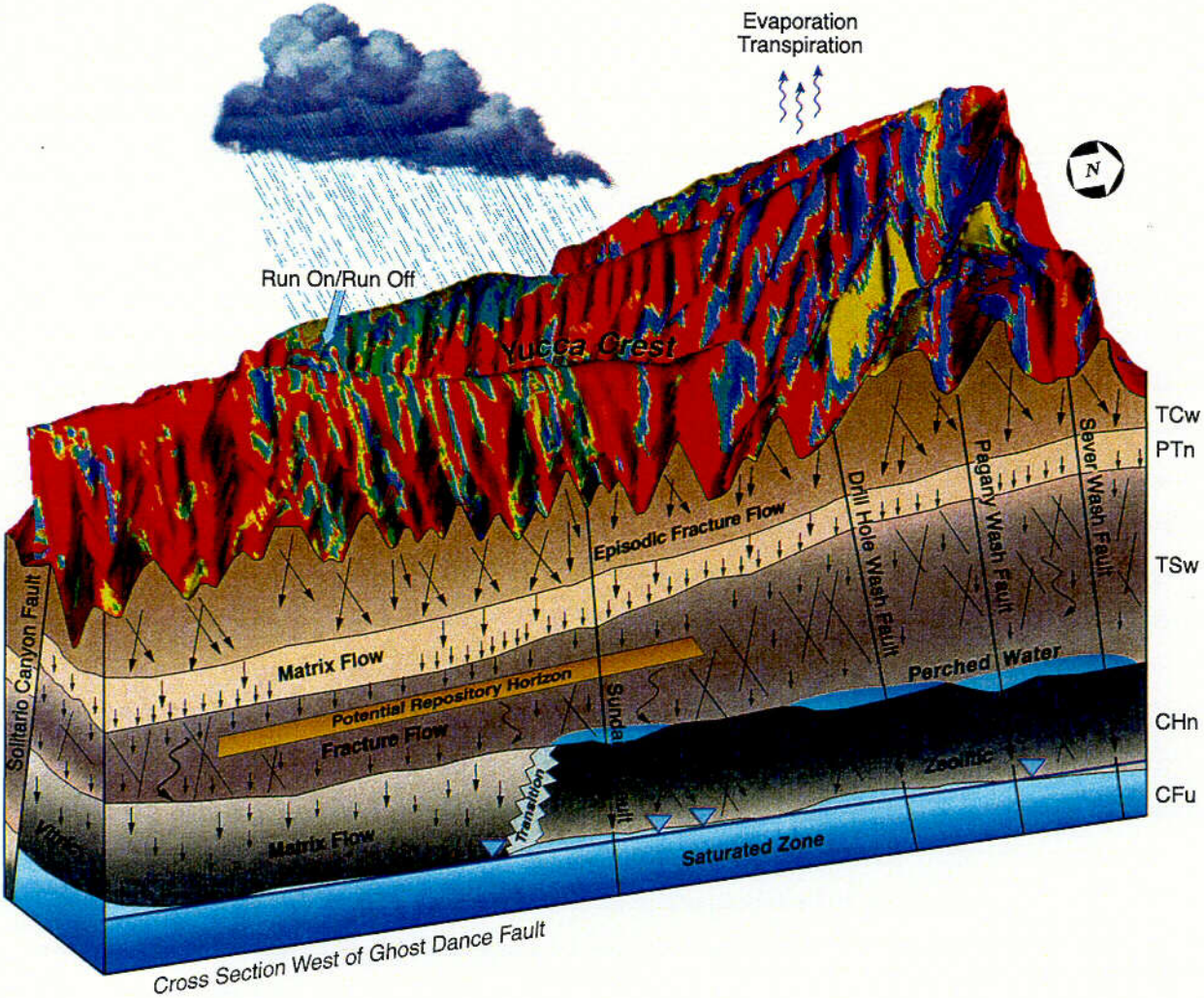

Figure 3.3-2. Schematic Showing Overall Water Flow Behavior in the UZ Including the Relative Importance of Fracture and Matrix Flow Components in the Different Hydrogeologic Units. The blue and red colors on the land surface correspond to high and low infiltration rates, respectively, while the other colors correspond to intermediate infiltration rates (CRWMS M&O 2000, U0030, Figure 1).

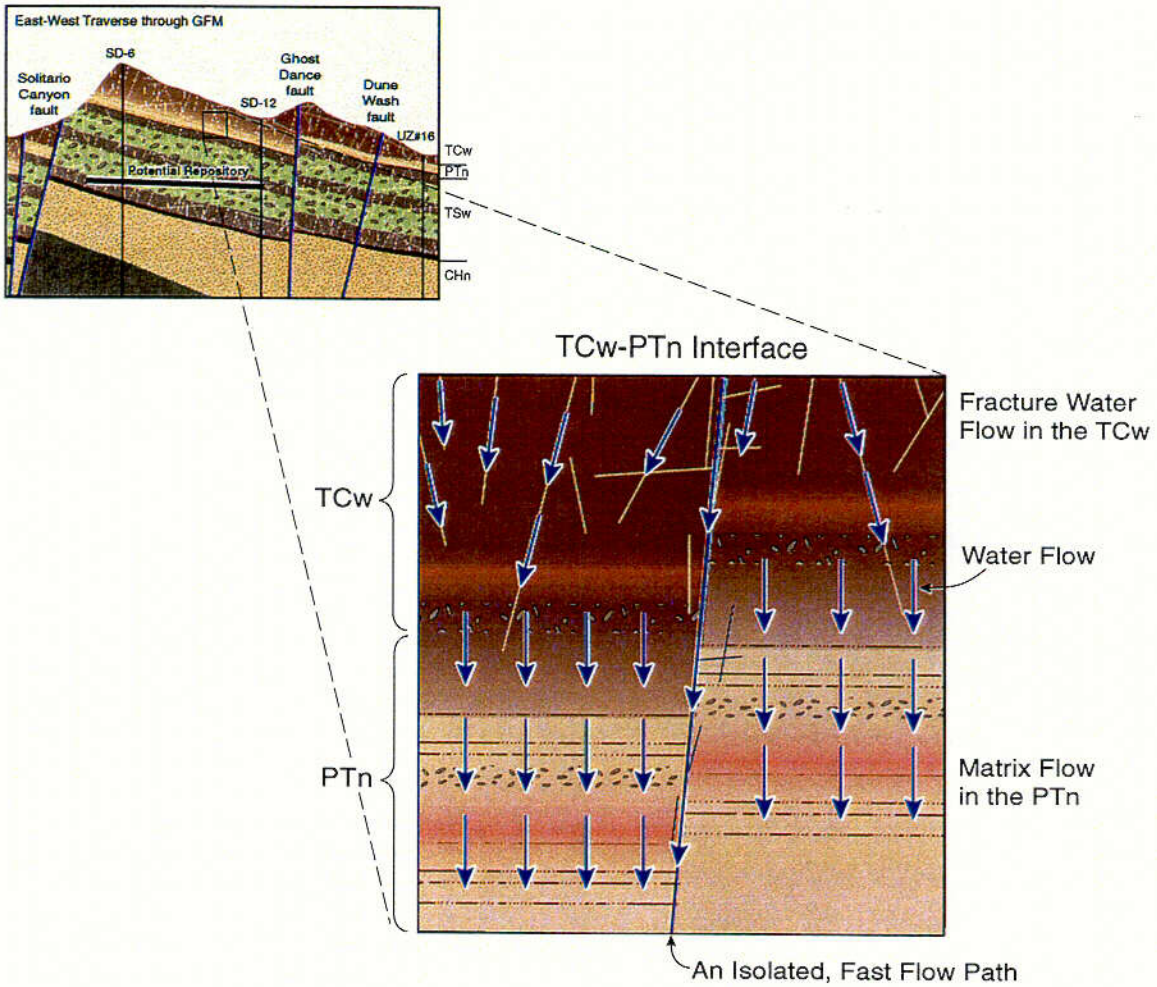

Figure 3.3-3. Schematic Showing Water Flow Behavior within the PTn Characterized by Dominant Matrix Flow and a Few Fast Flow Paths

C32

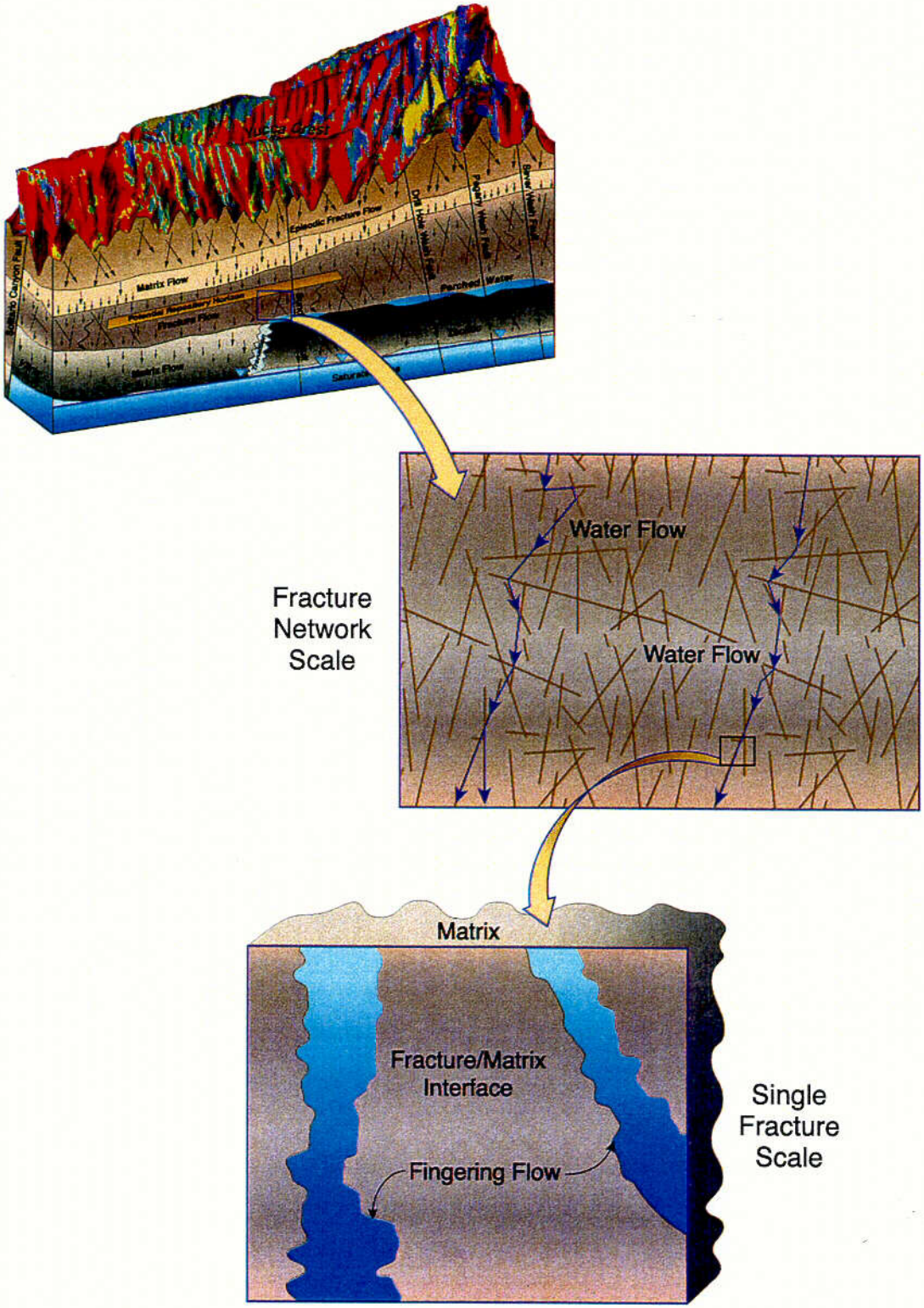

Figure 3.3-4. Water Flow in Fractures Characterized by Fingering Flow at Different Scales

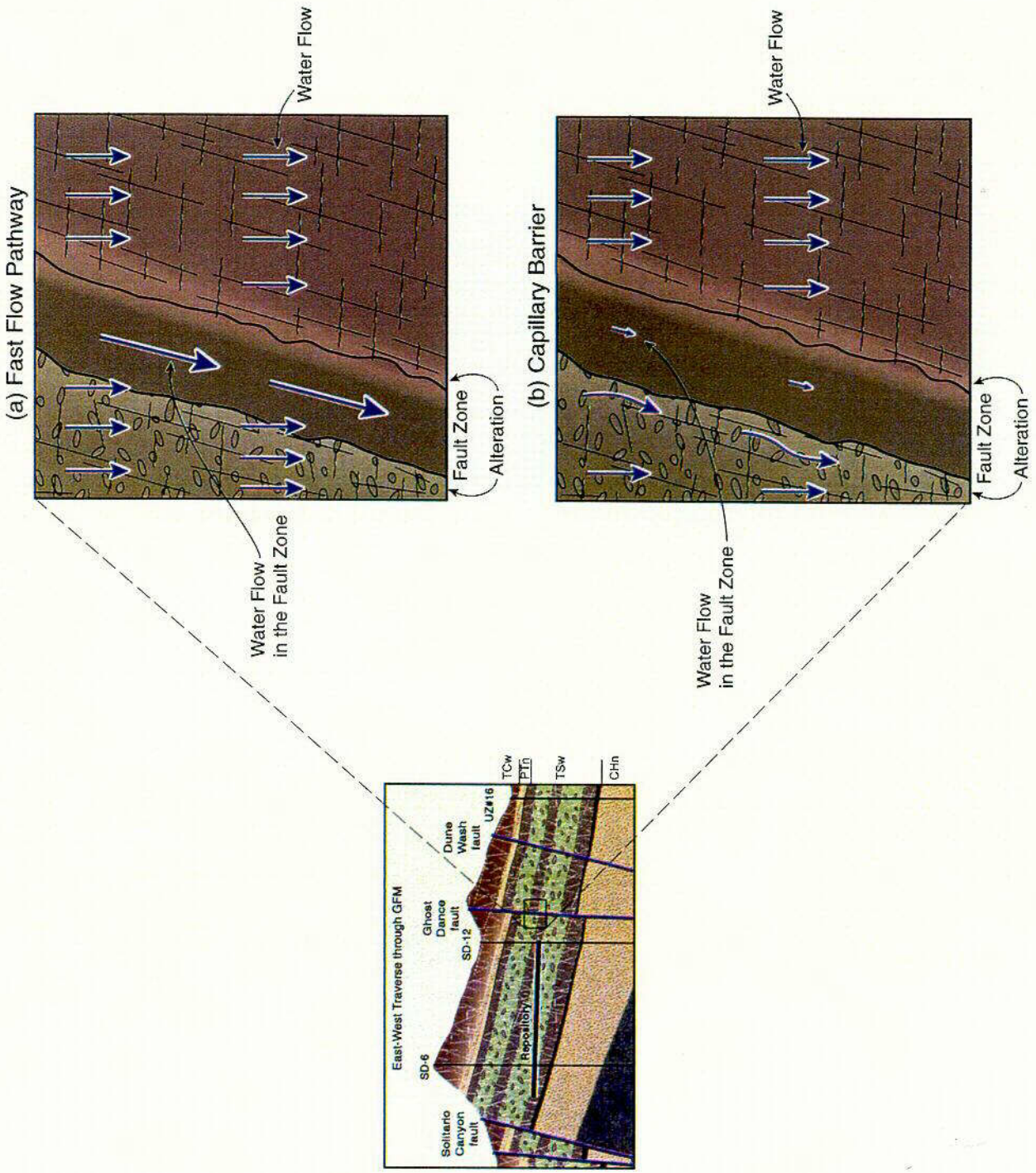

Figure 3.3-5. Major Faults Can Act as Fast-Flow Conduits or Capillary Barriers. The size of the arrows in (a) and (b) indicates the relative magnitude of flow.

C34

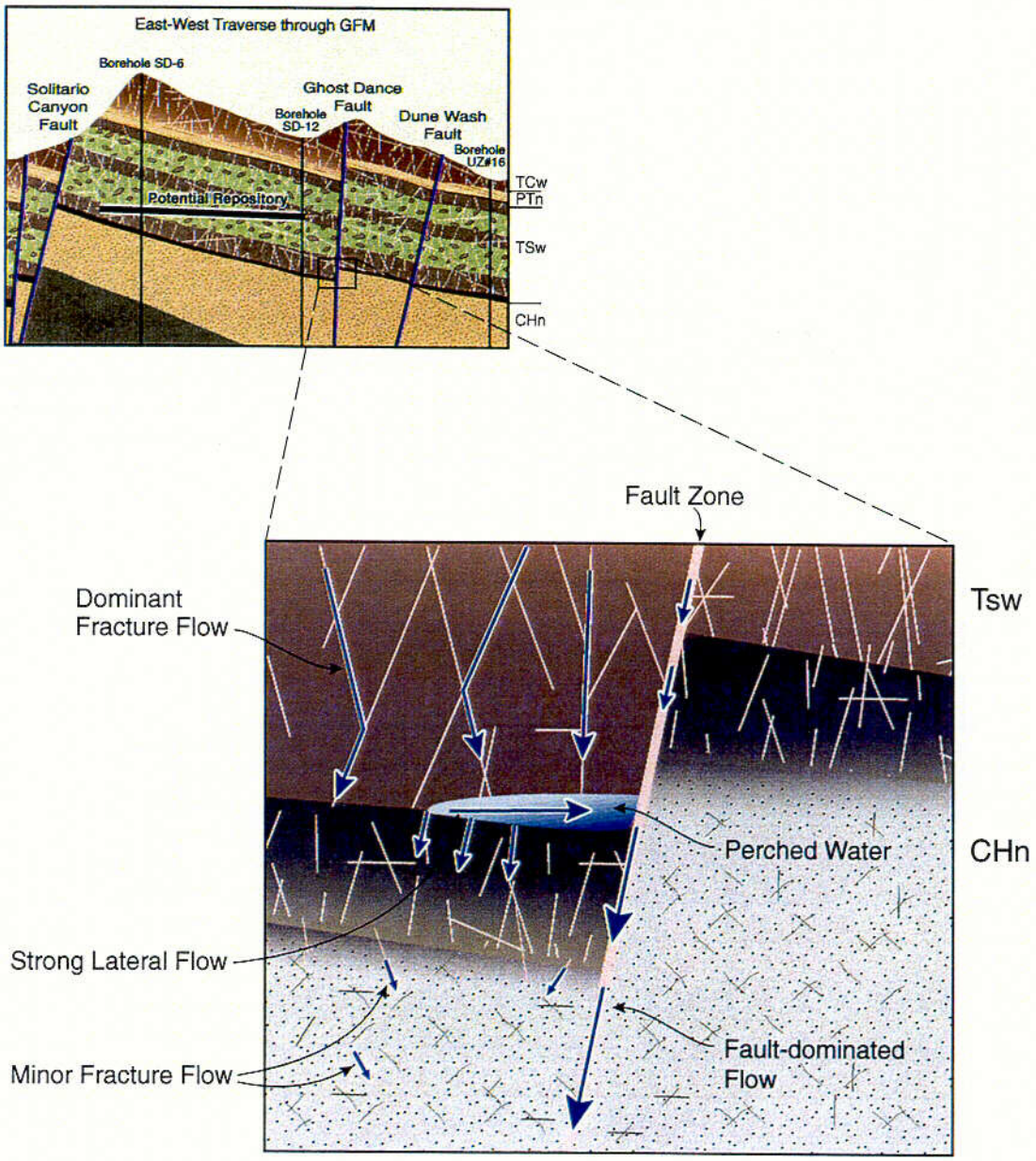

Figure 3.3-6. Schematic Showing Flow Patterns within and near a Perched Water Body Characterized by Strong Lateral Flow within the Perched Water Body and the Associated Fault-Dominated Flow

C35

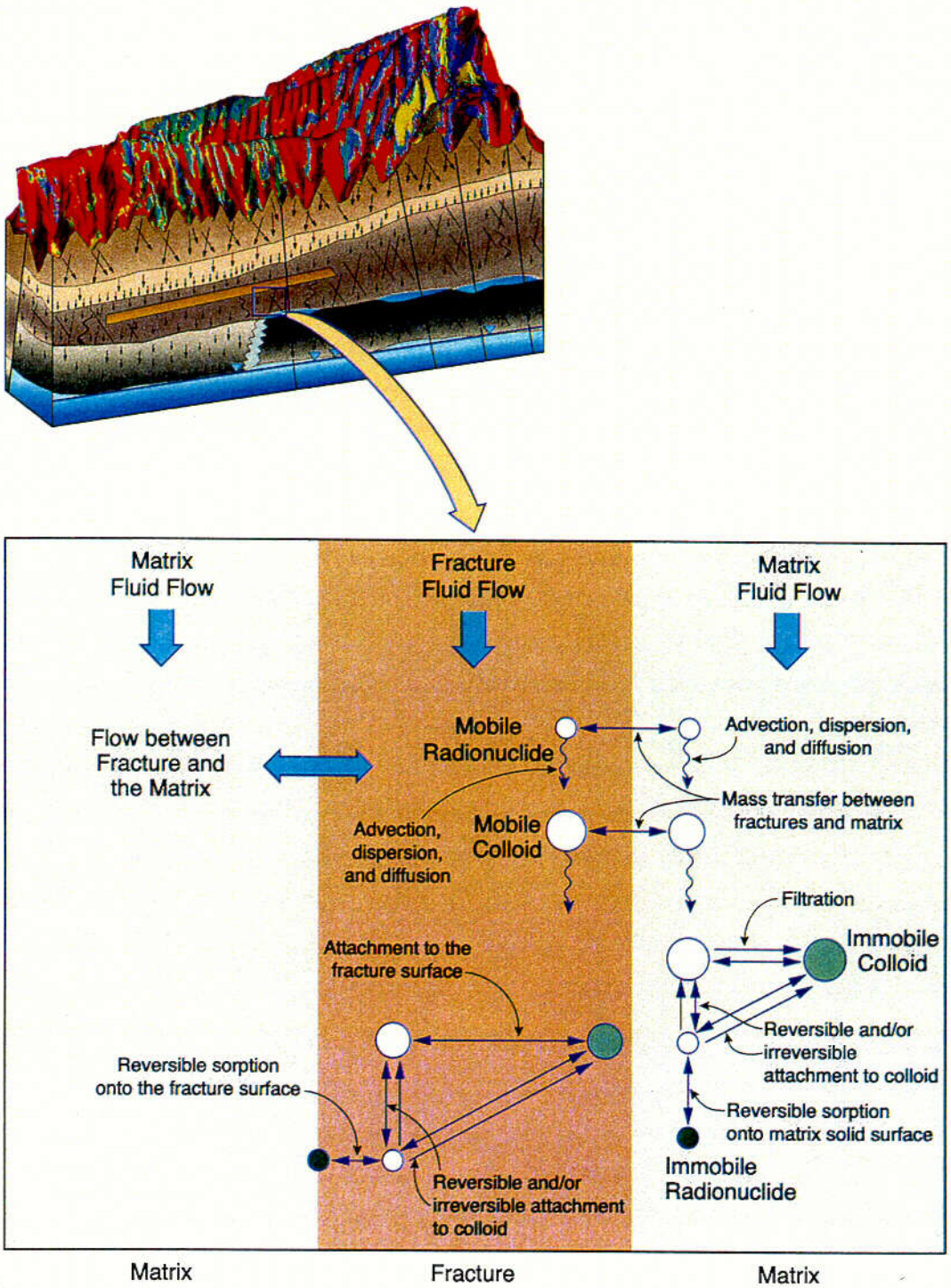

Figure 3.3-7. Important Radionuclide Transport Processes. (Note that the radionuclides also undergo radioactive decay, but this is not shown in the schematic.)

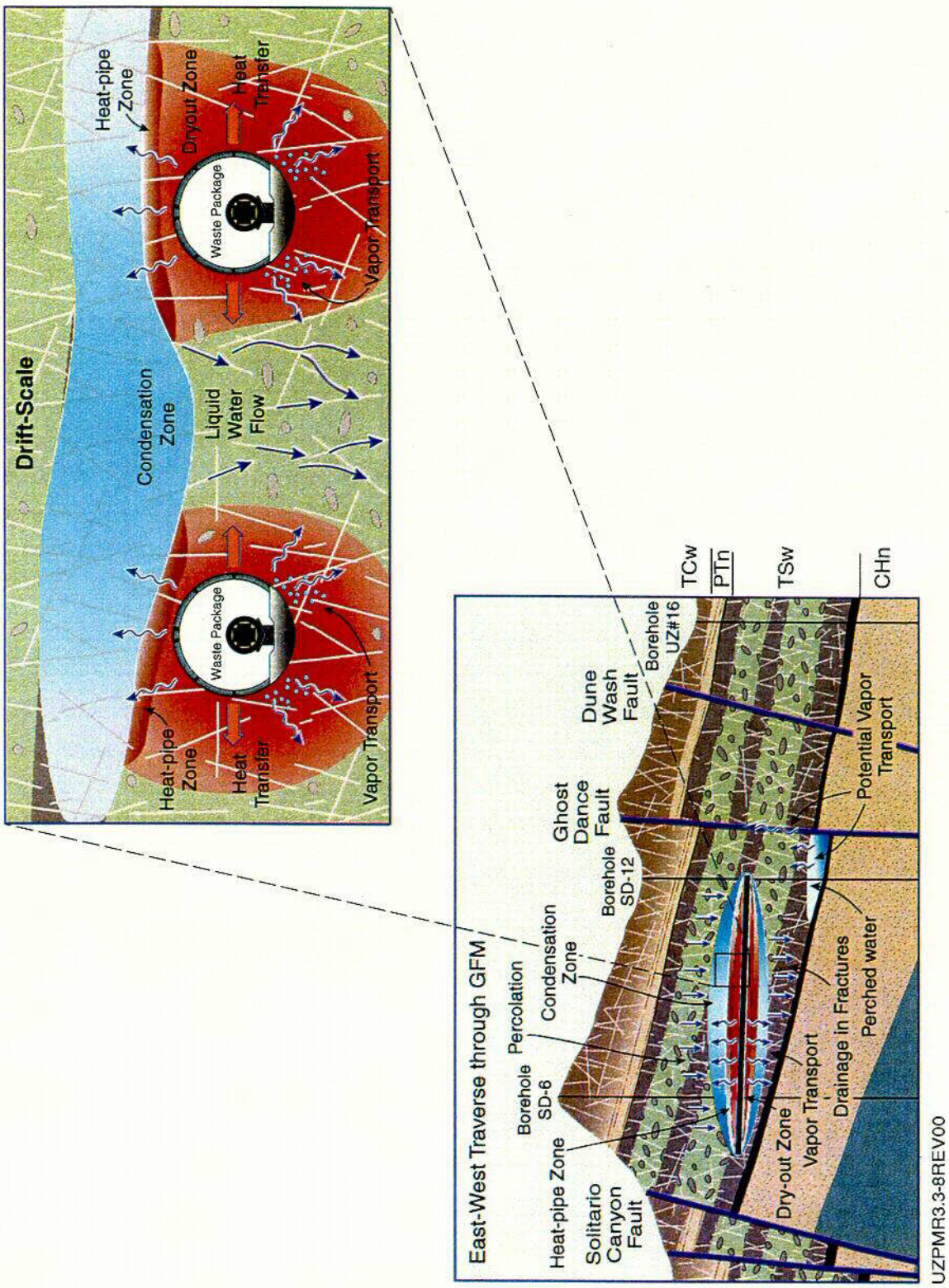

Figure 3.3-8. TH Processes at Mountain and Drift Scales

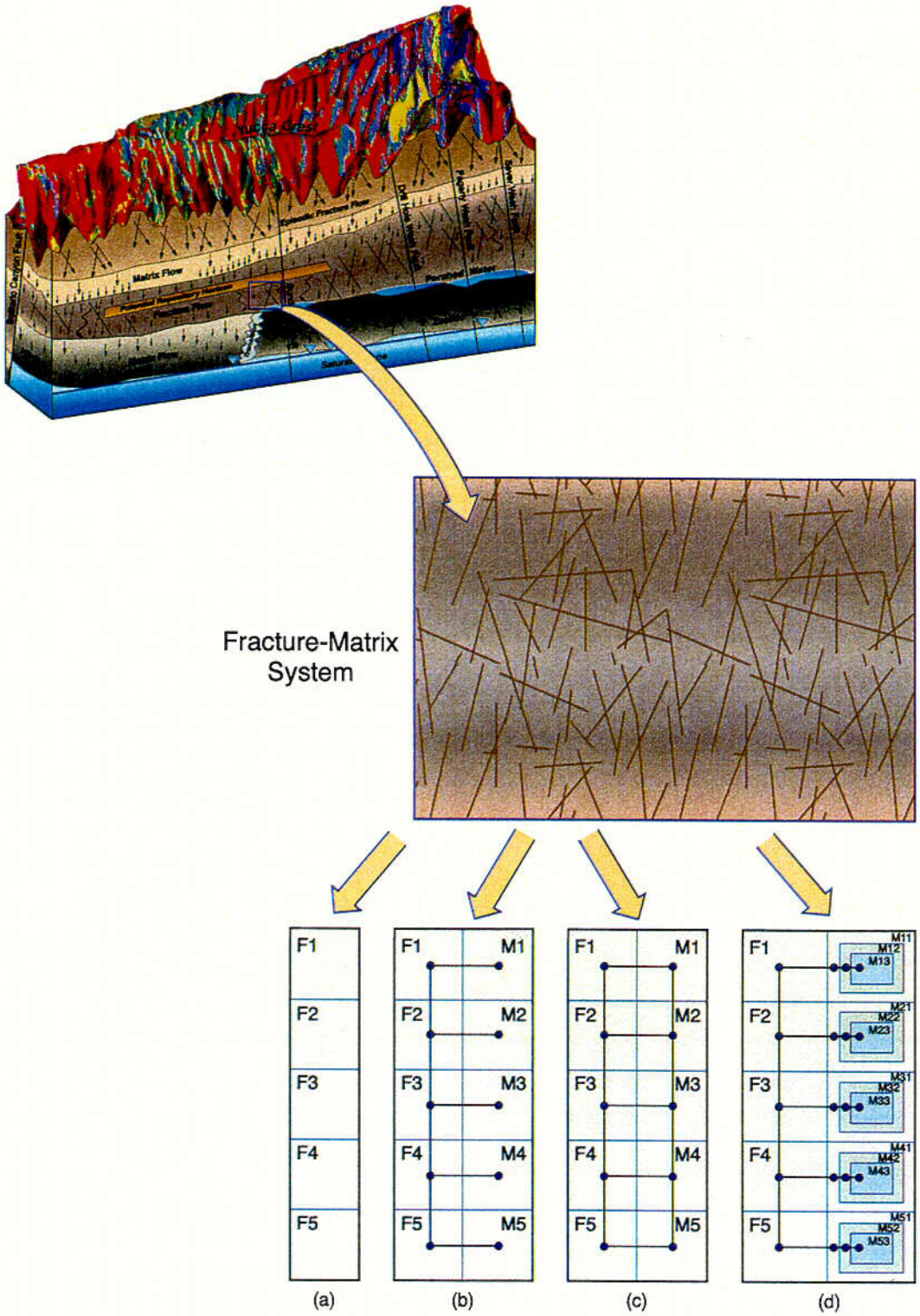

Figure 3.4-1. Schematic Demonstrating (a) ECM, (b) Dual-Porosity with One Matrix Gridblock, (c) Dual-Permeability with One Matrix Gridblock per Fracture Gridblock, and (d) MINC with Three Matrix Gridblocks per Fracture Gridblock

C38

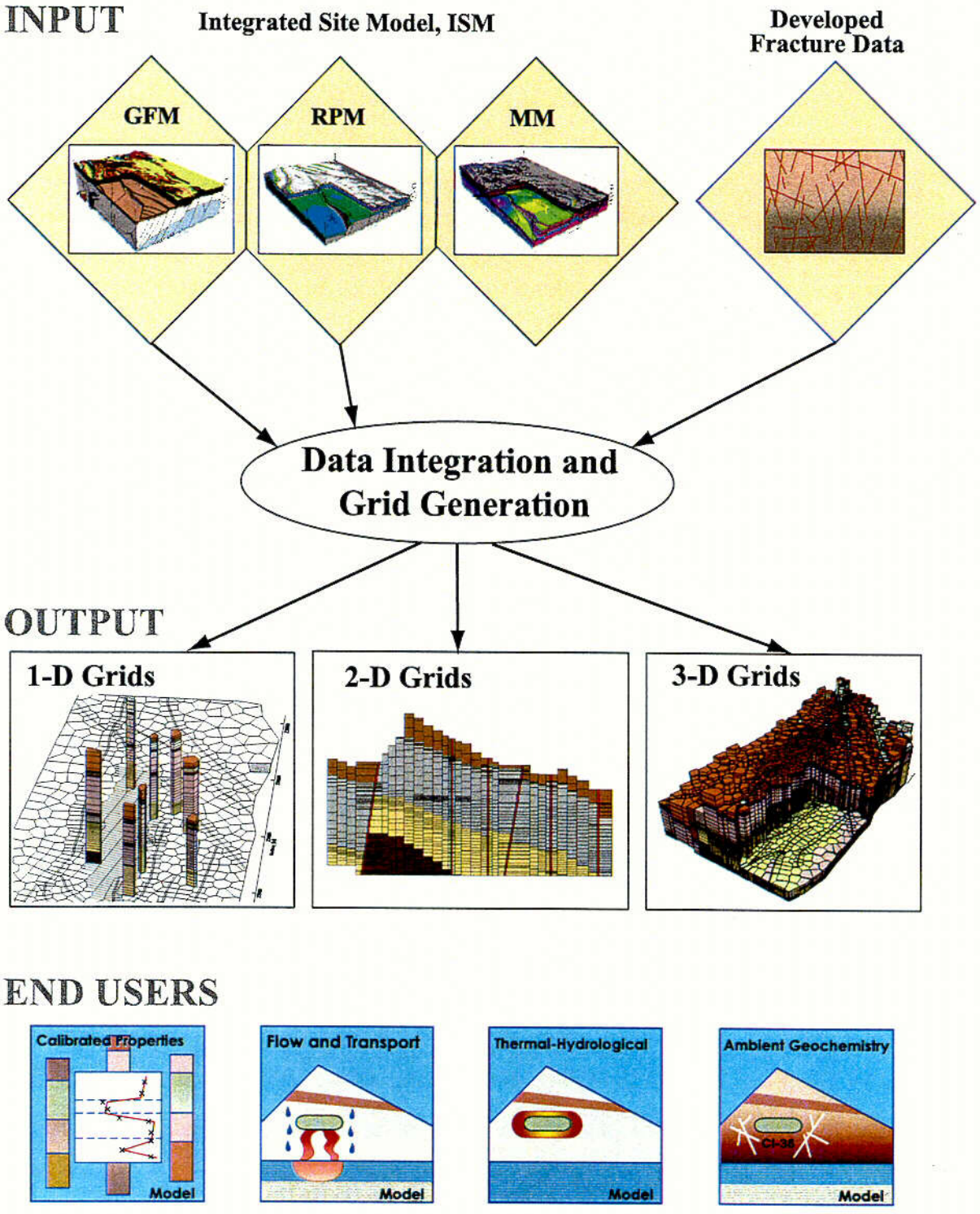

Figure 3.4-2. Flow Diagram Showing Key Input Data Used in Numerical Grid Development, the Types of Grids Generated, and their End Users

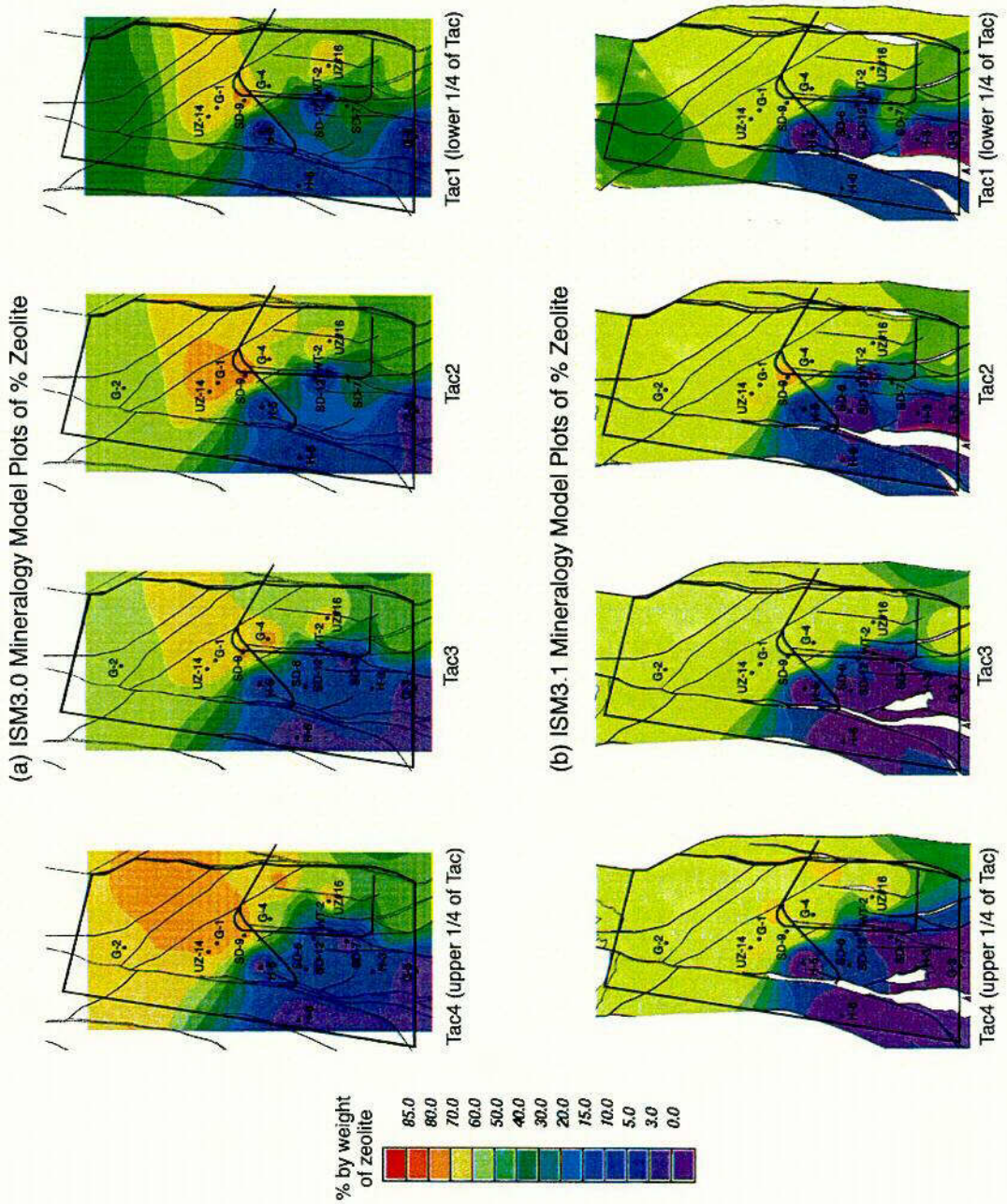

Figure 3.4-3. Distribution of Percent Zeolite Mineral Abundance in the Calico Hills Formation (lithostratigraphic unit Tac): (a) MM2.0, (b) MM3.0. (DTNs: MO9901MWDISMMM.000, MO9910MWDISMMM.003, respectively). Areas with less than or equal to 3% zeolite by weight are considered vitric, or unaltered.

C40

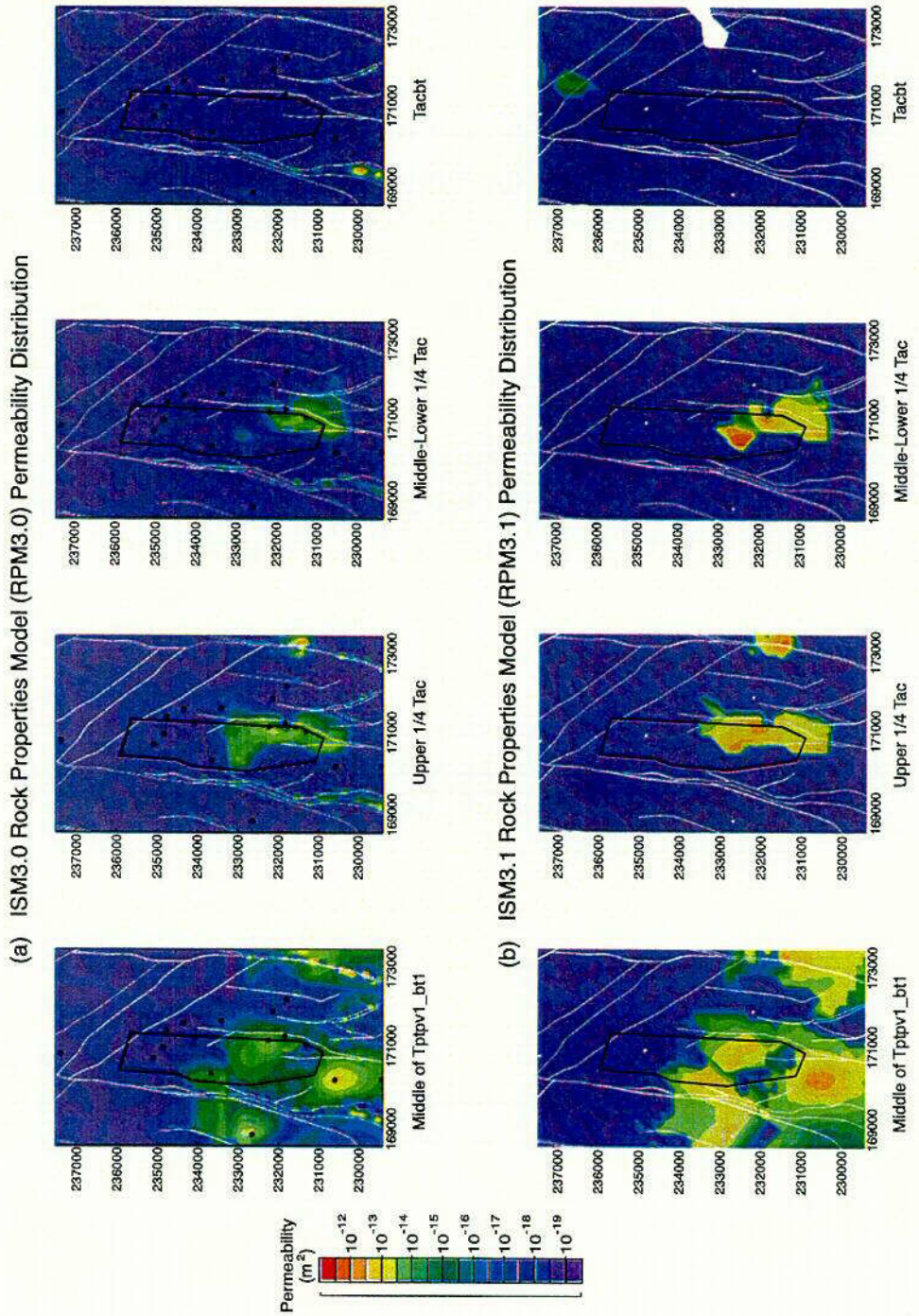

Figure 3.4-4. Distribution of Matrix Permeability (m^2) in Select Layers of the CHn Hydrogeologic Unit: (a) RPM3.0, (b) RPM3.1. (DTNs: MO9901MWDISMRP.000, MO9910MWDISMRP.002, respectively). In order to maintain consistent parameters within the UZ Flow and Transport Model PMR, saturated hydraulic conductivity (K_{sat}, m/s) from the RPM was converted to permeability (m^2) by multiplying K_{sat} values by 10^{-7}.

C41

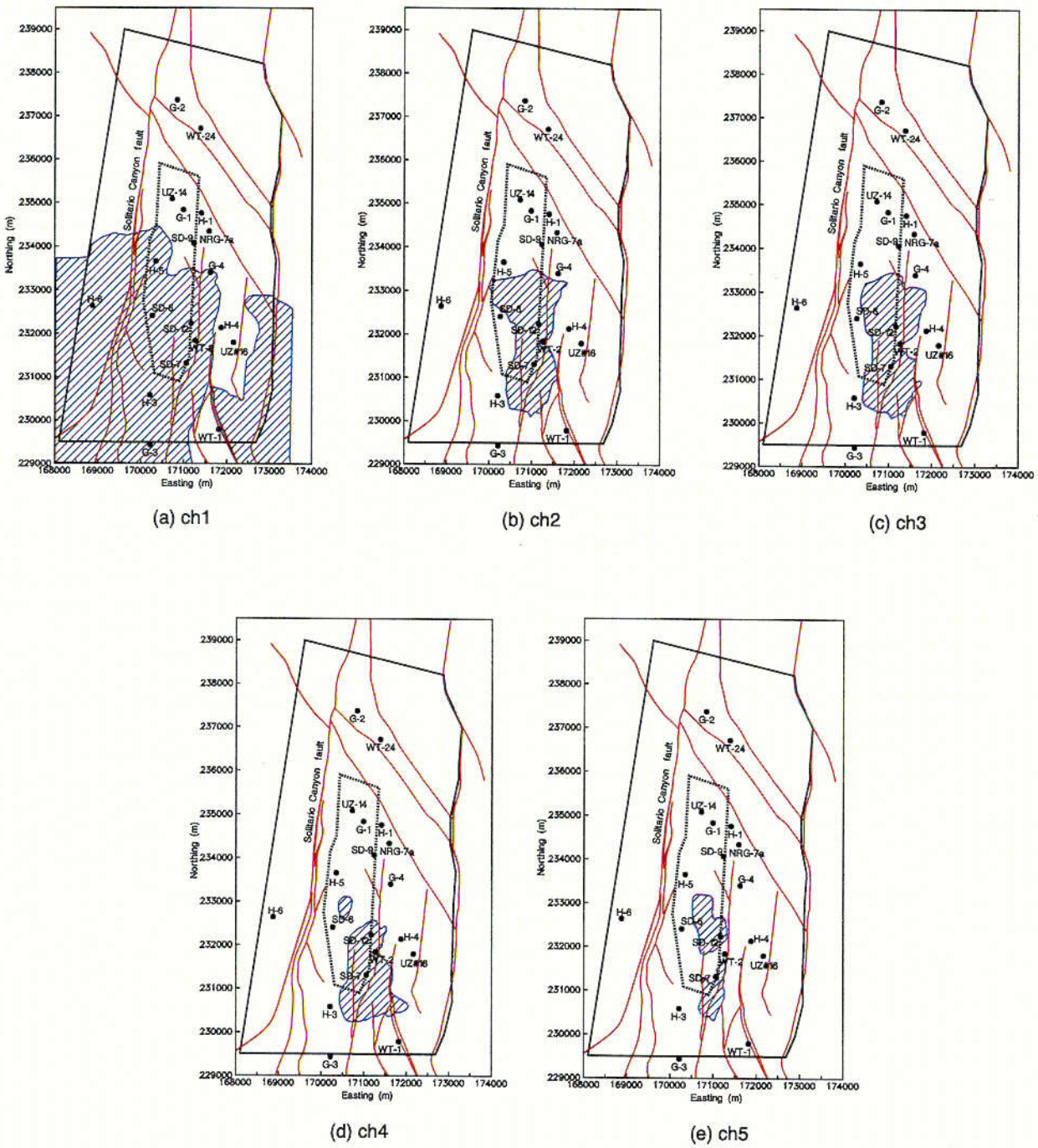

Figure 3.4-5. Extent of Vitric Region (Indicated by Pattern of Diagonal Lines) in Model Layers (a) ch1, (b) ch2, (c) ch3, (d) ch4, and (e) ch5. White areas indicate prevalent zeolitization (from CRWMS M&O 2000, U0000, Figure 5).

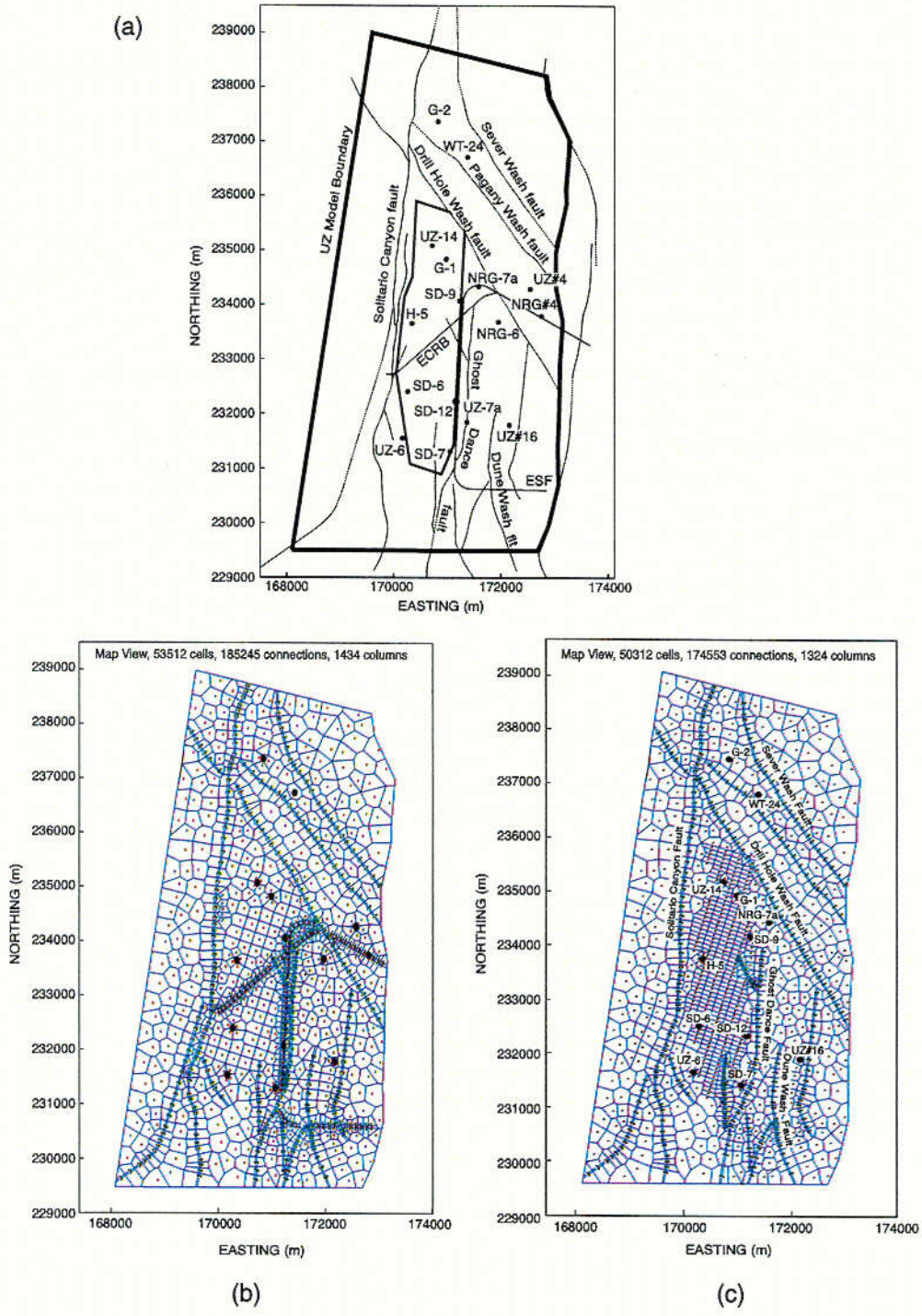

Figure 3.4-6. Plan-View (a) Schematic Showing the UZ Model Boundary, the Repository Outline, Major Fault Locations Adapted from GFM3.1, Select Boreholes, the ESF, and the ECRB, (b) Numerical Grid Design for the Mountain-Scale Model Used for UZ Calibration (adapted from Figure V-1 of CRWMS M&O 2000, U0000), and (c) Numerical Grid Design for the Mountain-Scale Model Used for PA Calculations (Adapted from CRWMS M&O 2000, U0000, Figure VI-1).

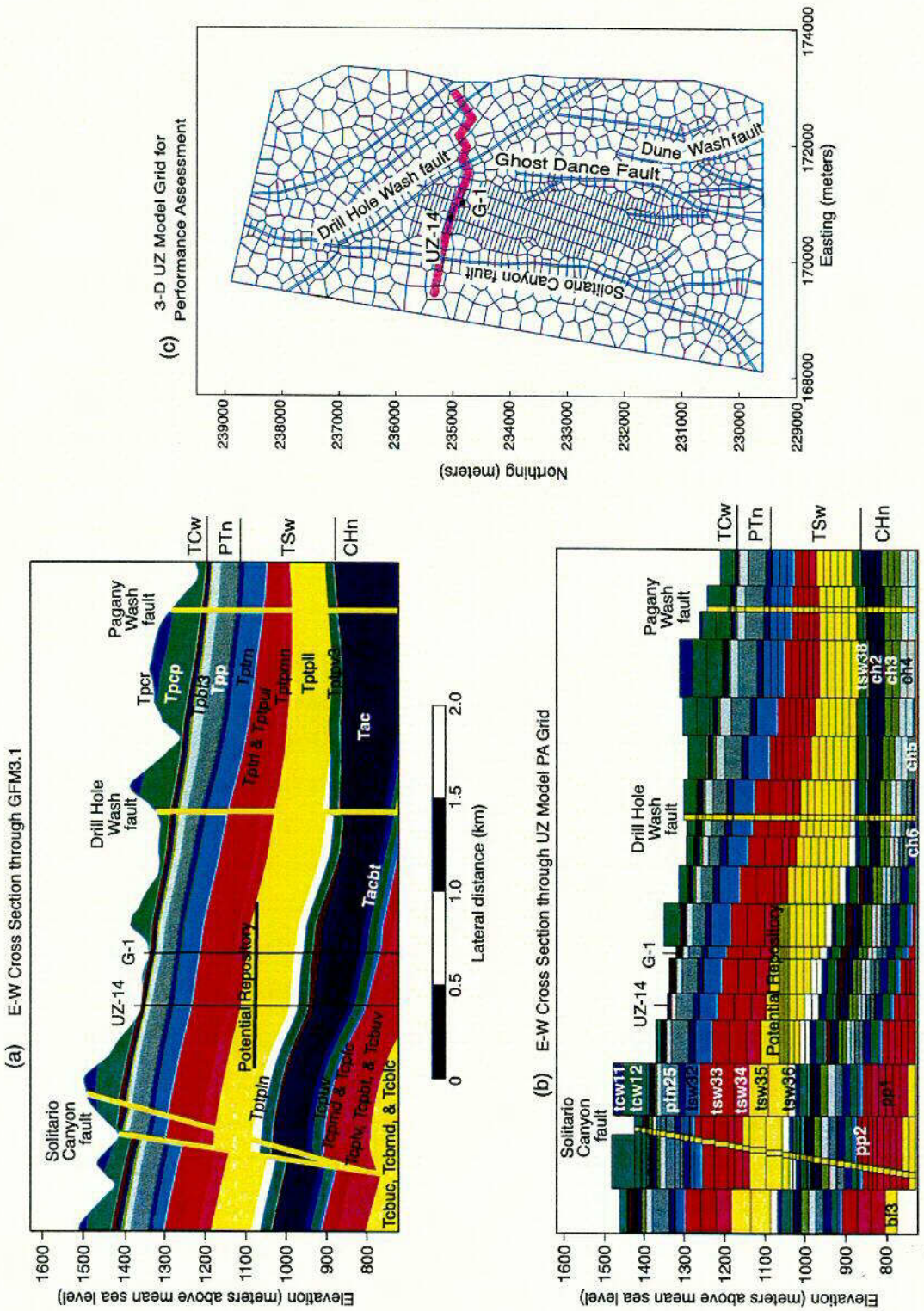

Figure 3.4-7. East-West Cross-Section through Borehole UZ-14: (a) Adapted from Data Contained in CRWMS M&O (2000, I0035) (b) from the 3-D UZ Model Numerical Grid for PA (Adapted from CRWMS M&O 1999a, Figure VI-2). The 3-D UZ Model Grid in plan view (c) shows the location of the cross section. Bottom elevation along cross sections is 730 m above mean sea level.

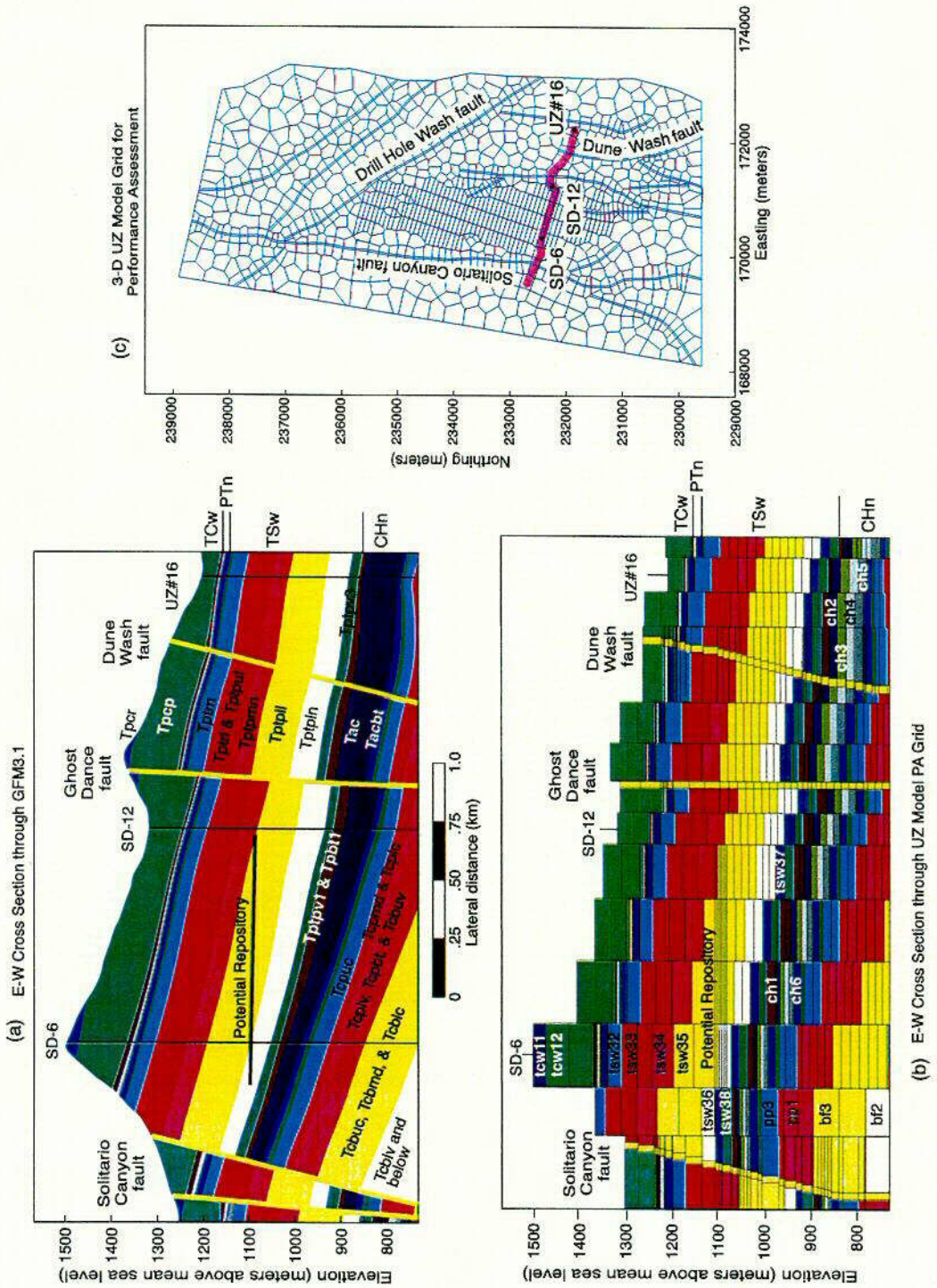

Figure 3.4-8. East-West Cross-Section through Boreholes SD-6, SD-12, UZ#16: (a) Adapted from Data Contained in CRWMS M&O (2000, I0035) (b) from the 3-D UZ Model Numerical Grid for PA (Adapted from CRWMS M&O 1999a, Figure VI-3). The 3-D UZ Model Grid in plan view (c) shows the location of the cross section. Bottom elevation along cross sections is 730 m above mean sea level.

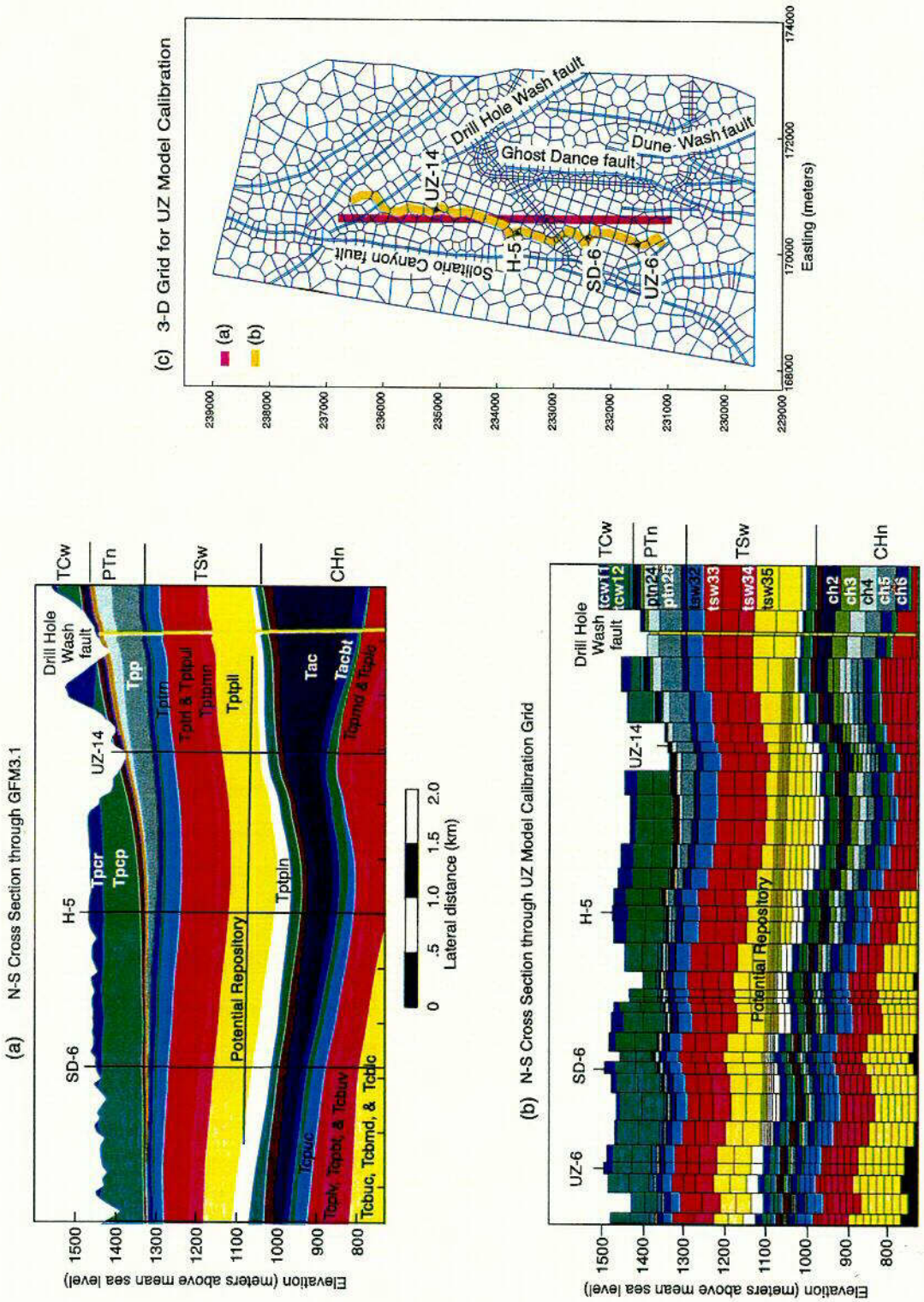

Figure 3.4-9. North-South Cross-Section through Boreholes UZ-14, H-5, and SD-6: (a) Adapted from Data Contained in CRWMS M&O (2000, I0035) (b) from the 3-D UZ Model Calibration Grid (Adapted from CRWMS M&O 1999a, Figure V-4). The 3-D UZ Model Calibration Grid in plan view (c) shows the location of the cross sections. Bottom elevation along cross sections is 730 m above mean sea level.

C46

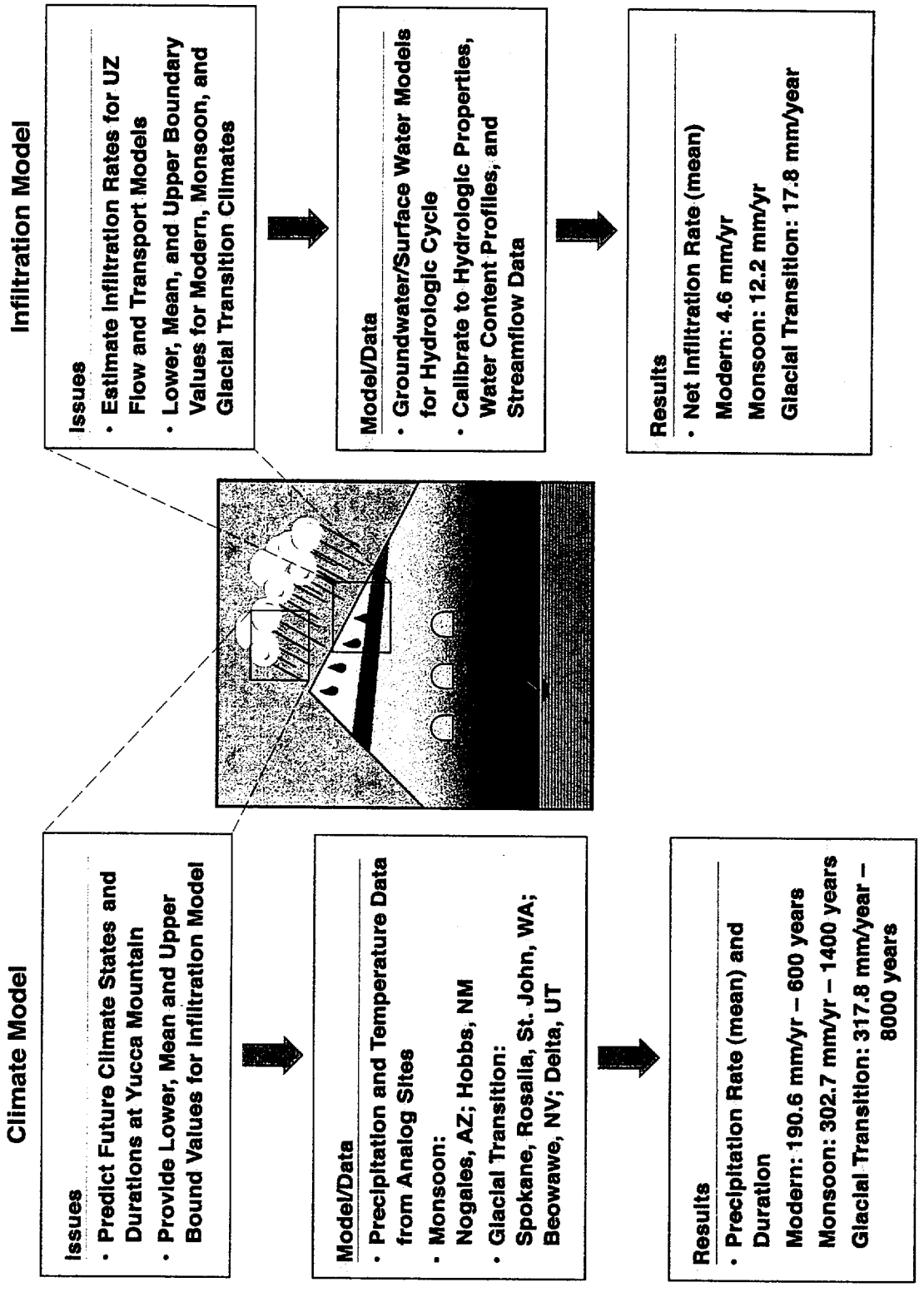

Figure 3.5-1. Summary of Issues, Modeling Methodology, Data, and Results for both the Climate and Infiltration Models

(a)

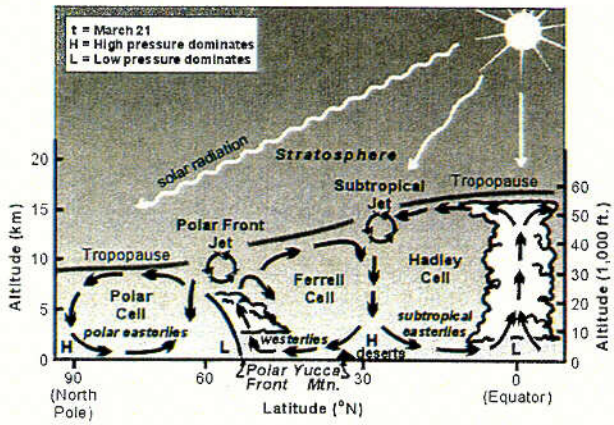

(b)

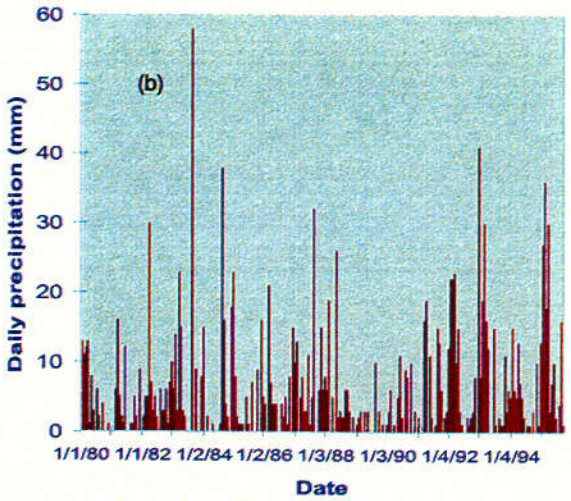

(c)

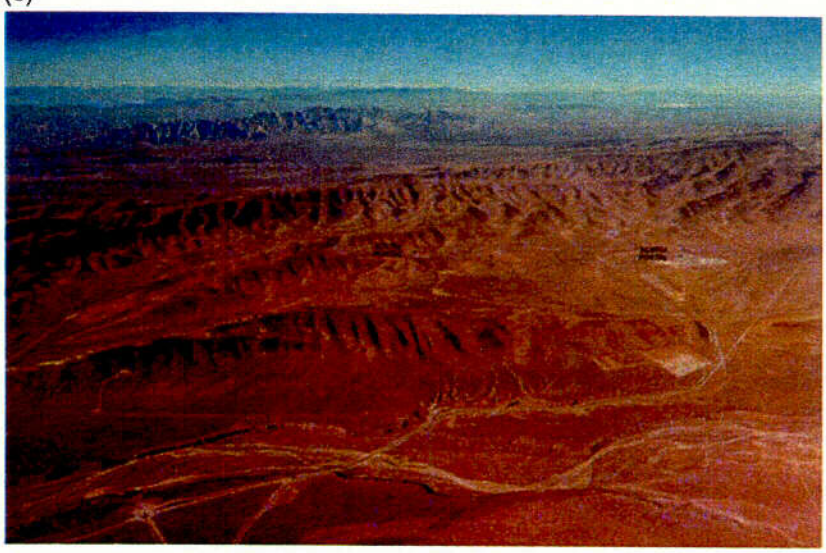

Figure 3.5-2. (a) Generalized View of Present-Day Atmospheric Circulation (USGS 2000, U0005, Figure 2) and (b) Daily Precipitation Record Between 1980 and 1995 at Yucca Mountain (USGS 2000, U0010, Figure 6-18) with (c) an Aerial View of the Arid Conditions at the Yucca Mountain Site

C47

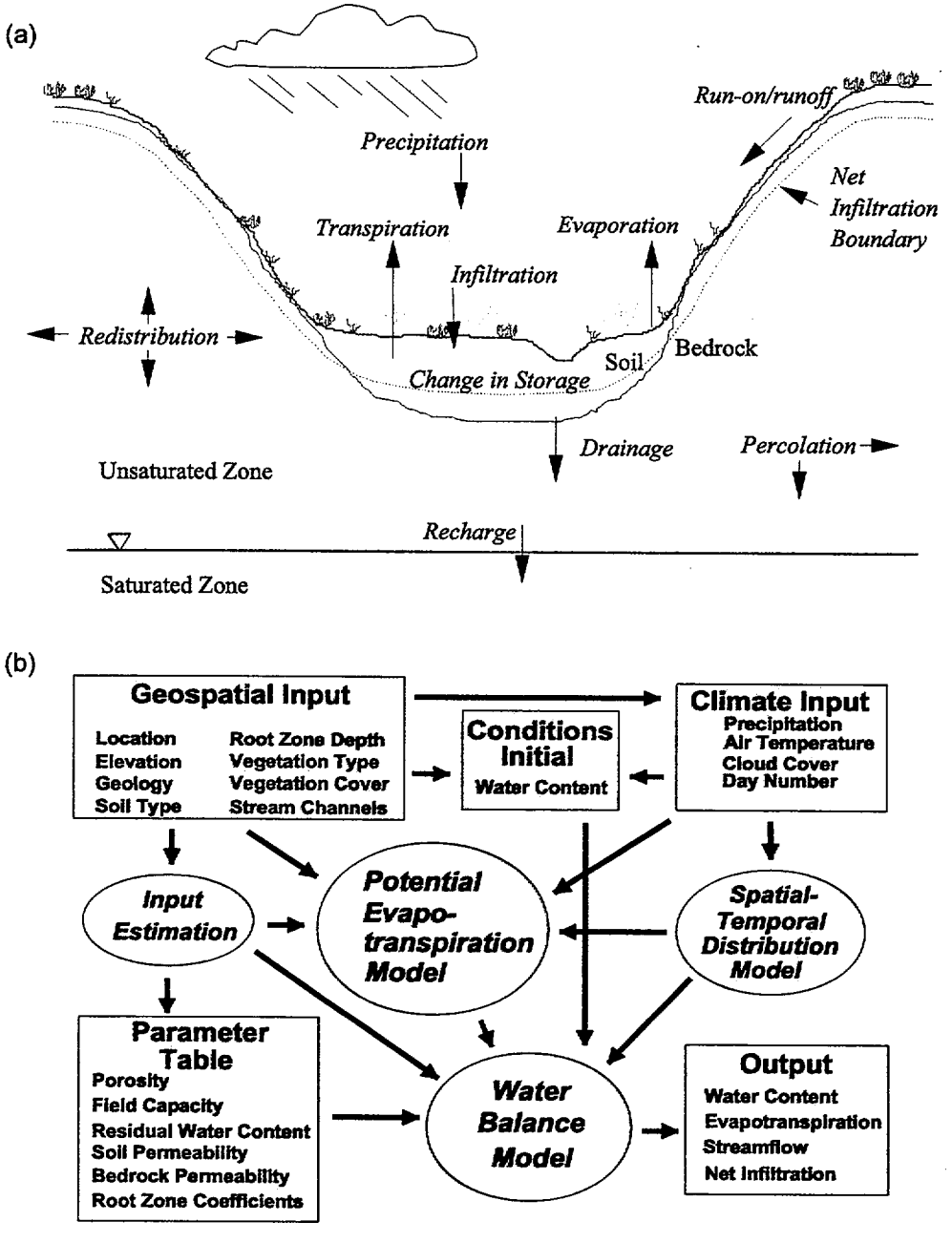

Figure 3.5-3. (a) Field-Scale Water Balance and Processes Controlling Net Infiltration (USGS 2000, U0010, Figure 5-1) and (b) Major Components of the Net Infiltration Modeling Process (USGS 2000, U0010, Figure 6-1)

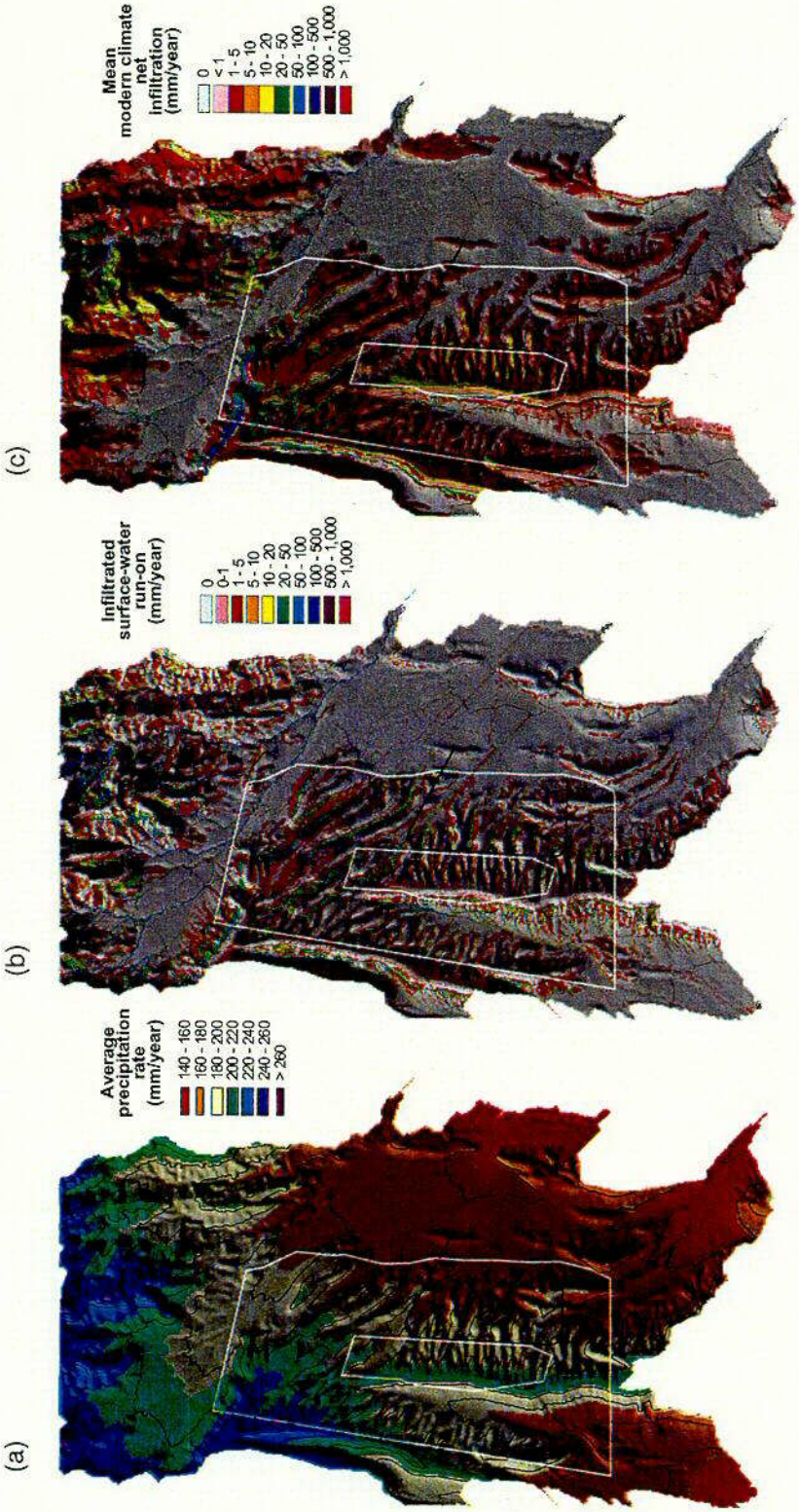

Figure 3.5-4. (a) Precipitation (USGS 2000, U0010, Figure 7-1), (b) Surface Run-On (USGS 2000, U0010, Figure 7-3) and (c) Net-Infiltration Rates (USGS 2000, U0010, Figure 7-4) for the Mean Modern Climate Scenario

C48

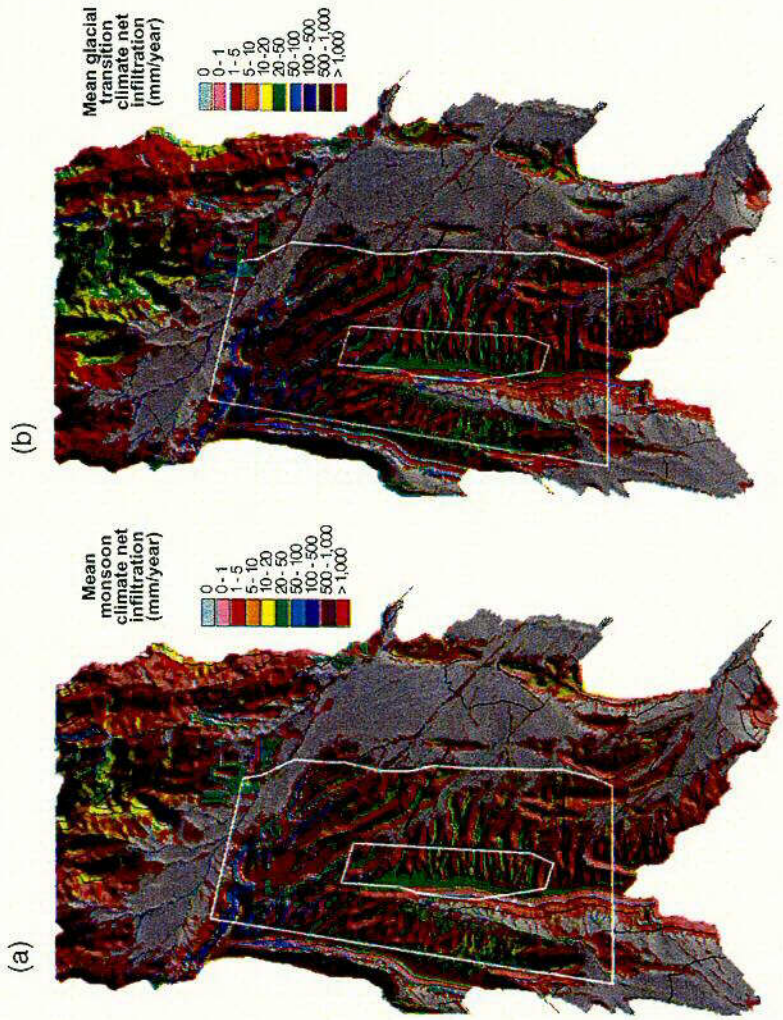

Figure 3.5-5. Net-Infiltration Rates for (a) Mean Monsoon (USGS 2000, U0010, Figure 7-7) and (b) Mean Glacial-Transition (USGS 2000, U0010, Figure 7-14) Climates

C49

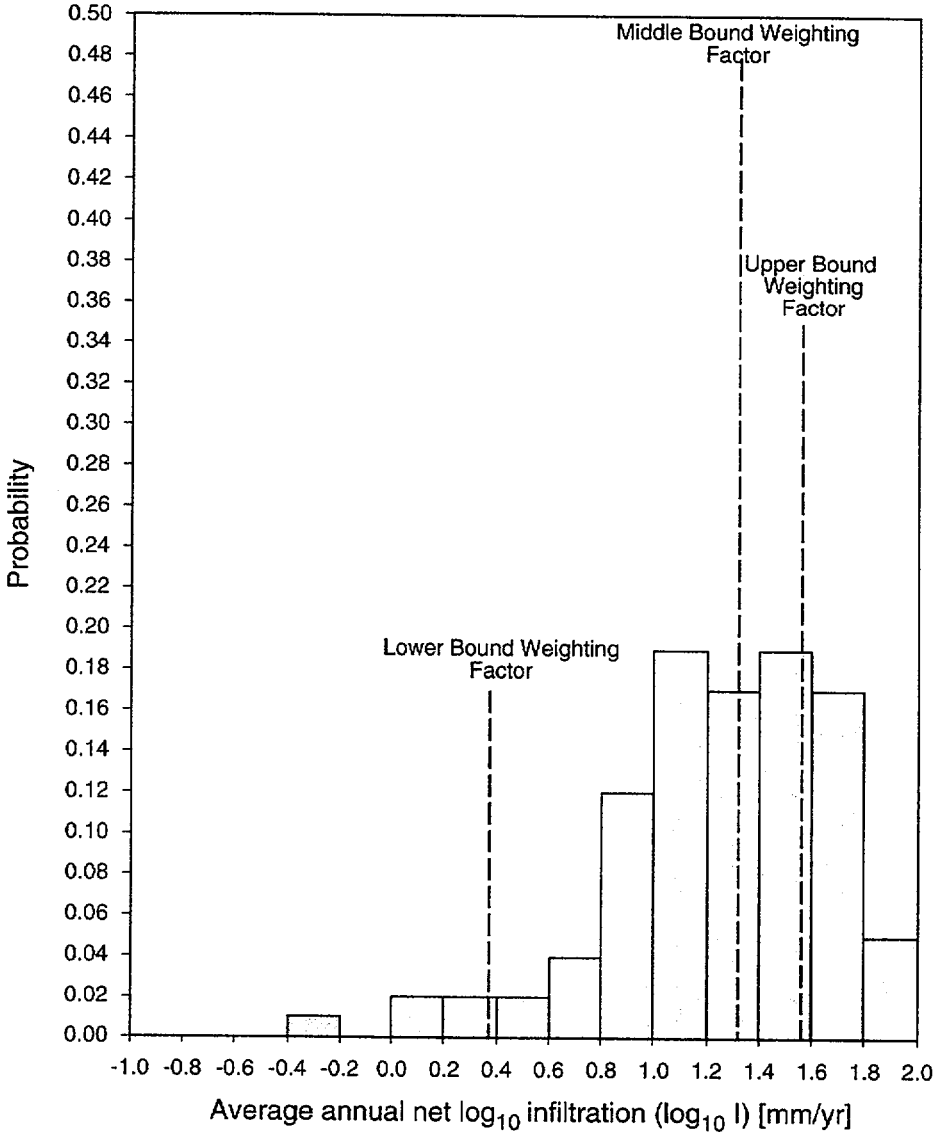

Figure 3.5-6. Histogram of Log of Potential Repository-Average Infiltration for Glacial-Transition Climate (adapted from CRWMS M&O 2000, U0095, Figure 6-2)

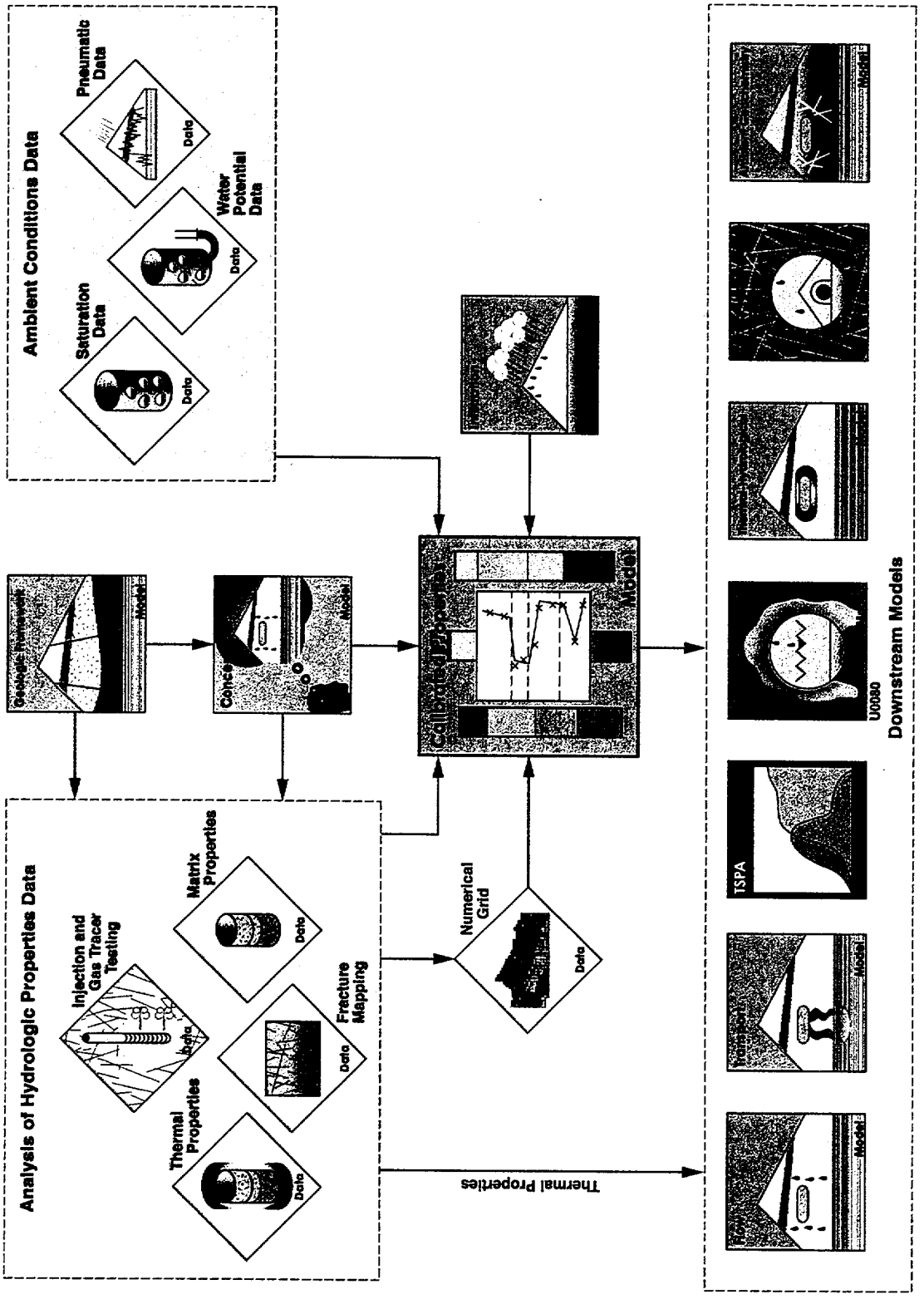

Figure 3.6-1. Relationship of the Analysis of Hydrologic Properties Data and the Calibrated Properties Model to Input Data and Models and to Analyses and Models that use the Developed UZ Properties

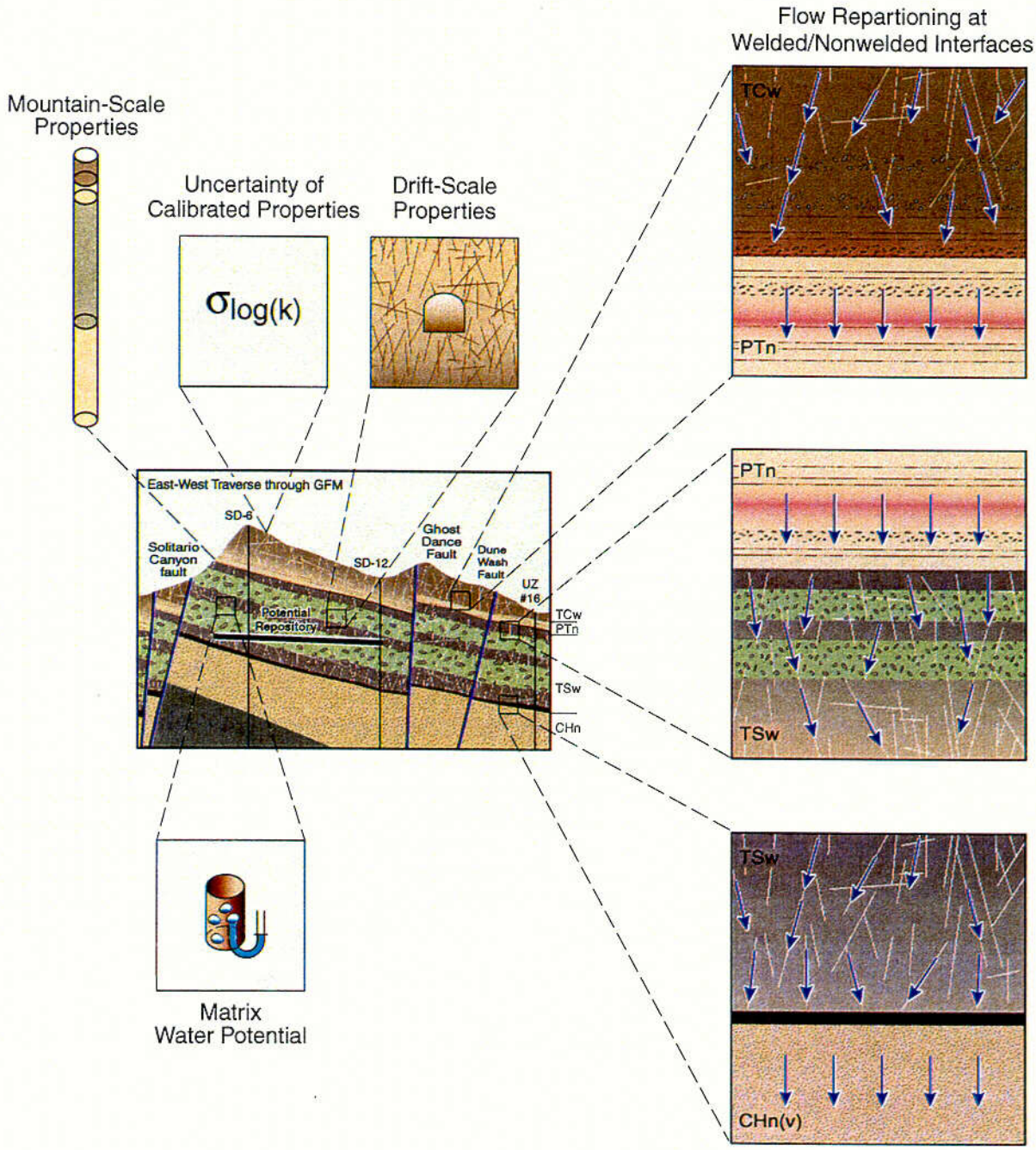

Figure 3.6-2. Issues for Development of UZ Properties

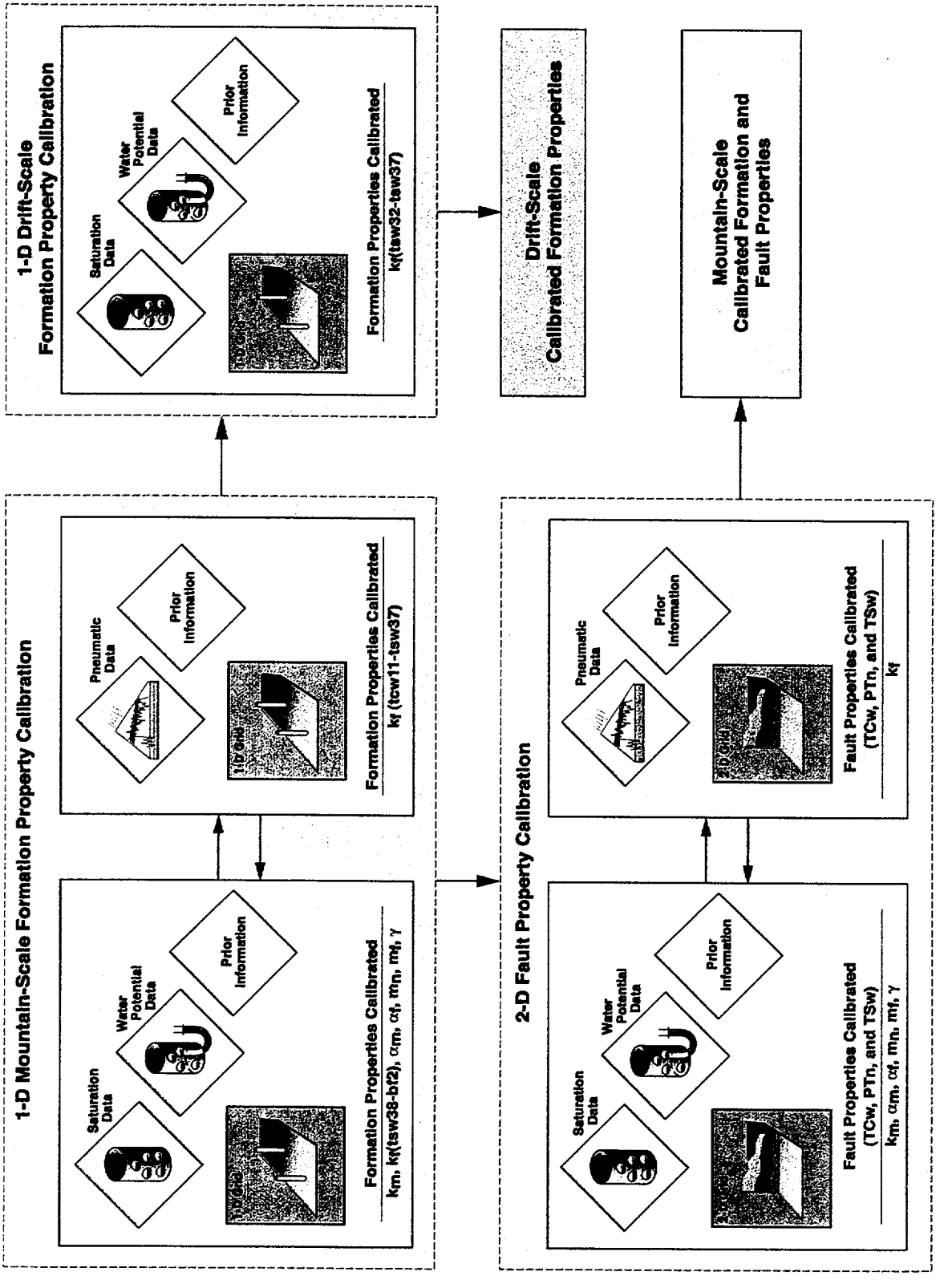

Figure 3.6-3. Calibrated Property Development

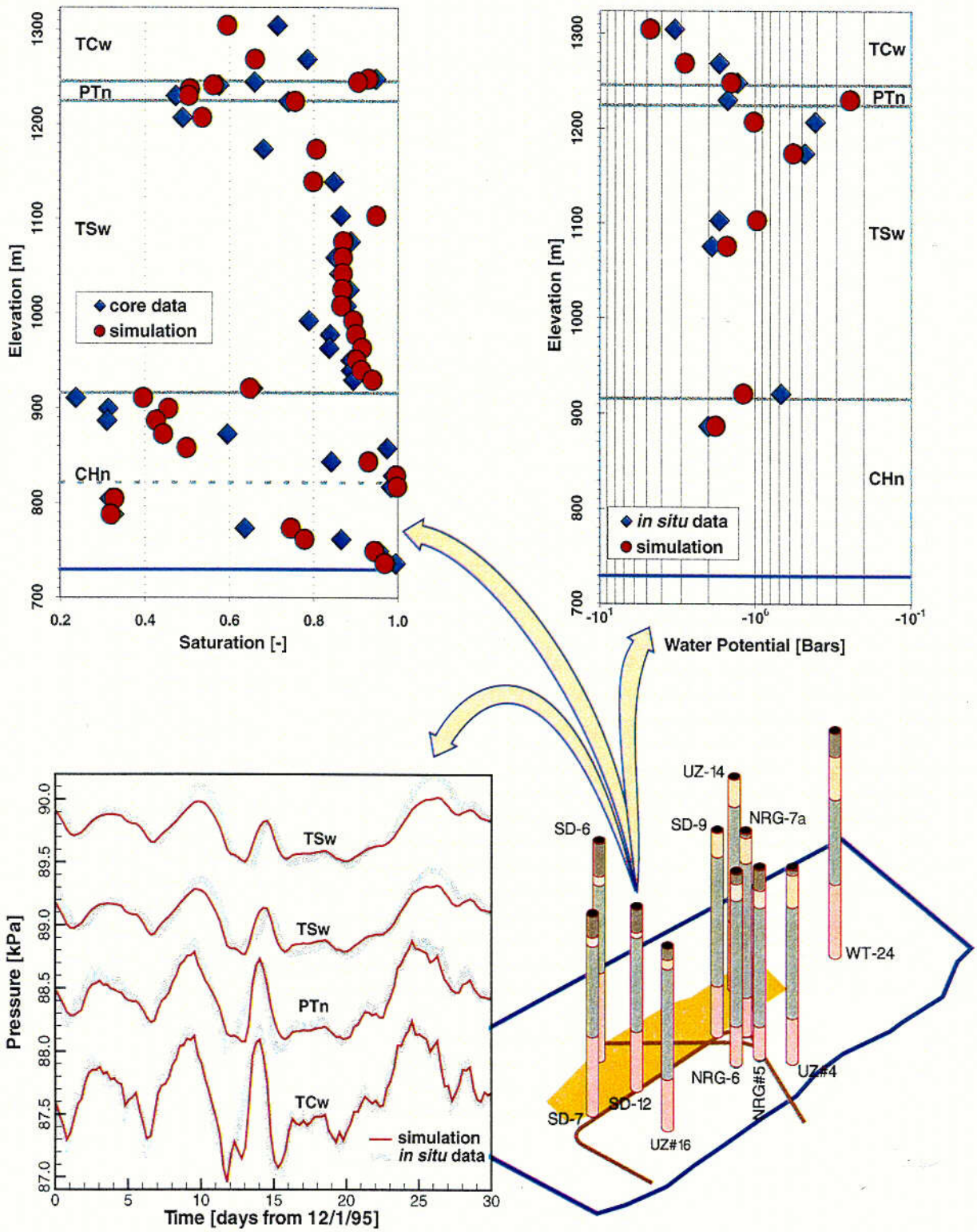

Figure 3.6-4. Calibrated 1-D Simulation Match to Saturation, Water Potential, and Pneumatic Data. Data from Borehole USW SD-12 for the Base Case Infiltration Scenario (adapted from CRWMS M&O 2000, U0035, Figures 2, 3, and 4)

C51

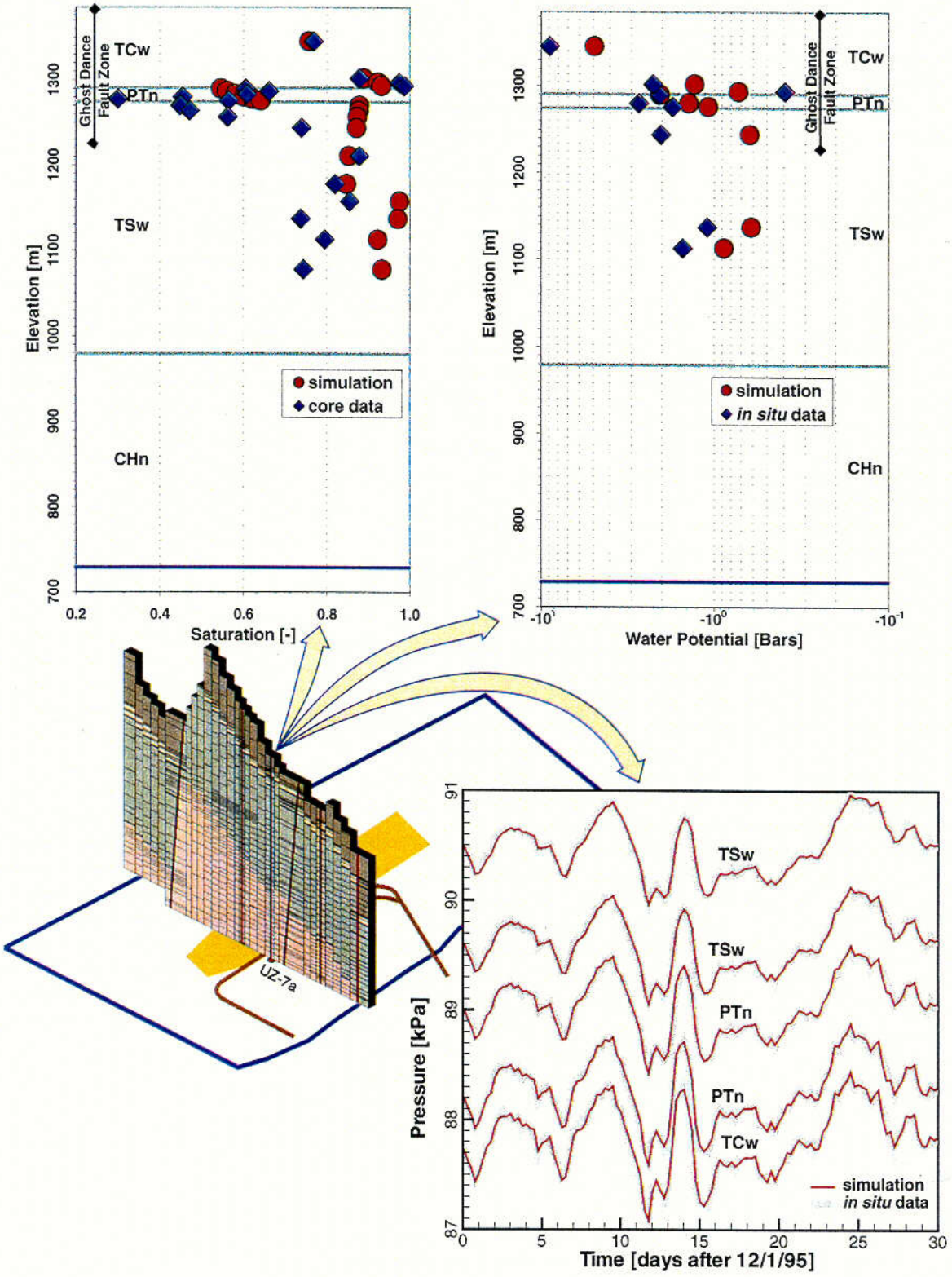

Figure 3.6-5. Calibrated 2-D Simulation Match to Saturation, Water Potential, and Pneumatic Data from Borehole USW UZ-7a Base Case Infiltration Scenario (adapted from CRWMS M&O 2000, U0035, Figures 9, 10, and 11)

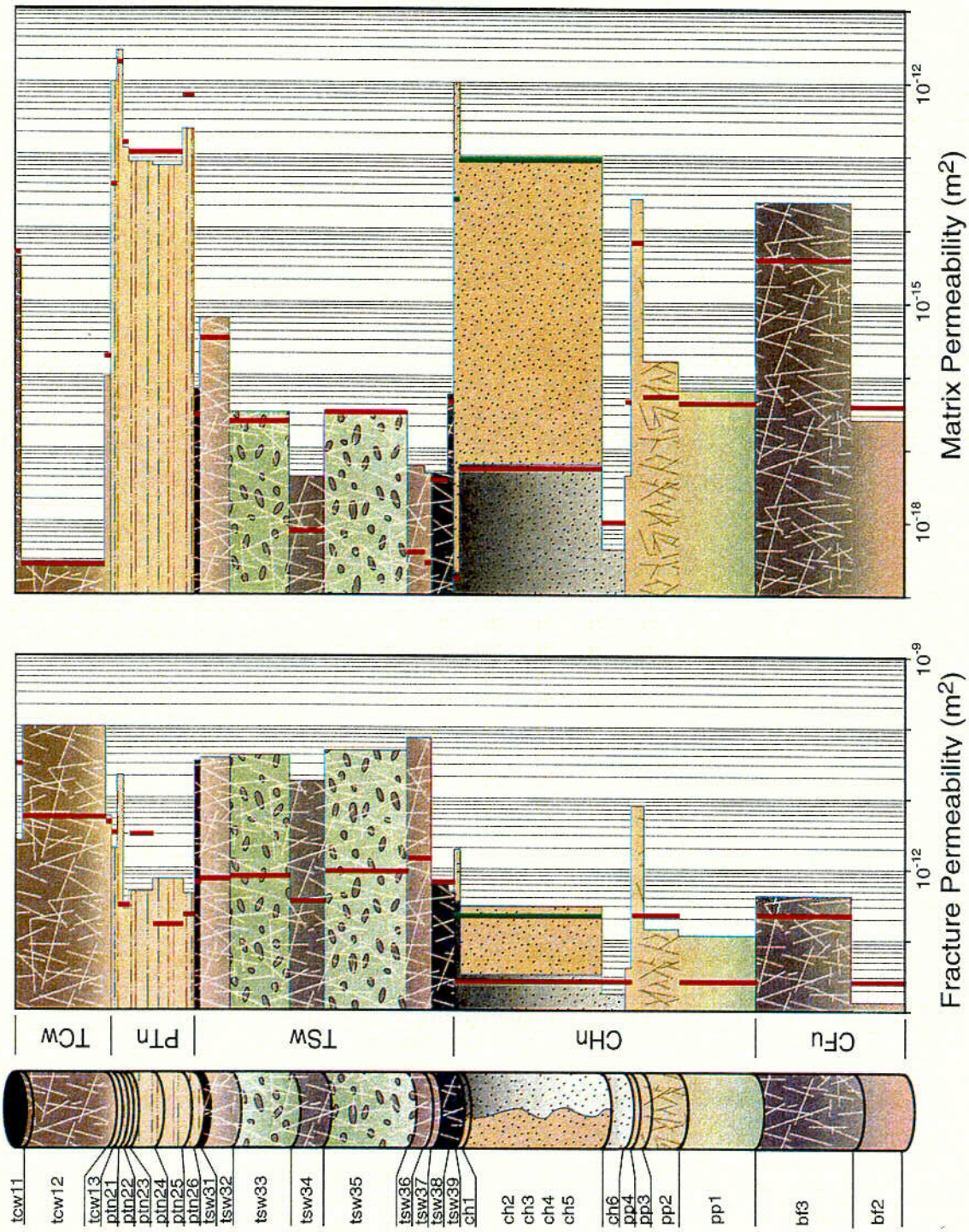

Figure 3.6-6. Initial Estimate of and Calibrated Fracture and Matrix Permeability for the Base Case, Present-Day Infiltration Scenario (adapted from data in CRWMS M&O 2000, U0035, Table 13). The calibrated values for the vitric ch1 through ch5 layers are shown in a lighter color than the zeolitic. The prior information (initial estimate) is shown as a red line (green for the vitric ch1 through ch5).

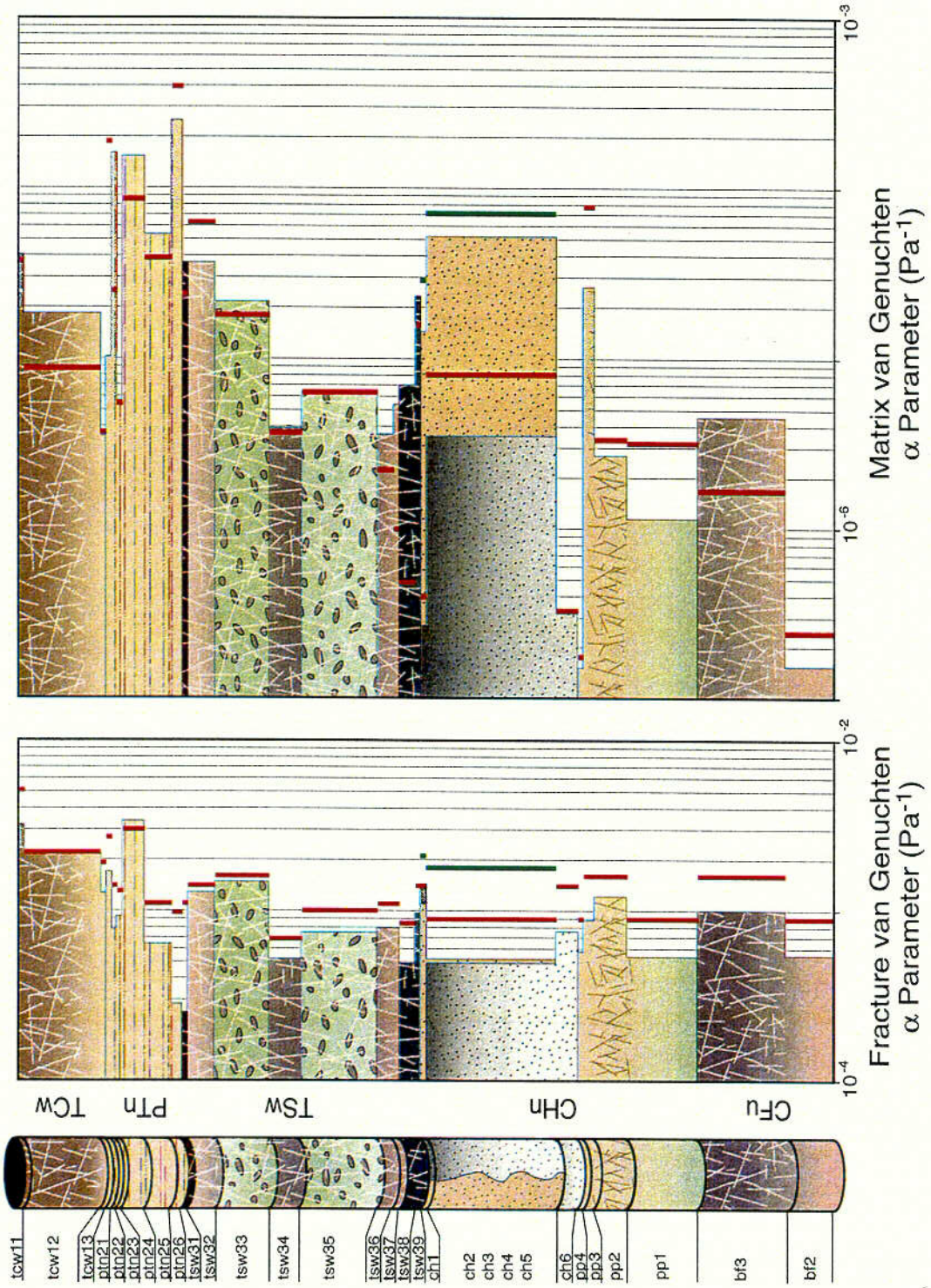

Figure 3.6-7. Initial Estimate of and Calibrated Fracture and Matrix van Genuchten α Parameter for the Base Case, Present-Day Infiltration Scenario (adapted from data in CRWMS M&O 2000, U0035, Table 13). The calibrated values for the vitric ch1 through ch5 layers are shown in a lighter color than the zeolitic. The prior information (initial estimate) is shown as a red line (green for the vitric ch1 through ch5).

C54

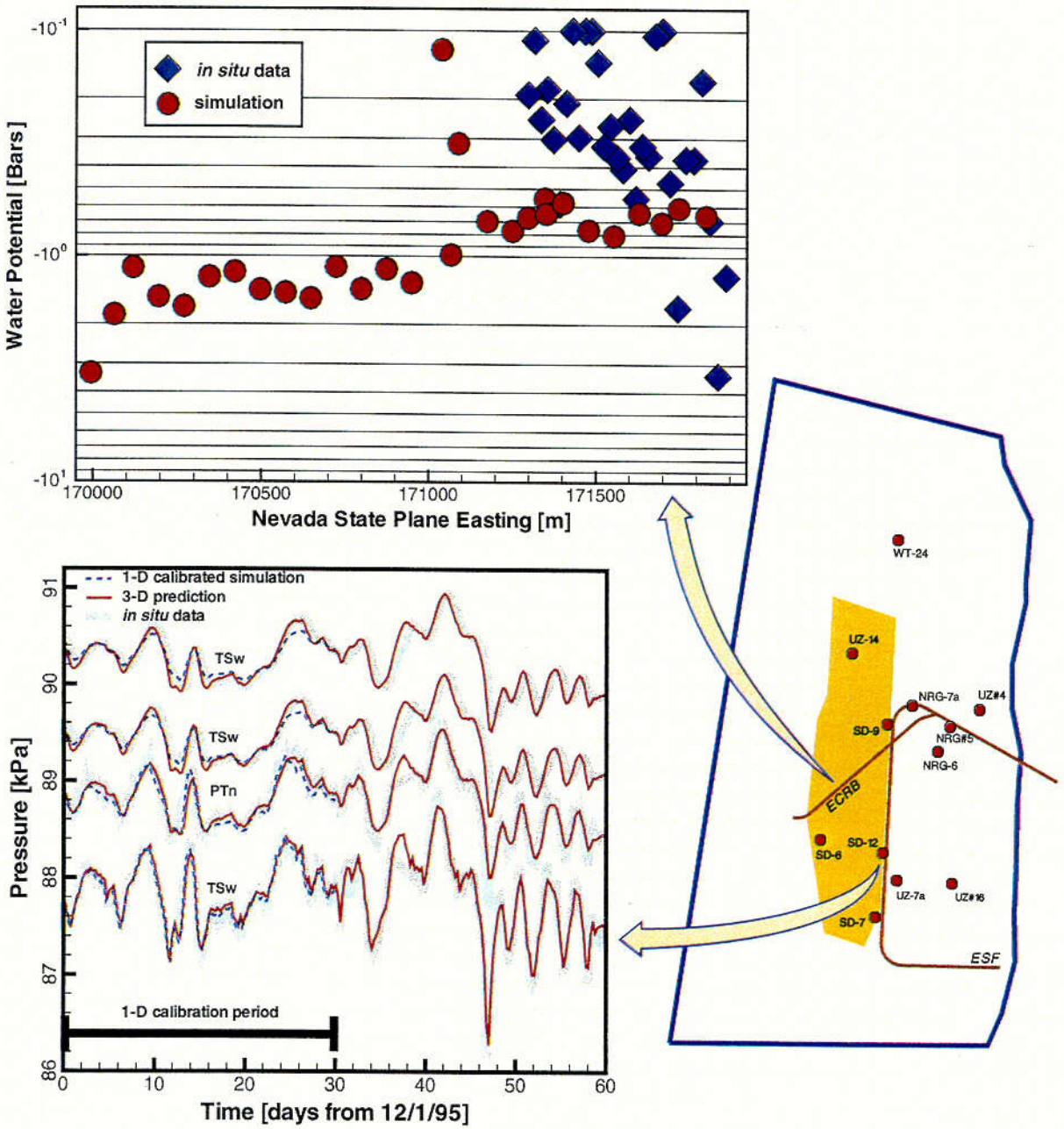

Figure 3.6-8. Comparison of Predictions from the 3-D Model with In Situ Water Potential Data from the ECRB Cross Drift and Pneumatic Pressure Data from Borehole USW SD-12 (adapted from CRWMS M&O 2000, U0050, Figures 6-69 and 6-70)

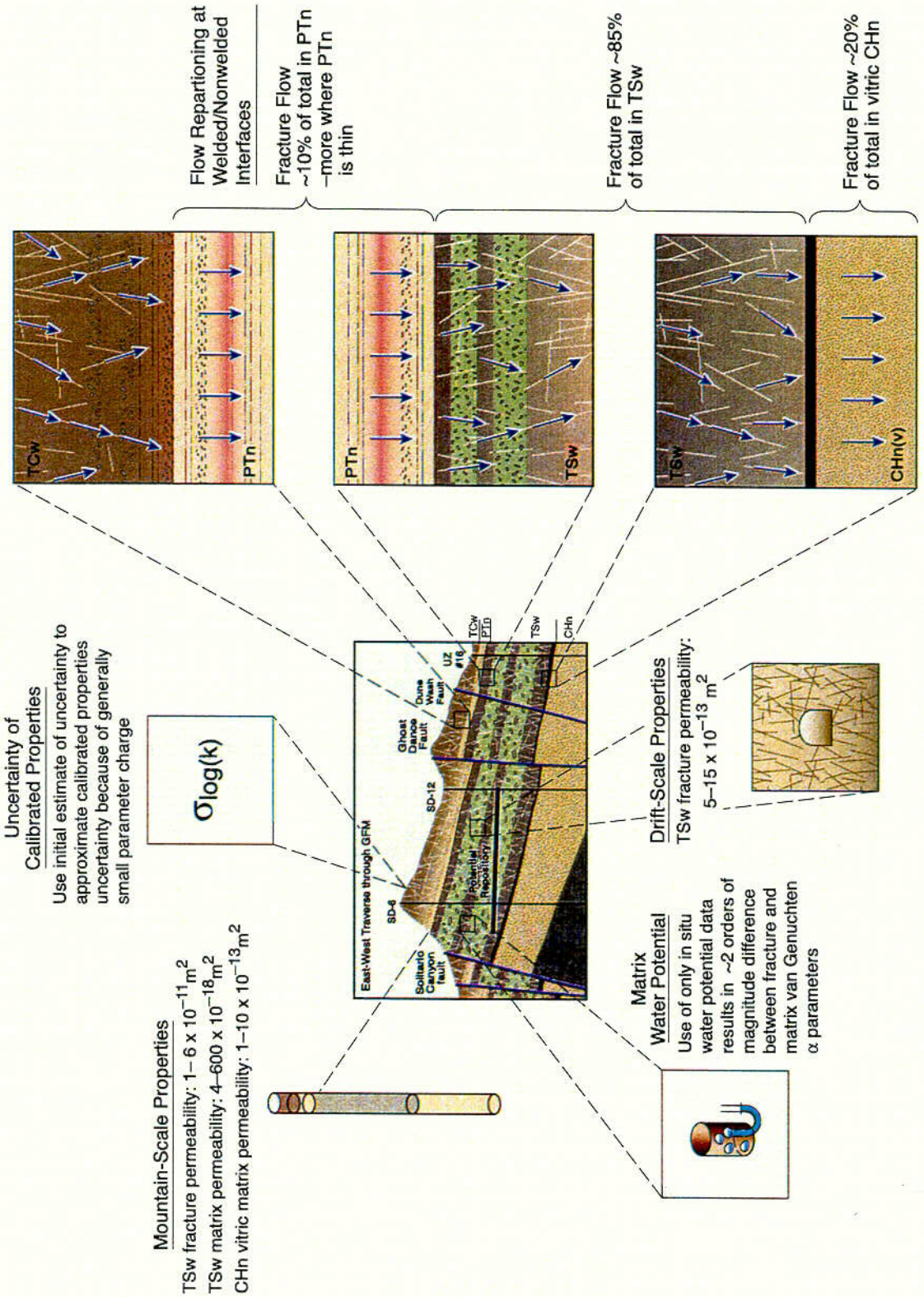

Figure 3.6-9. Important Results of Analysis of Hydrologic Properties Data and Calibrated Properties Model

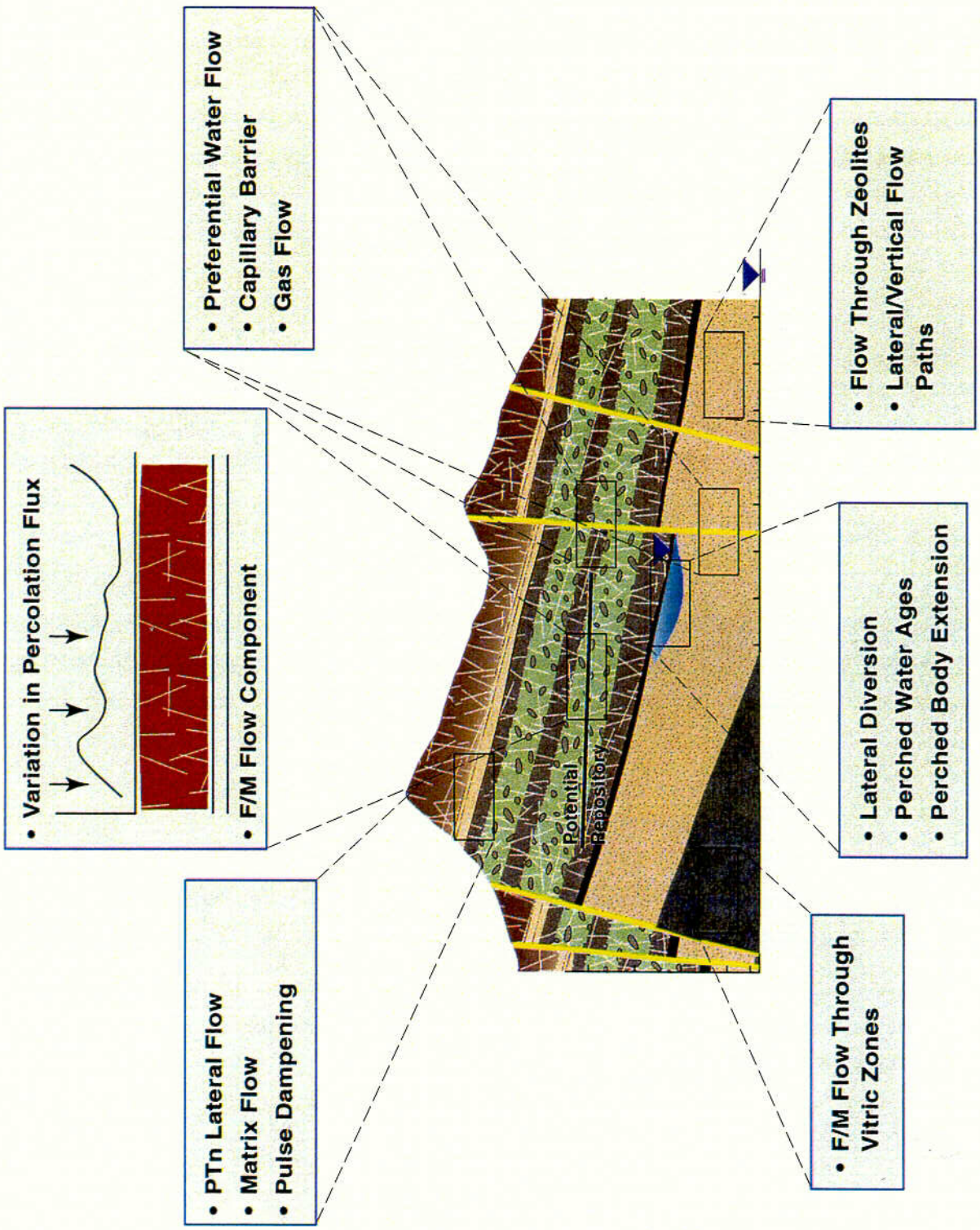

Figure 3.7-1. Diagram Showing the Important UZ Flow and Transport Issues, Addressed by the Flow Model and Its Submodels

C57

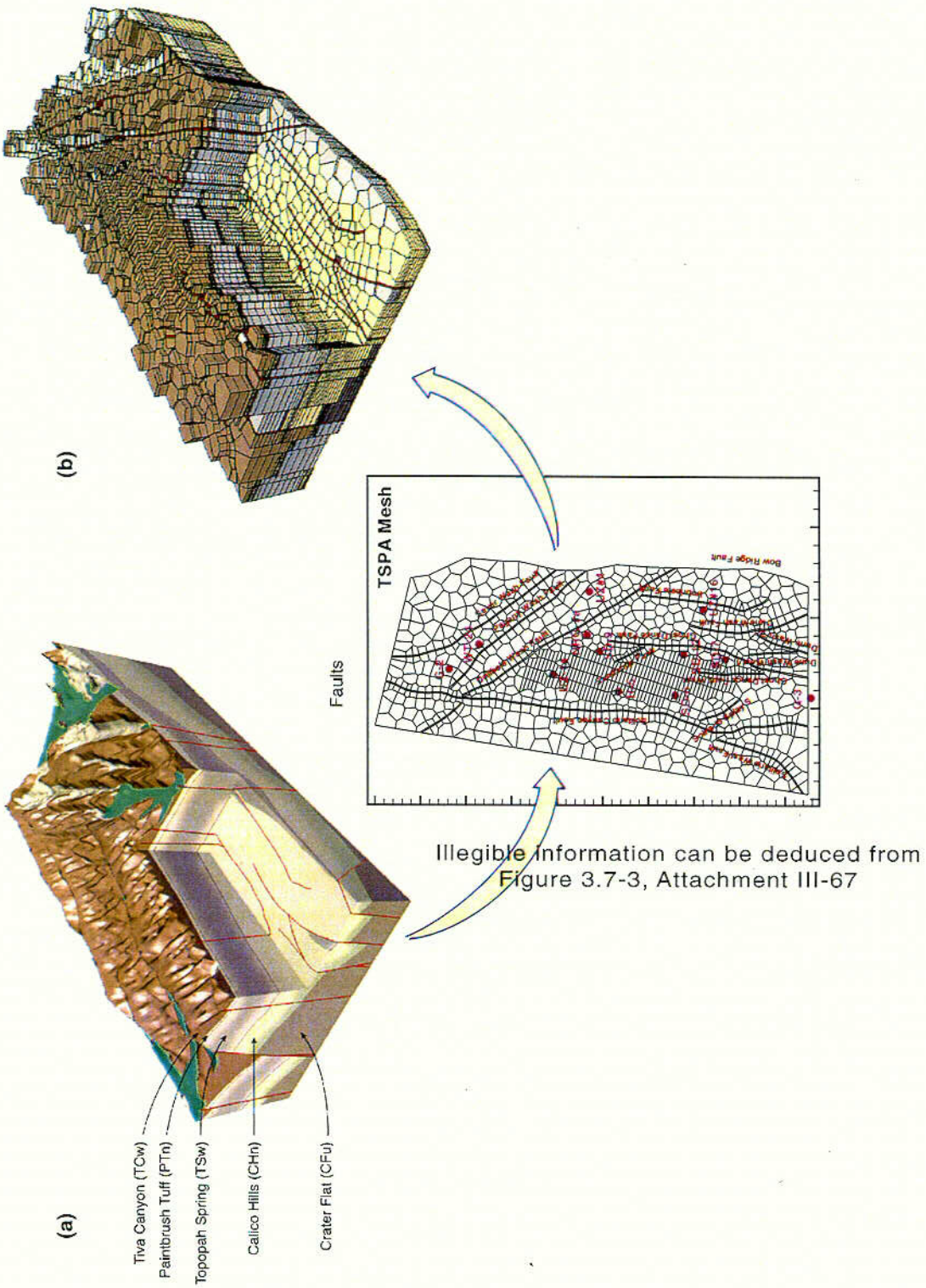

Figure 3.7-2. Perspective View of the UZ Model Domain of Yucca Mountain, Showing the Hydrogeological Units and Layers and Major Faults: (a) Geological Model and (b) Numerical Grid

C58

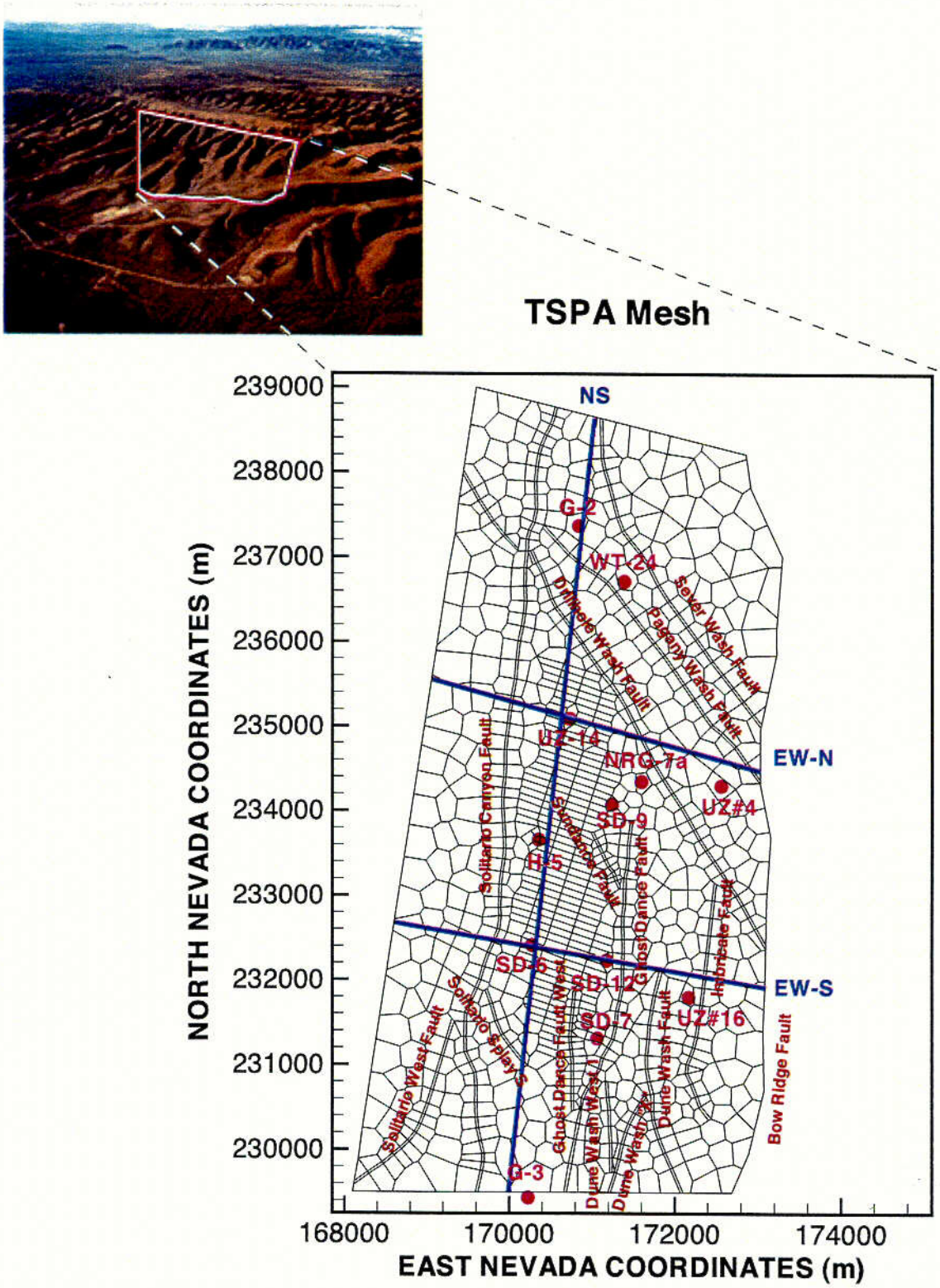

Figure 3.7-3. Plan View of the 3-D UZ TSPA Model Grid, Showing the Model Domain at Yucca Mountain, Faults Incorporated and Borehole Locations (Adapted from CRWMS M&O, 2000, U0000, Figure VI-1)

C59

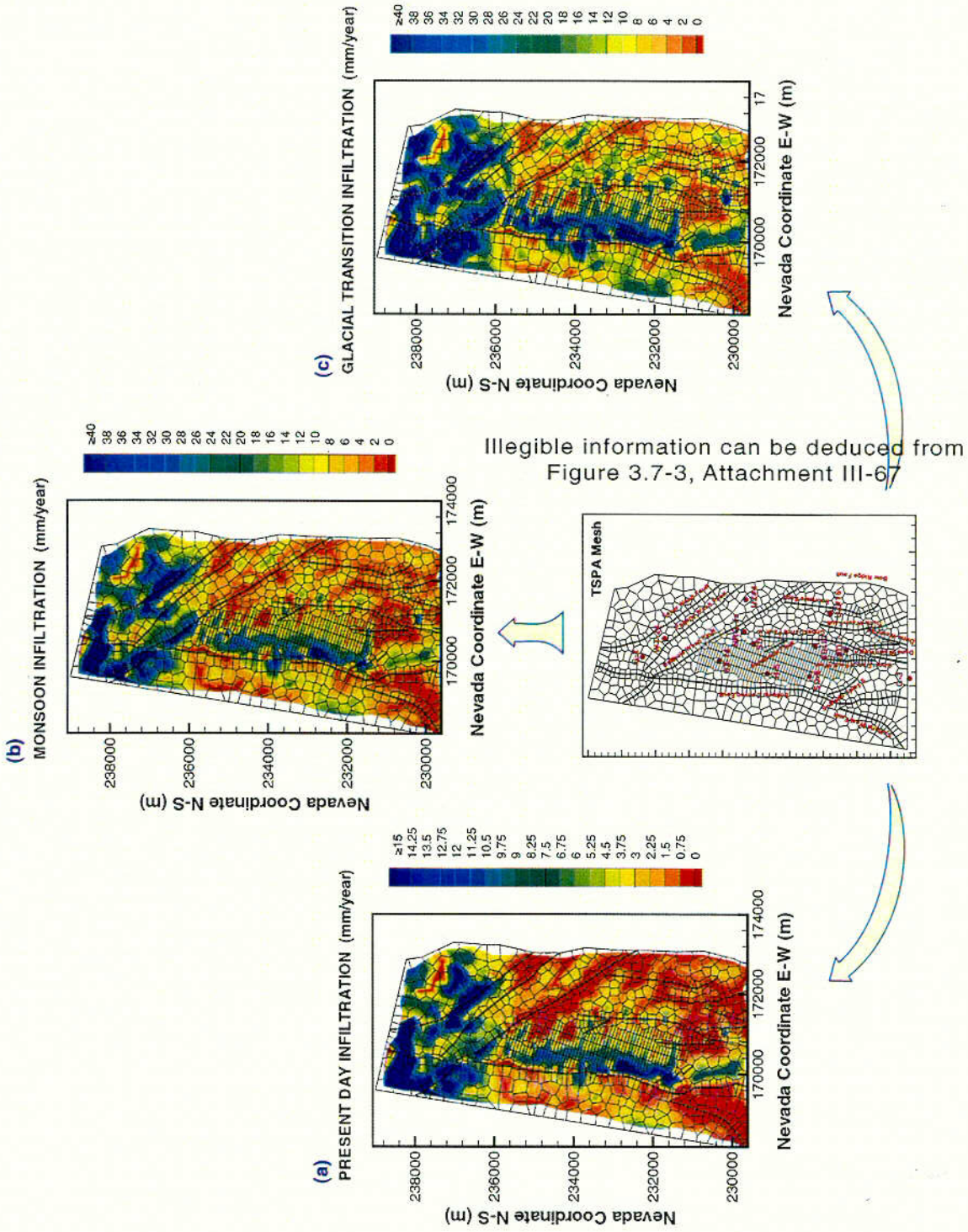

Figure 3.7-4. Three Base-Case Maps of Mean Surface Infiltration over the Flow Model Domain for (a) Present-Day Climate, (b) Monsoon Climate, (c) Glacial-Transition Climate (Adapted from CRWMS M&O, 2000, U0050, Figures 6-3, 6-4 and 6-5)

c60

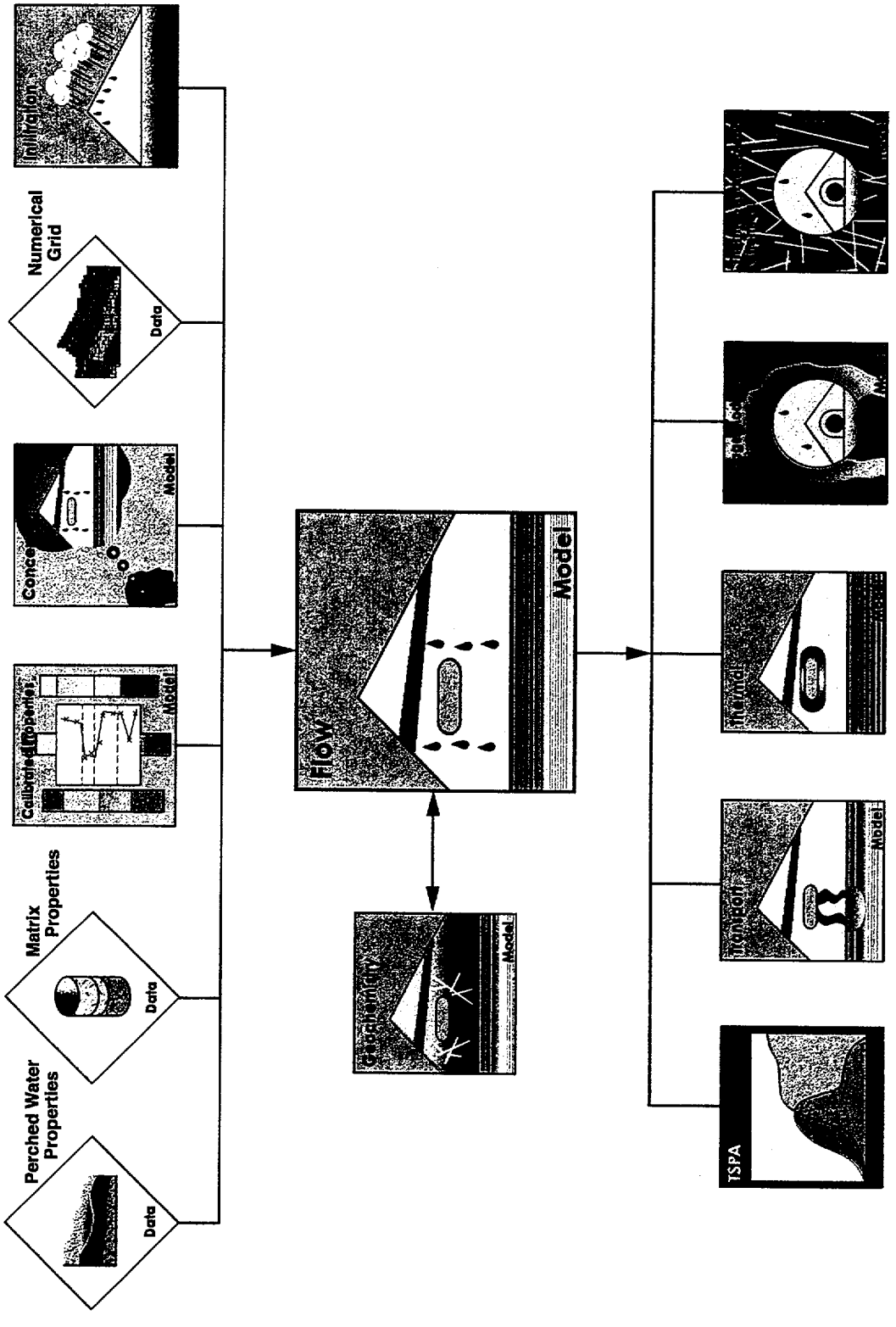

Figure 3.7-5. Schematic of the Major Input Data to, and Output Models from, the UZ Flow Model

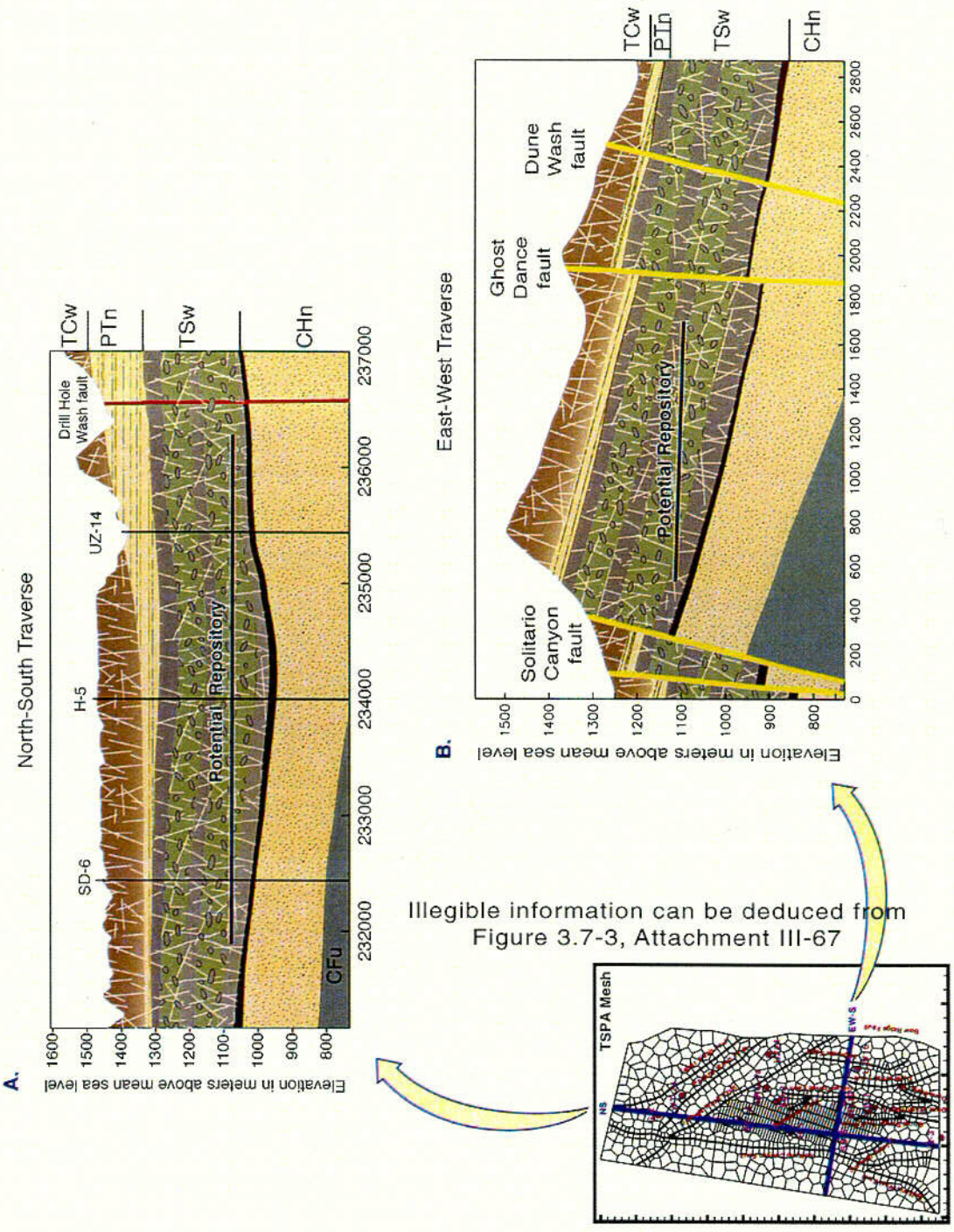

Figure 3.7-6. Geological Profiles in Cross Sections Crossing the Model Domain, (a) North-South Transect at Yucca Mountain, Showing Thickness of the Hydrogeologic Units (b) East-West Transect at Yucca Mountain, Showing Incorporated Faults and Displacements as well as Hydrogeologic Units.

C61

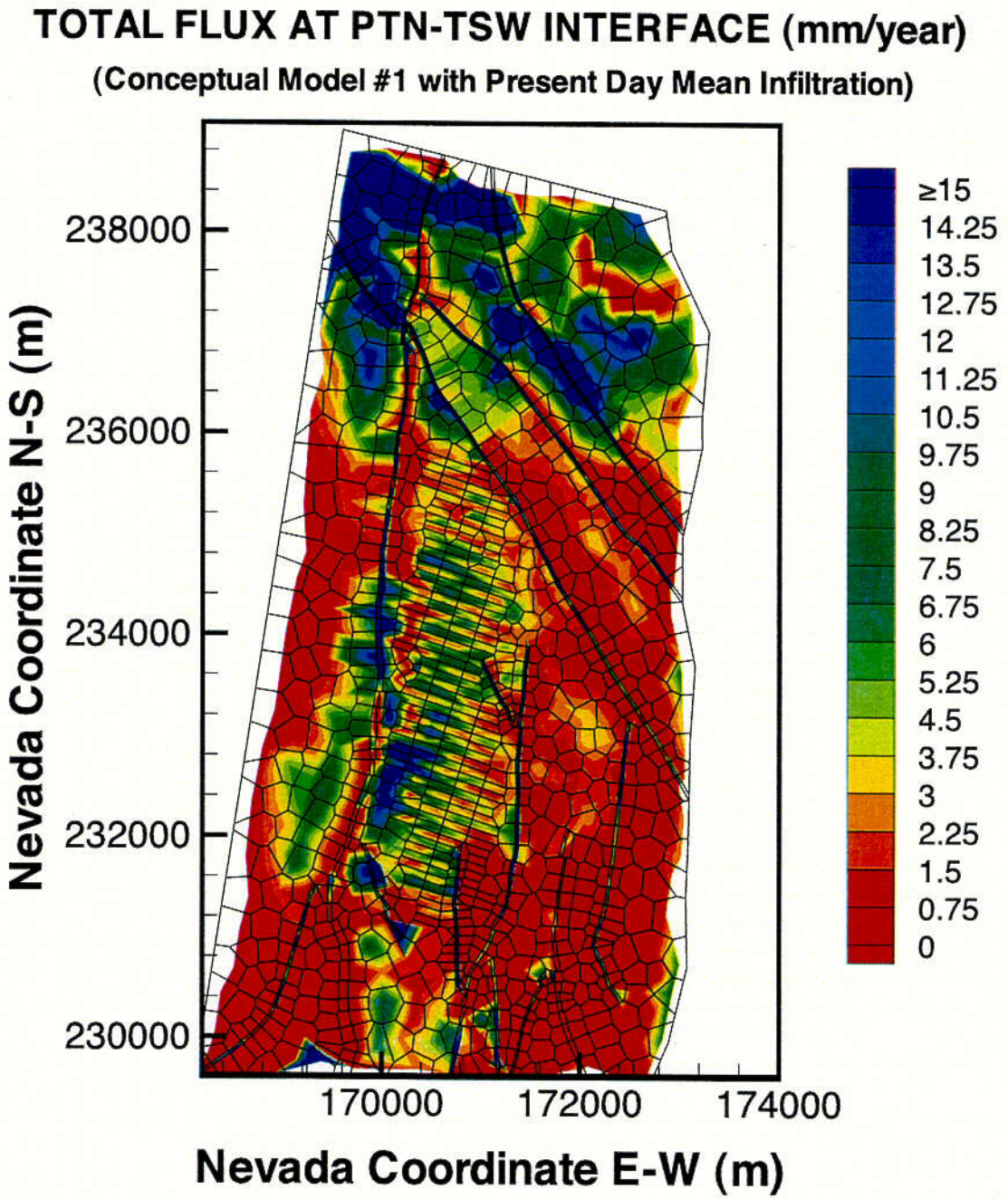

Figure 3.7-7. Simulated Vertical Percolation Fluxes at the PTn-TSw Interface with the Present-Day, Mean Infiltration Map (Data from CRWMS M&O, 2000, U0050, Section 6.6.3)

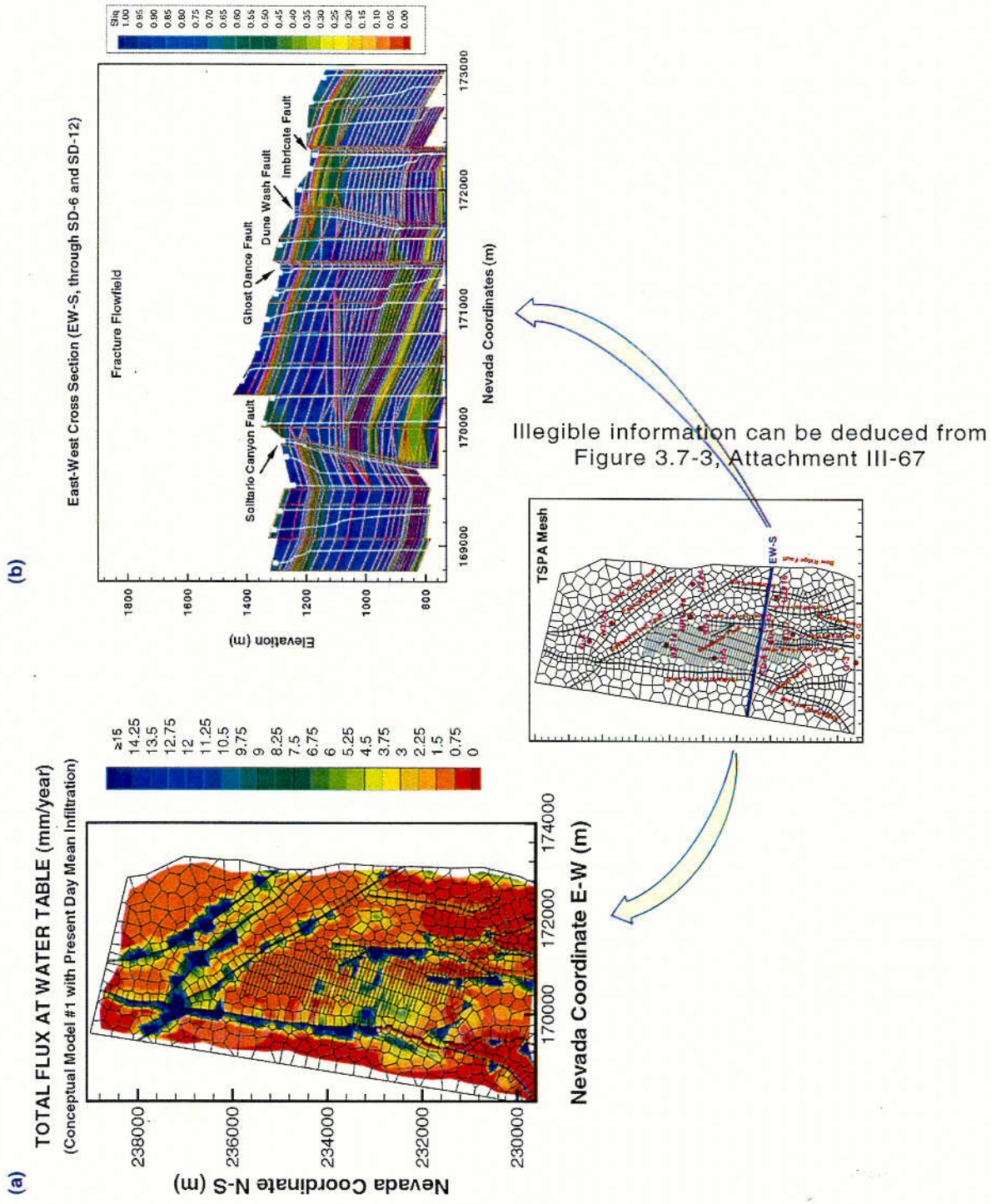

Figure 3.7-8. Effects of Faults on UZ Flow for the Present-Day, Mean Infiltration Rate; (a) Simulated Vertical Percolation Fluxes at the Water Table, (b) Simulated Groundwater Flow paths along the West-East Cross Section within Fracture-Fracture Flow Fields (Data from CRWMS M&O, 2000, U0050, Section 6.6.3)

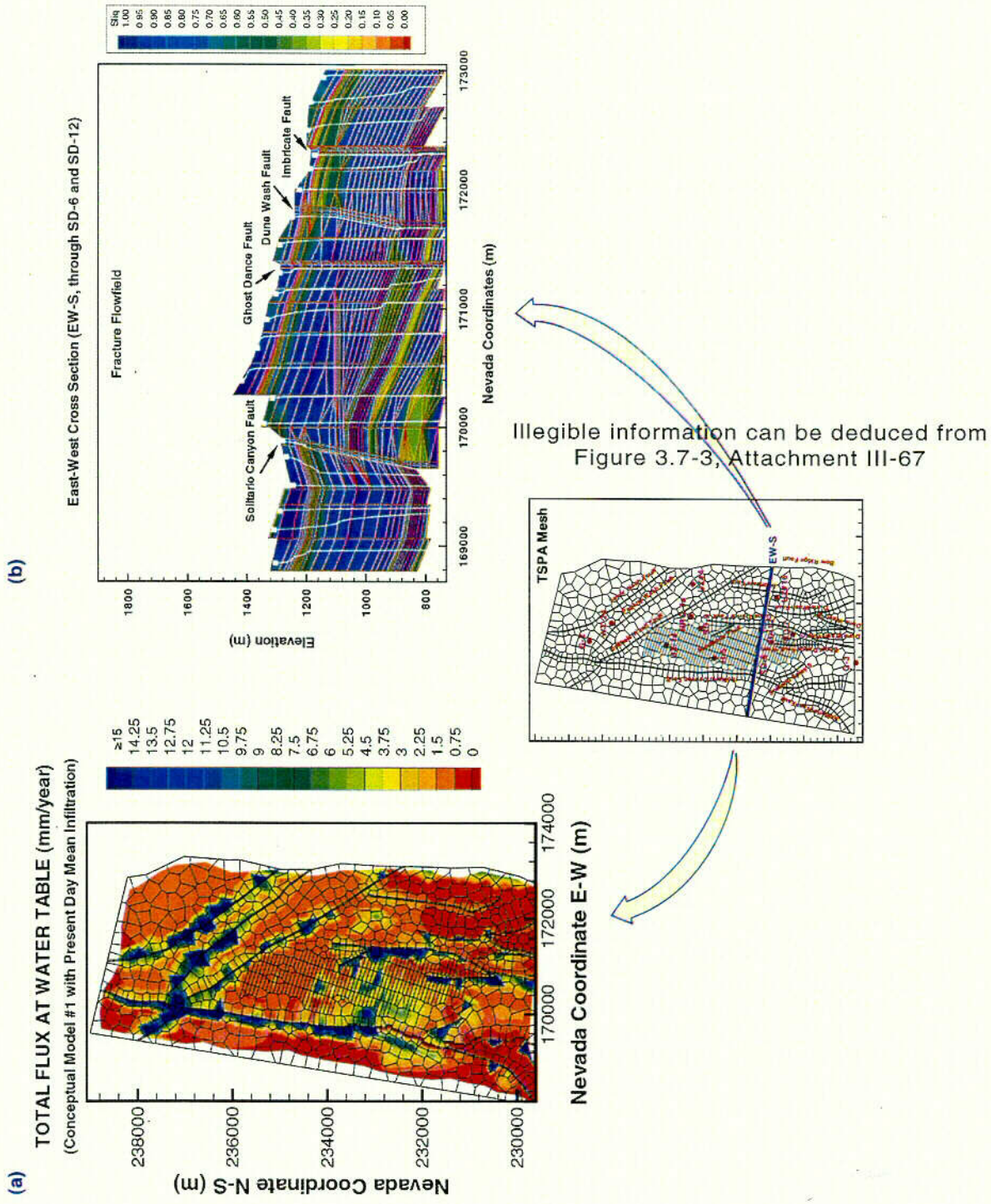

Figure 3.7-8. Effects of Faults on UZ Flow for the Present-Day, Mean Infiltration Rate; (a) Simulated Vertical Percolation Fluxes at the Water Table, (b) Simulated Groundwater Flow paths along the West-East Cross Section within Fracture-Fracture Flow Fields (Data from CRWMS M&O, 2000, U0050, Section 6.6.3)

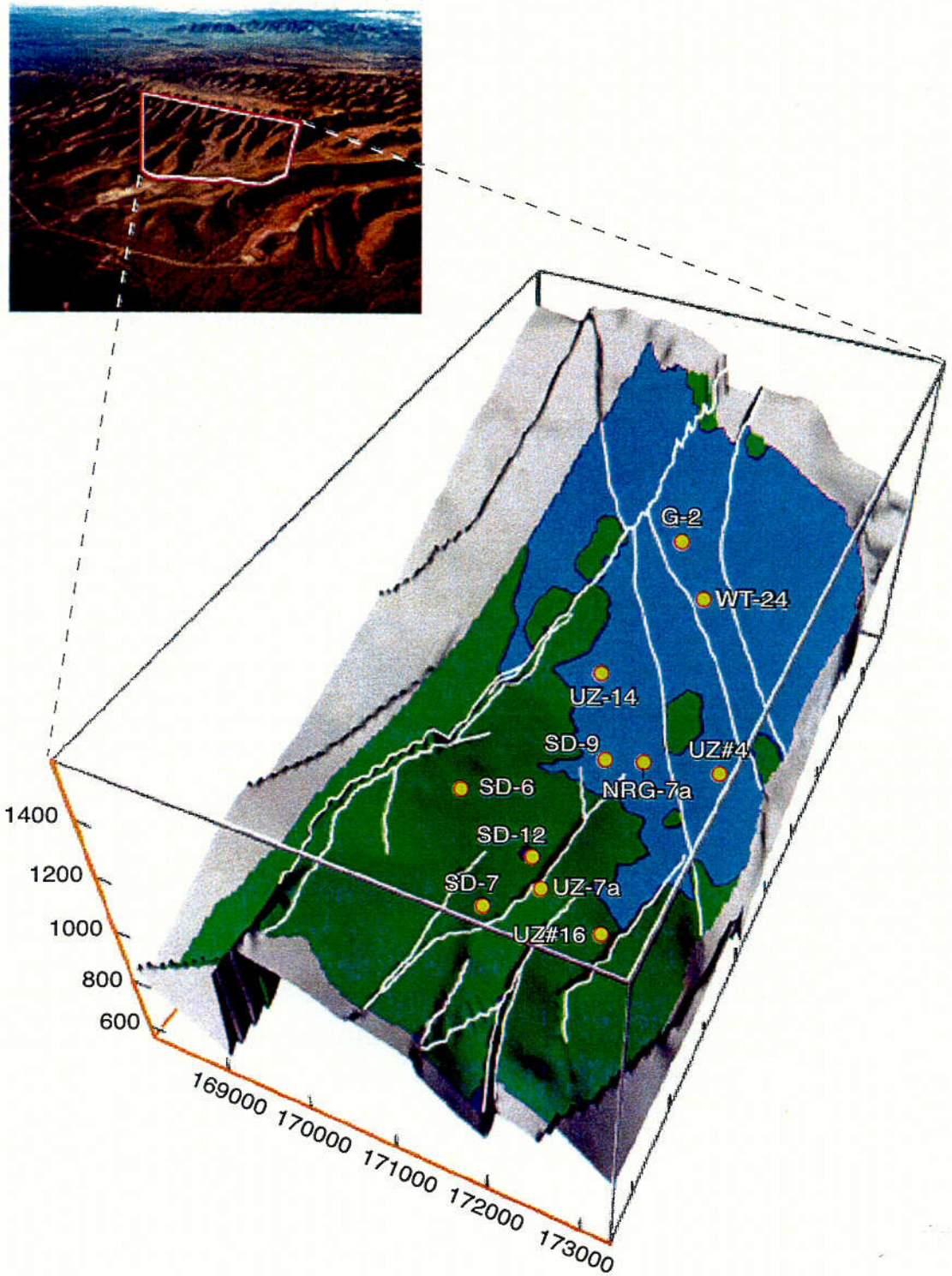

Figure 3.7-9. Simulated 3-D View of Perched Water Bodies along the Base of the TSw, Using the Simulation Results of Conceptual Model #1 with Present-Day, Mean Infiltration Rate (the blue contours denote the domain with 100% water saturation and the green for the areas with less than 100% water saturation) (CRWMS M&O, 2000, U0050, Figure 6.9)

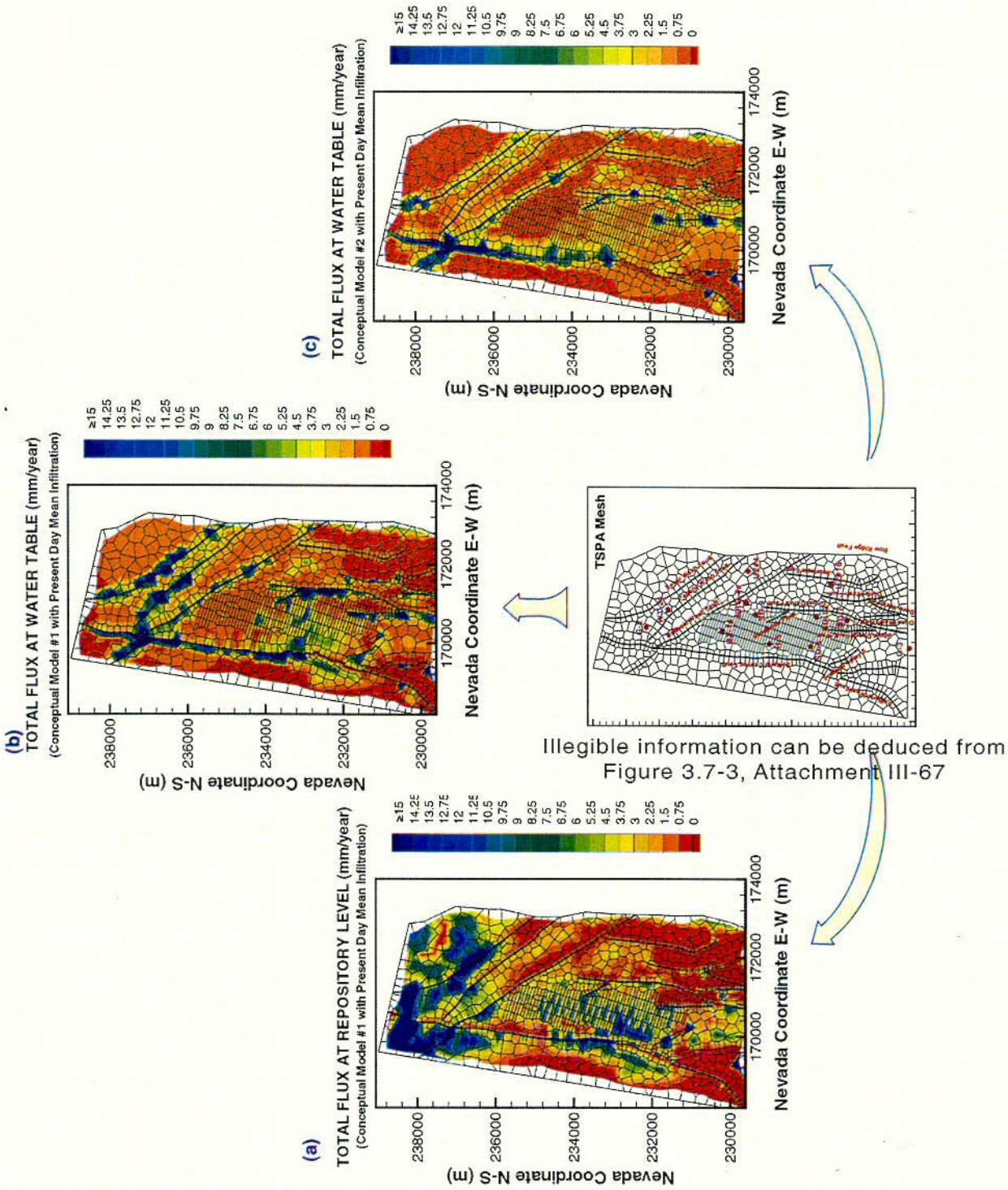

Figure 3.7-10. Comparison between Percolation Flux (mm/yr) Contours Simulated: (a) at the Potential Repository Horizon; (b) at the Water Table with Conceptual Model #1; and (c) at the Water Table with Conceptual Model #2, under the Present-Day, Mean Infiltration Rate (Data from CRWMS M&O, 2000, U0050, Section 6.6.3)

C65

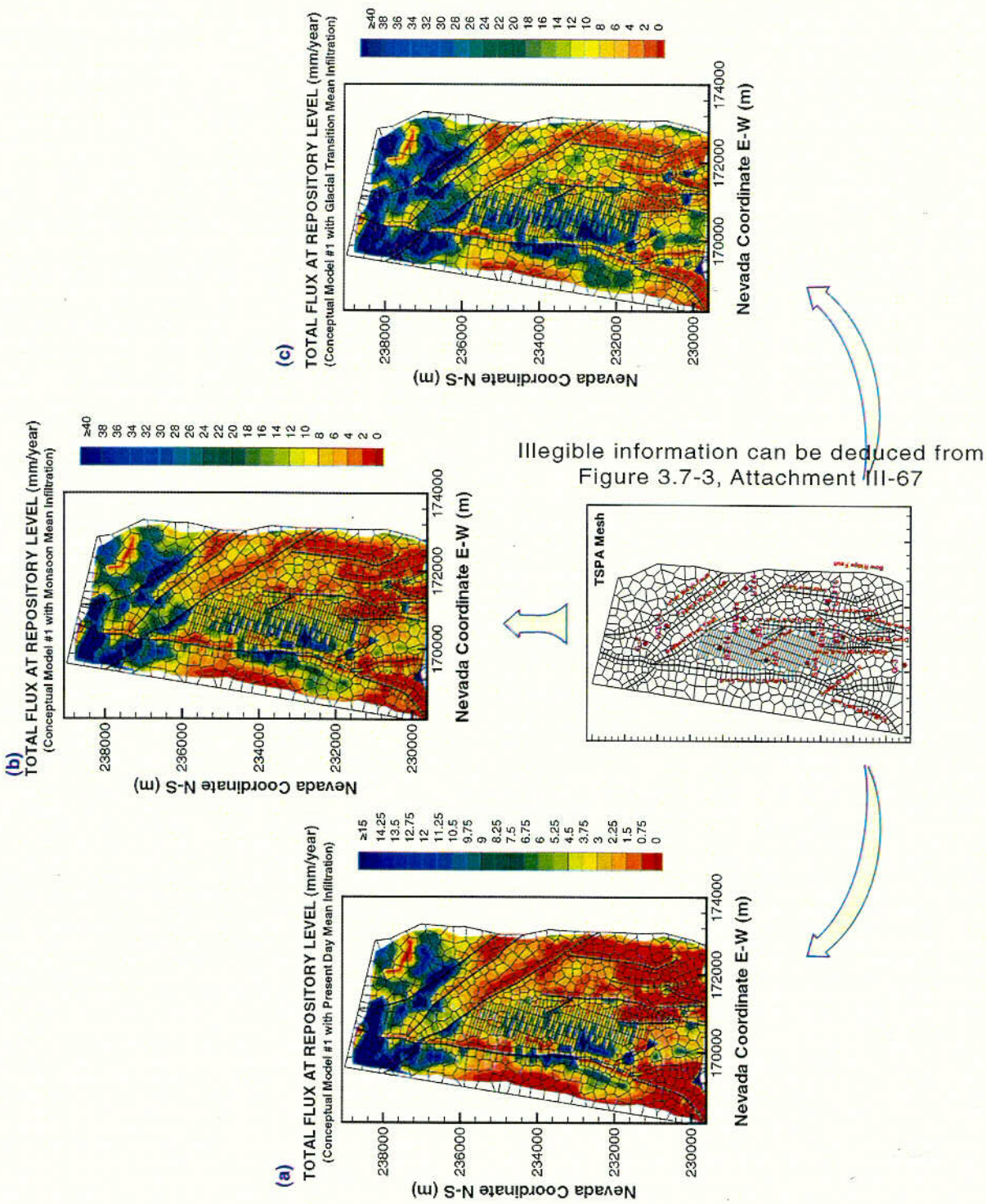

Figure 3.7-11. Simulated Percolation Fluxes at the Potential repository Under Three Mean Infiltration Rates: (a) Present-Day; (b) Monsoon; and (c) Glacial-Transition (Data from CRWMS M&O, 2000, U0050, Section 6.6.3)

C66

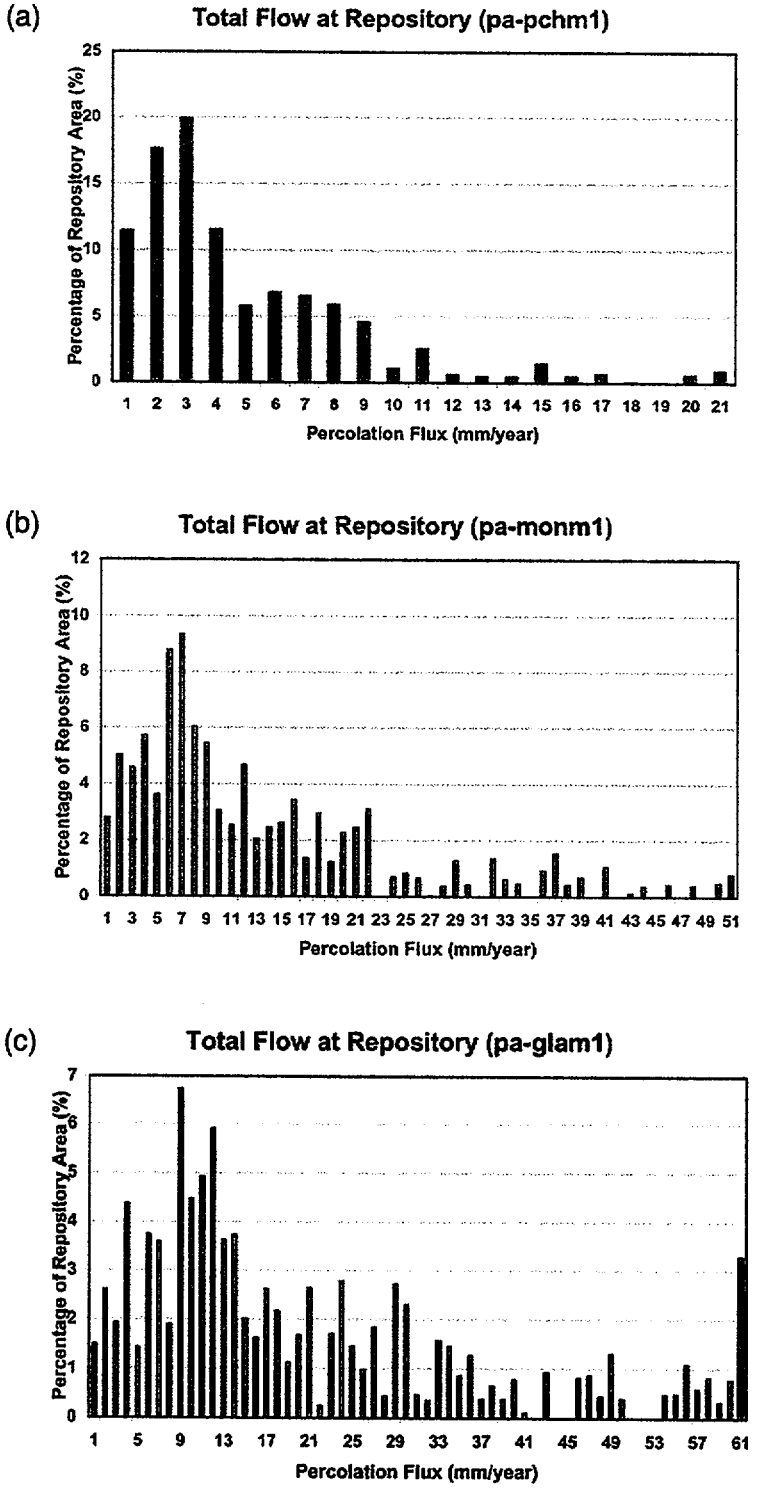

Figure 3.7-12. Areal Frequency and Distribution of Simulated Percolation Fluxes within the Potential Repository Horizon Under Three Mean Infiltration Rates: (a) Present Day; (b) Monsoon; and (c) Glacial Transition (Data from CRWMS M&O, 2000, U0050, Section 6.6.3)

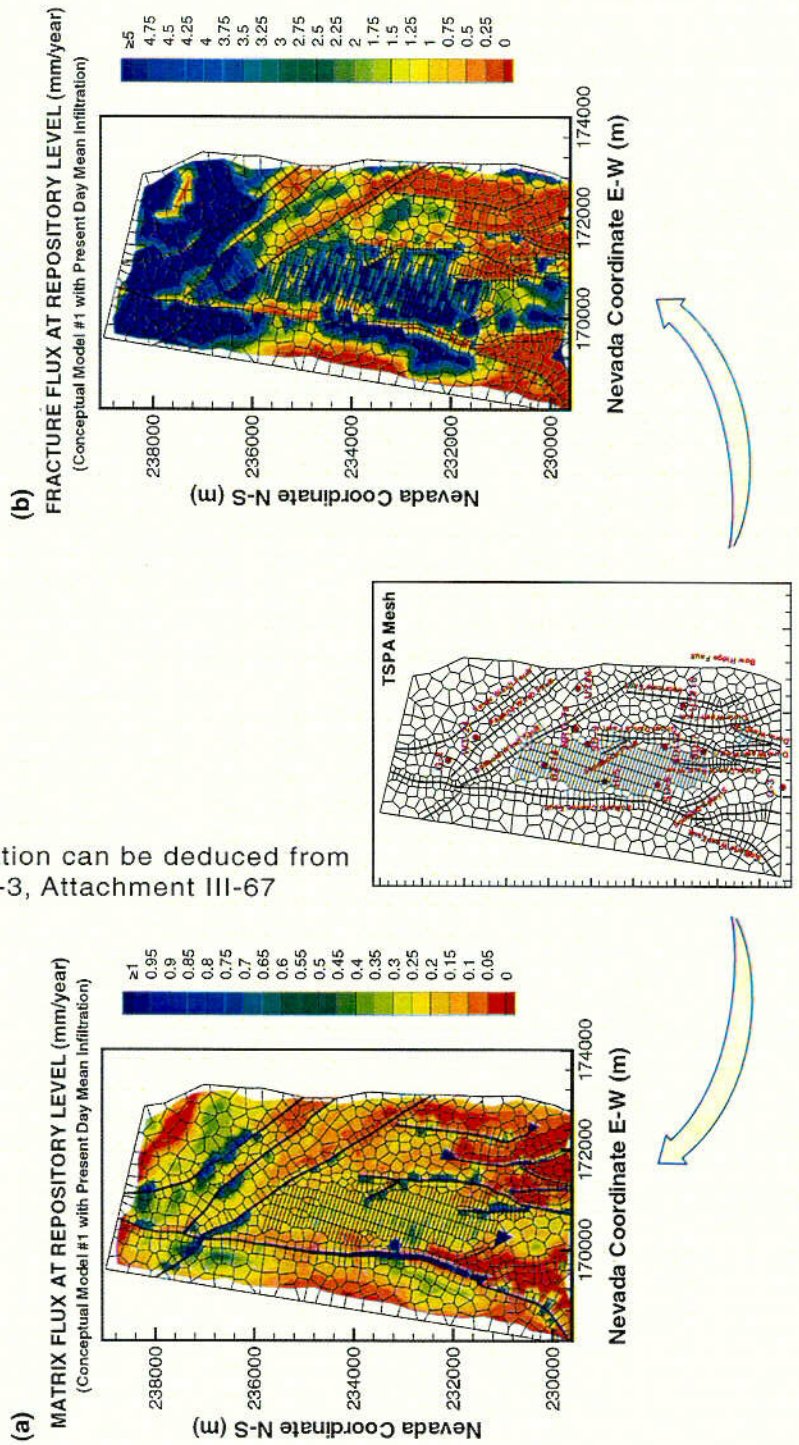

Illegible information can be deduced from Figure 3.7-3, Attachment III-67

Figure 3.7-13. (a) Matrix Flow (mm/yr) and (b) Fracture Flow at Potential Repository Horizon, Simulated Using the Present-Day, Mean Infiltration Rate. Data from CRWMS M&O, 2000, U0050, Section 6.6.3.

C67

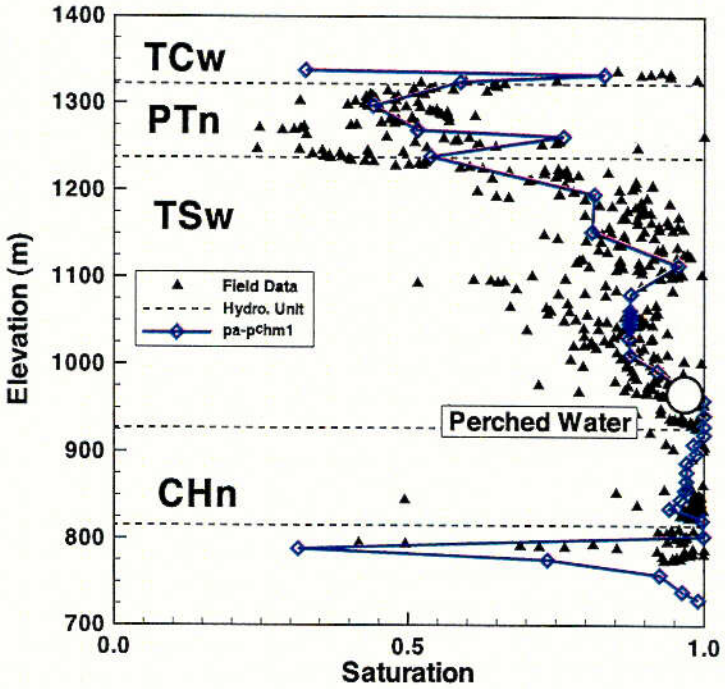

Figure 3.7-14. Comparison to the Simulated and Observed Matrix Liquid Saturations and Perched Water Elevations for Borehole UZ-14, Using the Simulation Results for the Mean Infiltration Rates of the Three Climates Scenarios (Data from CRWMS M&O, 2000, U0050, Section 6.6.3, Figure 6-41)

C68

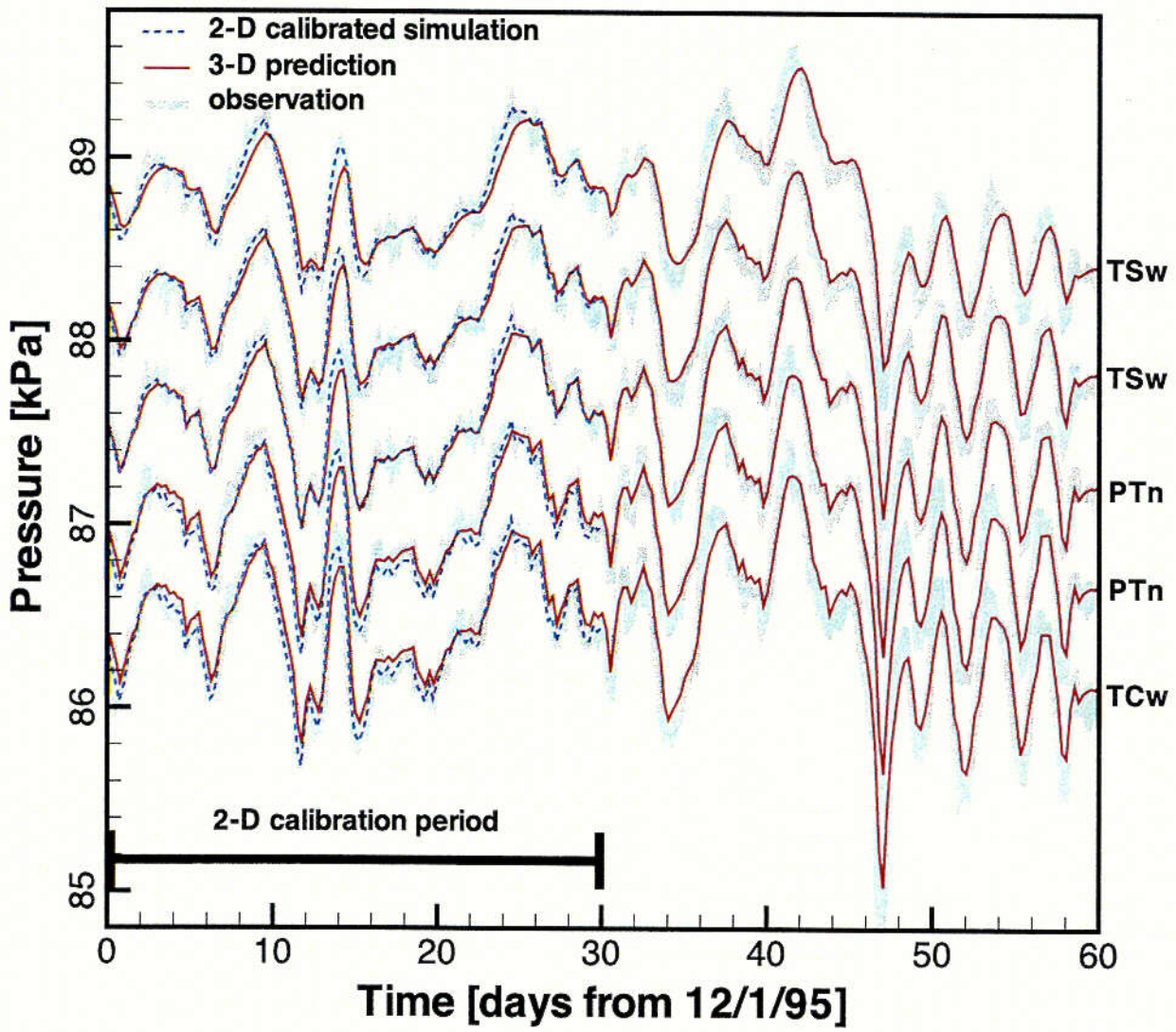

Figure 3.7-15. Comparison of 3-D Pneumatic Prediction to Data from Borehole UZ-7a (CRWMS M&O 2000, U0050, Figure 6-70)

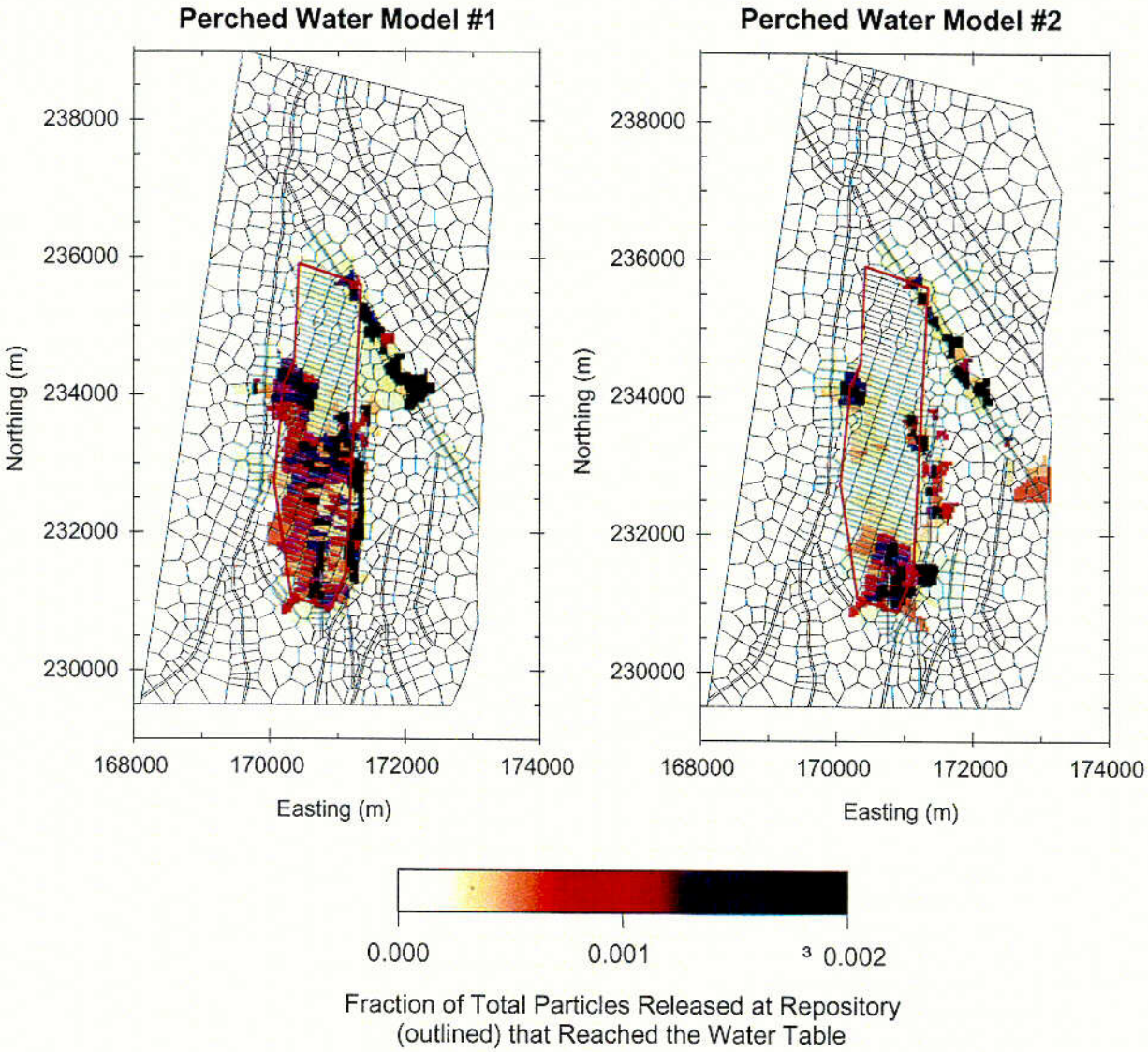

Figure 3.7-16. Locations of Particle Breakthrough at the Water Table for the Mean Infiltration, Glacial-Transition Climate Using Two Perched Water Models (CRWMS M&O 2000, U0160, Figure 3)

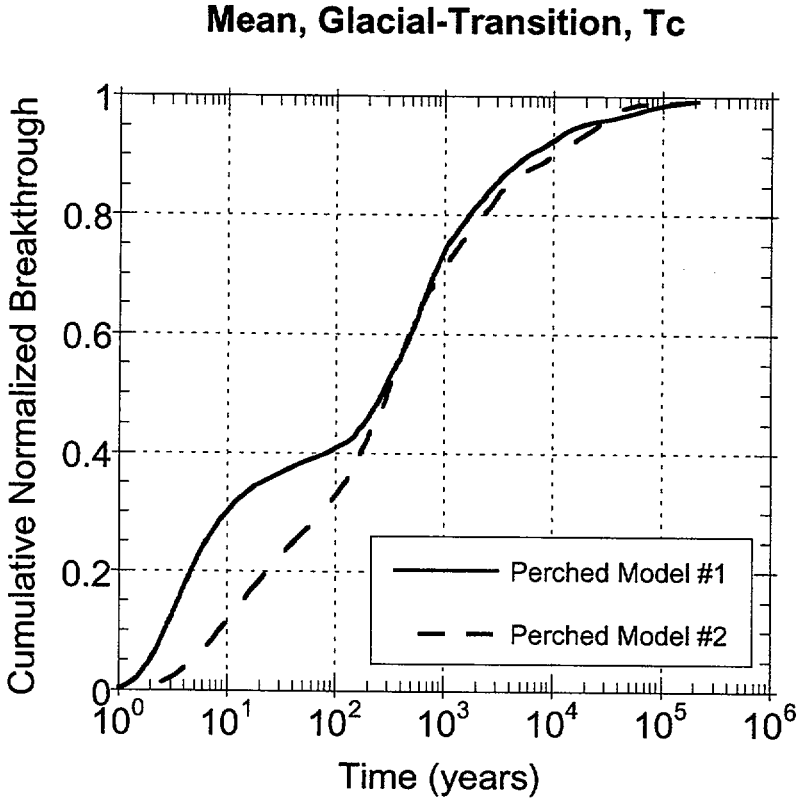

Figure 3.7-17. Comparison of Cumulative Normalized Breakthrough Curves at the Water Table Using Perched Water Model #1 and #2 with a Non-Sorbing Tracer (Tc) for Mean-Infiltration, Glacial-Transition Climate (CRWMS M&O 2000, U0160, Figure 8. The data shown in this figure are based on a model that is appropriately conservative for TSPA analysis and consequently should not be used to evaluate expected breakthrough curves of radionuclides at the water table.)

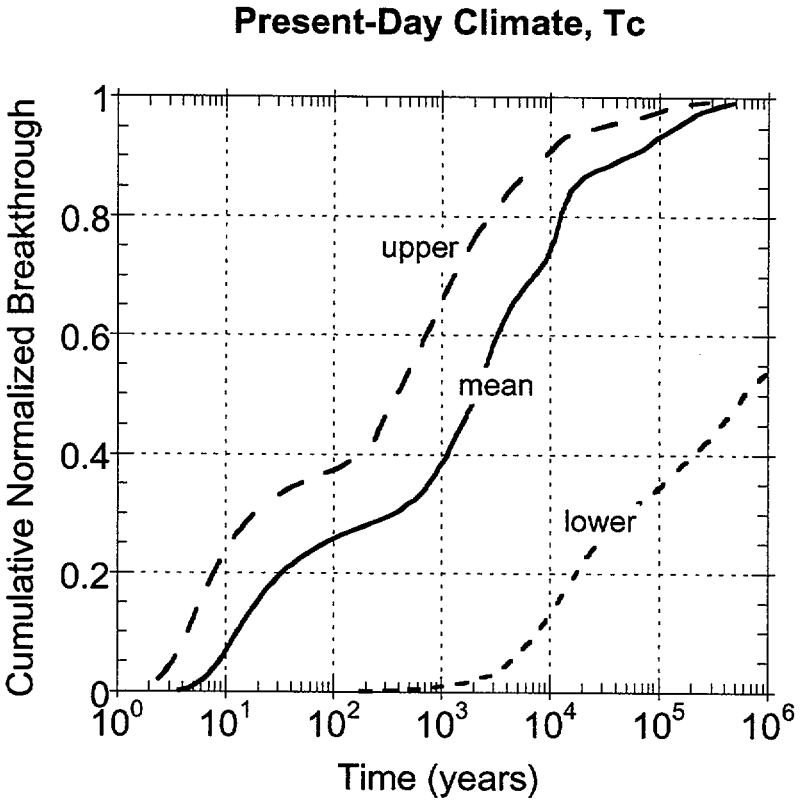

Figure 3.7-18. Effect of Infiltration (lower, mean, and upper) on Cumulative Normalized Breakthrough Curves at the Water Table for a NonSorbing Tracer (Tc) Using FEHM V2.0 (STN: 10031-2.00-00) with Present-Day Climate (CRWMS M&O 2000, U0160, Figure 12. The data shown in this figure are based on a model that is appropriately conservative for TSPA analysis and consequently should not be used to evaluate expected breakthrough curves of radionuclides at the water table.)

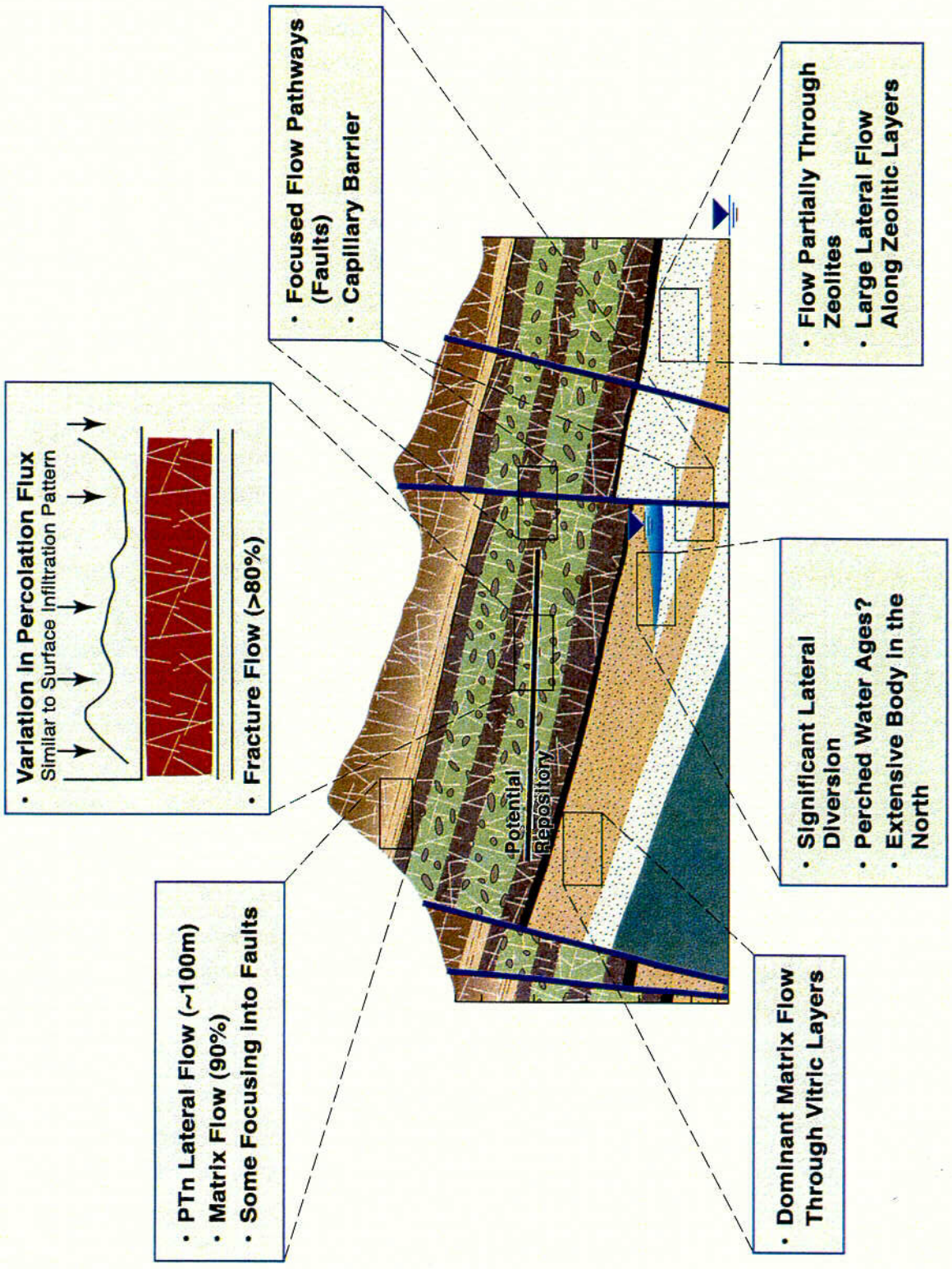

Figure 3.7-19. Summary of the UZ Flow Model Results and Issues to be Resolved

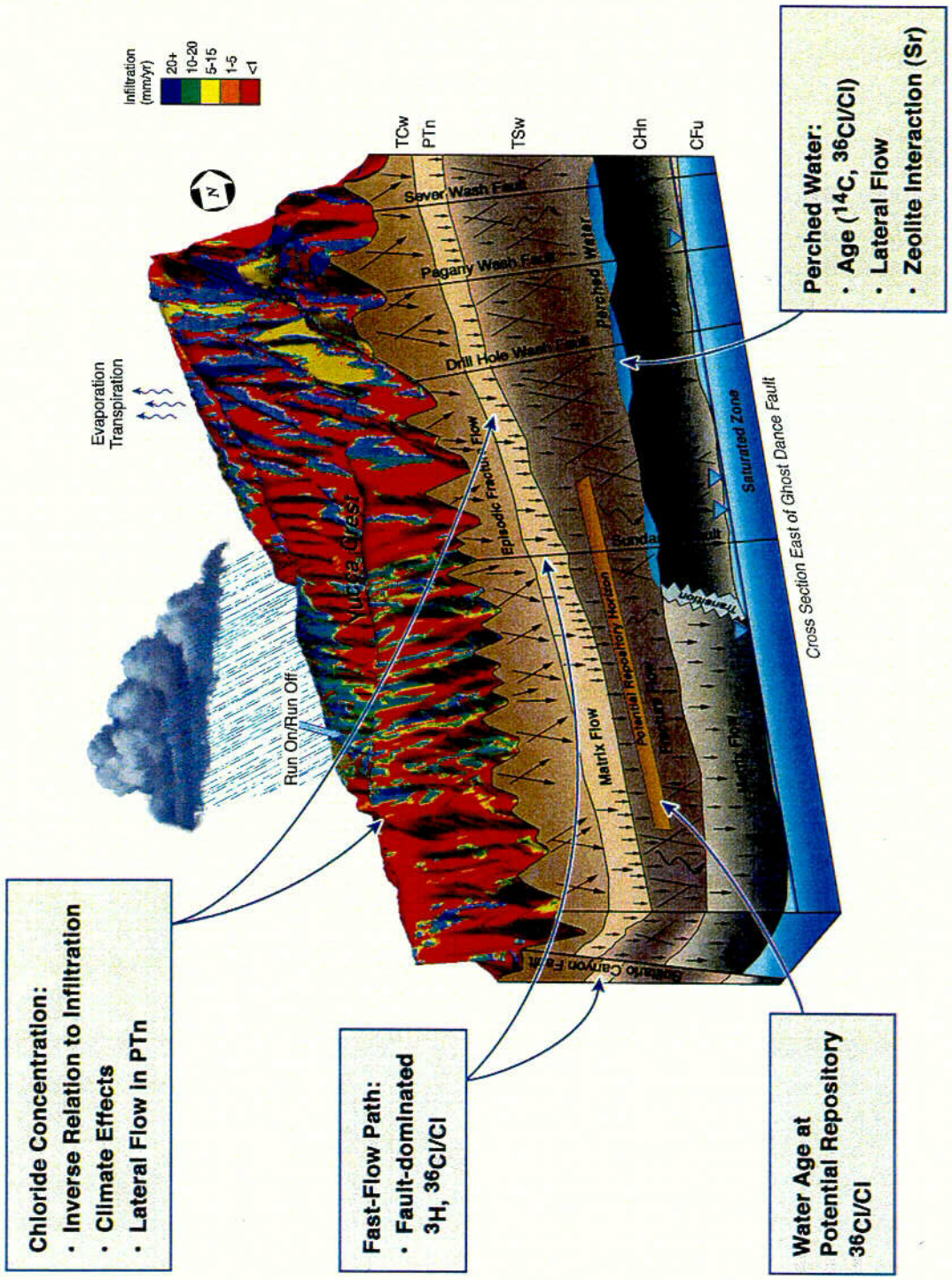

Figure 3.8-1. Conceptual Model of Yucca Mountain Showing Major Processes Affecting Cl and $^{36}Cl/Cl$ Distributions and Important Issues for Performance

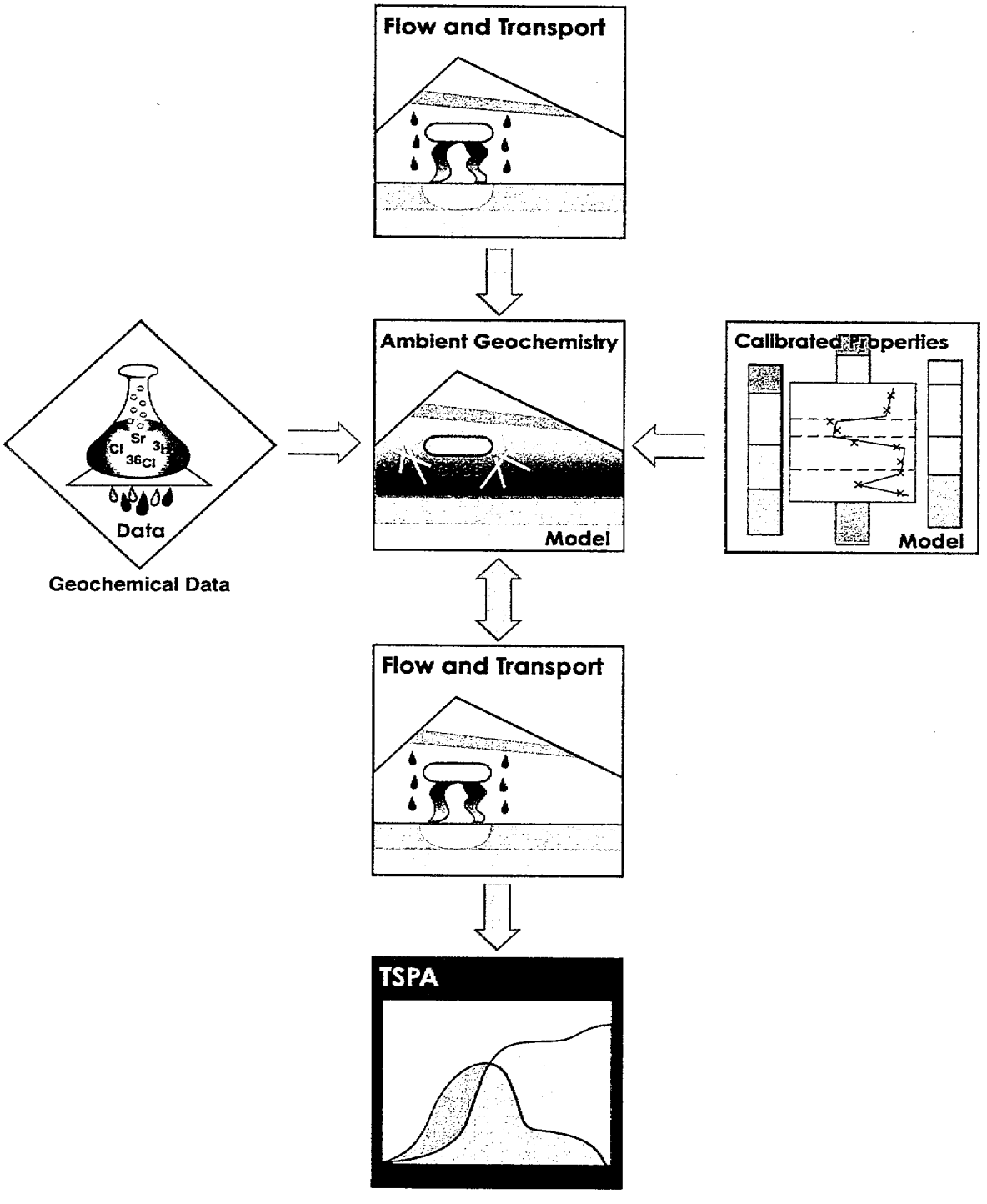

Figure 3.8-2. Model Diagram Showing Inputs and Outputs for Ambient Geochemistry Model. Icons are described in the text.

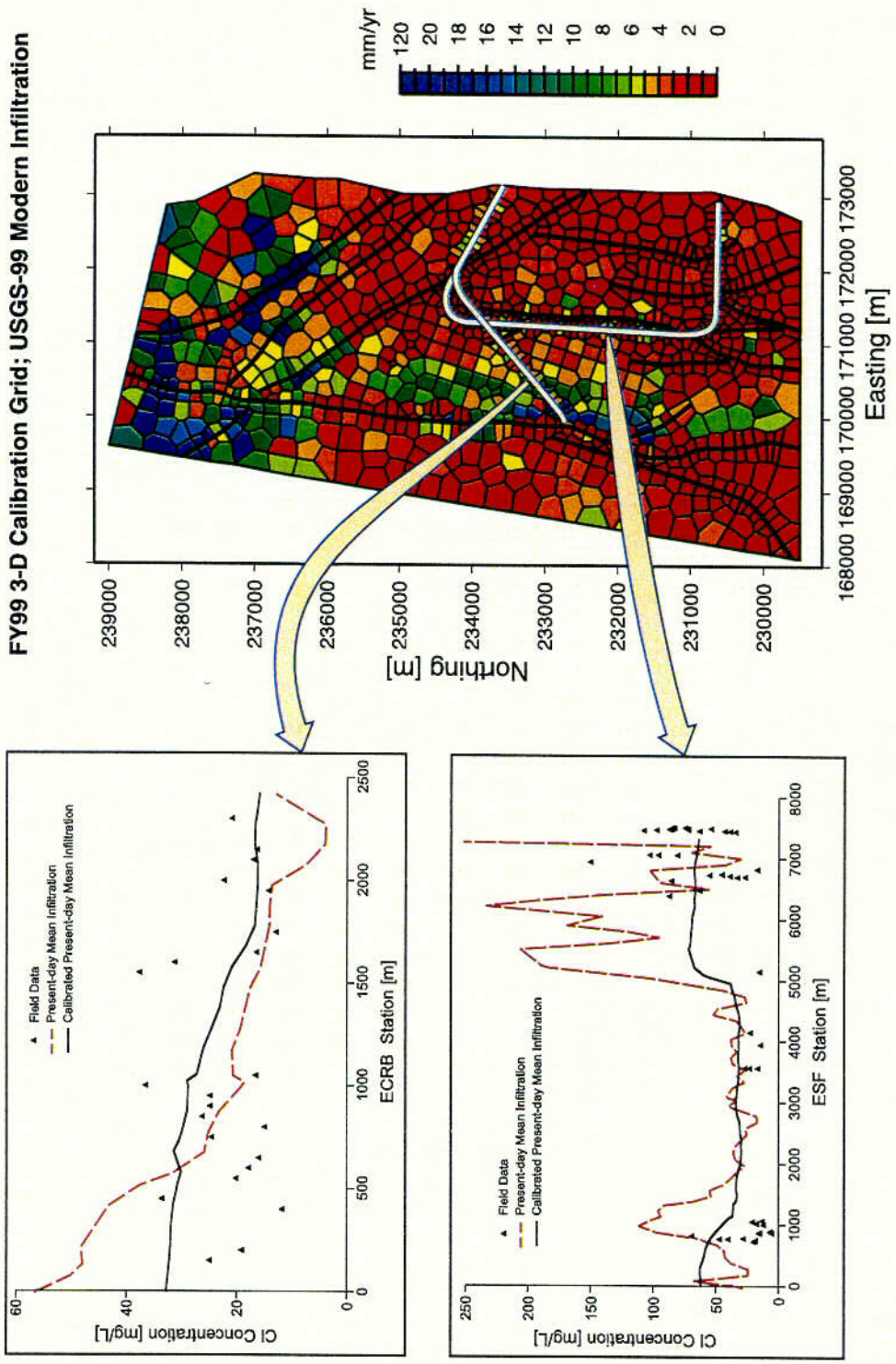

Figure 3.8-3. Infiltration Rates (USGS 2000, U0010) Plotted on UZ 3-D Calibration Grid. Simulated (using base-case infiltration rates), calibrated, and measured Cl concentrations in the ESF and the ECRB (Adapted from CRWMS M&O 2000, U0050, Figure 6-18).

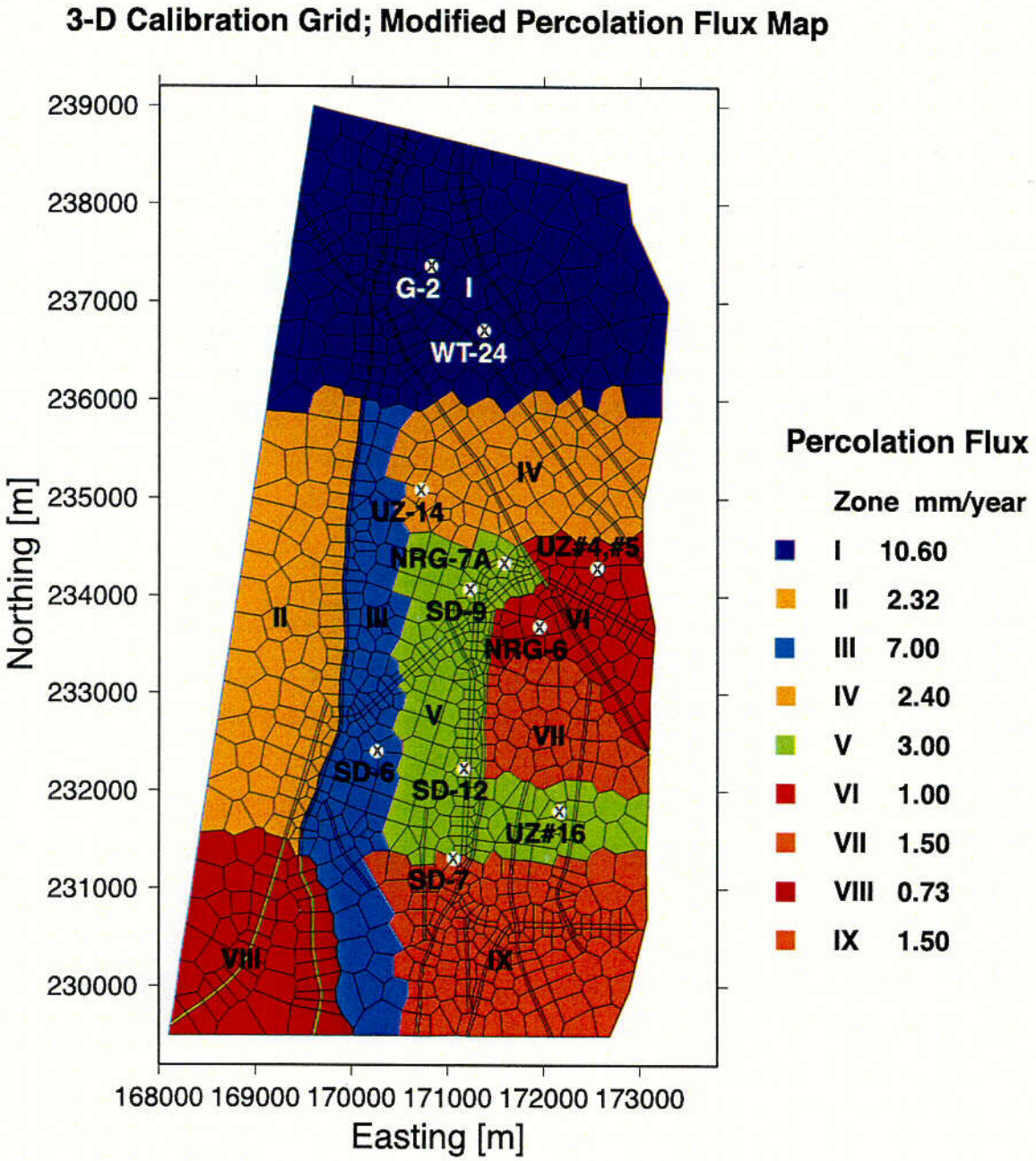

Figure 3.8-4. Percolation Flux Map for 3-D Calibration Grid (Adapted from CRWMS M&O 2000, U0050, Figure 6-24)

C74

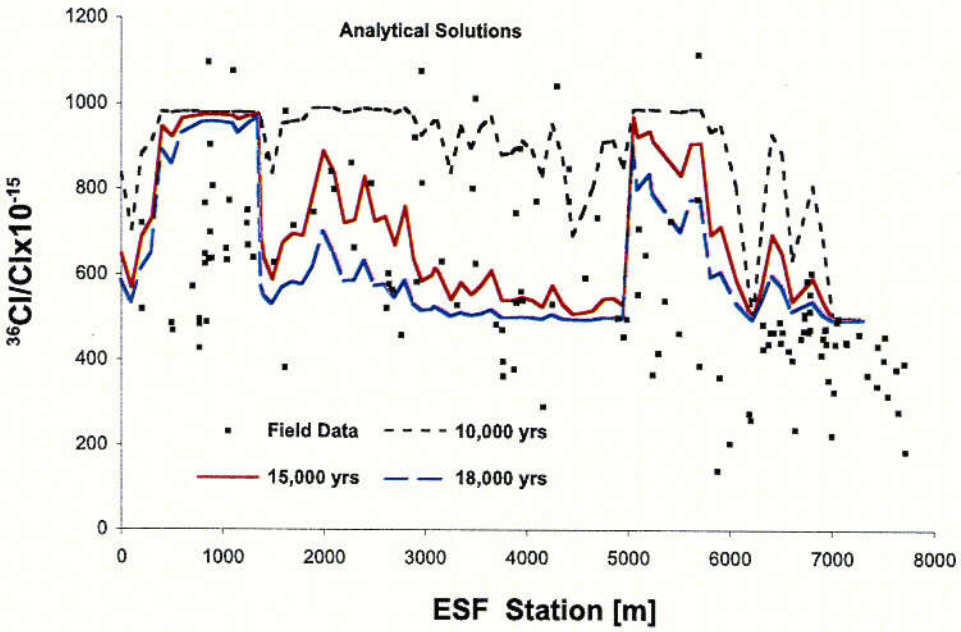

Figure 3.8-5. Analytical Results of $^{36}Cl/Cl$ Along ESF (Using Calibrated Infiltration) for Transient Changes in Initial Ratios, Compared to Measured Ratios (CRWMS M&O 2000, U0050, Figure 6-31)

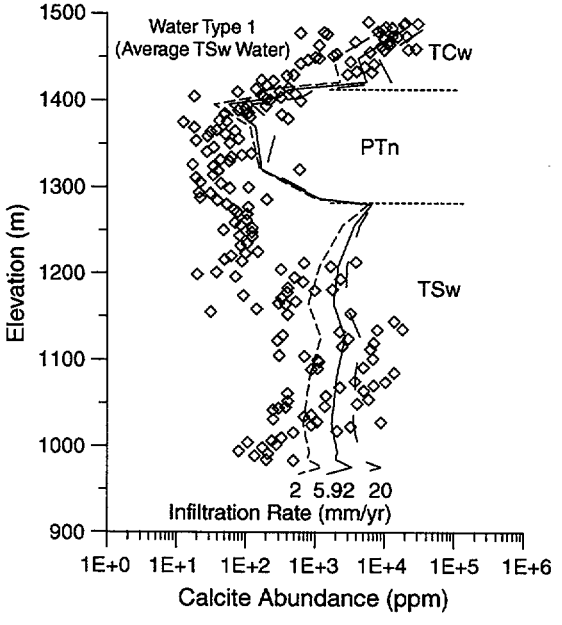

Figure 3.8-6. Simulated Calcite Abundance (Lines) with Infiltration Rate After 10 Million Years in the WT-24 Column Together with Measured Calcite Mass Abundances (Diamond Symbols) (Data from CRWMS M&O 2000, U0085, Section 6.10, Figure 53; CRWMS M&O 2000, U0050, Figure 6-36)

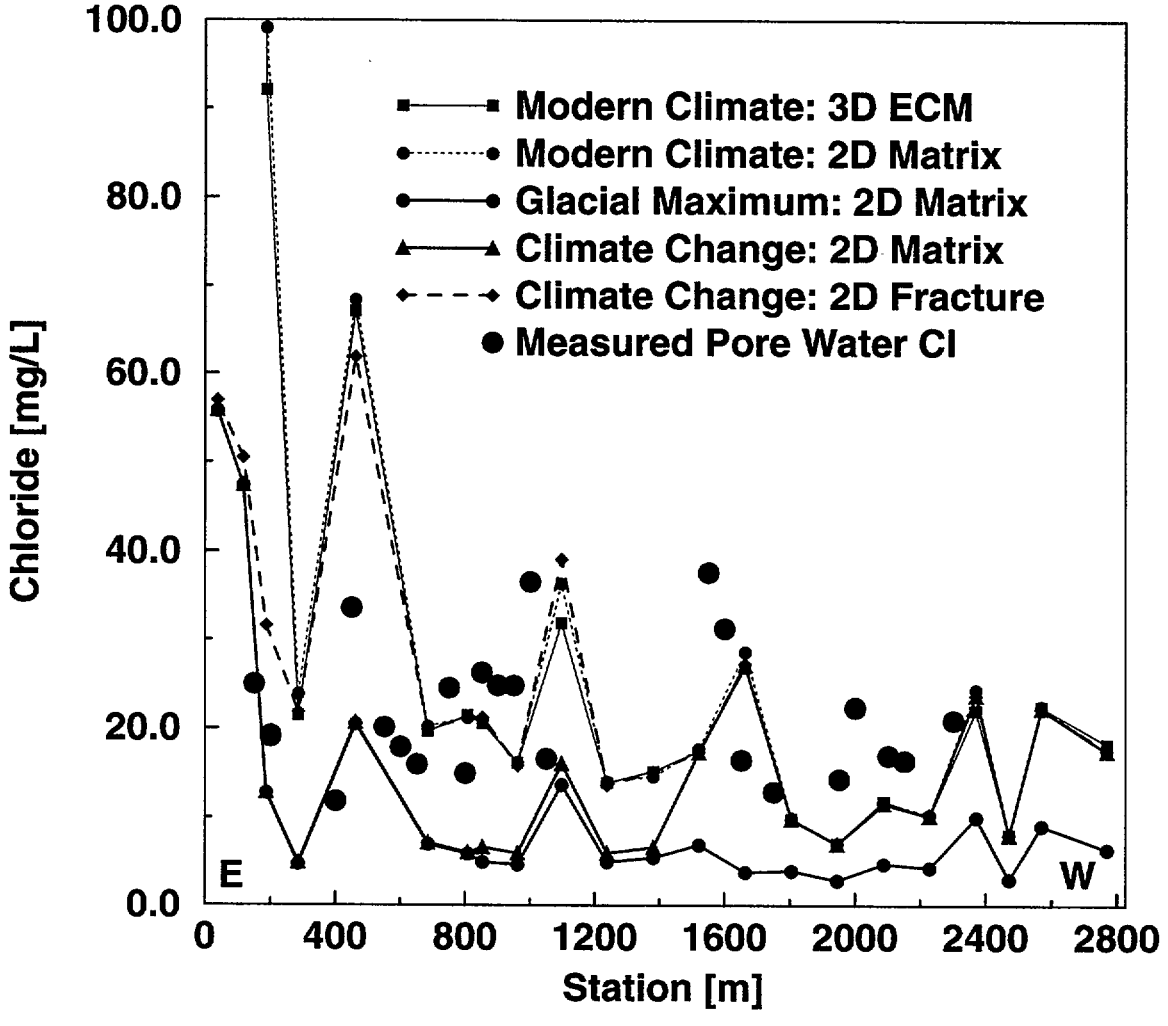

Figure 3.8-7. Prediction of Cl Concentrations in Pore Waters Made Prior to Excavation of the ECRB Compared to Data Collected Subsequently (Adapted from Sonnenthal and Bodvarsson (1999, Figure 14) and CRWMS M&O 2000, U0050, Figure 6-23)

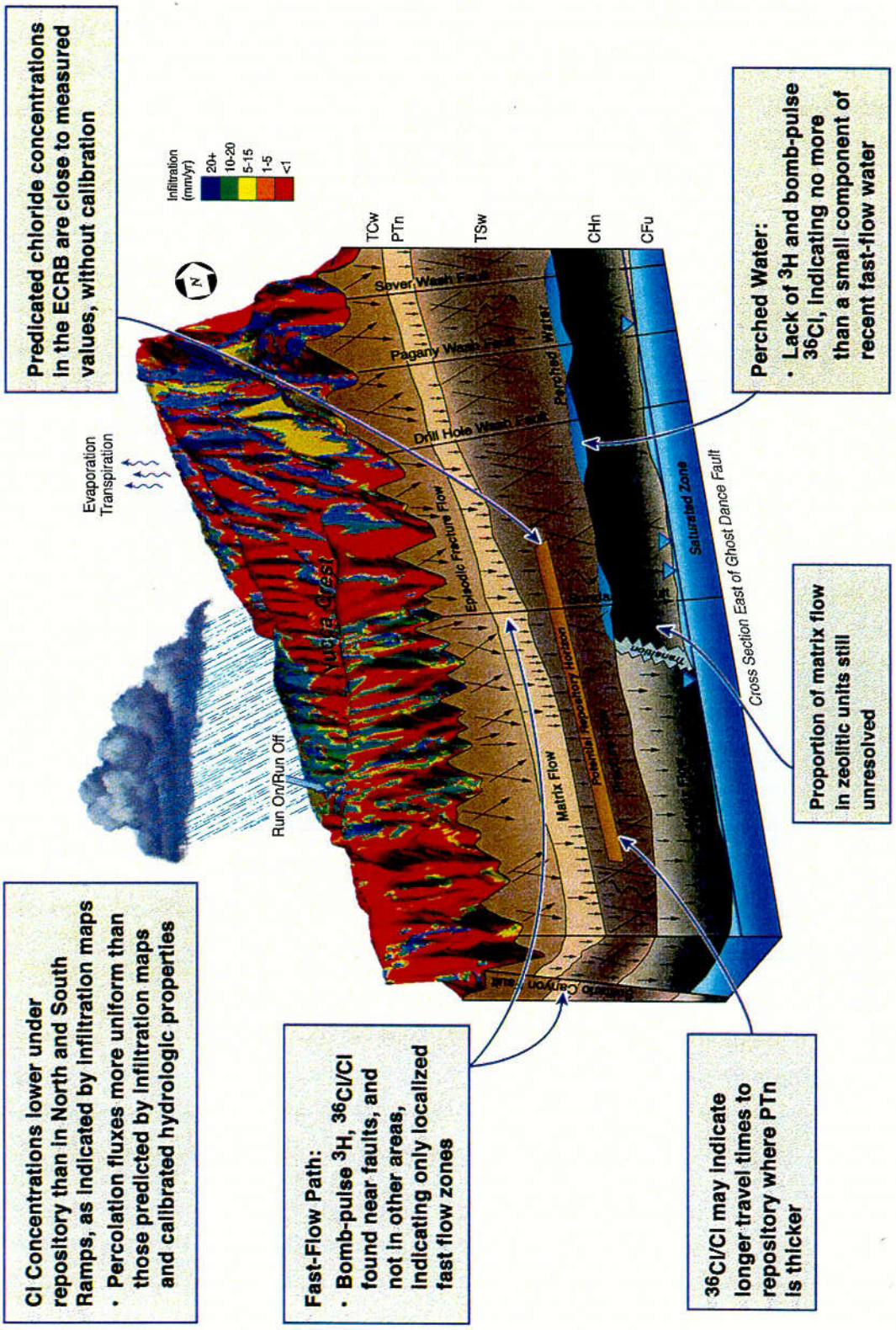

Figure 3.8-8. Conceptual Model of UZ Flow and Transport at Yucca Mountain, Showing Results Gained from Analysis of Geochemical Data and Modeling

C76

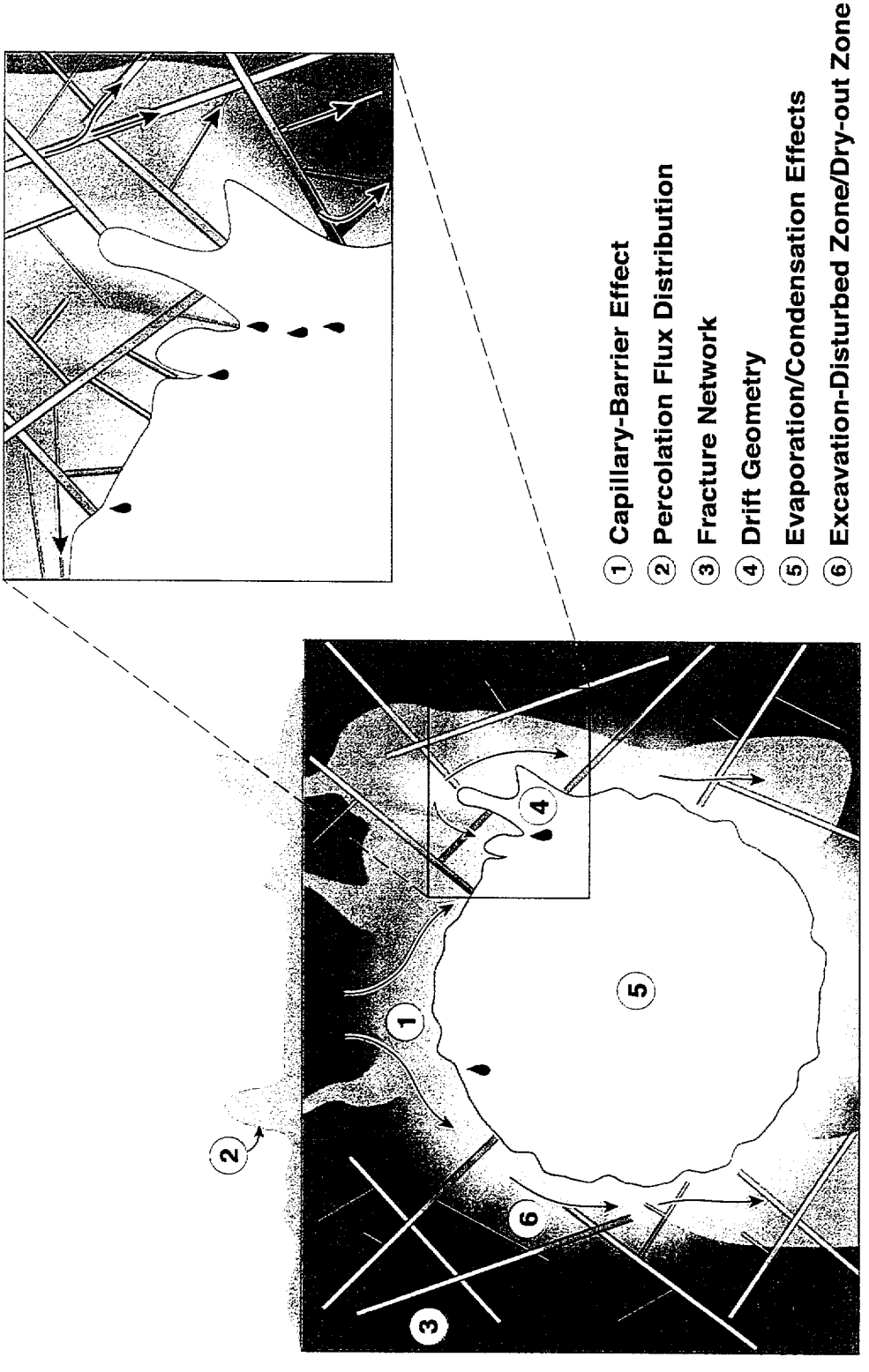

Figure 3.9-1. Schematic of Phenomena and Processes Affecting Drift Seepage. Numerals refer to list items in text.

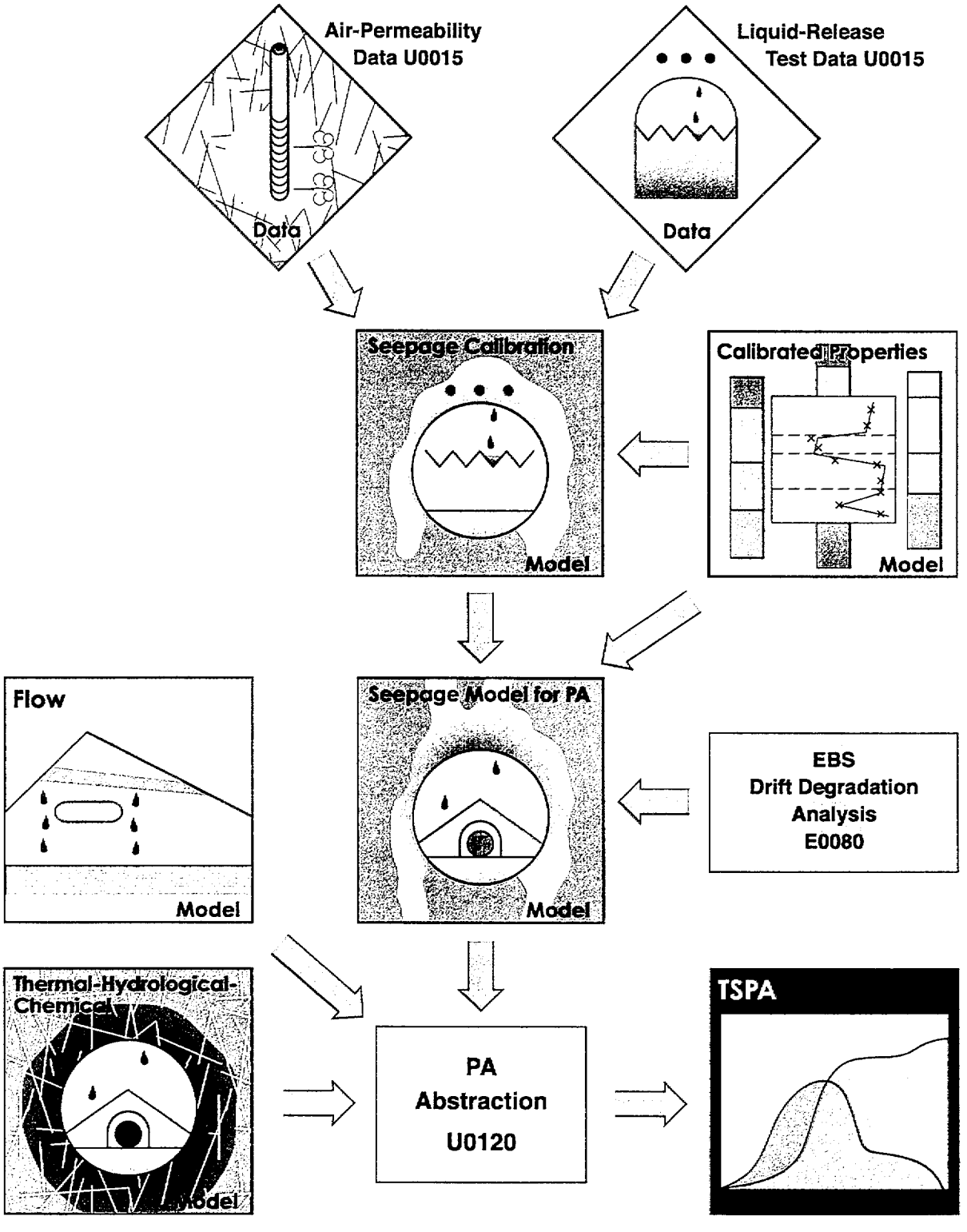

Figure 3.9-2. Schematic Showing Data Flow and Series of Models Supporting Evaluation of Drift Seepage

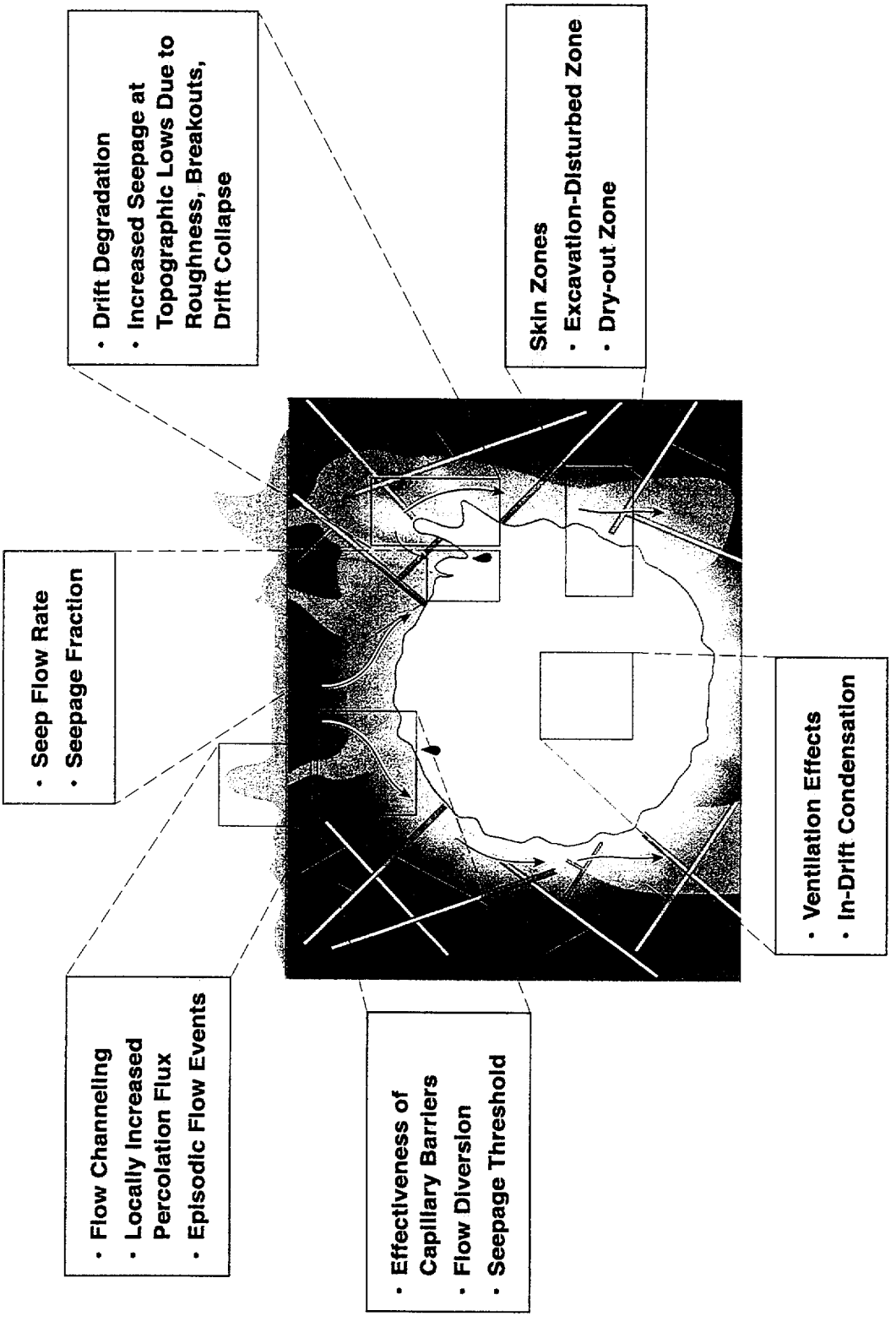

Figure 3.9-3. Seepage Issues

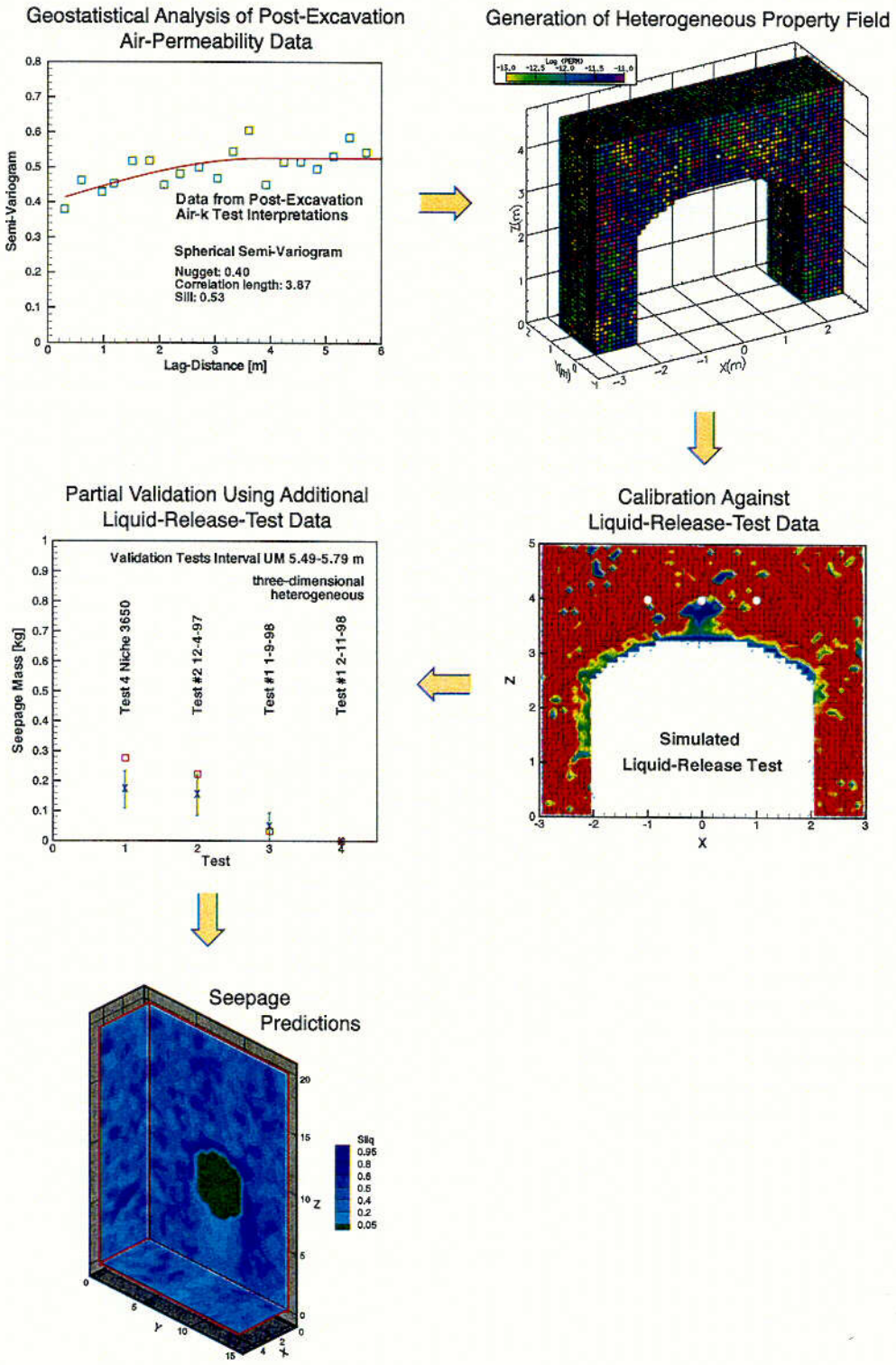

Figure 3.9-4. Schematic Showing General Approach for the Development of the Seepage Calibration Model (Adapted from CRWMS M&O 2000, U0080, Section 6)

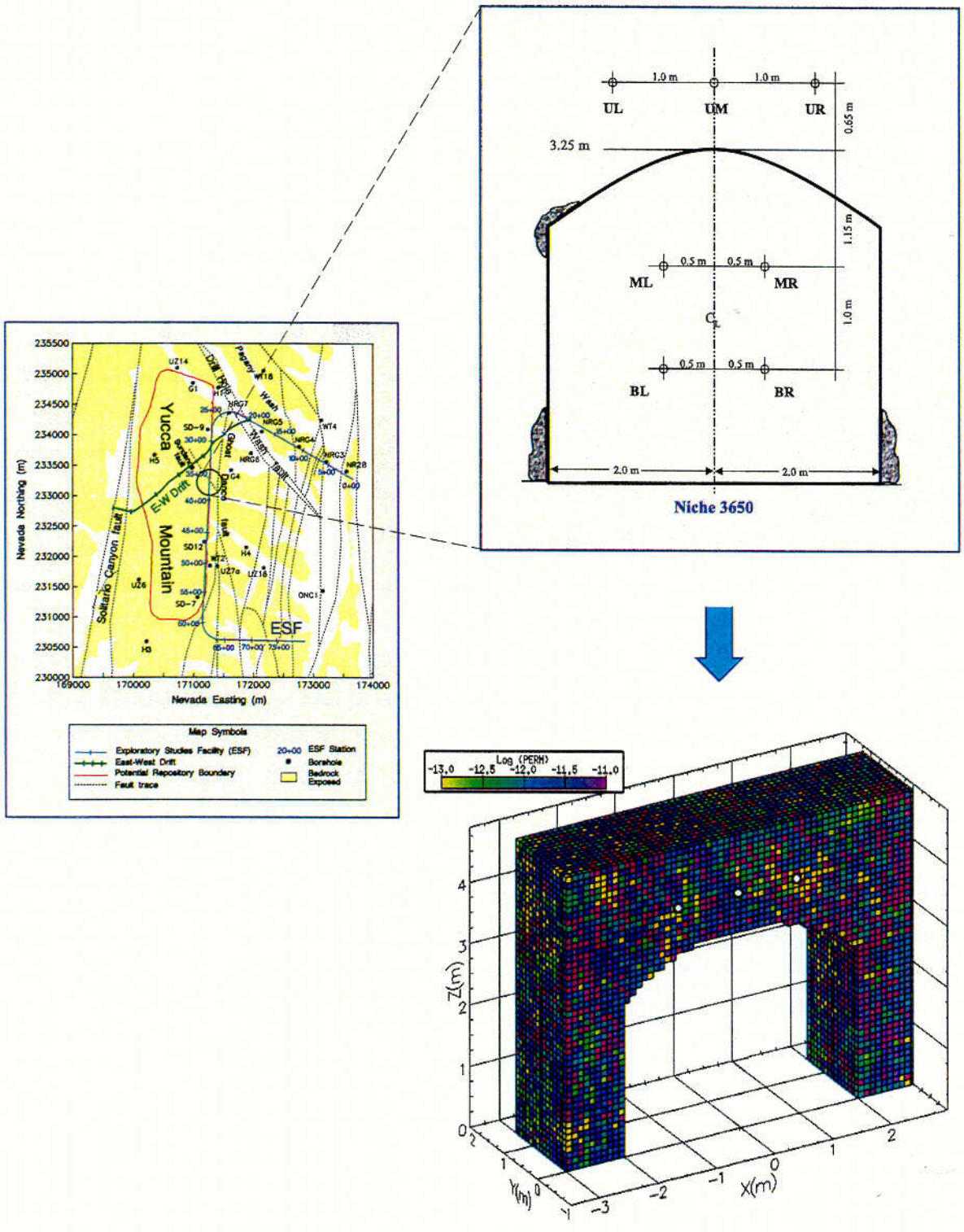

Figure 3.9-5. Schematic Showing Location and Layout of Niche 3650 as well as Log-Permeability Field of the Three-Dimensional Seepage Calibration Model (Adapted from CRWMS M&O 2000, U0080, Figures 12, 13, and 18)

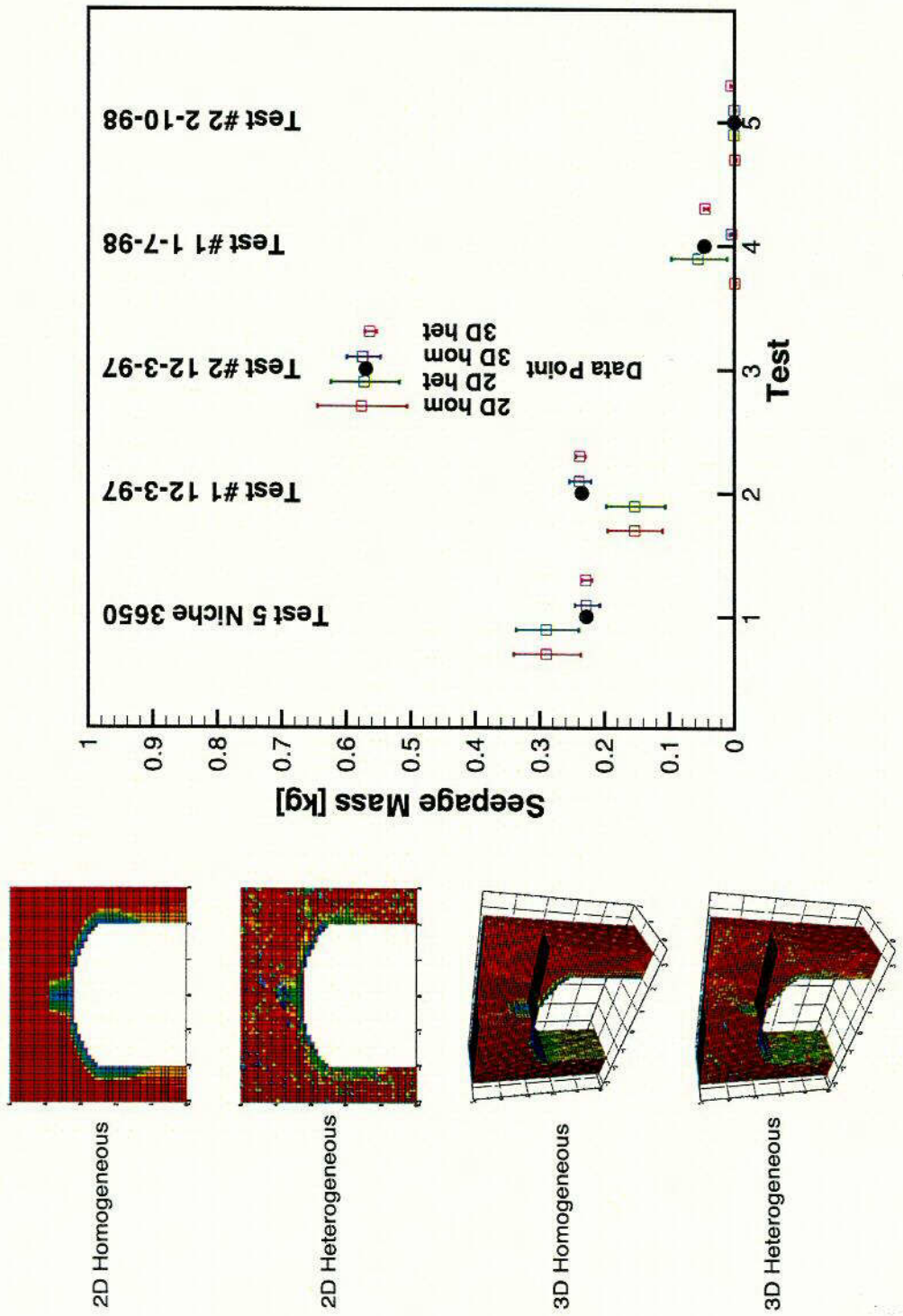

Figure 3.9-6. Comparison between the Measured Seepage Mass (Circles) and That Calculated with Two- and Three-Dimensional, Homogeneous and Heterogeneous Models (Squares). The four models are visualized on the left. The uncertainty of the model predictions is shown as error bars on the 95% confidence level. The three-dimensional heterogeneous Seepage Calibration Model matches the data best (Adapted from CRWMS M&O 2000, U0080, Figure 19).

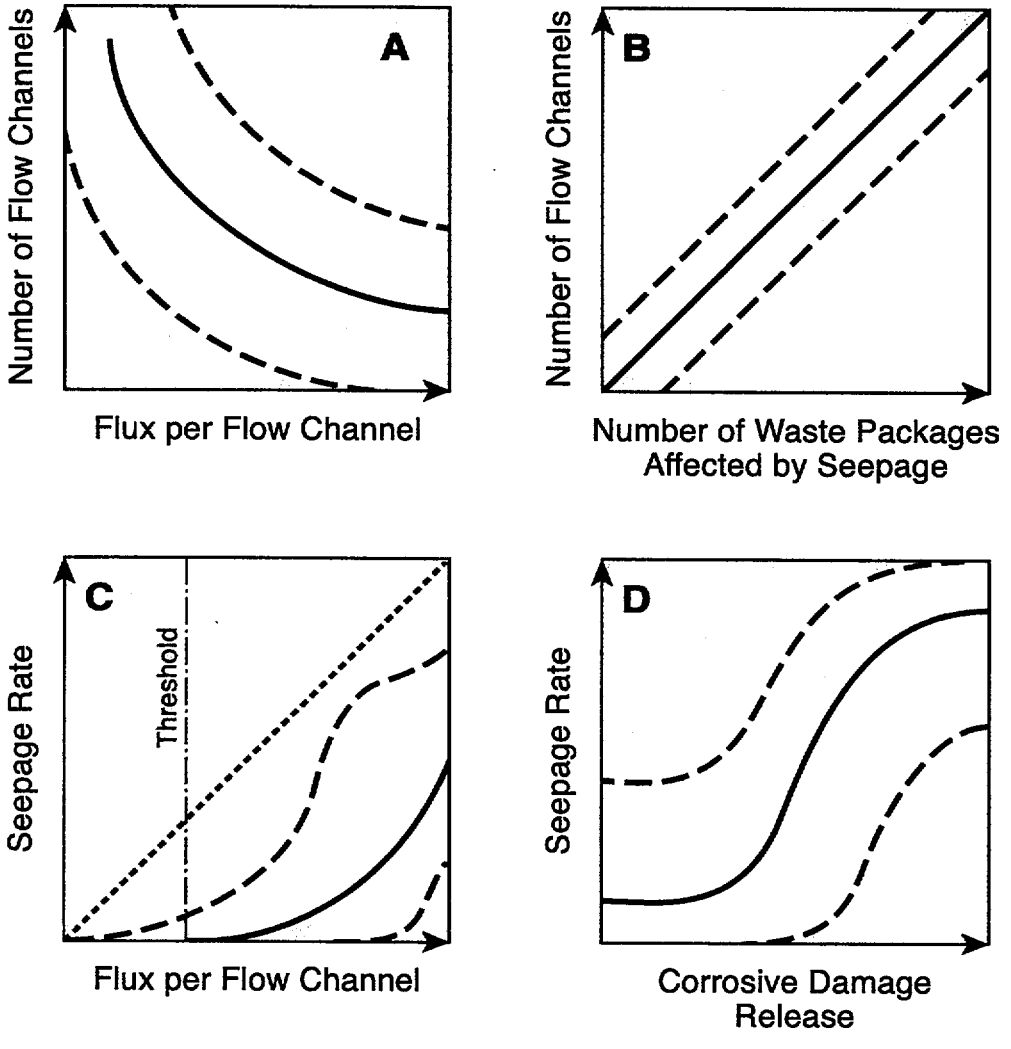

Figure 3.9-7. Schematic Showing Relationships between Seepage-Relevant Factors. The red solid lines schematically indicate the expected behavior; uncertainty is schematically shown as blue dashed lines; the green dotted line shows the conservative assumption that no capillary-barrier effect exists.

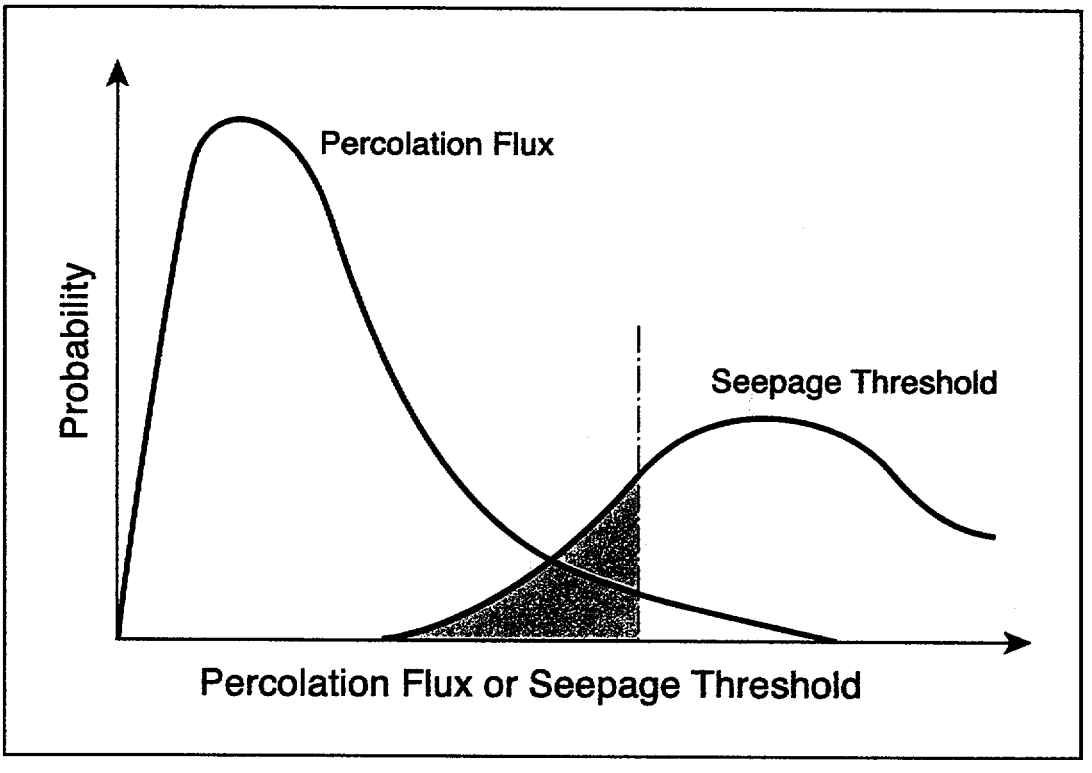

Figure 3.9-8. Schematic Showing Percolation-Flux and Seepage-Threshold Distributions, Which Determine the Seepage-Fraction Probability

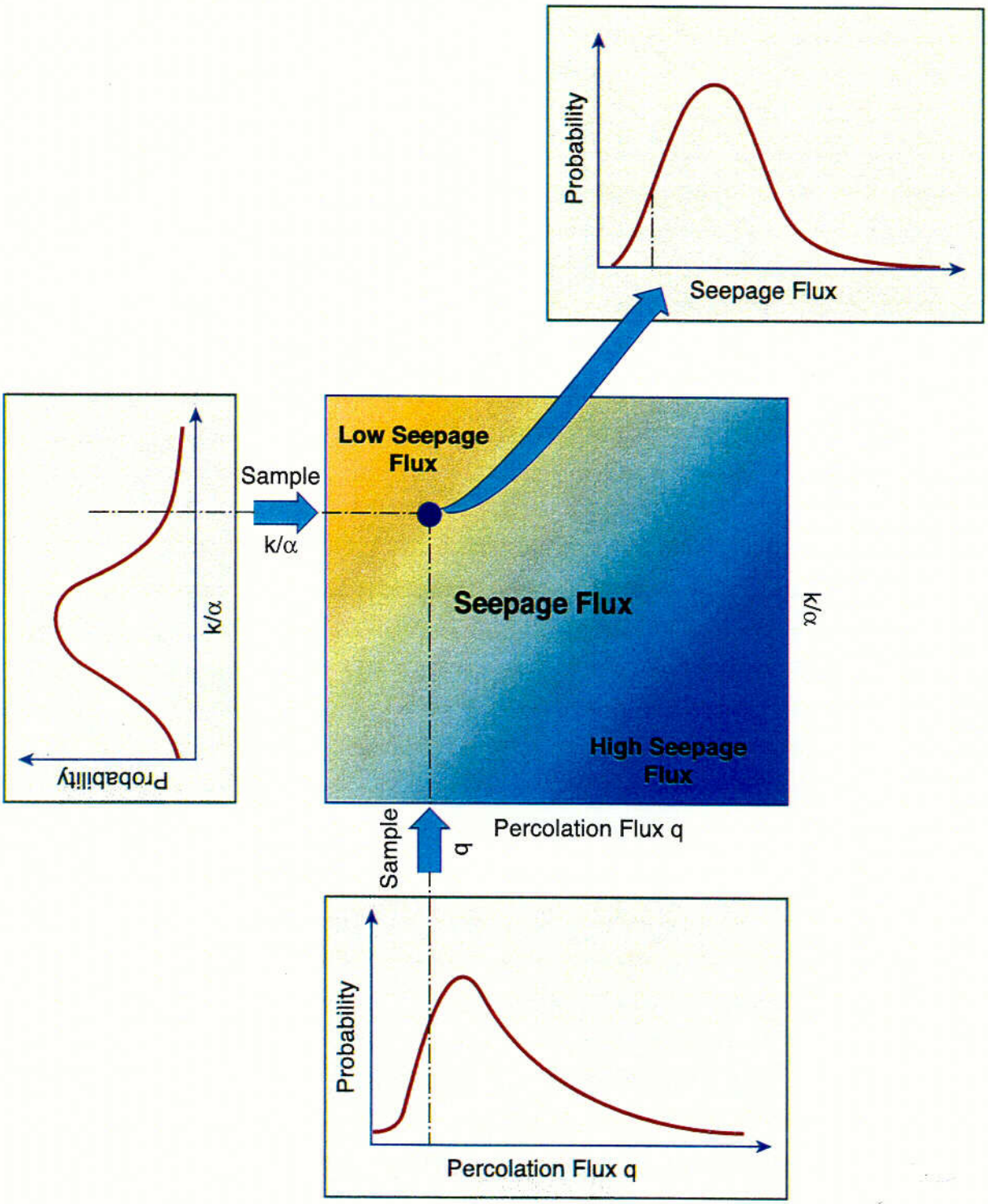

Figure 3.9-9. Schematic Illustrating Monte Carlo Sampling Approach for Seepage TSPA Calculations

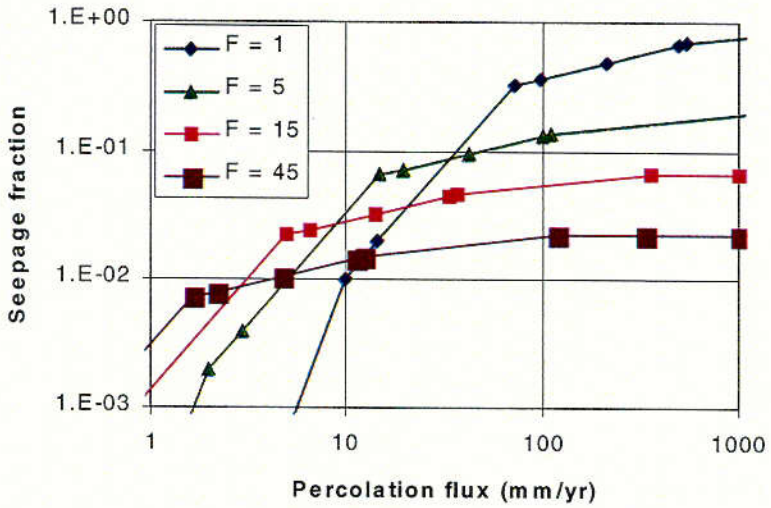

Figure 3.9-10. Effect of Flow Focusing on Seepage Fraction (CRWMS M&O 2000, U0120, Figure 5)

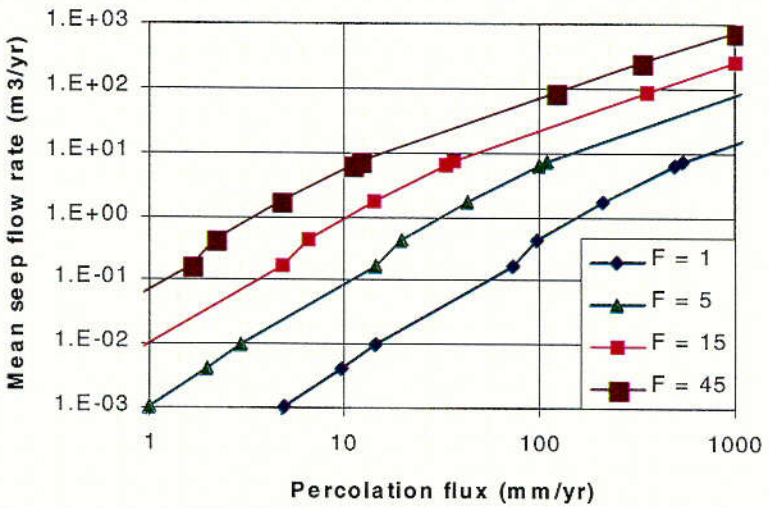

Figure 3.9-11. Effect of Flow Focusing on Mean Seep Flow Rate (CRWMS M&O 2000, U0120, Figure 6)

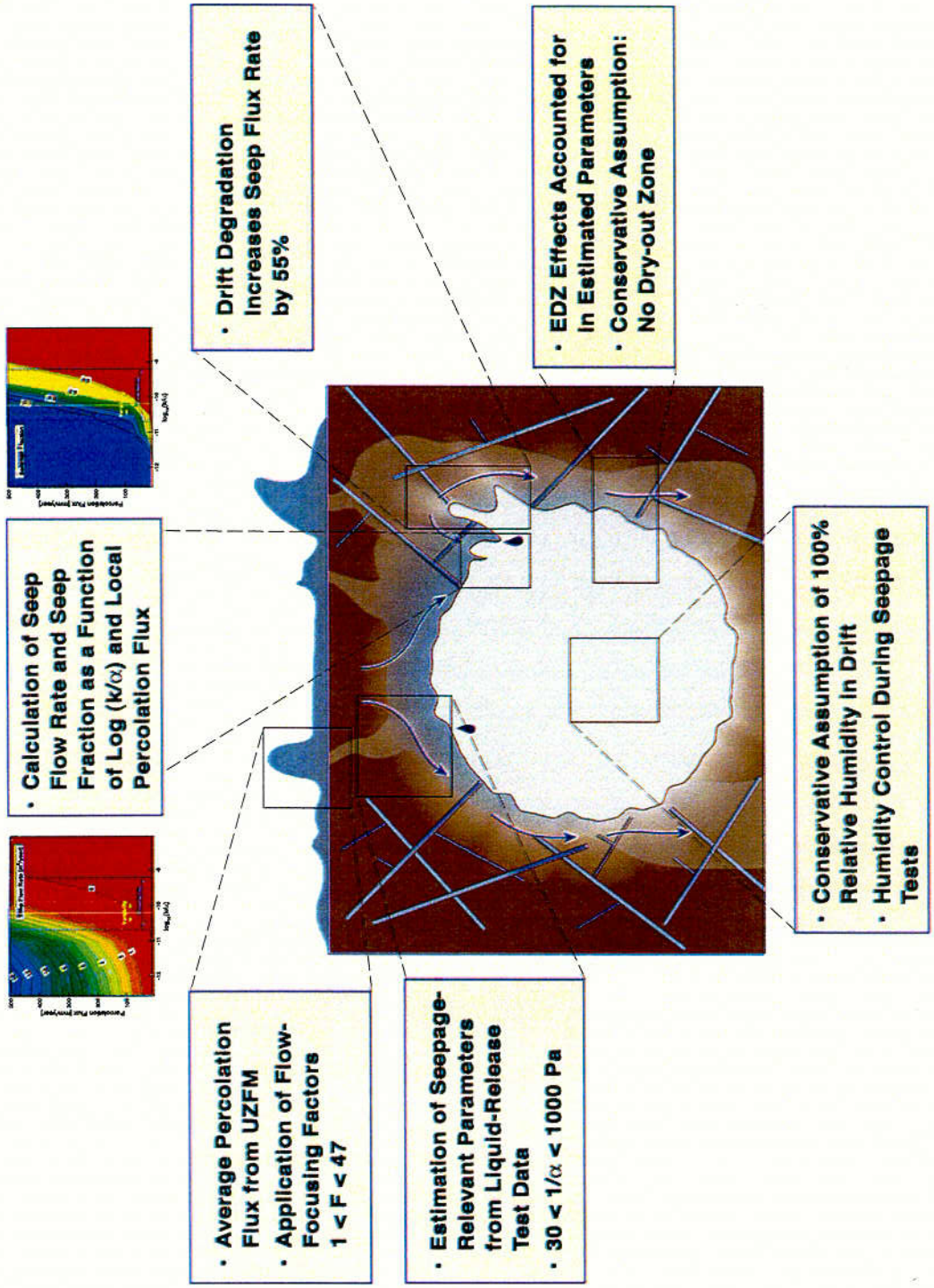

Figure 3.9-12. Summary of Results

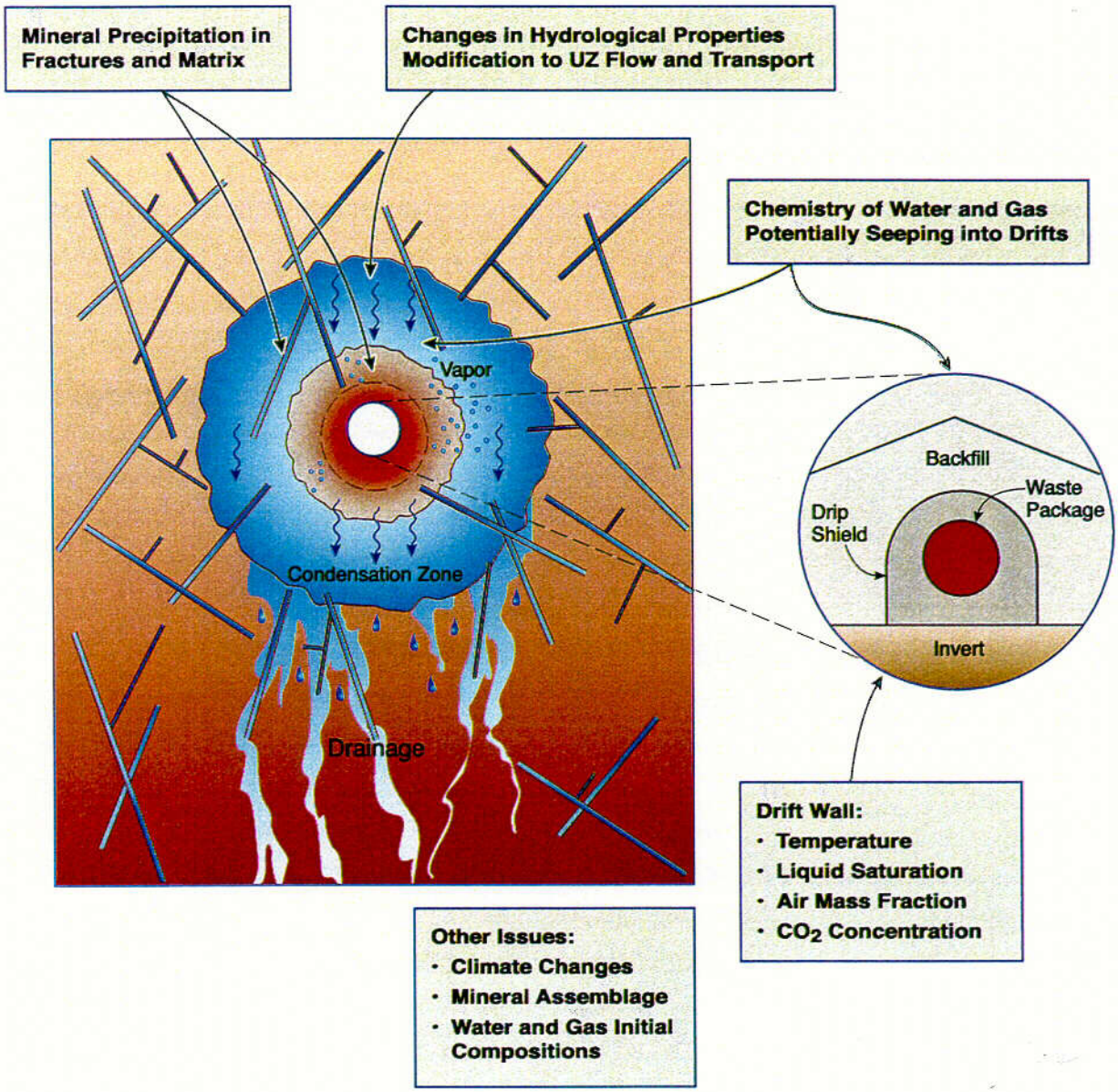

Figure 3.10-1. Schematic Diagram of THC Processes Around a Heated Drift

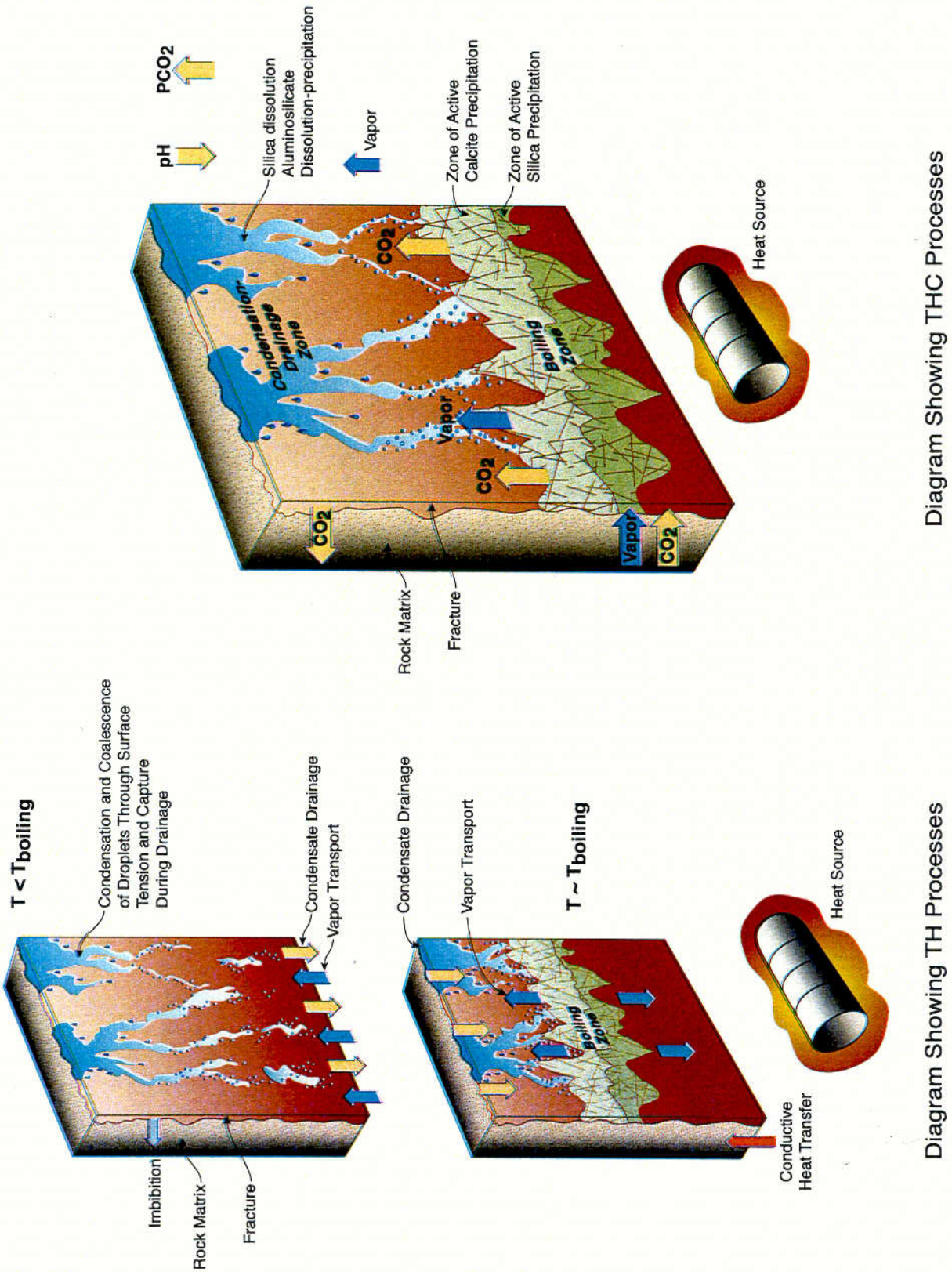

Figure 3.10-2. Schematic Diagram Showing Relation Between TH Processes and Geochemical Processes

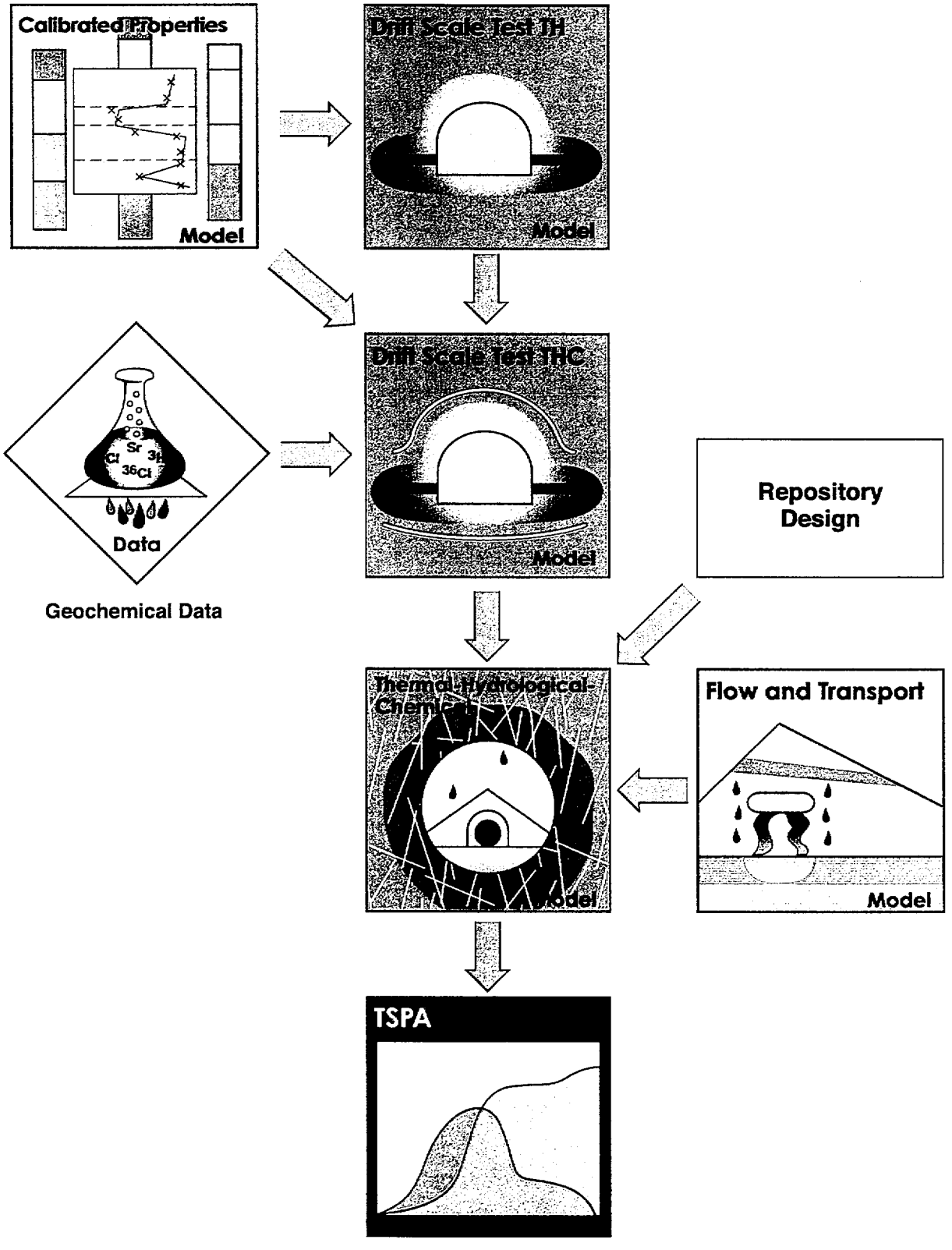

Figure 3.10-3. Model Diagram Relating Inputs and Outputs for the THC Seepage Model and Drift Scale Test THC Model

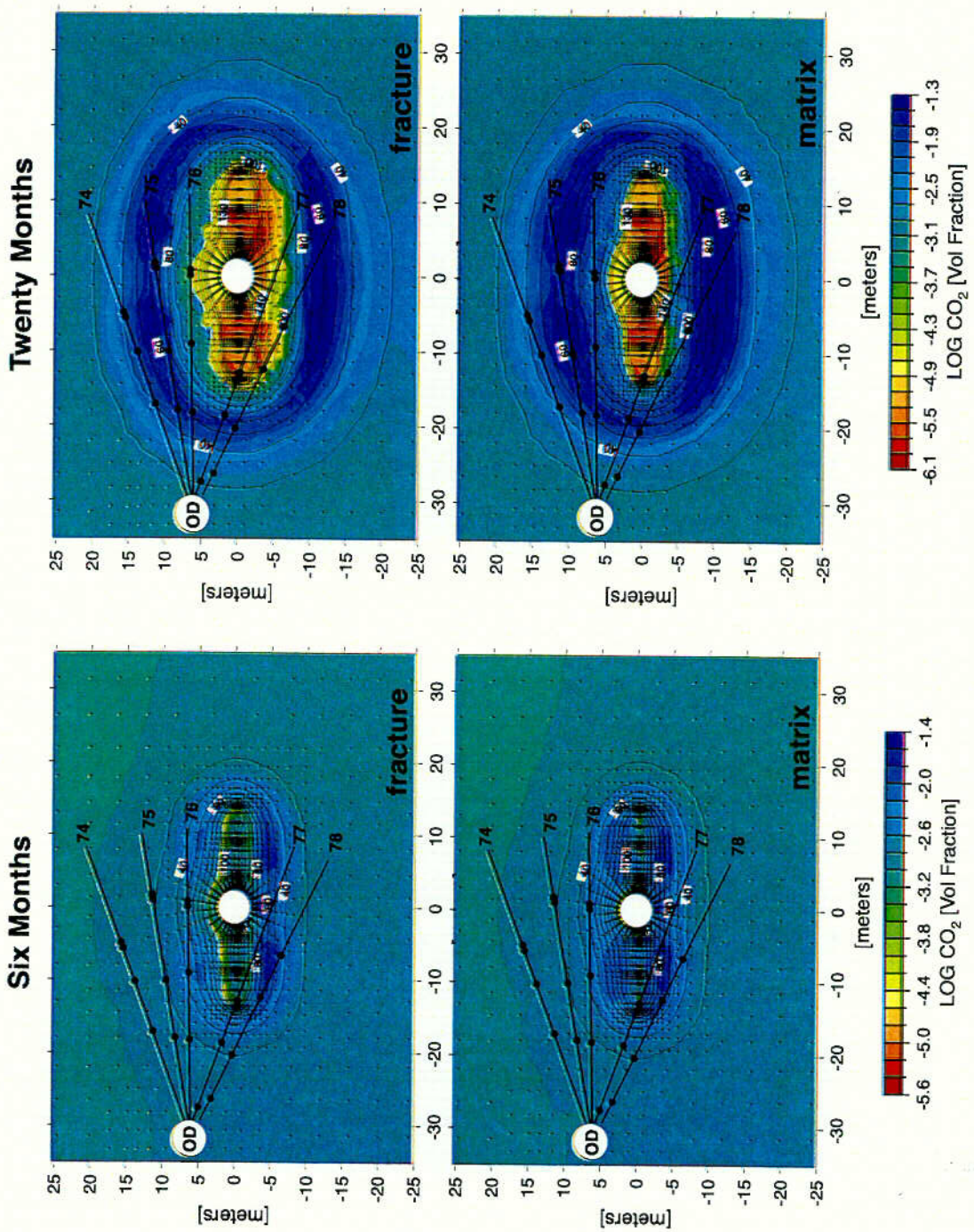

Figure 3.10-4. Simulated CO_2 Volume Fractions in Fractures and Matrix After 6 (a&b) and 20 (c&d) Months of Heating During the Drift Scale Test (adapted from CRWMS M&O 2000, N0120/U0110, Figures 5 and 6). Temperature contours are superimposed. "OD" refers to the Observation Drift.

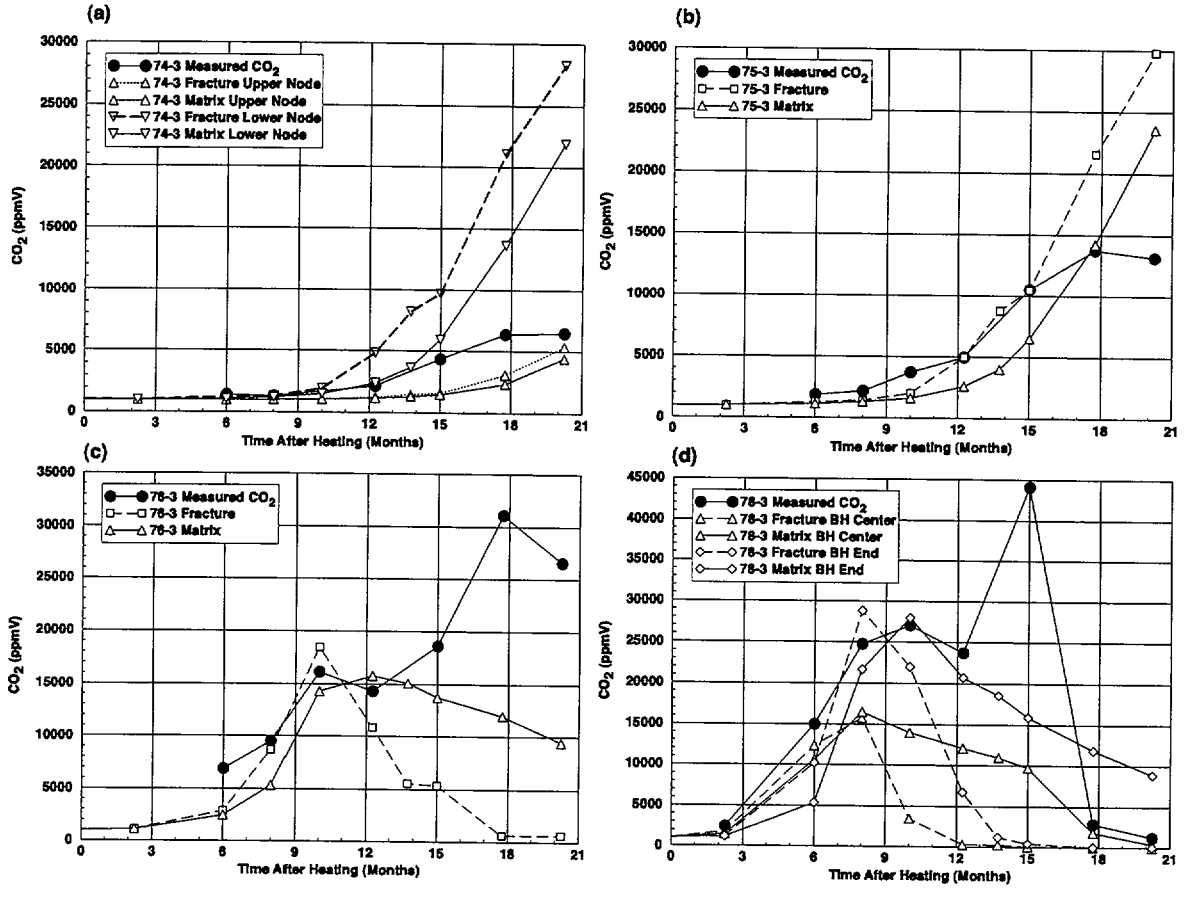

Figure 3.10-5. Simulated CO_2 Volume Fractions at Grid Nodes near Borehole (BH) Intervals Where Gas-Phase CO_2 Measurements were Made (CRWMS M&O 2000, N0120/U0110, Figure 10). Filled circles are measured CO_2 concentrations in the gas phase. Modeled data come from locations in 2-D grid close to center of borehole interval.

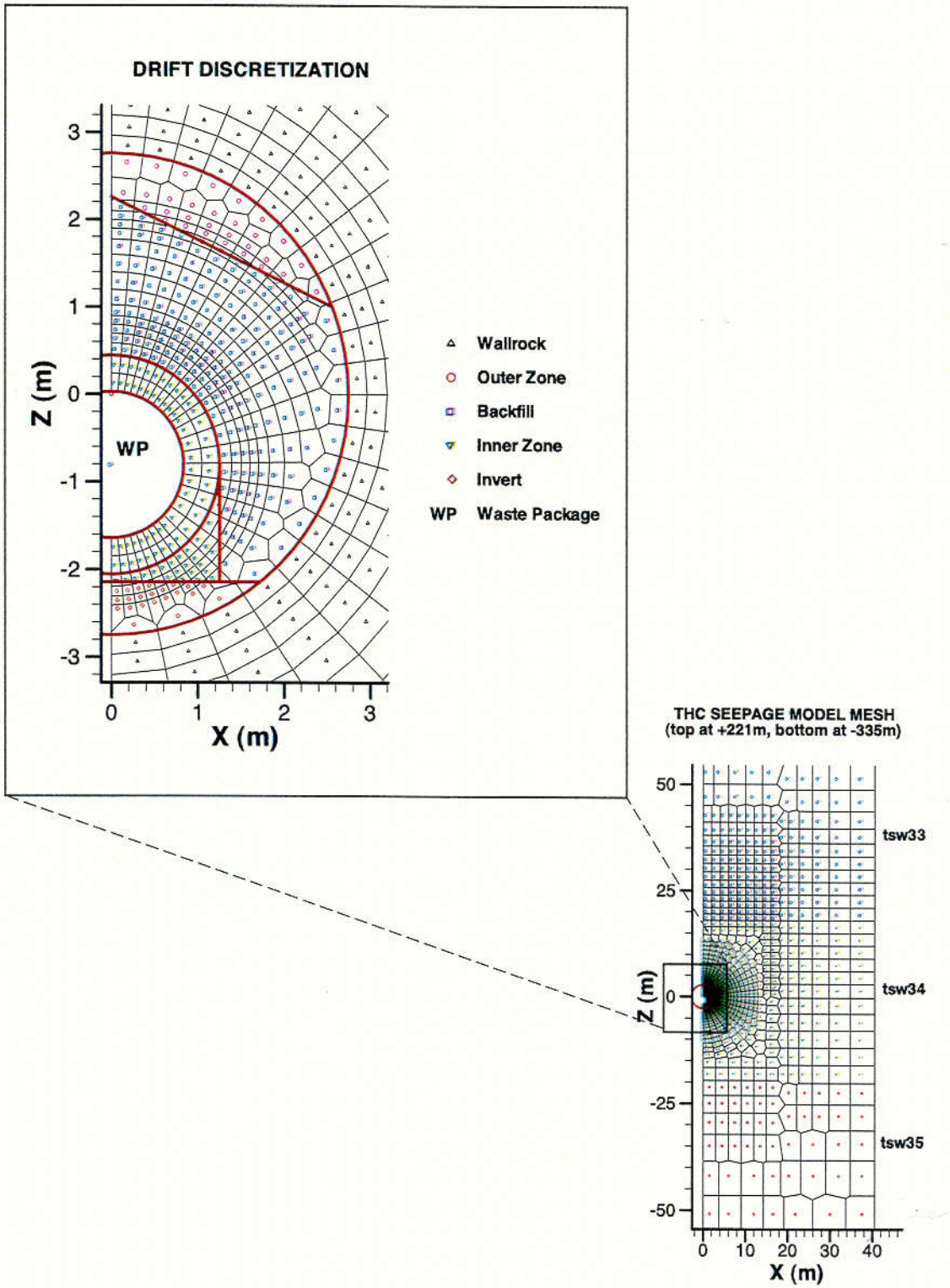

Figure 3.10-6. THC Seepage Model Mesh Showing Hydrogeologic Units in Proximity of the Drift: Topopah Spring Tuff Upper Lithophysal (tsw33), Middle Nonlithophysal (tsw34), and Lower Lithophysal (tsw35) Units, and Blowup Showing Discretization of In-Drift Design Components (adapted from CRWMS M&O 2000, N0120/U0110, Figures 18 and 19)

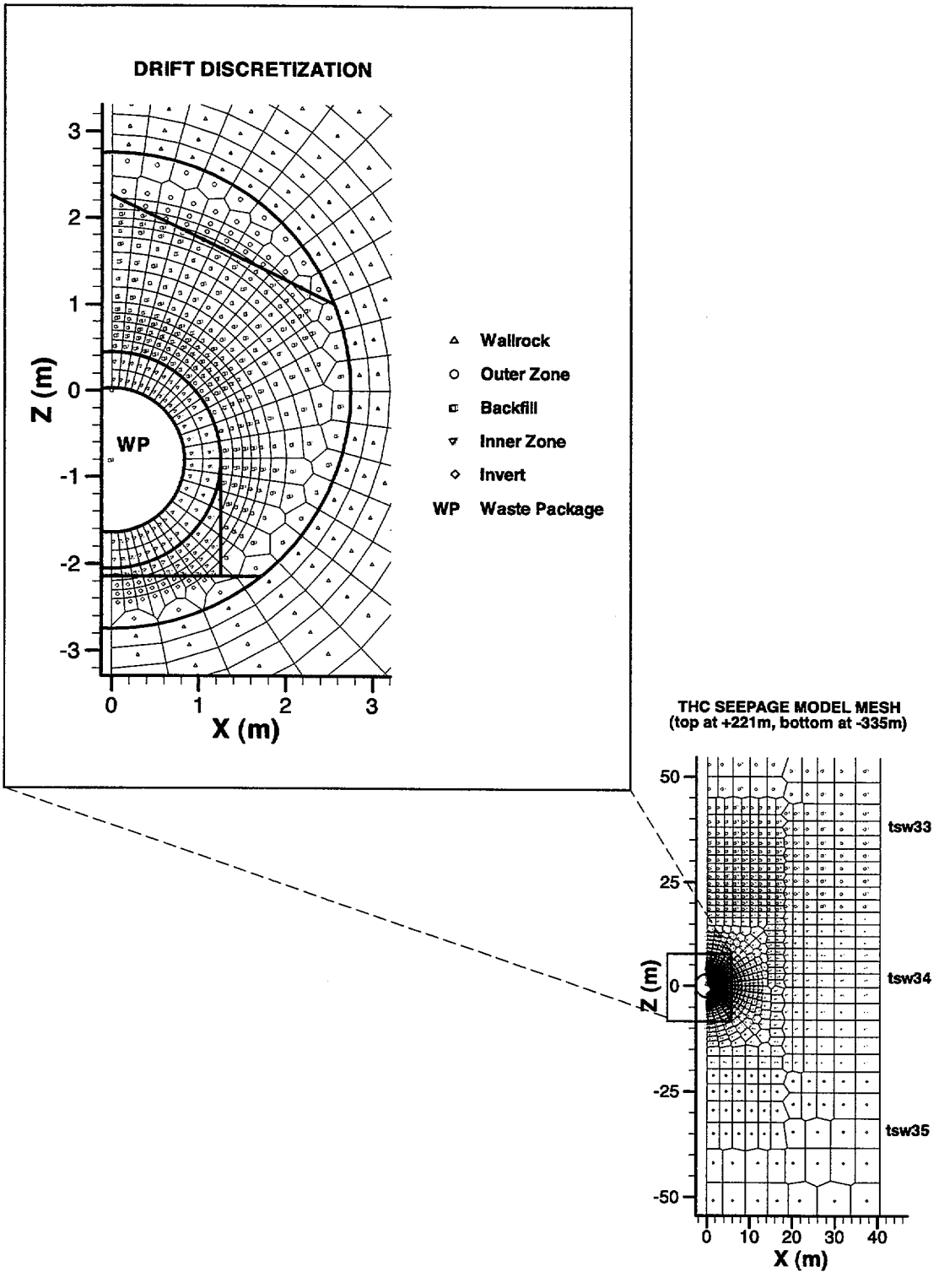

Figure 3.10-6. THC Seepage Model Mesh Showing Hydrogeologic Units in Proximity of the Drift: Topopah Spring Tuff Upper Lithophysal (tsw33), Middle Nonlithophysal (tsw34), and Lower Lithophysal (tsw35) Units, and Blowup Showing Discretization of In-Drift Design Components (adapted from CRWMS M&O 2000, N0120/U0110, Figures 18 and 19)

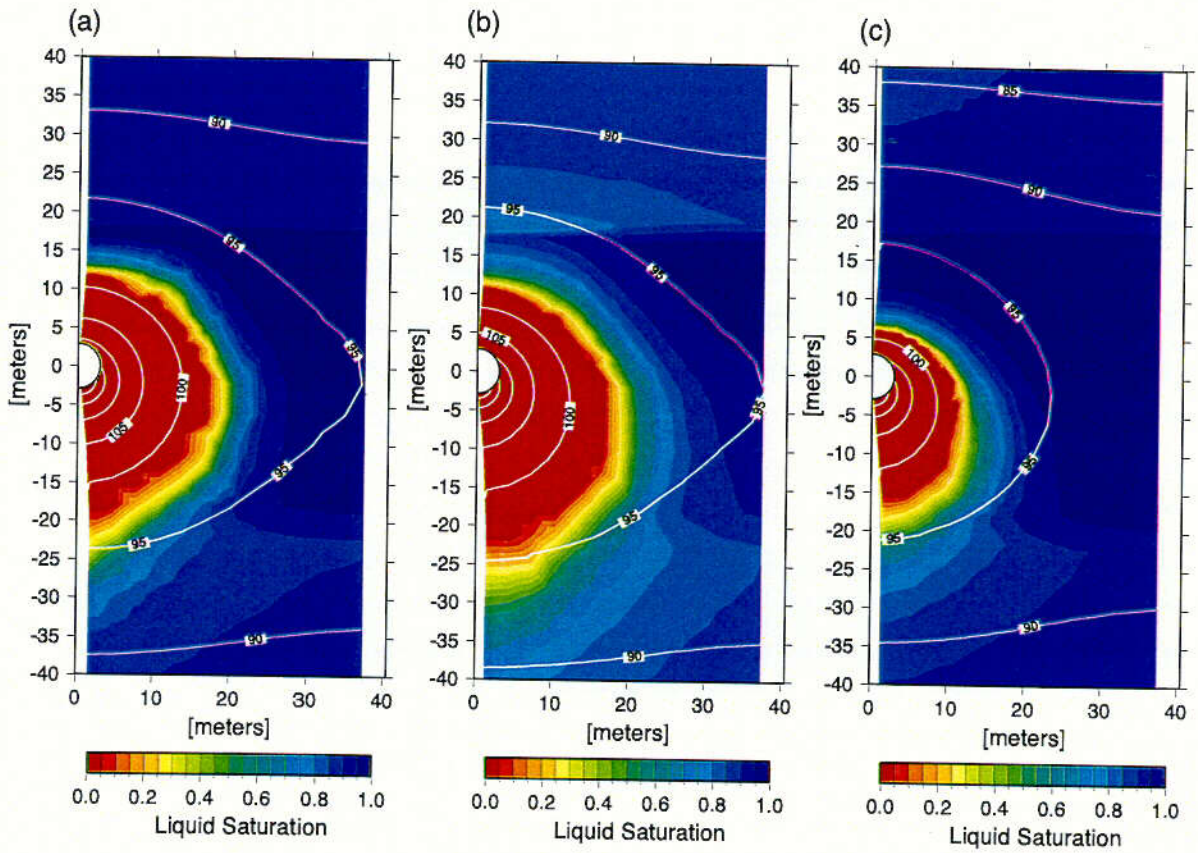

Figure 3.10-7. Contour Plot of Modeled Liquid Saturations and Temperatures (Labeled Contour Lines) in the Matrix at 600 Years (Near Maximum Dryout) for Three Climate Change Scenarios: (a) Lower Bound, (b) Mean, and (c) Upper Bound (Calcite-Silica-Gypsum System) (CRWMS M&O 2000, N0120/U0110, Figure 26)

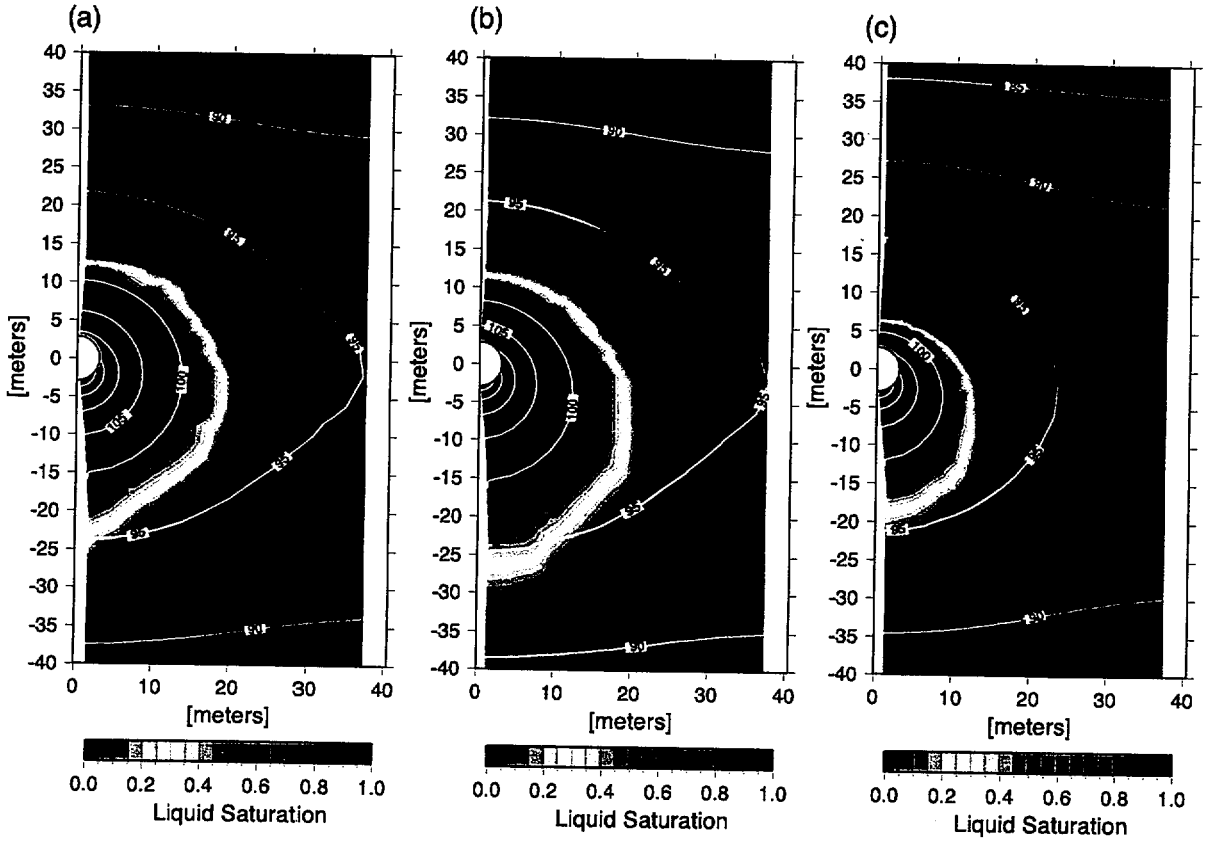

Figure 3.10-7. Contour Plot of Modeled Liquid Saturations and Temperatures (Labeled Contour Lines) in the Matrix at 600 Years (Near Maximum Dryout) for Three Climate Change Scenarios: (a) Lower Bound, (b) Mean, and (c) Upper Bound (Calcite-Silica-Gypsum System) (CRWMS M&O 2000, N0120/U0110, Figure 26)

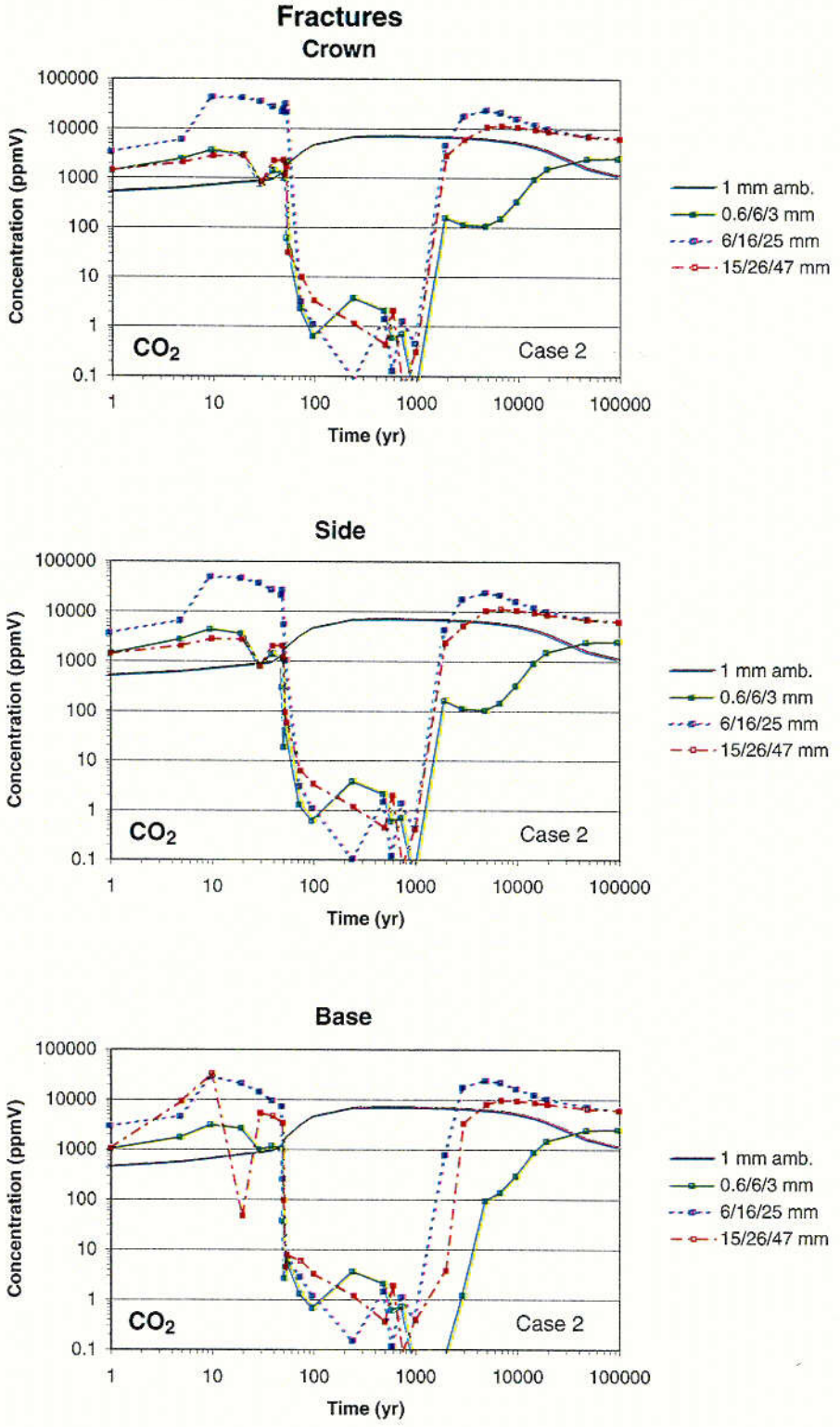

Figure 3.10-8. Time Profiles of Modeled CO_2 Concentrations in the Gas Phase in Fractures at Three Drift Wall Locations for Different Climate Change Scenarios (Calcite-Silica-Gypsum System) (CRWMS M&O 2000, N0120/U0110, Figure 29)

C89

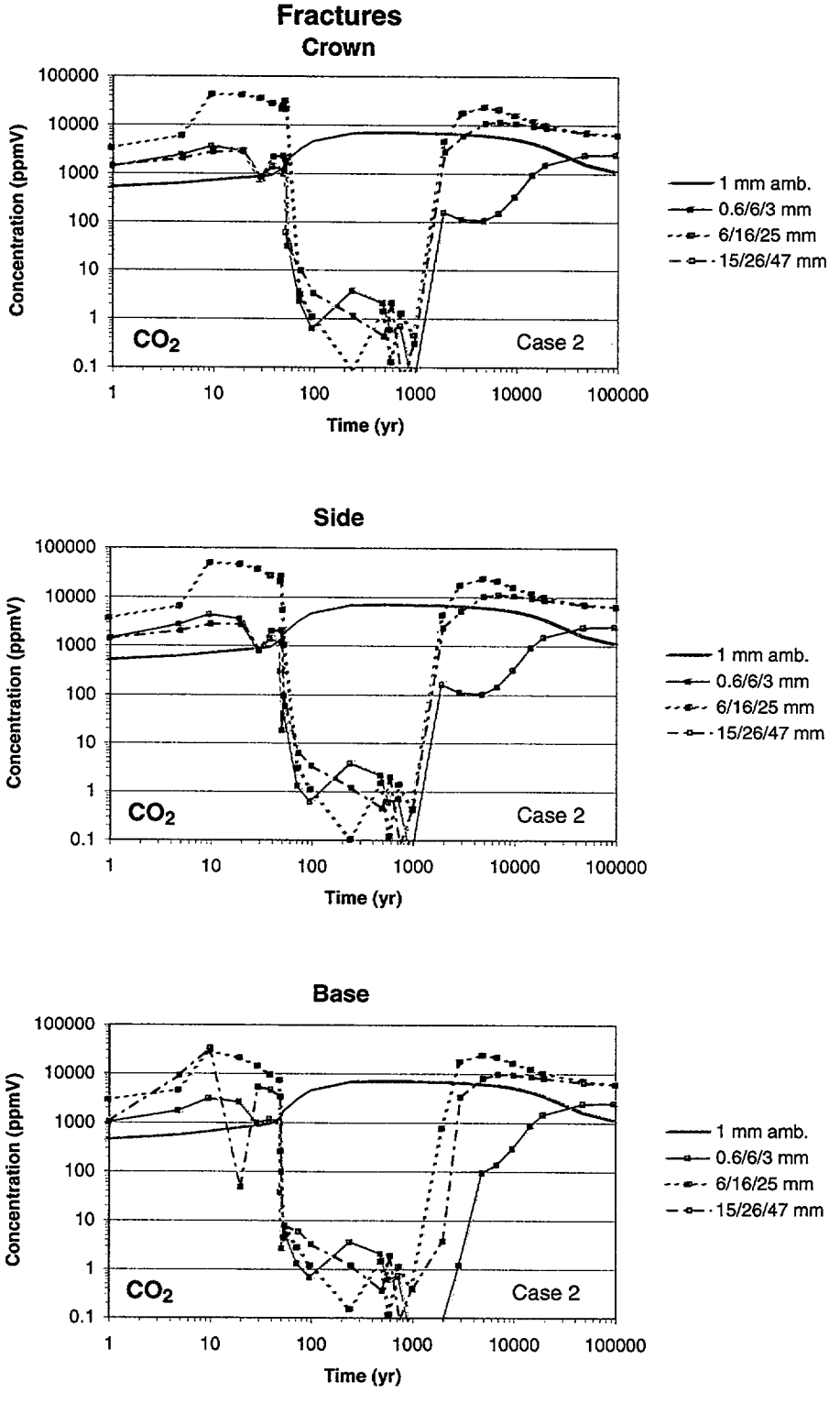

Figure 3.10-8. Time Profiles of Modeled CO_2 Concentrations in the Gas Phase in Fractures at Three Drift Wall Locations for Different Climate Change Scenarios (Calcite-Silica-Gypsum System) (CRWMS M&O 2000, N0120/U0110, Figure 29)

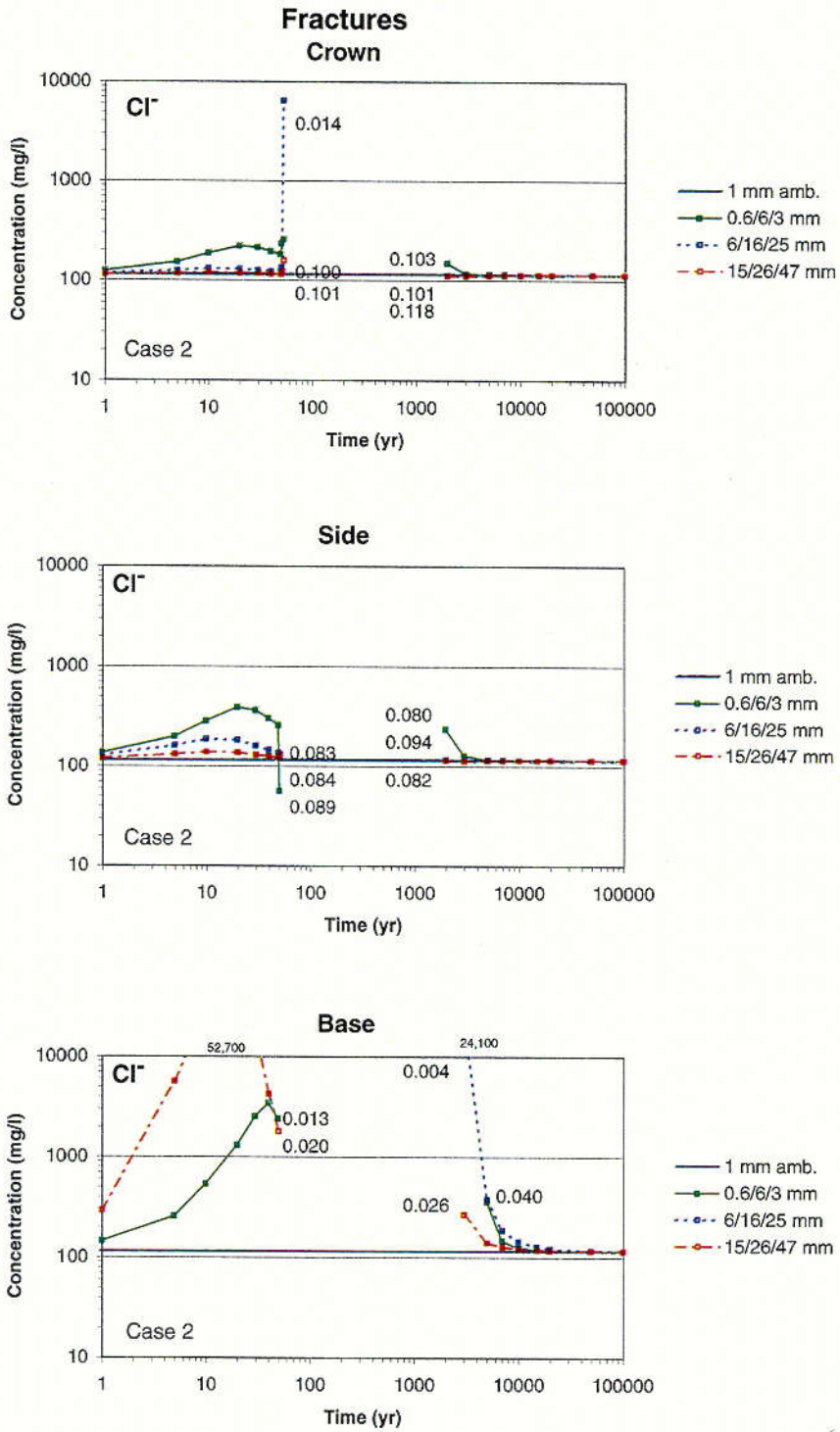

Figure 3.10-9. Time Profiles of Modeled Total Aqueous Chloride Concentrations in Fracture Water at Three Drift Wall Locations for Different Climate Change Scenarios (Case 2). The dryout period is left blank. Numbers by each curve indicate the last output liquid saturation before dryout and the first output liquid saturation during rewetting (CRWMS M&O 2000, N0120/U0110, Figure 38).

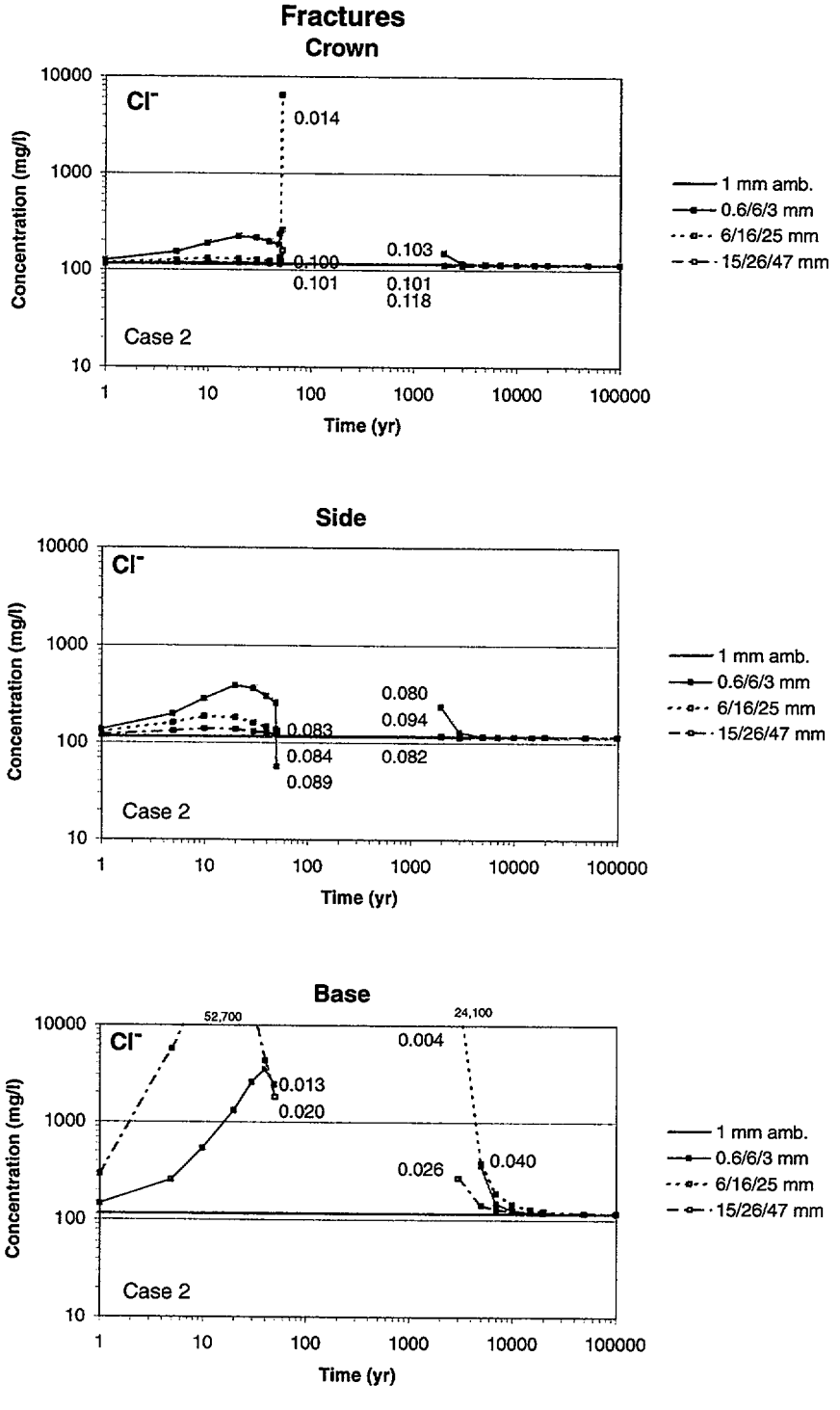

Figure 3.10-9. Time Profiles of Modeled Total Aqueous Chloride Concentrations in Fracture Water at Three Drift Wall Locations for Different Climate Change Scenarios (Case 2). The dryout period is left blank. Numbers by each curve indicate the last output liquid saturation before dryout and the first output liquid saturation during rewetting (CRWMS M&O 2000, N0120/U0110, Figure 38).

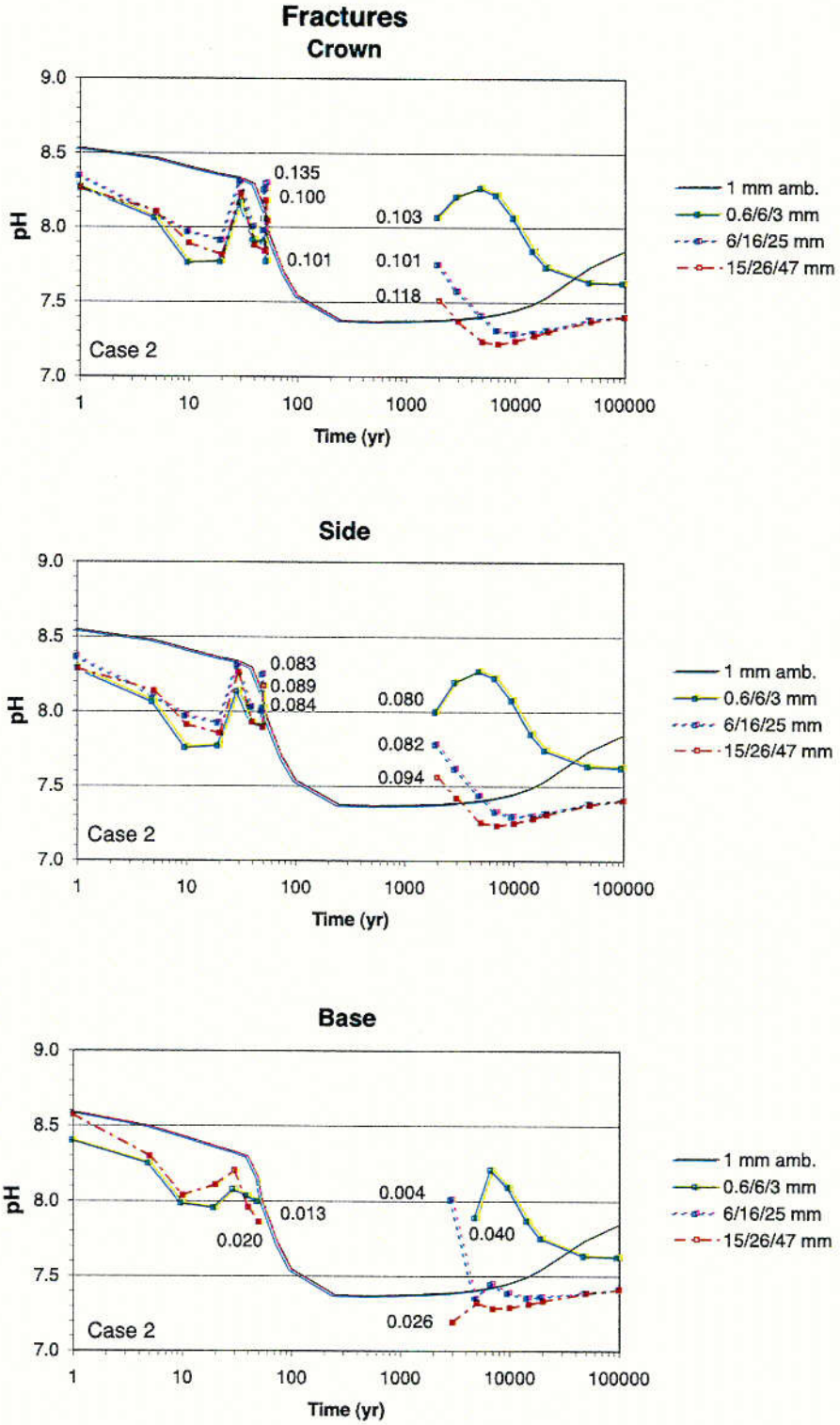

Figure 3.10-10. Time Profiles of the Modeled pH of Fracture Water at Drift Wall Locations for Different Climate Change Scenarios (Case 2 Calcite-Silica-Gypsum System). The dryout period is left blank. The last output liquid saturation before dryout and the first output liquid saturation during rewetting are noted on each curve (CRWMS M&O 2000, N0120/U0110, Figure 31).

C91

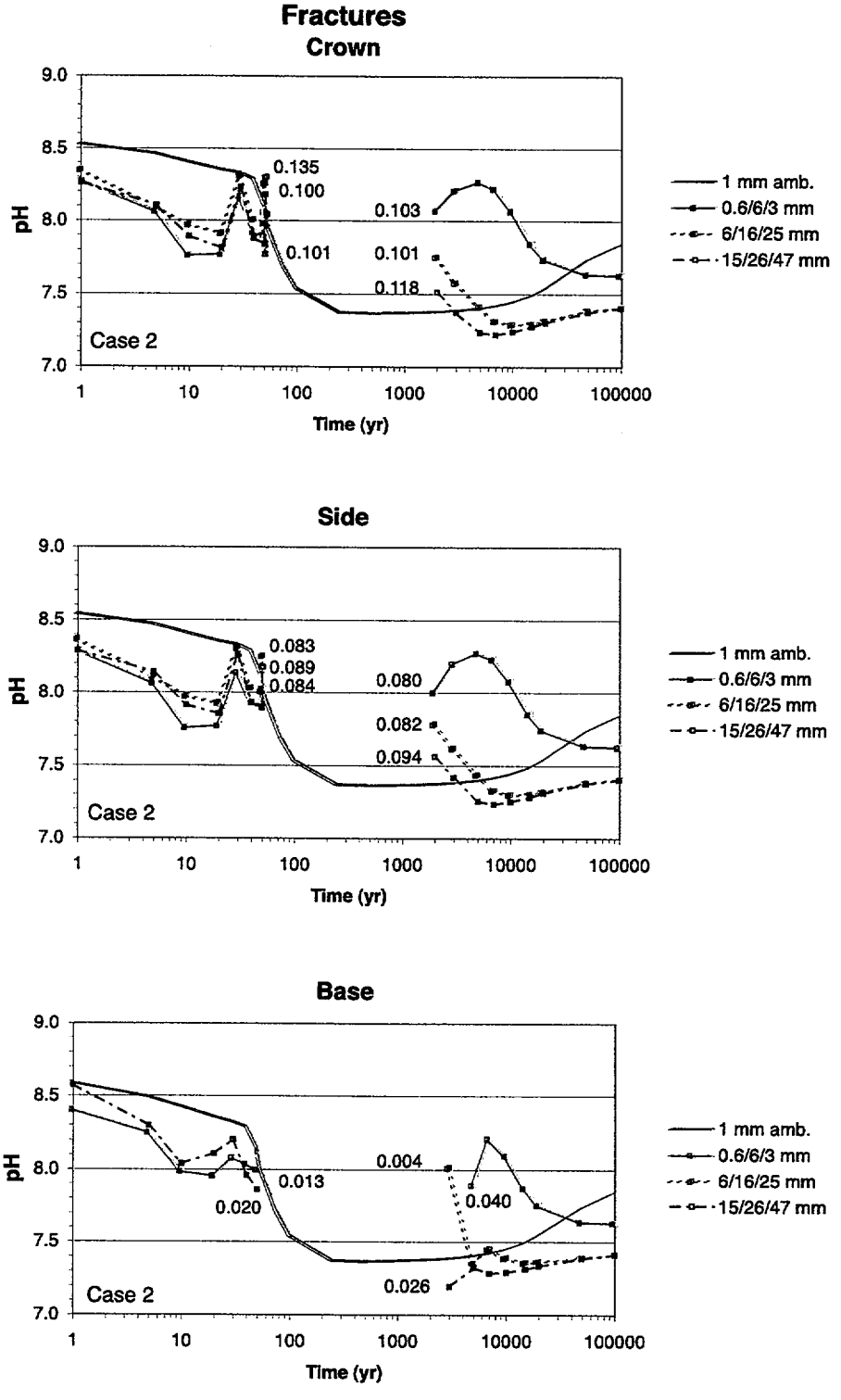

Figure 3.10-10. Time Profiles of the Modeled pH of Fracture Water at Drift Wall Locations for Different Climate Change Scenarios (Case 2 Calcite-Silica-Gypsum System). The dryout period is left blank. The last output liquid saturation before dryout and the first output liquid saturation during rewetting are noted on each curve (CRWMS M&O 2000, N0120/U0110, Figure 31).

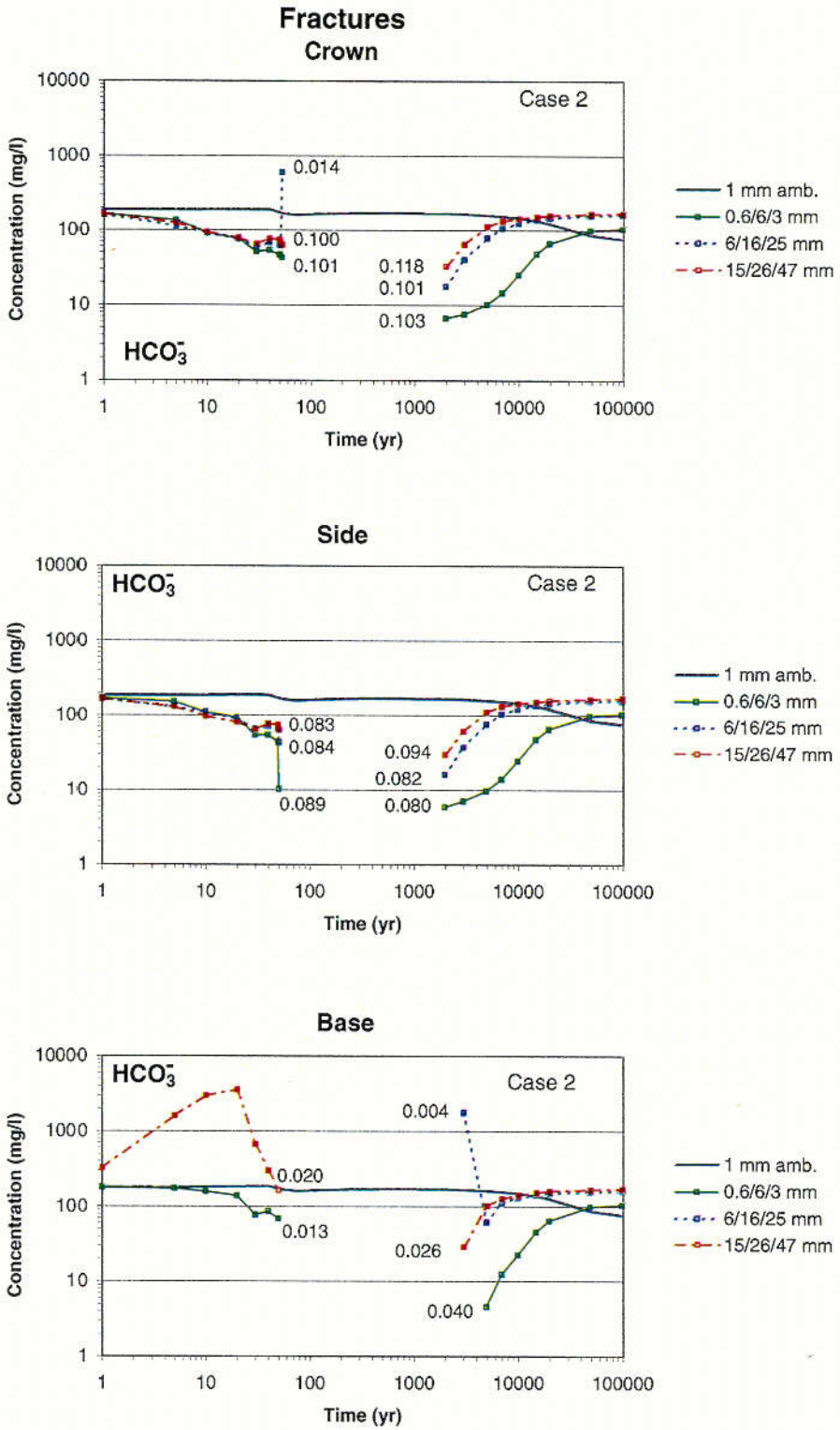

Figure 3.10-11. Time Profiles of Modeled Total Aqueous Carbonate Concentrations (as HCO_3^-) in Fracture Water at Drift Wall Locations for Different Climate Scenarios (Calcite-Silica-Gypsum System) (CRWMS M&O 2000, N0120/U0110, Figure 33)

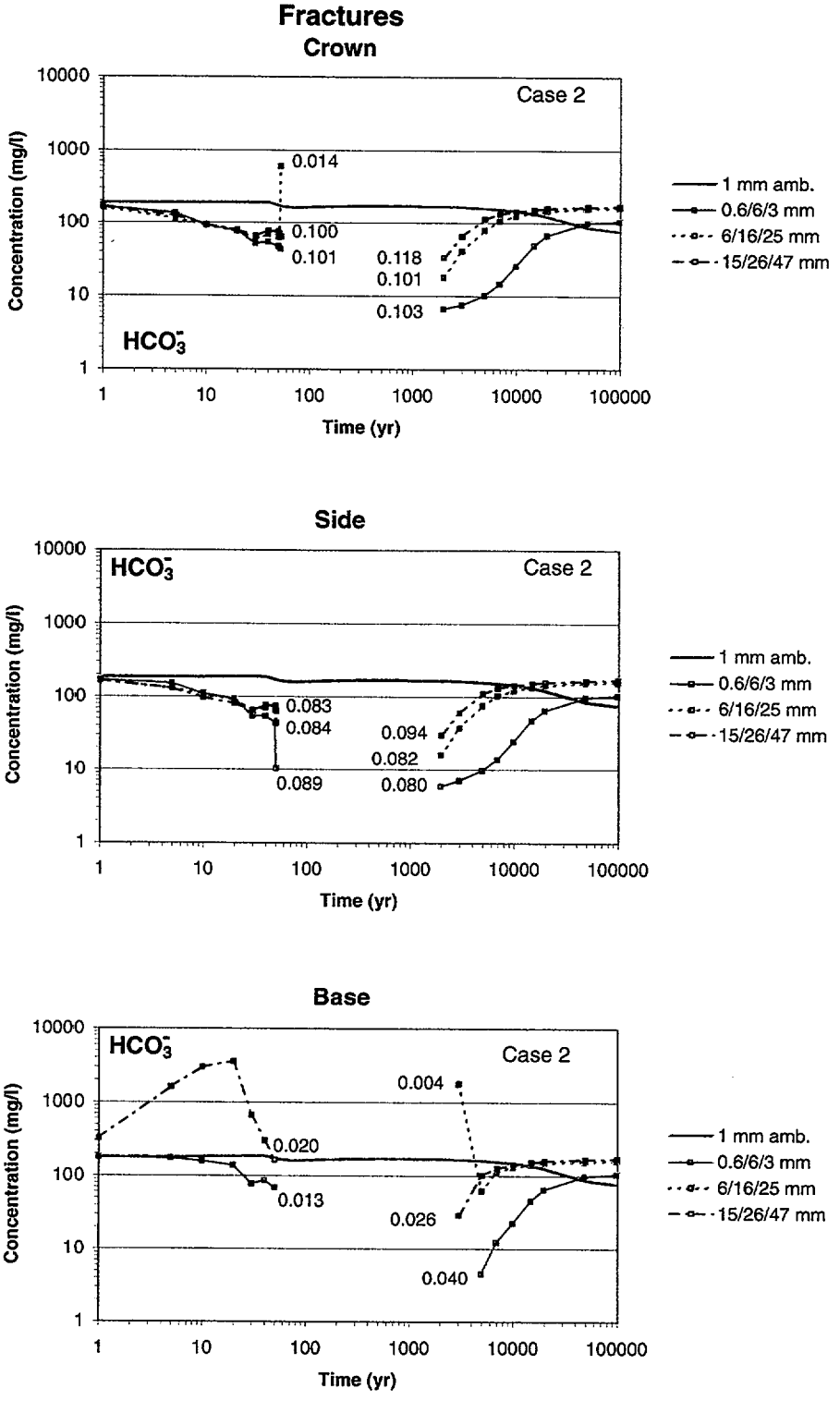

Figure 3.10-11. Time Profiles of Modeled Total Aqueous Carbonate Concentrations (as HCO_3^-) in Fracture Water at Drift Wall Locations for Different Climate Scenarios (Calcite-Silica-Gypsum System) (CRWMS M&O 2000, N0120/U0110, Figure 33)

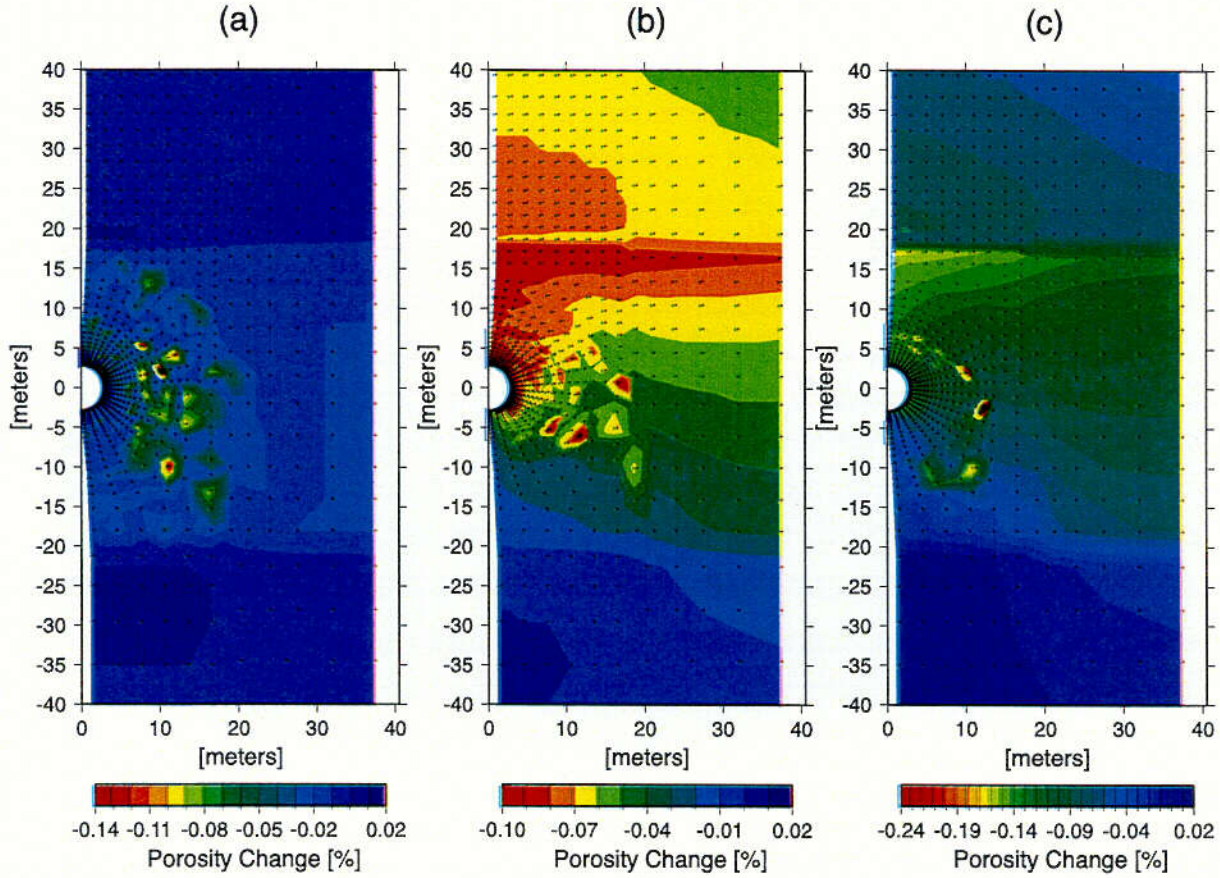

Figure 3.10-12. Contour Plot of Calculated Total Fracture Porosity Change at 10,000 Years for Three Climate Change Scenarios (Calcite-Silica-Gypsum System): (a) Lower Bound, (b) Mean, and (c) Upper Bound. Red areas indicate the maximum decrease in porosity as a result of mineral precipitation (CRWMS M&O 2000, N0120/U0110, Figure 42).

C93

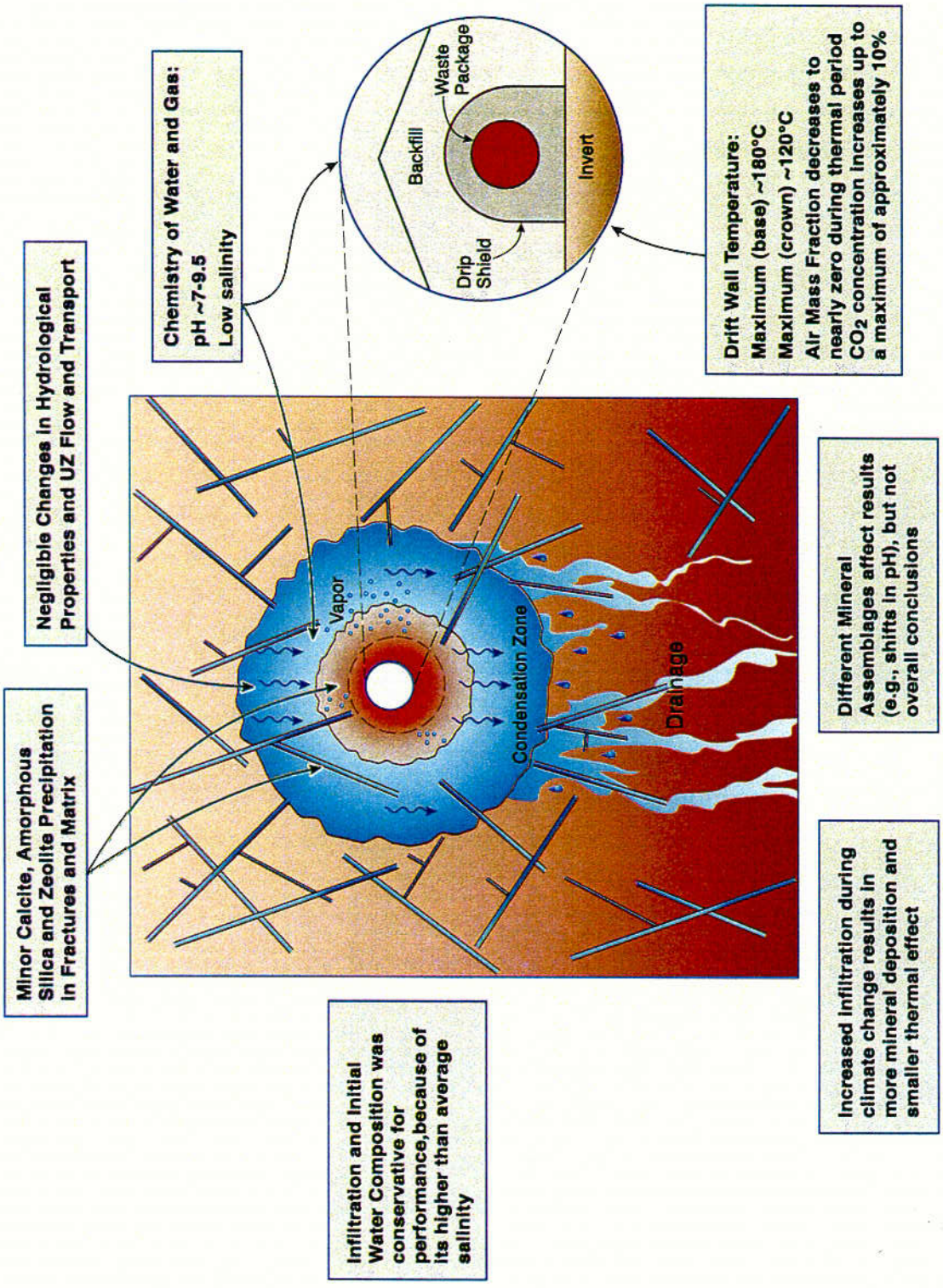

Figure 3.10-13. Conceptual Model of TH Processes Around a Heated Drift and Summaries of Important Results of Drift-Scale THC Simulations and Analyses

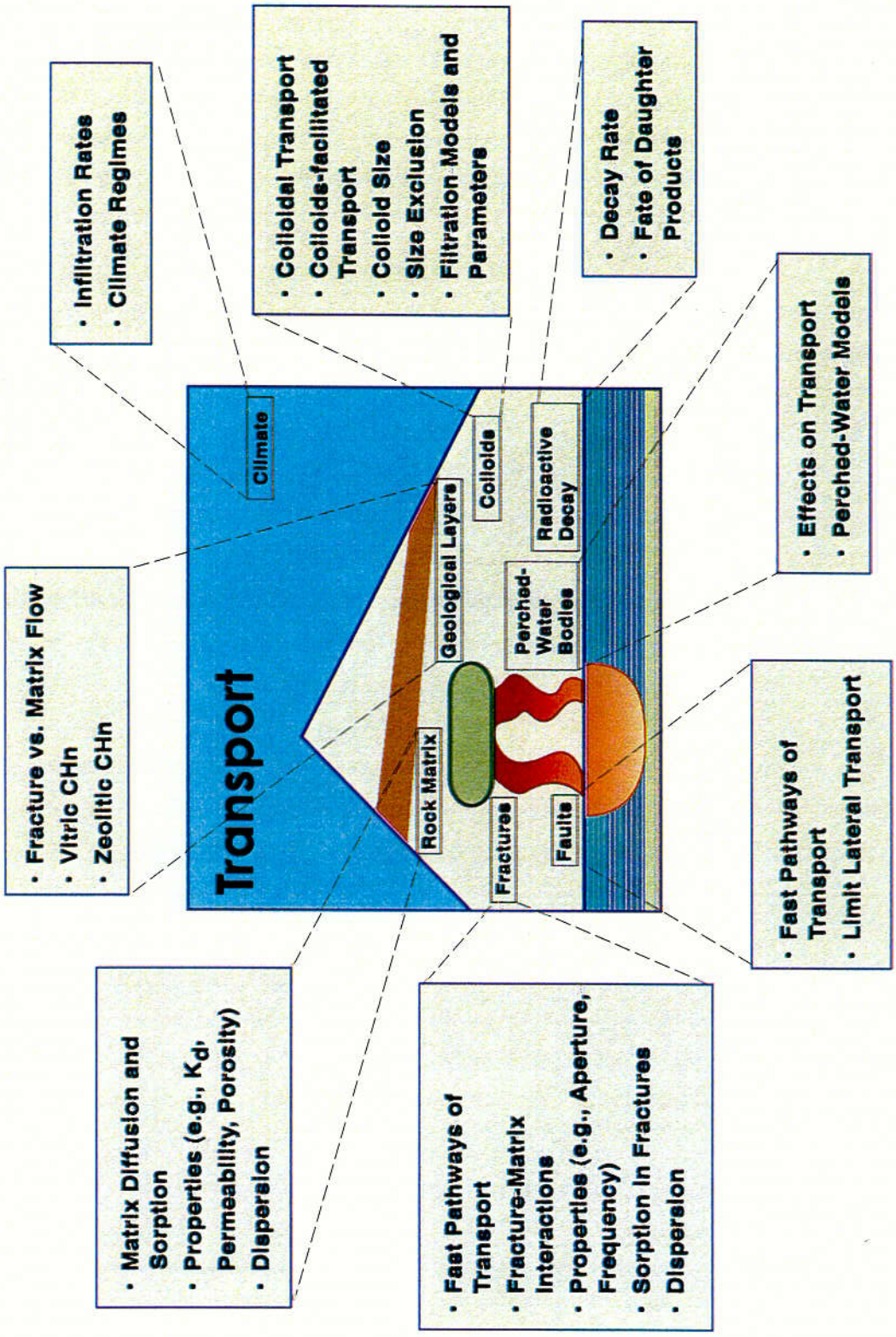

Figure 3.11-1. Key Issues Related to Potential Radionuclide Transport in the UZ

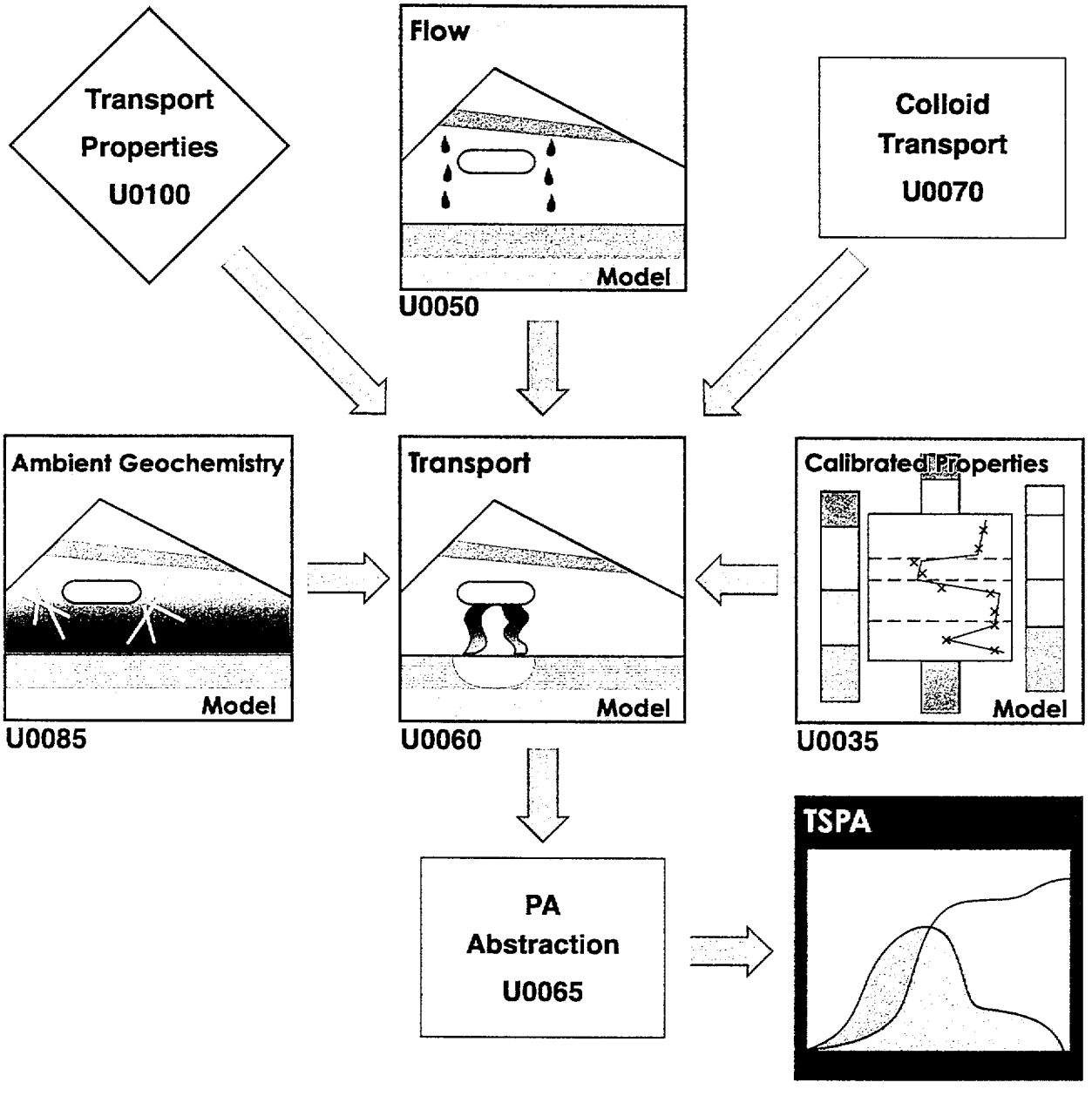

Figure 3.11-2. Relationships of Other Models and Data Feeds to the Transport Model

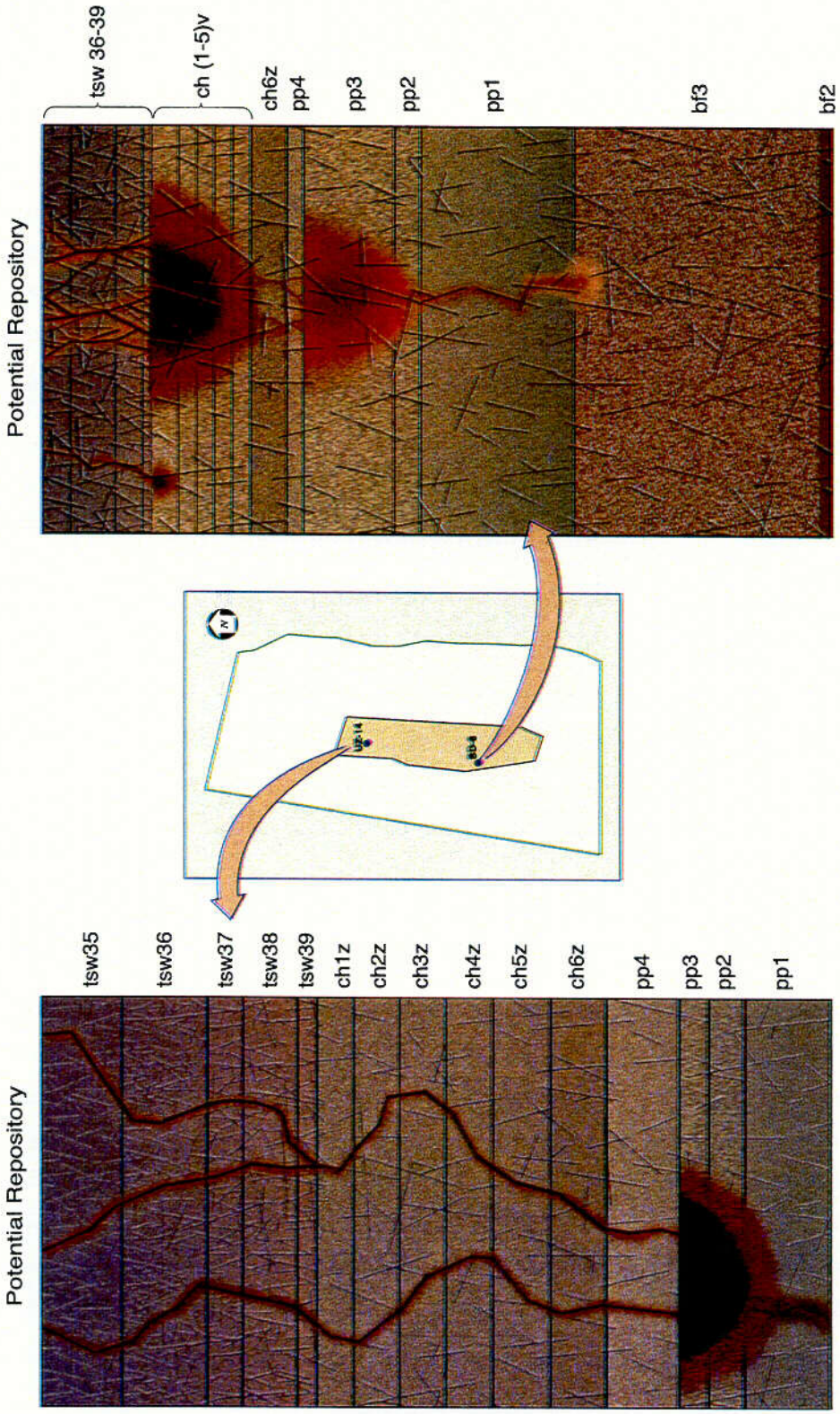

Figure 3.11-3. Schematic Illustration of Flow and Transport in the UZ Model Layers below the Potential Repository (Boreholes SD-6 and UZ-14)

c96

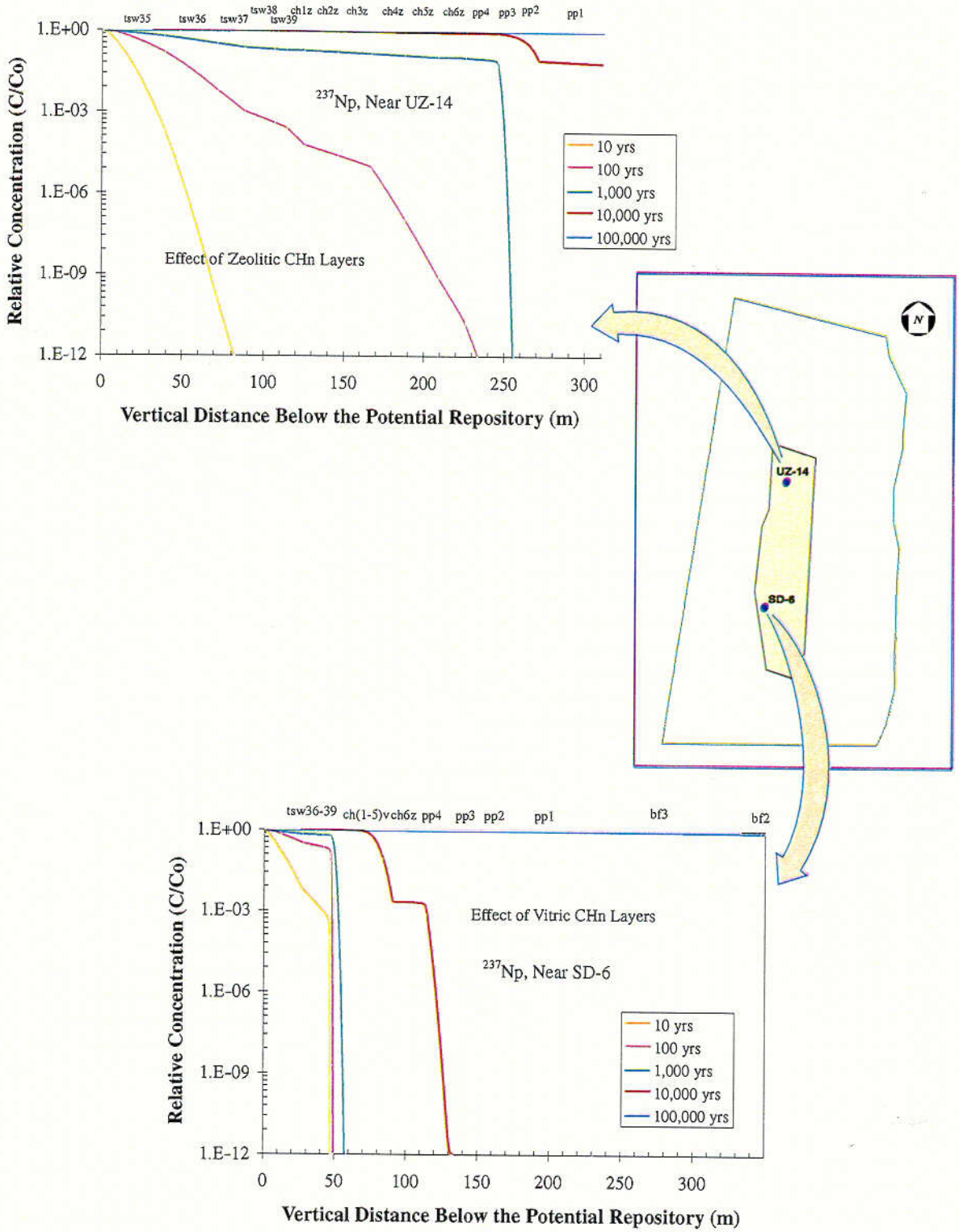

Figure 3.11-4. Concentration Profiles of ^{237}Np in 2-D Cross Sections of SD-6 and UZ-14 (Adapted from CRWMS M&O 2000, U0060, Figures V.2 and V.8)

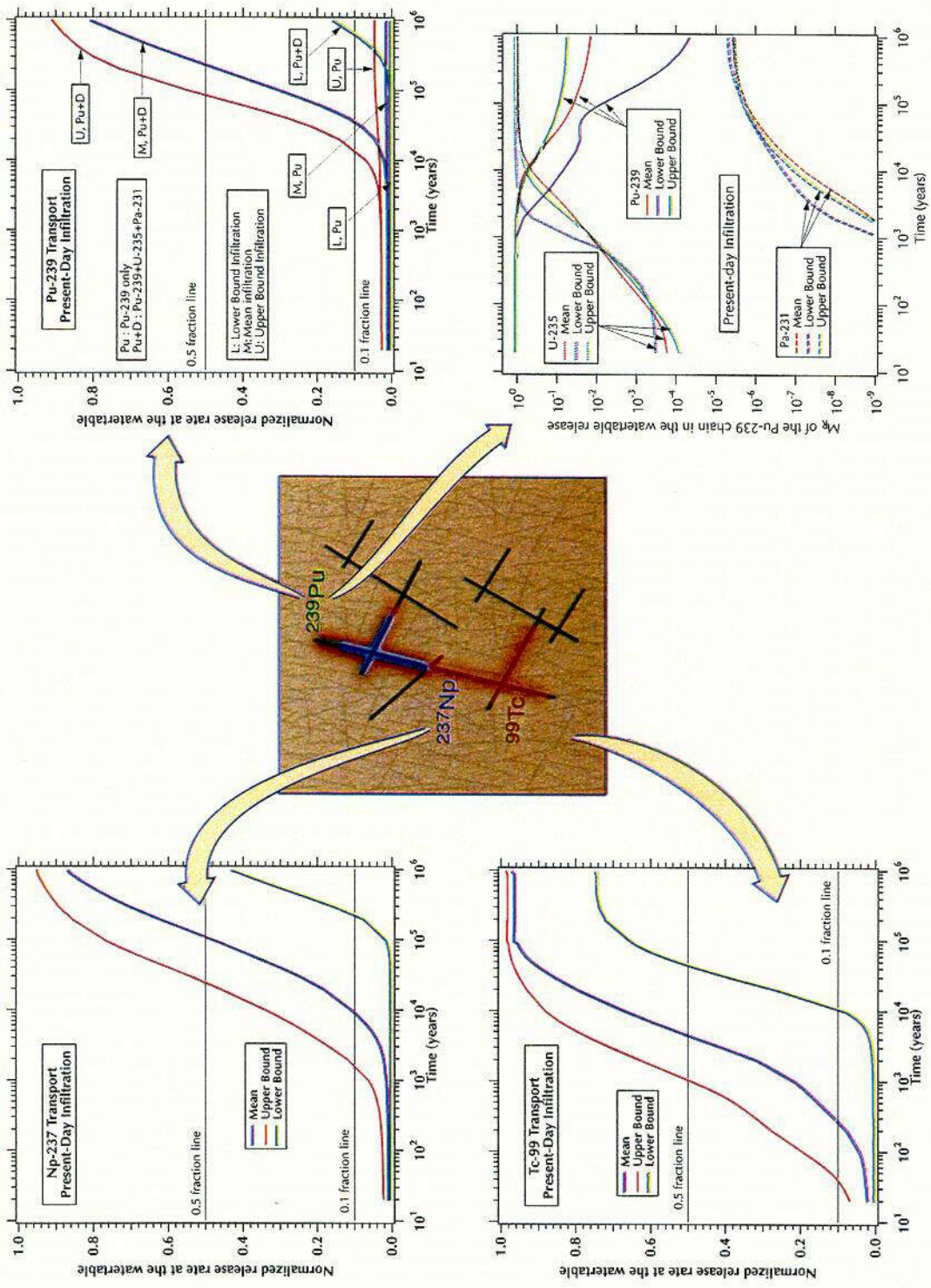

Figure 3.11-5. Concentration Profiles of ^{99}Tc, ^{237}Np, ^{239}Pu and its Daughters at the Water Table for Varying Present-day Climatic Scenarios (Adapted from CRWMS M&O 2000, U0060, Figures 6.12.1, 6.13.1, 6.14.1, and 6.14.2. The data shown in this figure are based on a model that is appropriately conservative for TSPA analysis and consequently should not be used to evaluate expected breakthrough curves of radionuclides at the water table.)

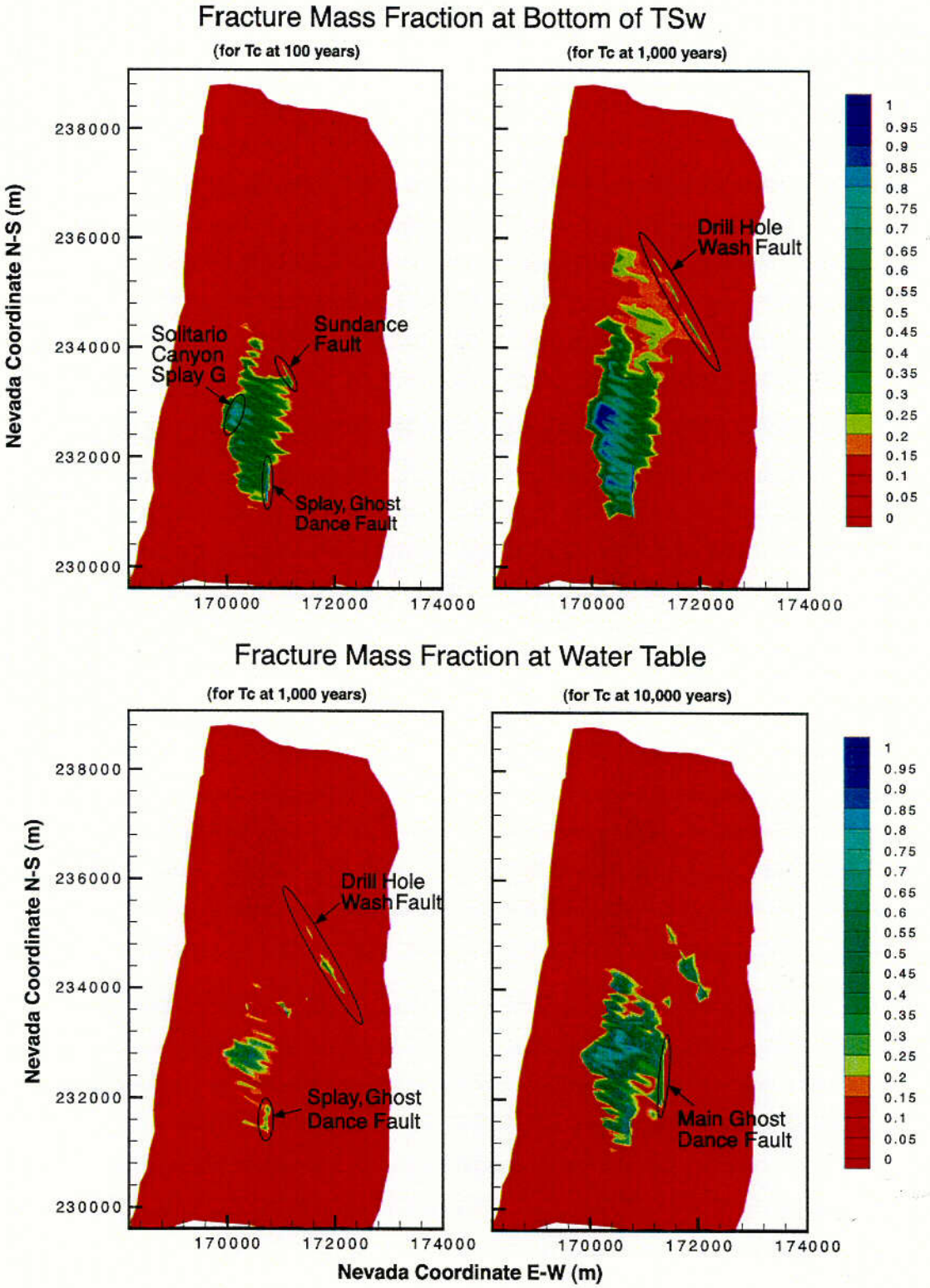

Figure 3.11-6. Normalized Mass Fraction Distribution of ^{99}Tc in the Fractures at the Bottom of the TSw and the Water Table (Adapted from CRWMS M&O 2000, U0060, Figures 6.12.2, 6.12.4, 6.12.12, and 6.12.14)

c99

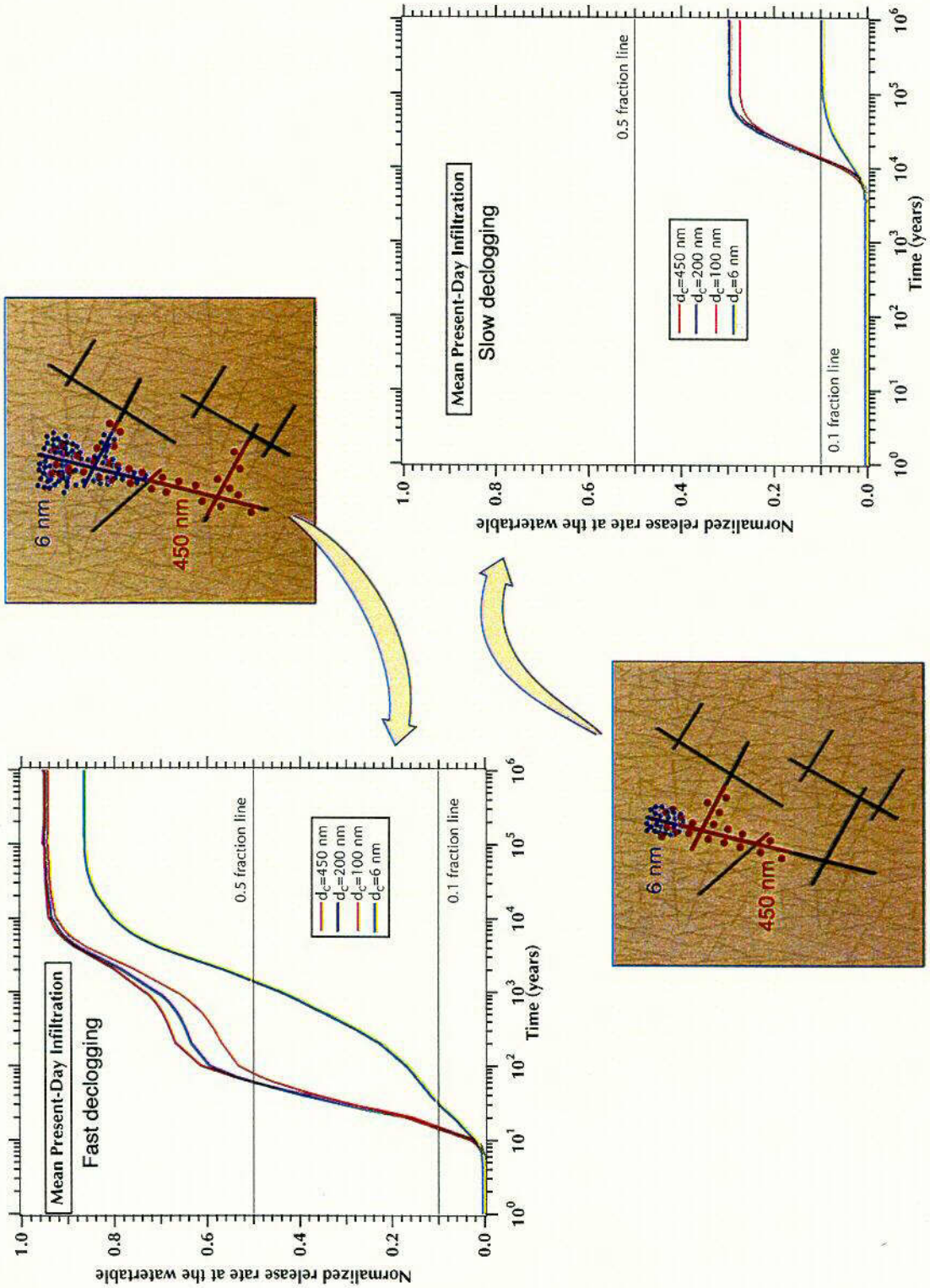

Figure 3.11-7. Influence of Colloid Size and Kinetic Model Parameters on Colloidal Transport (Adapted from CRWMS M&O 2000, U0060, Figures 6.16.1 and 6.16.2. The data shown in this figure are based on a model that is appropriately conservative for TSPA analysis and consequently should not be used to evaluate expected breakthrough curves of radionuclides at the water table.)

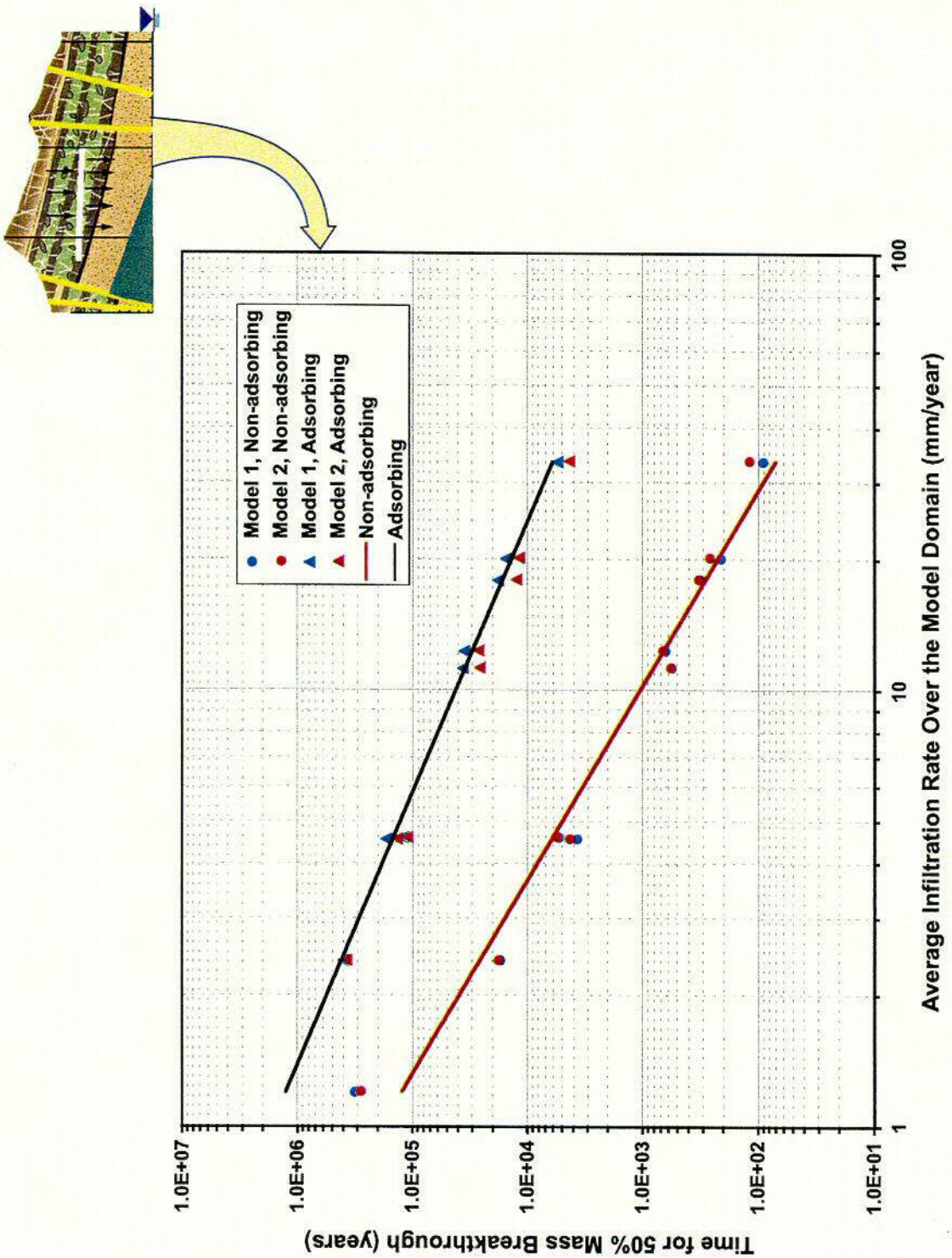

Figure 3.11-8. Correlations of Average Infiltration Rates and Tracer Transport Times at 50% Mass Breakthrough for 36 Simulation Scenarios (Data from CRWMS M&O, 2000, U0050, Section 6.7.3. The data shown in this figure are based on a model that is appropriately conservative for TSPA analysis and consequently should not be used to evaluate expected breakthrough curves of radionuclides at the water table.)

C101

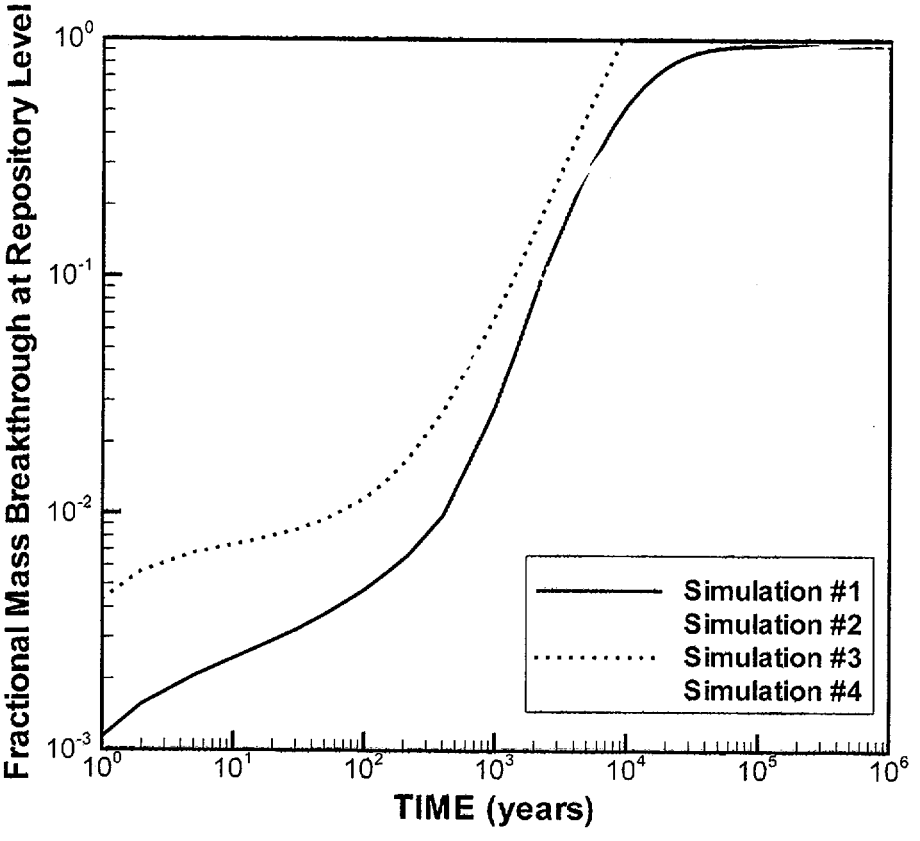

Figure 3.11-9. Simulated Breakthrough Curves of Cumulative Tracer (^{36}Cl) Mass Arriving at the Repository Level, Since Release from the Ground Surface, Using the Present-Day, Mean Infiltration and Four Simulation Scenarios (Data from CRWMS M&O, 2000, U0050, Section 6.7.3. The data shown in this figure are based on a model that is appropriately conservative for TSPA analysis and consequently should not be used to evaluate expected breakthrough curves of radionuclides at the water table.)

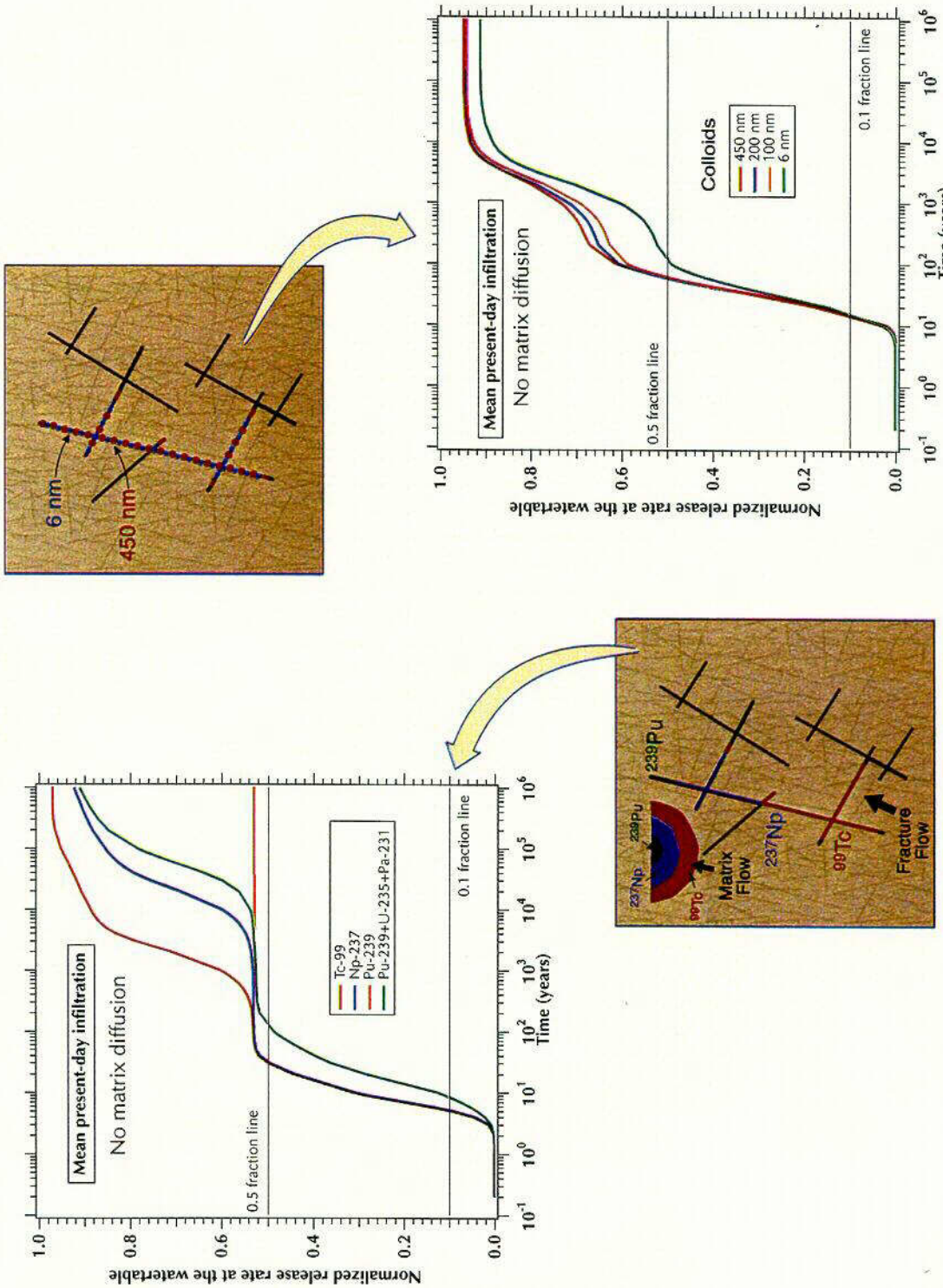

Figure 3.11-10. Effects of No Matrix Diffusion: Concentration of Radionuclides and Colloids at the Water Table for the No-diffusion Alternative Model (Adapted from CRWMS M&O 2000, U0060, Figures 6.17.1 and 6.17.2. The data shown in this figure are based on a model that is appropriately conservative for TSPA analysis and consequently should not be used to evaluate expected breakthrough curves of radionuclides at the water table.)

C102

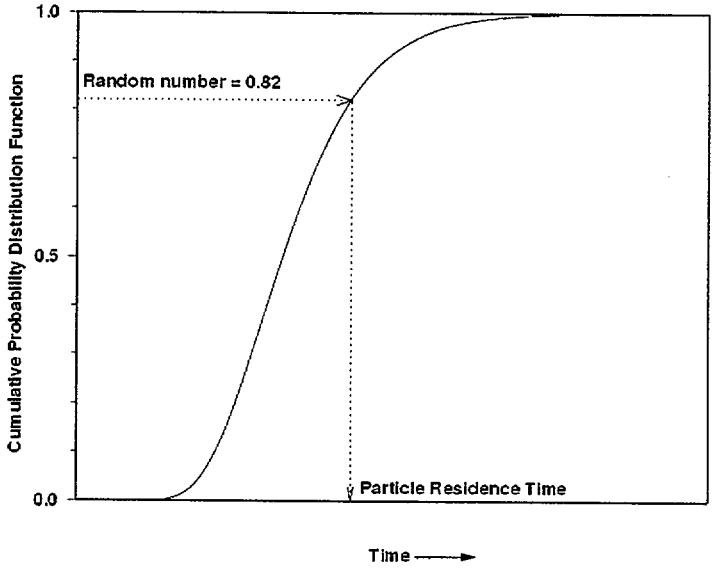

Figure 3.11-11. Schematic of the RTTF Technique for Determining Particle Residence Time in a Cell (CRWMS M&O 2000, U0065, Figure 2)

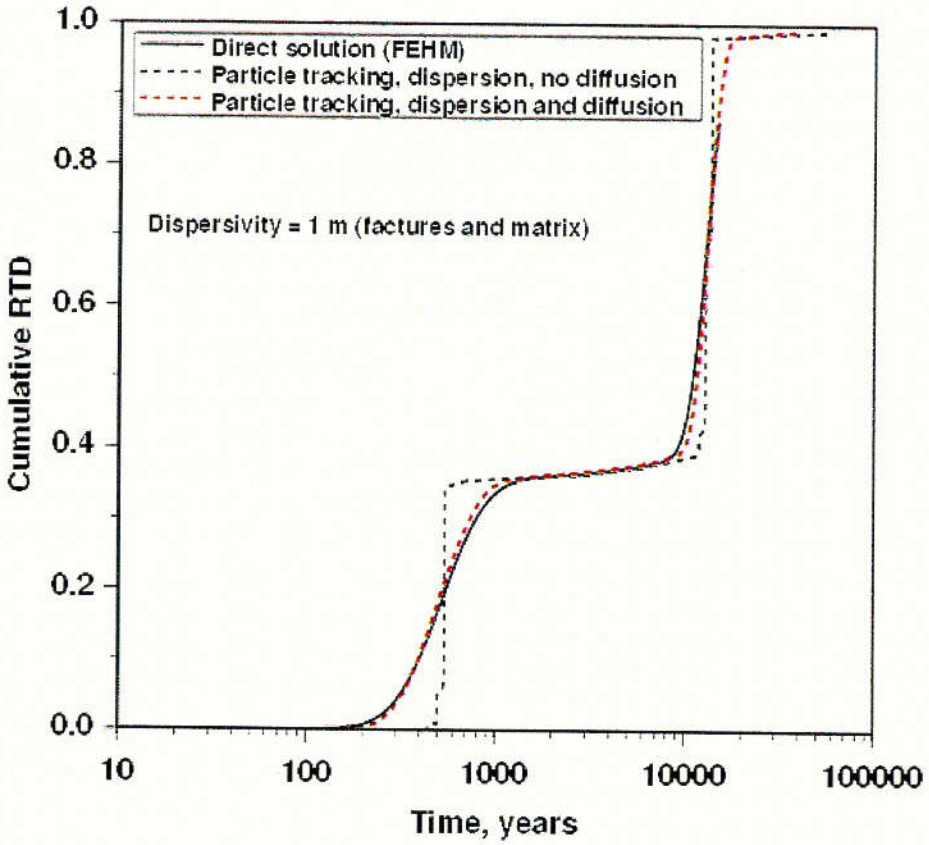

Figure 3.11-12. Comparison of the Particle-Tracking Solution and a Direct Finite-element Solution to the Transport (FEHM V2.10) for a 1-D, Dual-permeability Model (CRWMS M&O 2000, U0065, Figure 9. The data shown in this figure are based on a model that is appropriately conservative for TSPA analysis and consequently should not be used to evaluate expected breakthrough curves of radionuclides at the water table.)

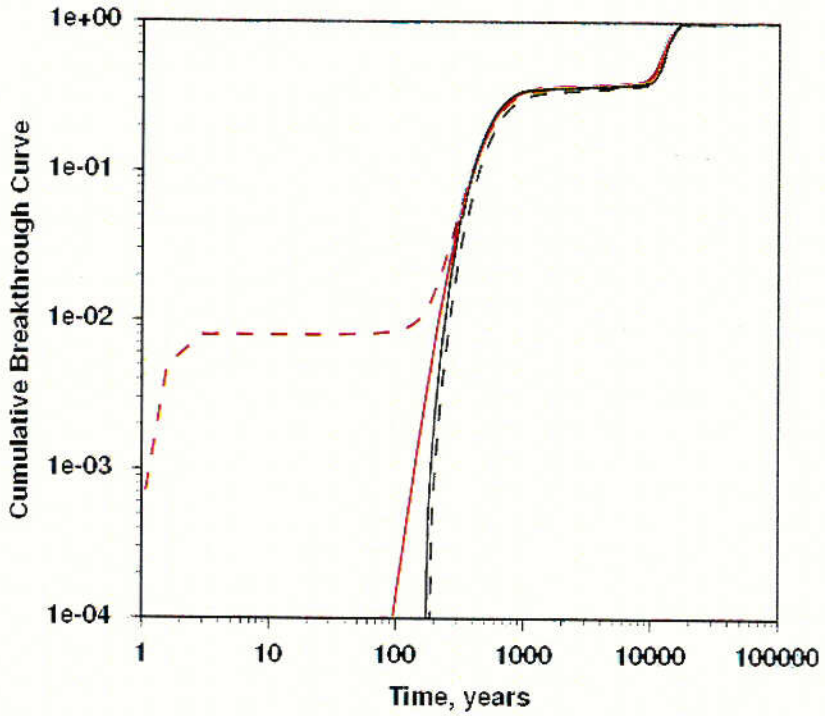

Figure 3.11-13. Comparison of the Particle-Tracking Solution and a Direct Finite-element Solution to the Transport for a 1-D, Dual-permeability Model. Red curves: finite element solution, black curves: particle tracking (solid - no diffusion, dashed - diffusion) (CRWMS M&O 2000, U0065, Figure 10. The data shown in this figure are based on a model that is appropriately conservative for TSPA analysis and consequently should not be used to evaluate expected breakthrough curves of radionuclides at the water table.)

C 104

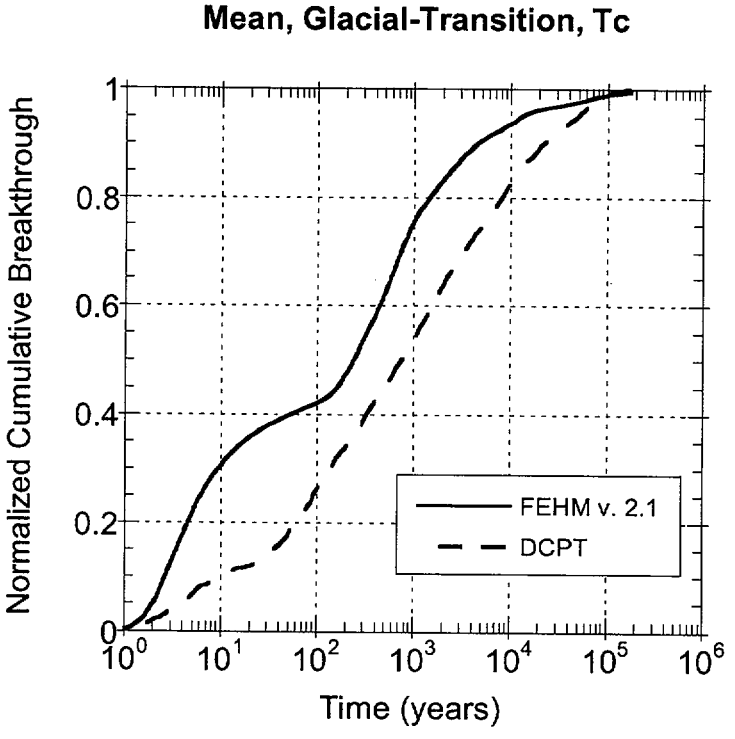

Figure 3.11-14. Comparison of Cumulative Normalized Breakthrough Curves at the Water Table Using FEHM V2.10 and DCPT V1.0 software with the Nonsorbing Tc for Mean-Infiltration, Glacial-Transition Climate (CRWMS M&O 2000, U0160, Figure 11. The data shown in this figure are based on a model that is appropriately conservative for TSPA analysis and consequently should not be used to evaluate expected breakthrough curves of radionuclides at the water table.)

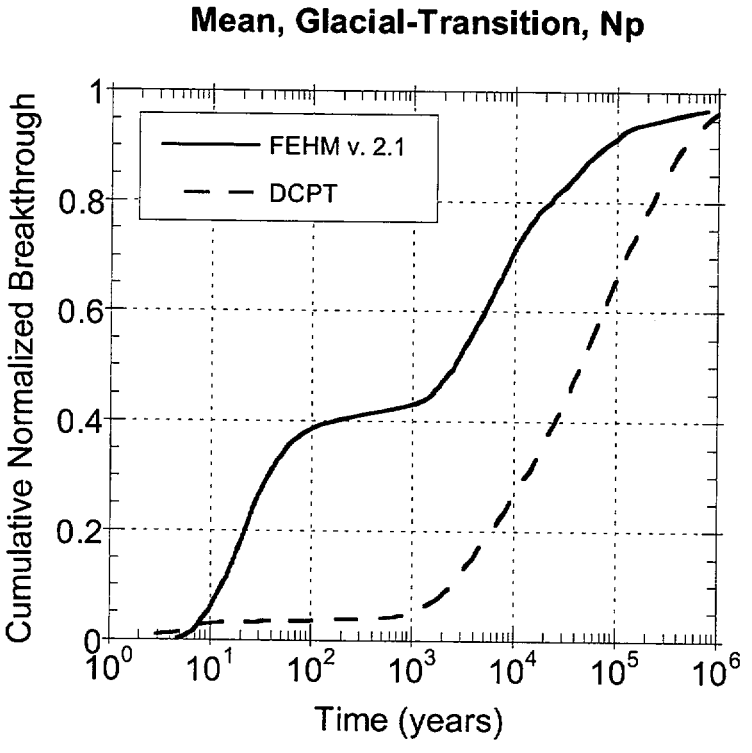

Figure 3.11-15. Comparison of Cumulative Normalized Breakthrough Curves at the Water Table Using FEHM V2.10 and DCPT V1.0 software with the Sorbing Np for Mean-Infiltration, Glacial-Transition Climate (CRWMS M&O 2000, U0160, Figure 11. The data shown in this figure are based on a model that is appropriately conservative for TSPA analysis and consequently should not be used to evaluate expected breakthrough curves of radionuclides at the water table.)

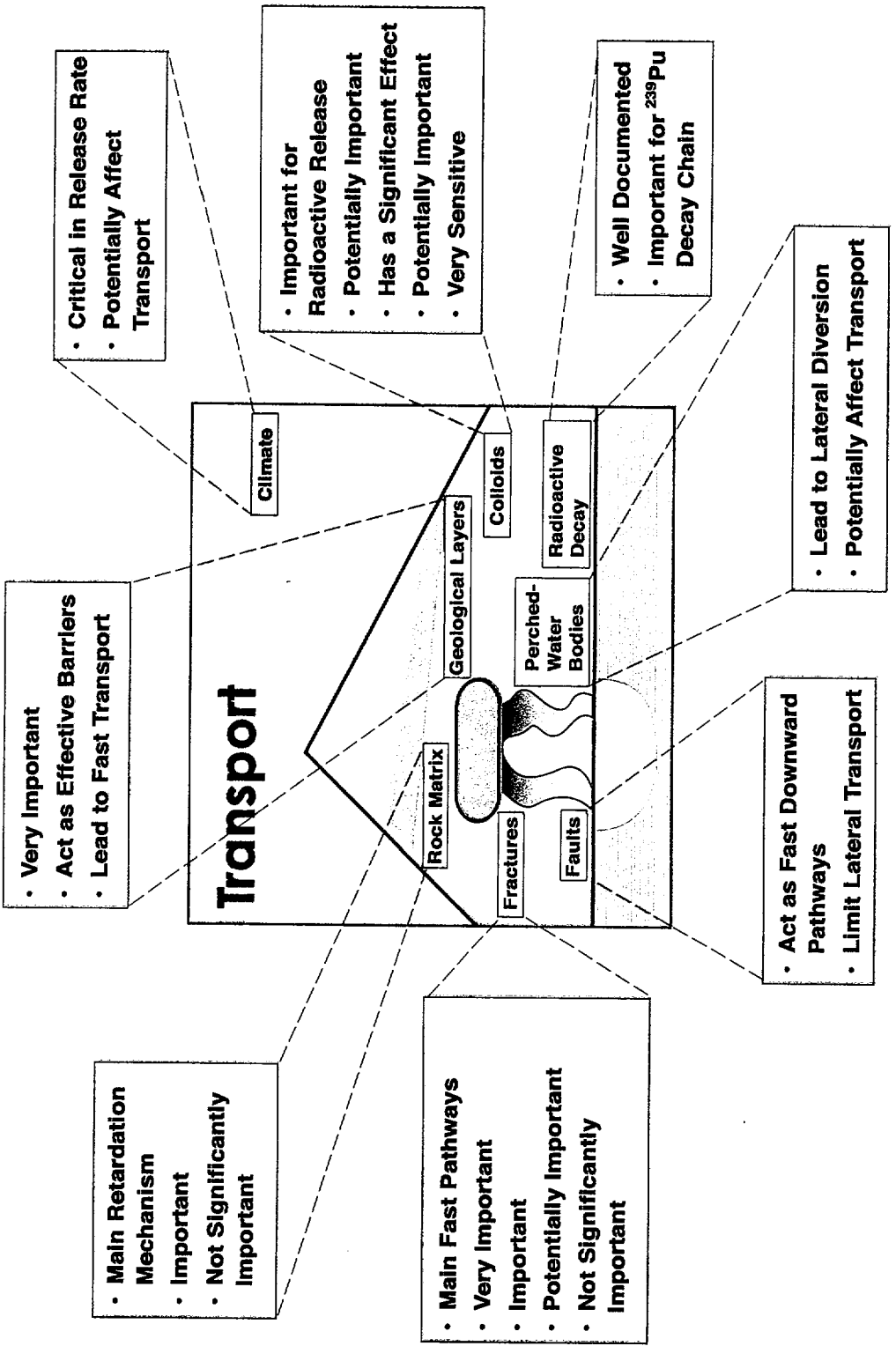

Figure 3.11-16. Results Related to Radionuclide Transport in the UZ

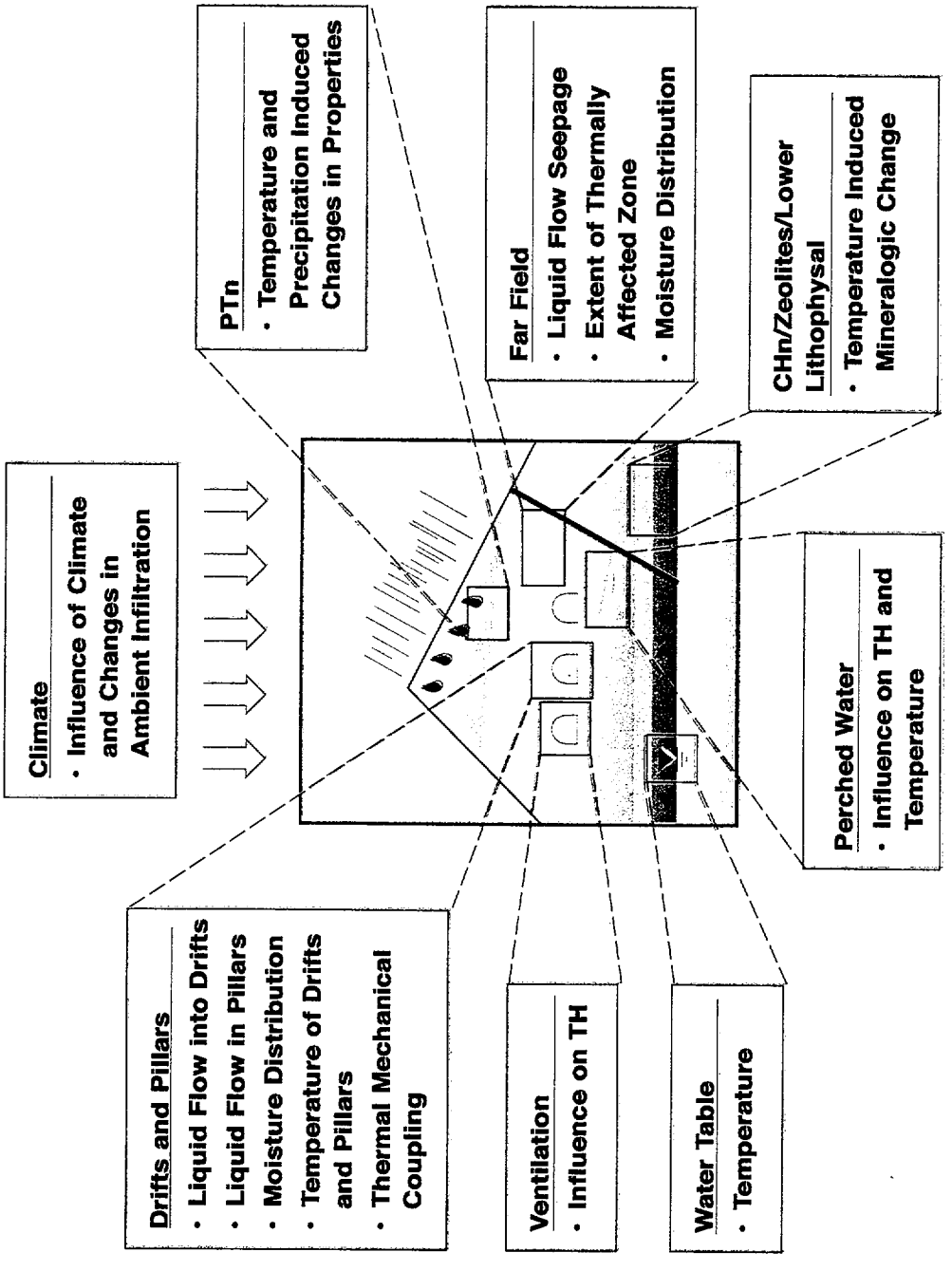

Figure 3.12-1. Schematic of the TH Modeling Issues

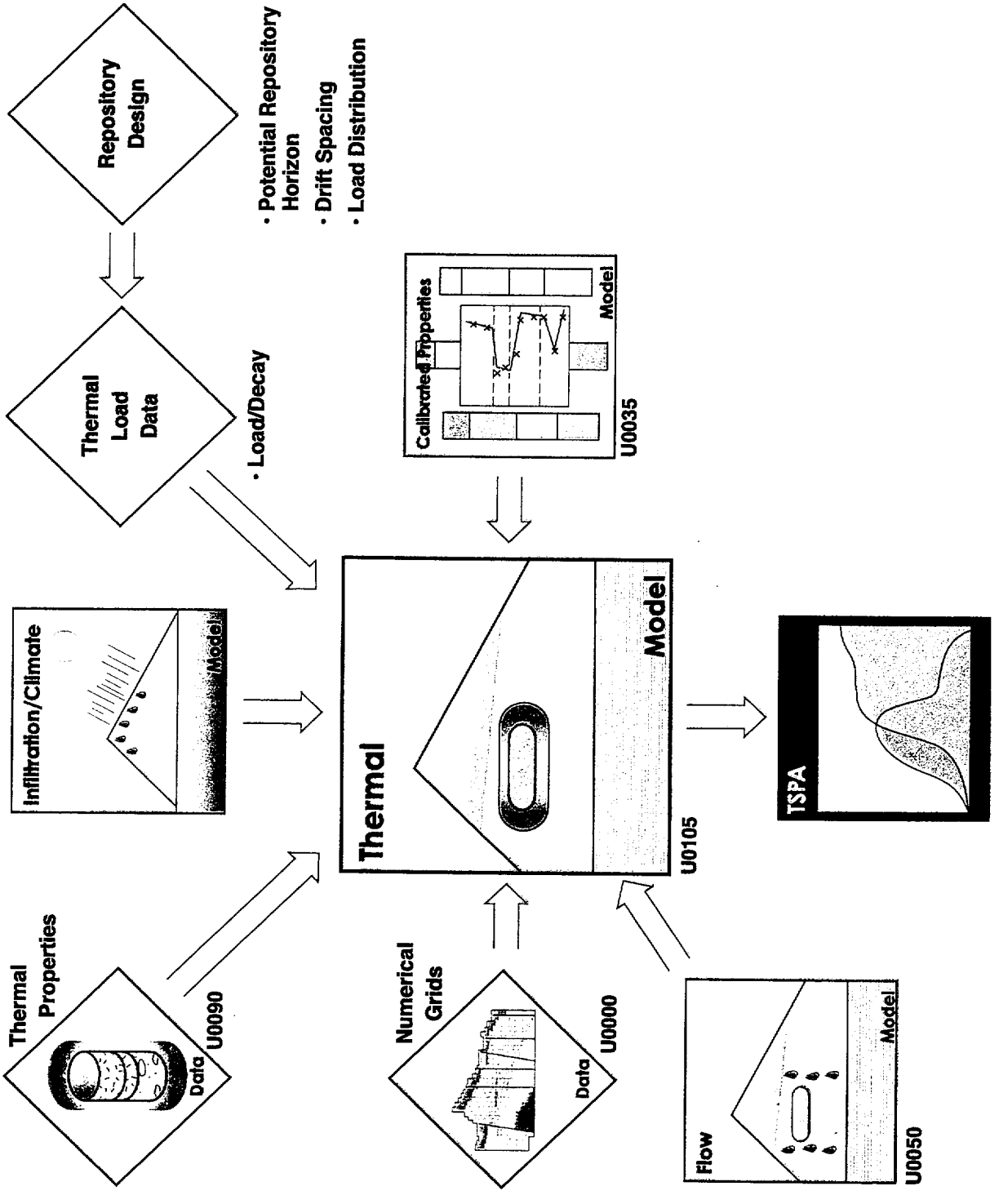

Figure 3.12-2. Schematic Showing Input Data and the UZ Models that Support the Development of the TH Model

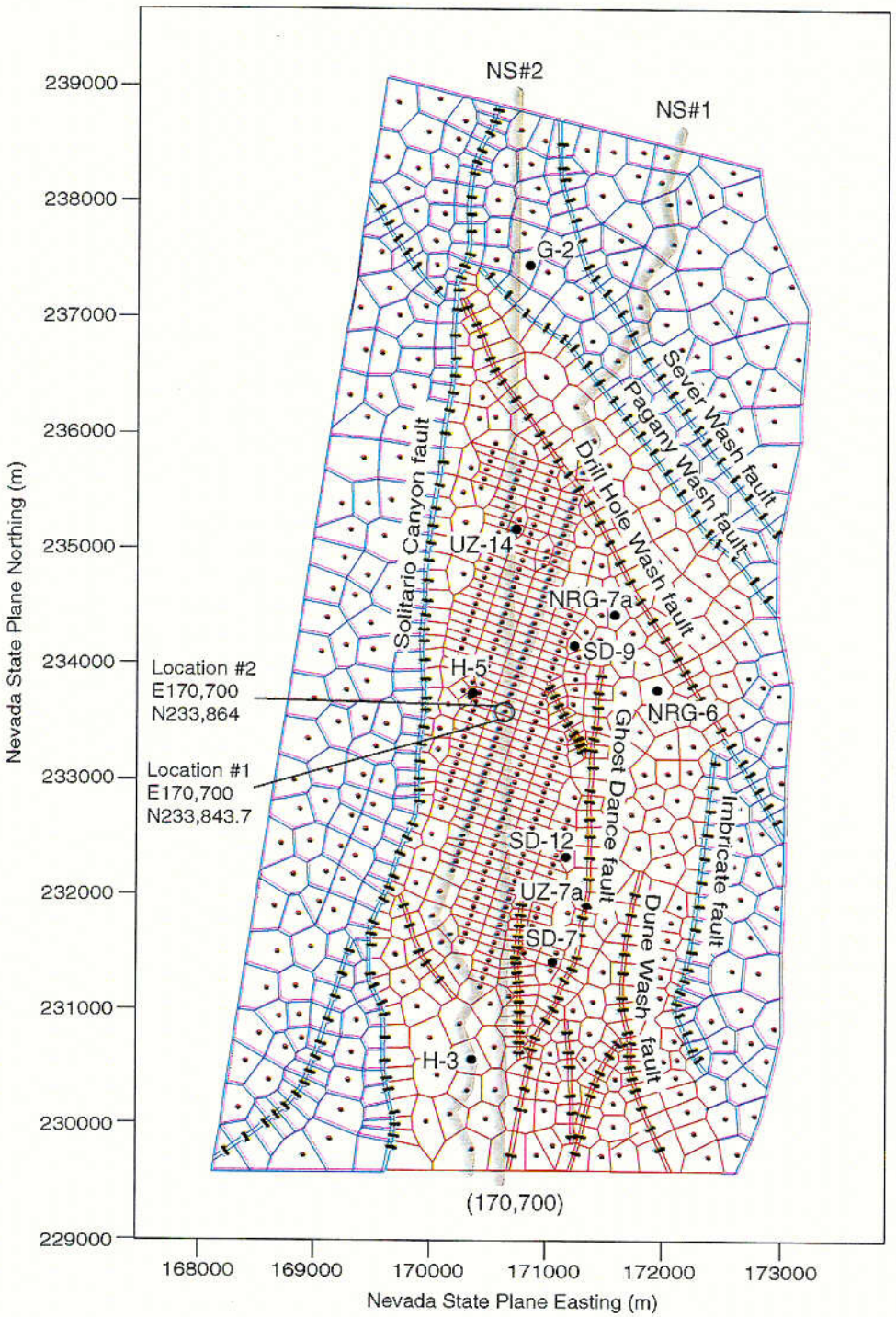

Figure 3.12-3. Plan View of the UZ TSPA Grid, Showing the Location of the Potential Repository Submodel Domain (in Red) and the Cross Sections, NS#1 and NS#2. Locations #1 and #2 are Used for Detail Plots. Large solid circles refer to boreholes; small circles refer to centers of grid columns (adapted from CRWMS M&O 2000, U0105, Figure 1).

C105

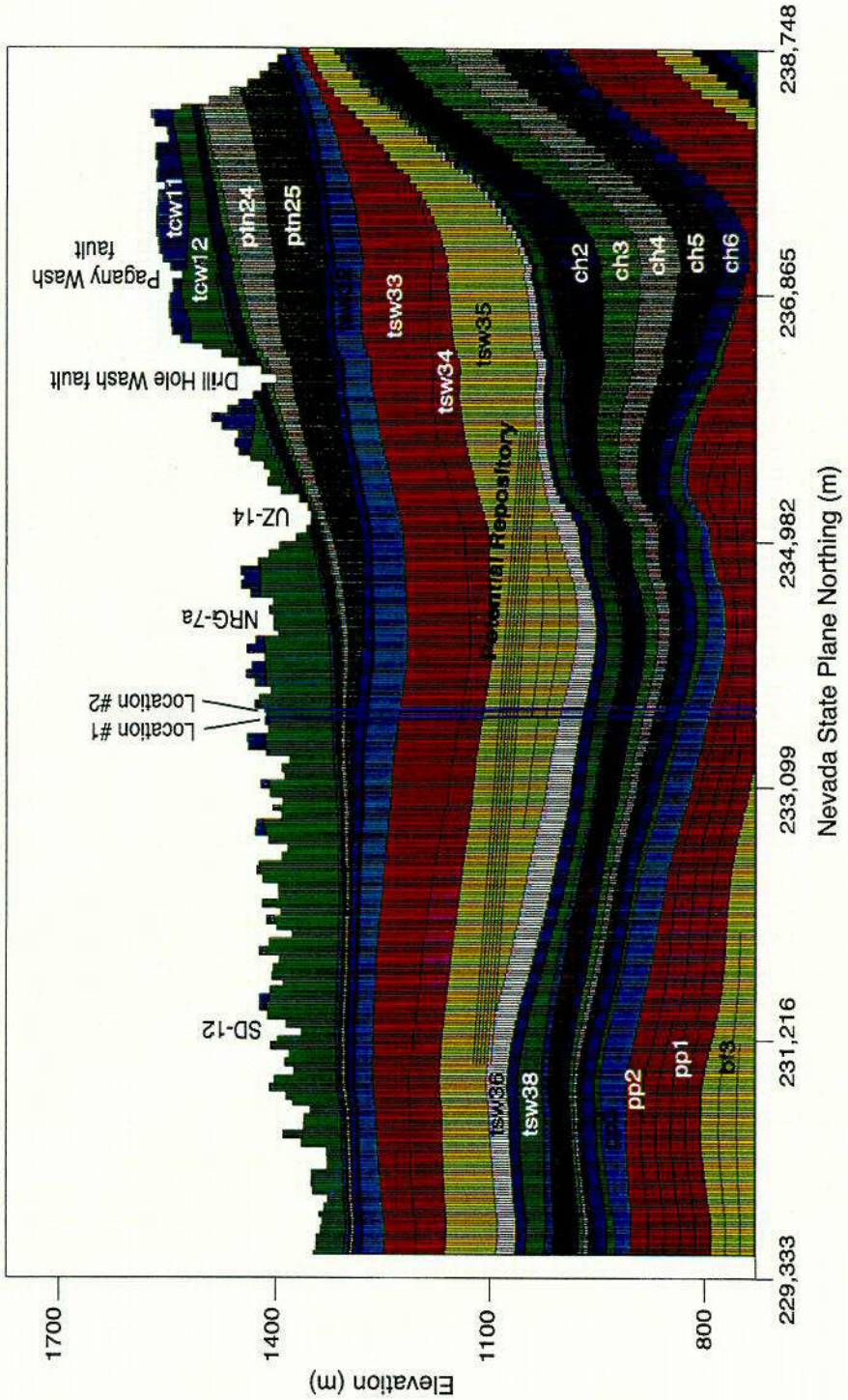

Figure 3.12-4. Lateral and Vertical Discretization at the NS#2 Cross-Section Based on the Refined Numerical Grid. Plot shows location of the potential repository and the hydrogeologic units layering (adapted from CRWMS M&O 2000, U0105, Figure 3).

C106

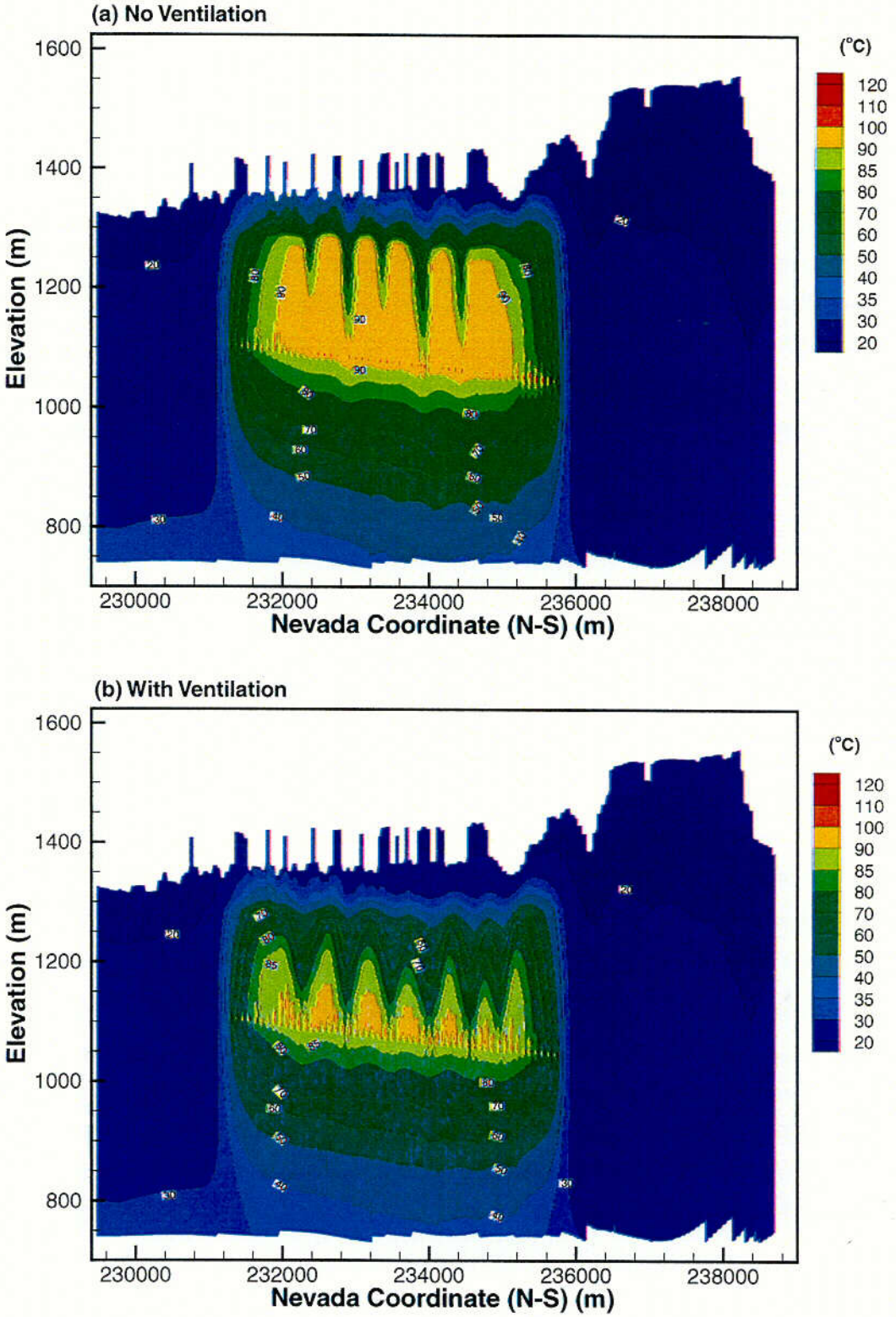

Figure 3.12-5. Temperature Distribution along NS#2 Cross-Section Grid at 1,000 Years (a) No Ventilation, (b) with Ventilation (Adapted from CRWMS M&O 2000, U0105, Figures 45 and 59).

C107

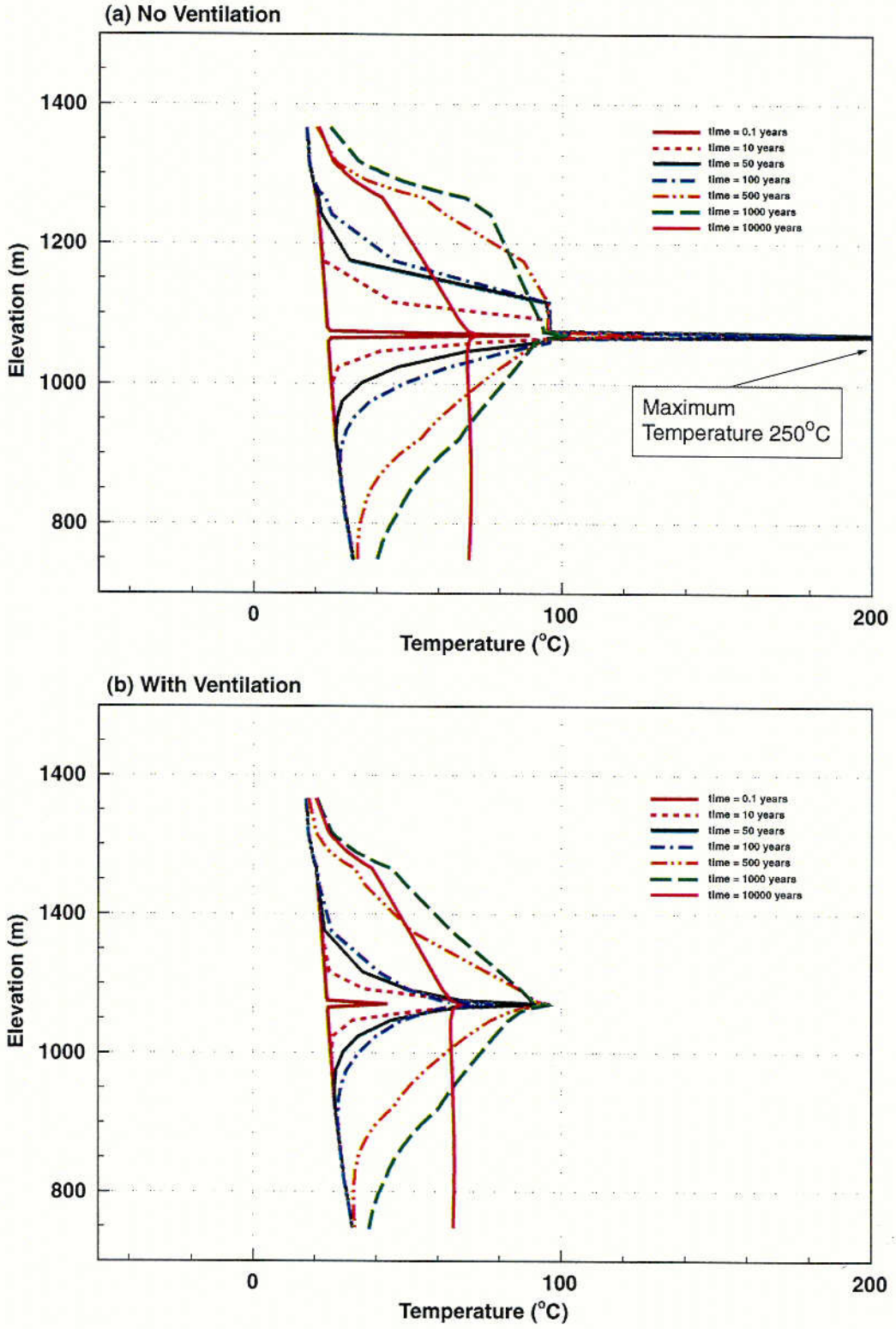

Figure 3.12-6. Temperature at Location #1, NS#2 Cross-Section Grid (a) No Ventilation (b) with Ventilation (Adapted from CRWMS M&O 2000, U0105, Figures 46 and 60).

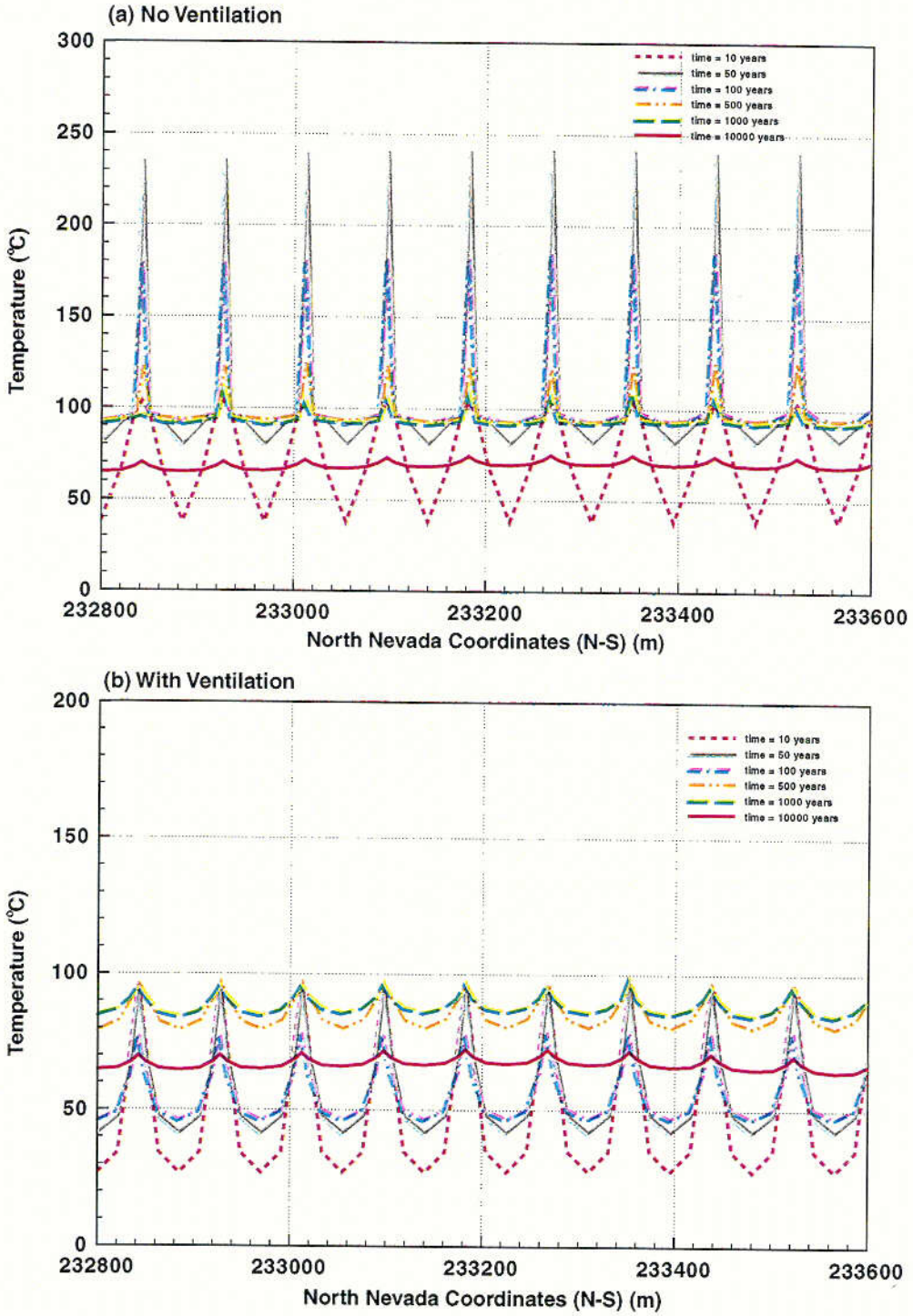

Figure 3.12-7. Temperature along a Section of the Potential Repository Horizon of the NS#2 Cross-Section Grid (a) No Ventilation, (b) with Ventilation (Adapted from CRWMS M&O 2000, U0105, Figures 48 and 62).

C109

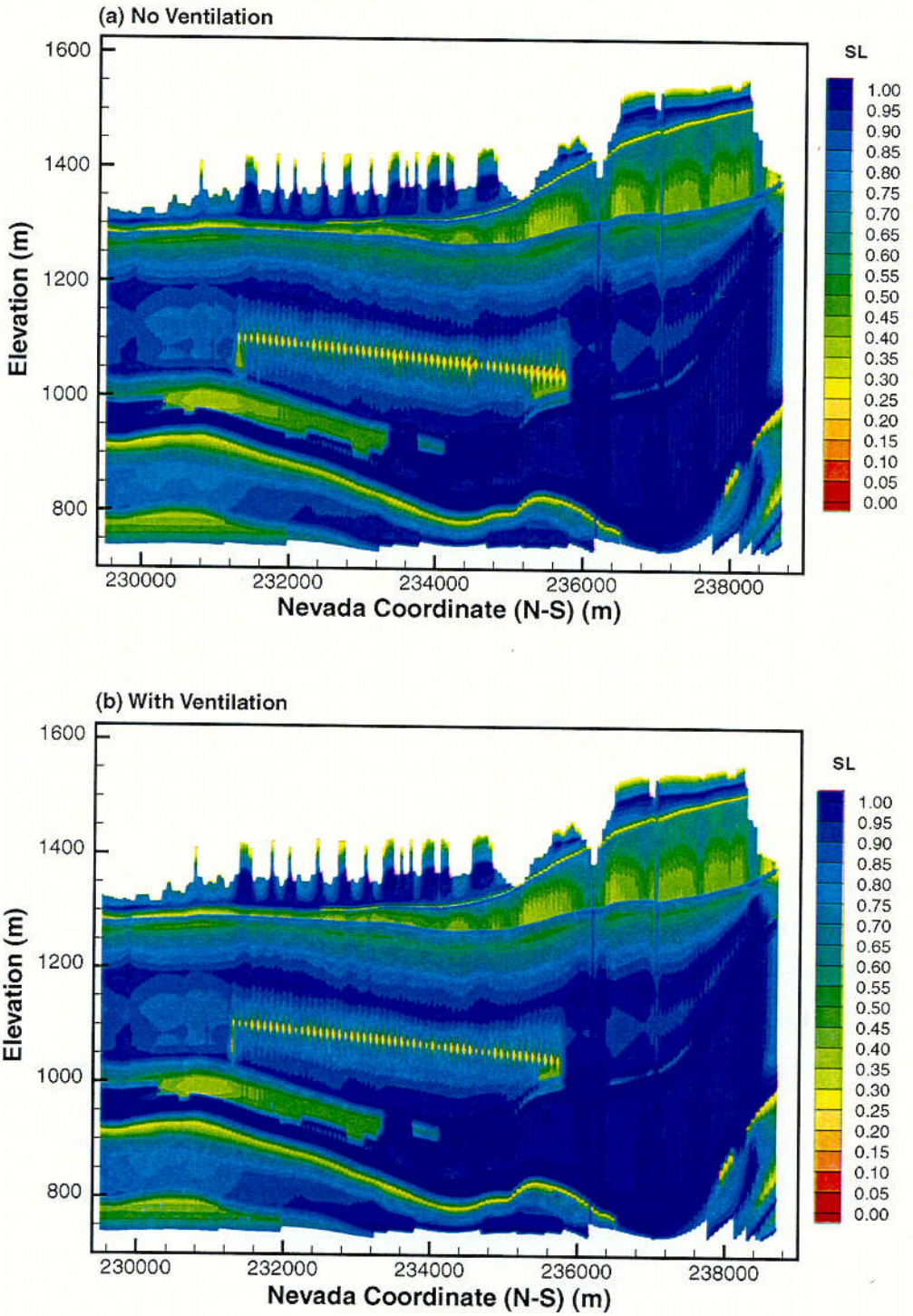

Figure 3.12-8. Matrix Liquid Saturation (Sl) along NS#2 Cross-Section Grid at 1,000 Years (a) No Ventilation, (b) with Ventilation (Adapted from CRWMS M&O 2000, U0105, Figures 50 and 64).

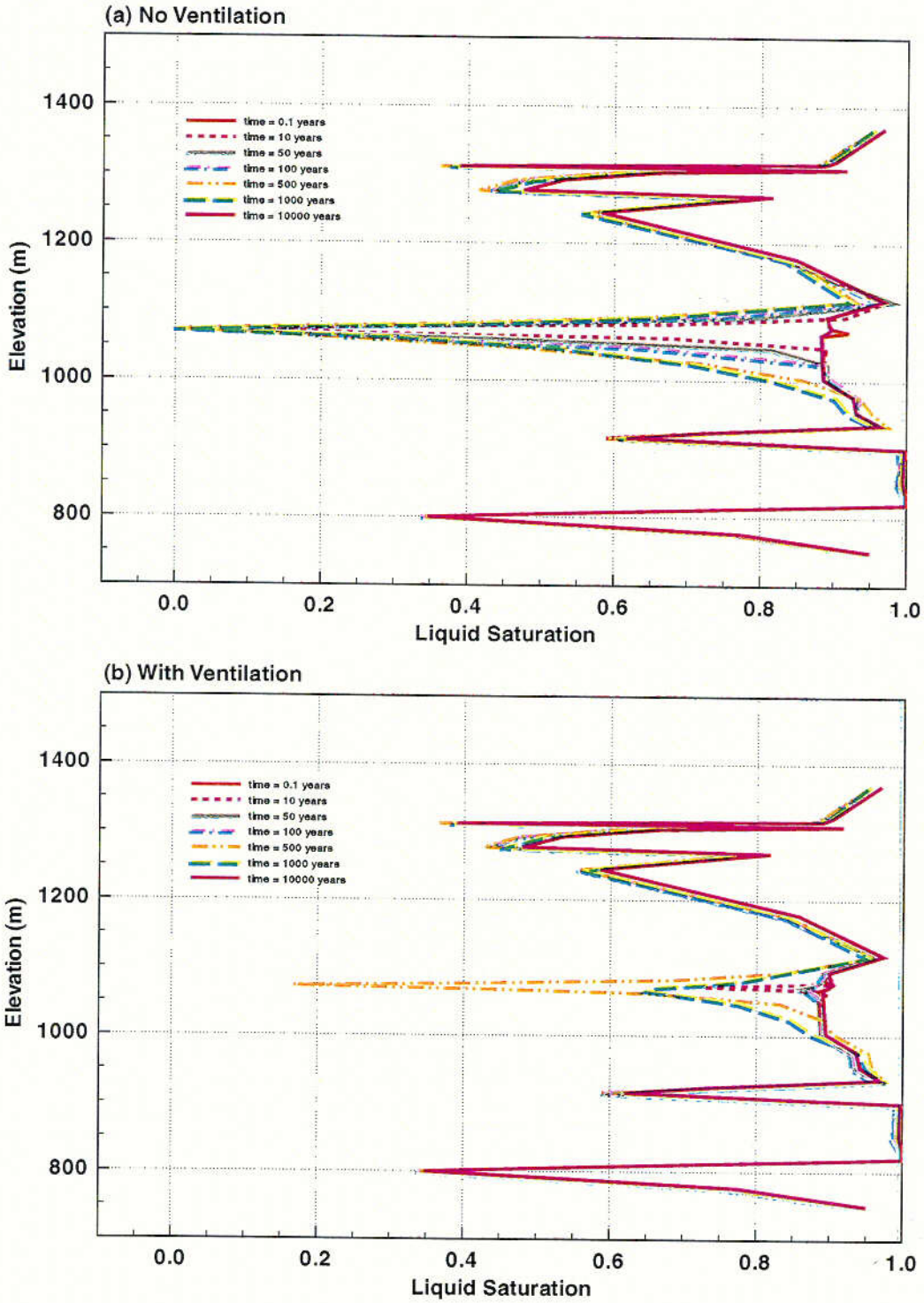

Figure 3.12-9. Matrix Liquid Saturation at Location#1, NS#2 Cross-Section Grid (a) No Ventilation, (b) with Ventilation (Adapted from CRWMS M&O 2000, U0105, Figures 51 and 65).

C111

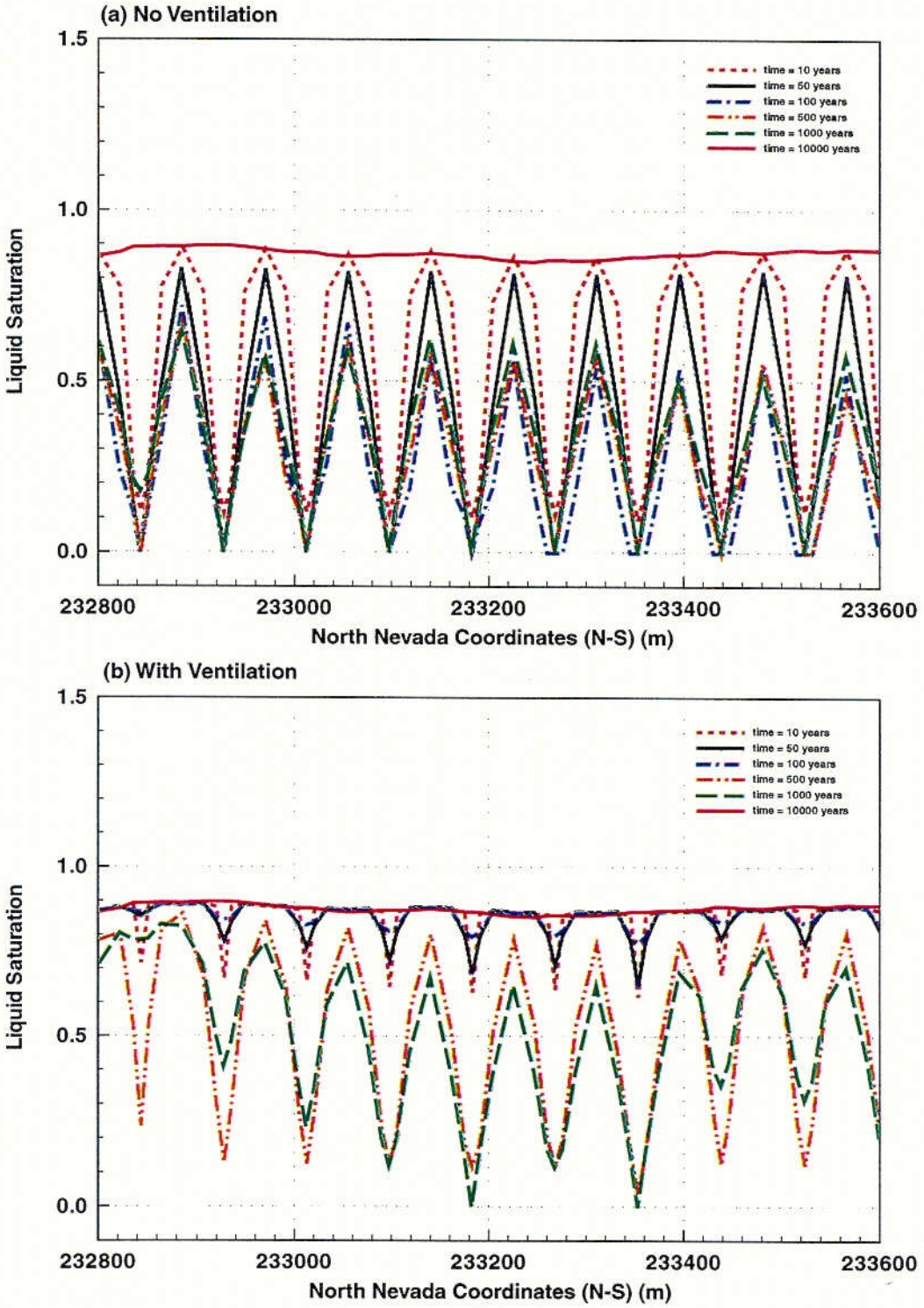

Figure 3.12-10. Matrix Liquid Saturation along a Section of the Potential Repository Horizon, NS#2 Cross-Section Grid (a) No Ventilation, (b) with Ventilation (Adapted from CRWMS M&O 2000, U0105, Figures 52 and 66).

C112

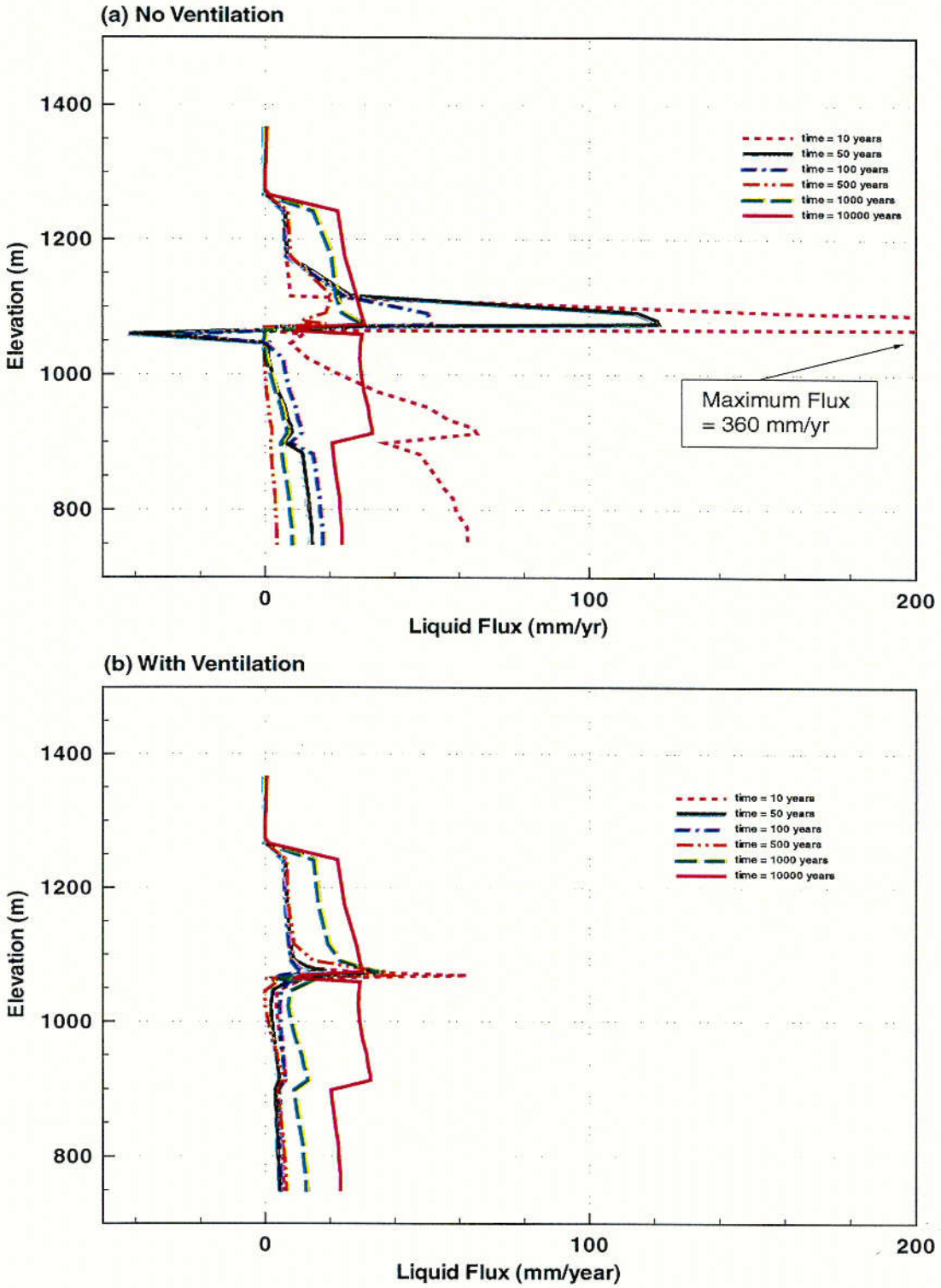

Figure 3.12-11. Fracture Liquid Flux at Location #1,NS#2 Cross-Section Grid (a) No Ventilation, (b) With Ventilation (Adapted from CRWMS M&O 2000, U0105, Figures 53 and 67).

C113

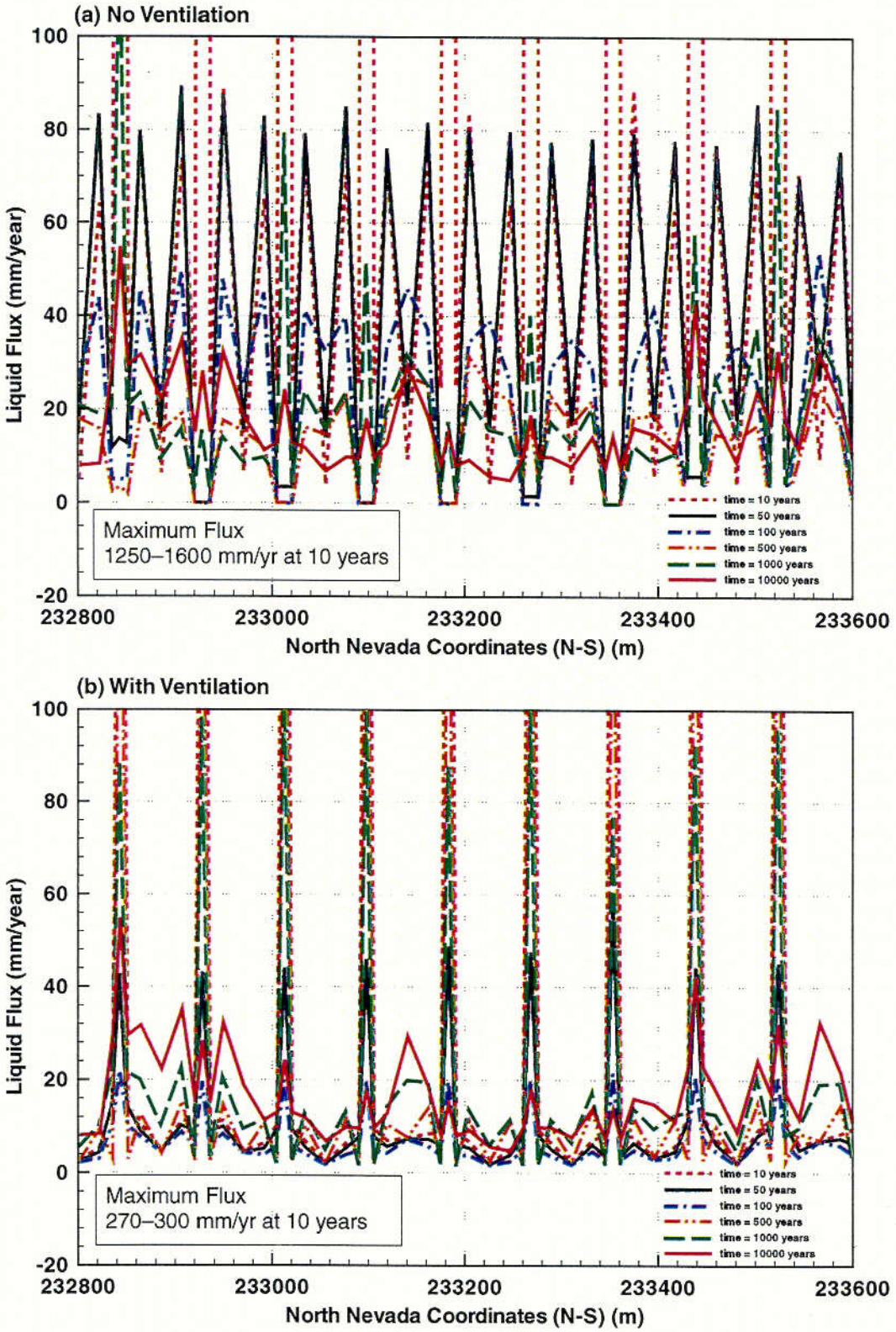

Figure 3.12-12. Fracture Liquid Flux along a Section of the Potential Repository Horizon, NS#2 Cross-Section Grid (a) No Ventilation, (b) with Ventilation (Adapted from CRWMS M&O 2000, U0105, Figures 55 and 69).

C114

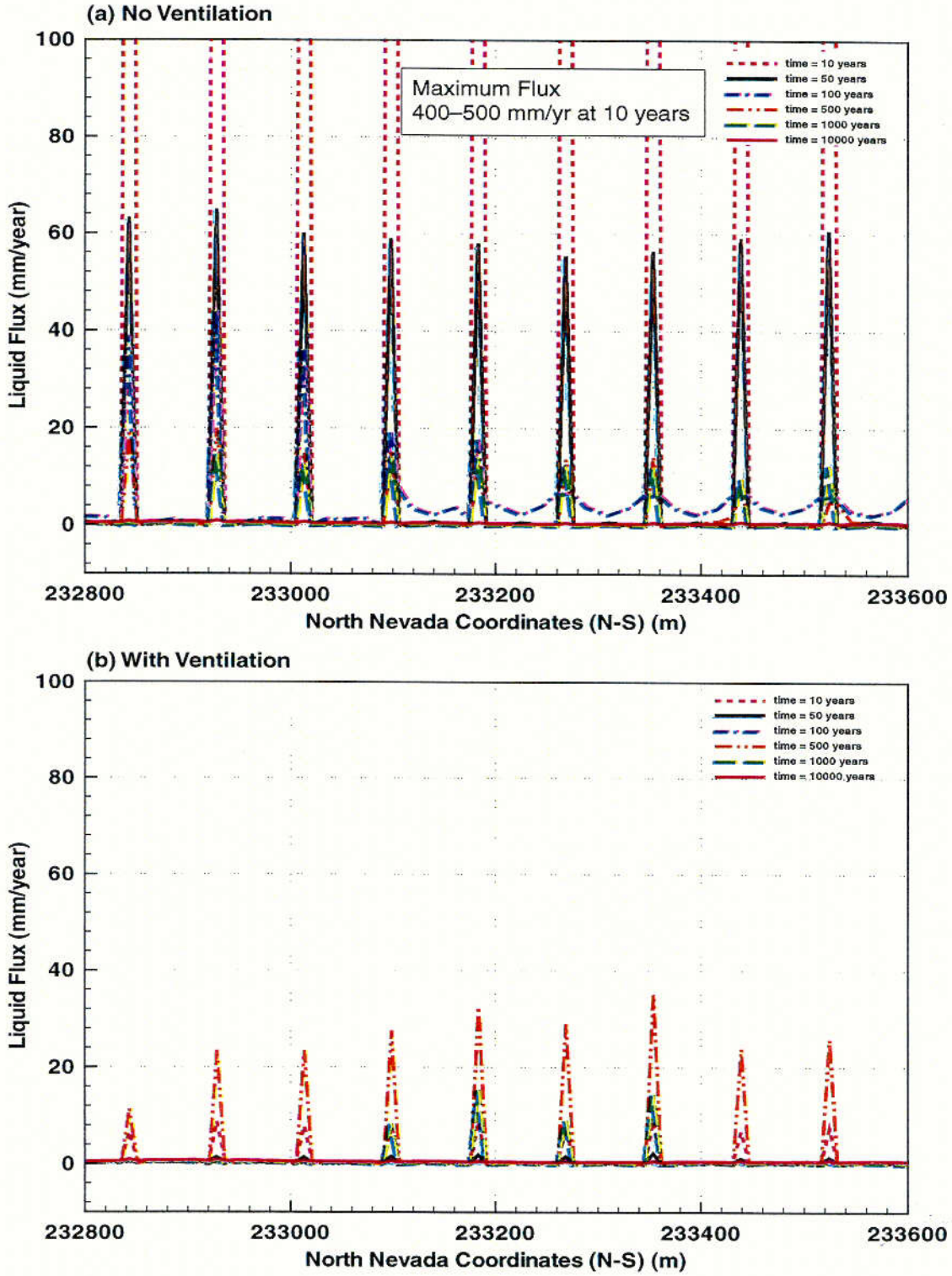

Figure 3.12-13. Matrix Liquid Flux along a Section of the Potential Repository Horizon, NS#2 Cross-Section Grid (a) No Ventilation, (b) with Ventilation (Adapted from CRWMS M&O 2000, U0105, Figures 56 and 70).

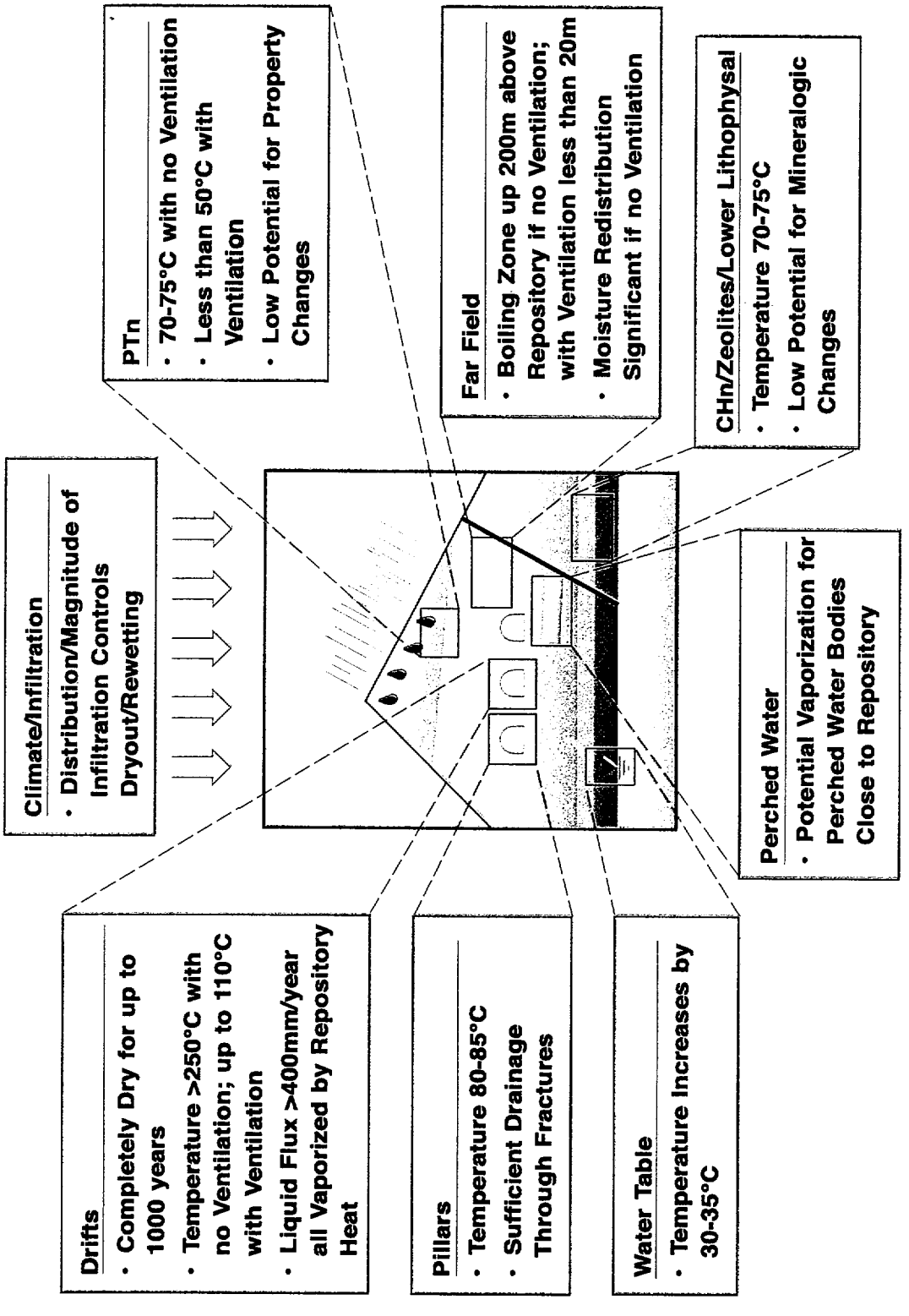

Figure 3.12-14. Summary of TH Model Results

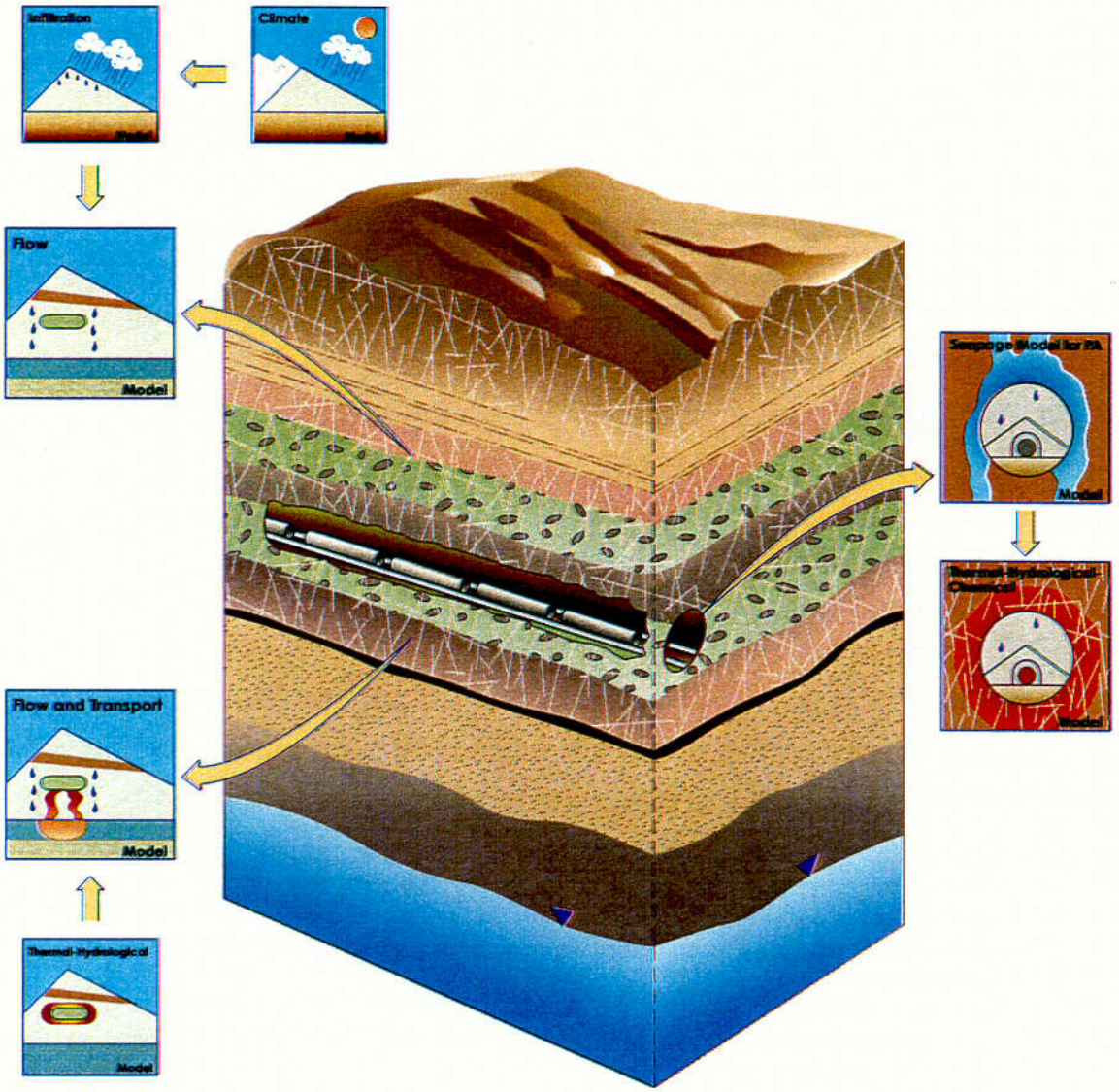

Figure 5.1-1. Conceptual Sketch of the UZ with Icons Representing Major Model Components

C1/6

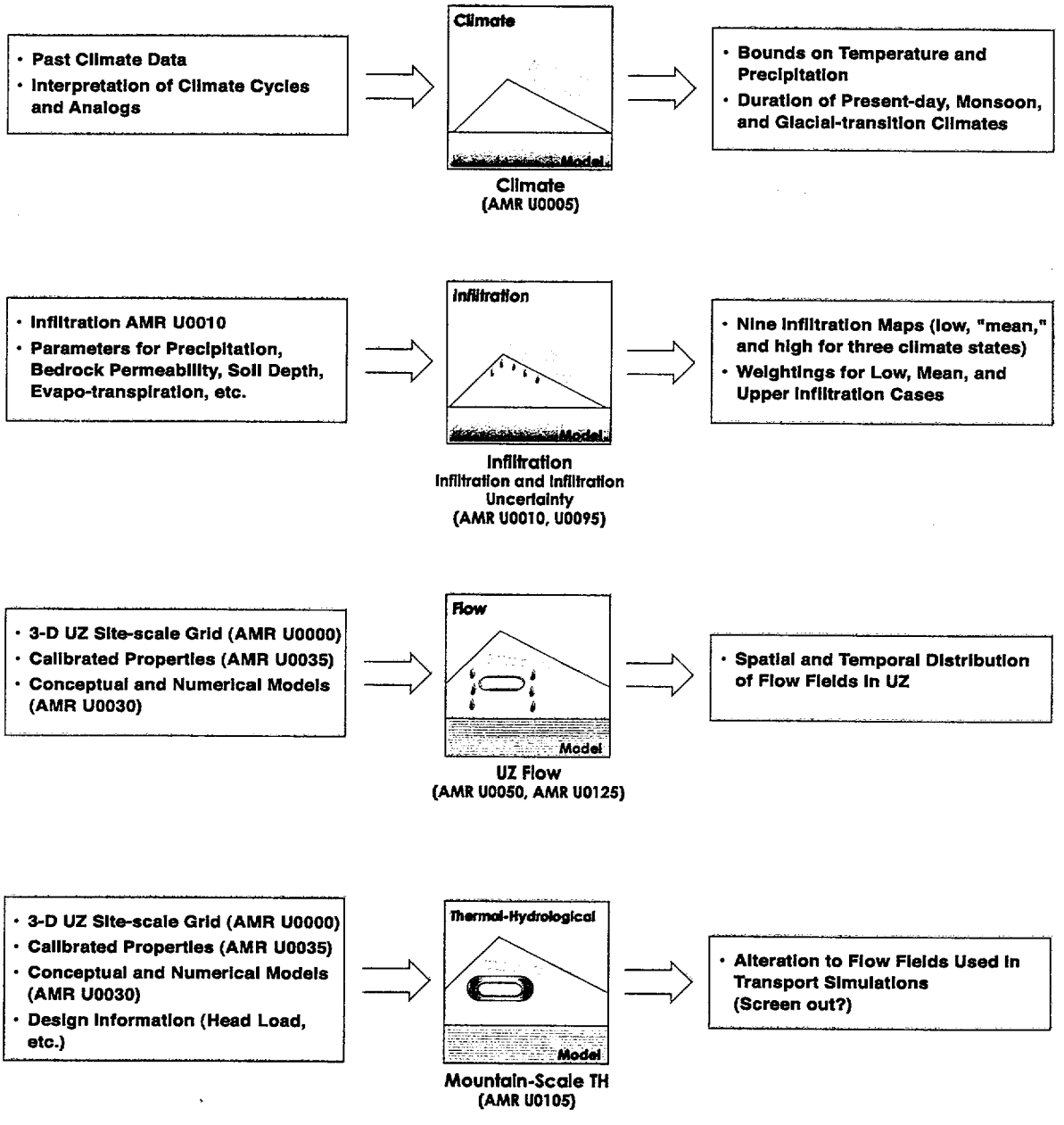

Figure 5.1-2. Schematic of Major Inputs and Outputs for UZ Flow Model and its Submodels

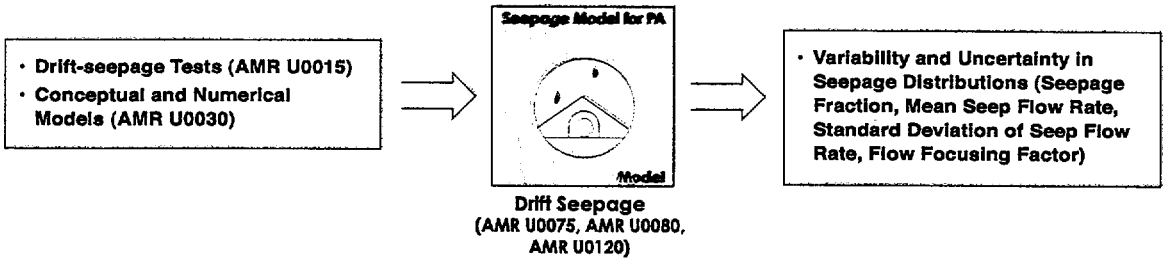

Figure 5.1-3. Schematic of Major Inputs and Outputs of the Drift Seepage Models

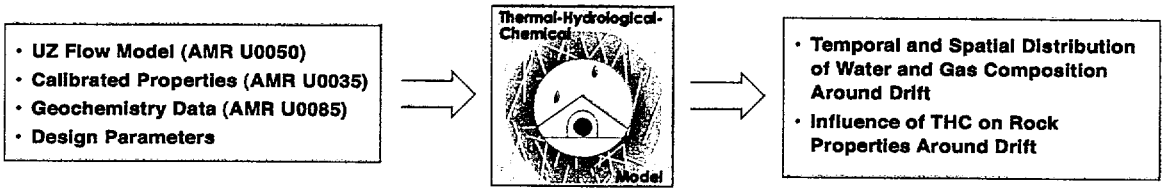

Figure 5.1-4. Schematic of Major Inputs and Outputs of the Drift-Scale THC Models

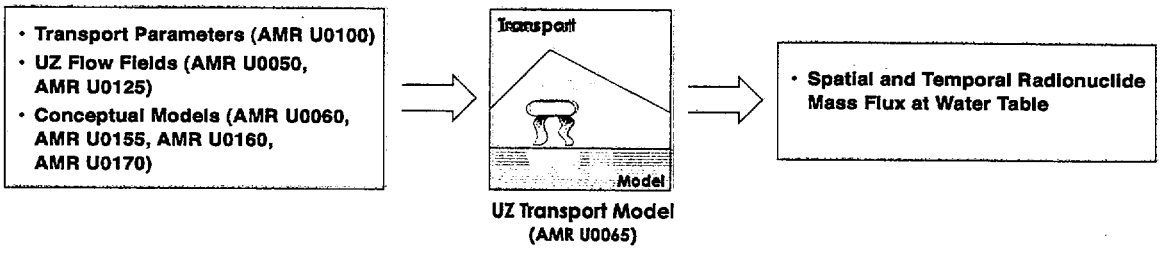

Figure 5.1-5. Schematic of Major Inputs and Outputs of the UZ Transport Models